Three-dimensional dislocation dynamics modelling of particle-reinforced ferrous alloys for nuclear applications



Daniel H. Thompson, MPhys

St Edmund Hall

University of Oxford

A thesis submitted for the degree of

Doctor of Philosophy

Trinity Term 2015

Abstract

Three-dimensional dislocation dynamics modelling of particle-reinforced ferrous alloys for nuclear applications

Daniel H. Thompson, MPhys
St Edmund Hall, University of Oxford

A thesis submitted for the degree of *Doctor of Philosophy*
Trinity Term 2015

An existing point defect bulk diffusion model of dislocation climb is developed to incorporate both vacancies and interstitials, and supersaturations of these defects. Calculations are carried out for body-centred cubic (bcc) iron using this model, which show that the interstitial nature of experimentally observed irradiation-induced damage loops can be explained by the preferential osmotic absorption of supersaturated interstitials over vacancies by damage loops.

The model is implemented into a 3D dislocation dynamics code, together with a dual glide and climb time step method, and spherical obstacles which are impenetrable to dislocations, all of which required original code development. Simulations of dislocation-inclusion unpinning via climb in particle-reinforced bcc iron are conducted, and the creep strain rate is estimated from the unpinning time data. The thermal creep strain rates are seen to be strongly temperature-dependent, as expected. Varying the applied load and dispersion properties is seen to have a relatively small effect, and remarkably the creep rates exhibit no dependence on the particle size and number density for a given volume fraction of obstacles. The thermal creep strain rates predicted are consistent with experimental observation.

The irradiation creep strain rates are seen to vary much less strongly with temperature, also as expected. These results suggest that in particle-reinforced alloys under advanced nuclear reactor operating conditions, it is possible the irradiation creep rate will be orders of magnitude larger than the thermal creep rate at this temperature, depending on the value of the steady-state point defect supersaturations available to drive dislocation climb. In this case, the use of such alloys for advanced nuclear applications will be somewhat limited.

Preface

The research described in this thesis was carried out by the author in the Department of Materials at the University of Oxford between October 2011 and September 2015, under the supervision of Prof Steve Roberts, Dr Steve Fitzgerald and Dr Ed Tarleton. All the work is original, and where work from others has been included it has been clearly referenced and acknowledged. No part of this thesis has been submitted or accepted for any other degree at this university or elsewhere.

Parts of this work have been presented at conferences and workshops as follows:

Thompson, D. H., Fitzgerald, S. P., Tarleton, E., and Roberts, S. G. (2014). 3D discrete dislocation dynamics modelling of dislocation-inclusion interactions in nano-structured steels. *Poster presentation* at Materials for Fusion & Fission Power Showcase Meeting, 10 December 2014, Oxford, UK.

Thompson, D. H., Fitzgerald, S. P., Tarleton, E., and Roberts, S. G. (2014). 3D discrete dislocation dynamics modelling of dislocation-inclusion interactions in nano-structured steels. *Poster presentation* at Dislocations: The Legacy of Alan Head, 1–2 September 2014, Oxford, UK.

Thompson, D. H., Fitzgerald, S. P., Tarleton, E., and Roberts, S. G. (2013). 3D discrete dislocation dynamics modelling of dislocation-inclusion interactions in nano-structured steels. *Poster presentation* at Modelling of Radiation Damage and its Effects on Materials, 25–27 September 2013, Oxford, UK.

Thompson, D. H., Fitzgerald, S. P., Tarleton, E., Dudarev, S. L., and Roberts, S. G. (2013). 3D discrete dislocation dynamics modelling of dislocation-inclusion interactions in nano-structured steels. *Oral presentation* at EUROMAT 2013, 8–13 September, Seville, Spain.

Thompson, D. H., Fitzgerald, S. P., Roberts, S. G., and Dudarev, S. L. (2012). Dislocation-inclusion interactions for dislocation dynamics modelling of nano-structured steels. *Poster presentation* at 2012 MRS Fall Meeting & Exhibit, 25–30 November, Boston, Massachusetts, USA.

Acknowledgements

Firstly, I would like to acknowledge the guidance, support, and encouragement of my supervisors. Specifically, I am grateful to: Prof Steve Roberts, for overseeing the project; Dr Steve Fitzgerald, for his enthusiasm; and Dr Ed Tarleton, for his practical advice. I would also like to acknowledge Dr Sergei Dudarev, for interesting and challenging discussions, and Dr Daniel Balint and Prof Roger Reed, for acting as my examiners.

I would like to thank all my colleagues in the Materials for Fusion & Fission Power group for their help and friendship, in particular Dr Ele Grieveson and Dr Mike Gorley. A special mention must go to Chris Akinola, who managed to resurrect my computer on several occasions, even the time I melted its insides. I would also like to recognise Andrew Breakspear and the late Mike McShane for their support at Teddy Hall.

This research would not have been possible without the financial support provided by the Engineering and Physical Sciences Research Council on behalf of UK taxpayers, and I would like to show my appreciation for being given this opportunity.

I would like to express my gratitude to Prof David Andrews and Prof Todd Huffman, both of whom played a huge part in making me the physicist and tutor I am today.

Most of all, I would like to thank Hemma and Nick Thompson (Mum and Dad) for their love, encouragement, and boundless generosity in supporting and providing for both me and my brother Liam.

Finally, I would like to disacknowledge Chris Jones, Dr Linda Briggs, Renugan Raidoo, Gemma Prata, the Teddy Hall Family, the Hall MCR, Boat Club and Choir, Hertford MCR, Andy Skinner, OUJO, and — worst of all — Lucy Erickson. This thesis is presented in spite of their best efforts.

This thesis is dedicated to my parents,

Nick and Hemma

Contents

1 Introduction **1**

1.1 Nuclear fusion energy 1

1.2 Research objectives 4

1.3 Thesis outline 4

2 Dislocations and irradiation literature review **7**

2.1 Introduction 7

2.2 Point defects 8

2.3 Dislocations 11

2.3.1 Dislocation motion 12

2.3.2 Glide 13

2.3.3 Dislocation glide and mechanical properties 15

2.3.4 Cross slip 16

2.3.5 Climb 17

2.3.6 Dislocation mobility 21

2.3.7 Dislocation interactions 22

2.3.8 Dislocations and strengthening mechanisms 25

2.3.9 Creep 26

2.3.10 Dislocation sources 27

2.3.11 Dislocations in bcc metals 29

2.3.12 Effects of anisotropic elasticity in bcc iron 31

2.4 Computational modelling of dislocations 33

2.4.1 3D discrete dislocation dynamics (DDD) 35

2.4.2 Modelling climb in DDD . . . 39
2.5 Irradiation damage . . . 43
2.5.1 Displacement cascades . . . 44
2.5.2 Damage defects . . . 46
2.5.3 Effects on mechanical properties . . . 48
2.5.4 Irradiation creep . . . 49
2.5.5 Irradiation resistant materials . . . 50

3 Theory and modelling of dislocation climb 53
3.1 Introduction . . . 53
3.2 Dislocation climb via point defect bulk diffusion . . . 54
3.3 Calculations for bcc iron . . . 60
3.3.1 Thermal point defect concentrations . . . 60
3.3.2 Dislocation climb mobilities . . . 61
3.3.3 Osmotic forces . . . 63
3.3.4 Osmotic climb velocities . . . 65
3.3.5 Comparison of thermal and osmotic climb velocities . . . 66
3.3.6 Defect supersaturation estimation from the interstitial loop behaviour transition temperature . . . 71
3.3.7 Circular prismatic loop self-force . . . 73
3.3.8 Comparison with experiment . . . 75
3.4 Summary . . . 76

4 Code development and testing: dislocation climb 79
4.1 Introduction . . . 79
4.2 `DDLab` functionality as released . . . 80
4.2.1 Mobility law for bcc metals . . . 81
4.3 Temperature-dependent climb . . . 83
4.3.1 Implementing thermal vacancy mediated climb . . . 83
4.3.2 Square prismatic loop . . . 84
4.3.3 Effect of introducing a compressive load . . . 86
4.3.4 Kinetics of a circular prismatic dislocation loop . . . 87

4.3.5 Comparison between simulation and theory: effect of varying minimum segment length . . . 88
4.3.6 Comparison between simulation and theory: effect of varying temperature . . . 90
4.3.7 Circular prismatic loop . . . 92
4.3.8 Implementing an osmotic force due to supersaturated vacancies . 94
4.3.9 Effect of an osmotic force due to supersaturated vacancies 95
4.3.10 Threshold vacancy supersaturation for vacancy loop growth . . . 98
4.3.11 Implementing interstitial mediated climb . . . 101
4.3.12 Supersaturations of both vacancies and interstitials . . . 102
4.4 Calibrating `DDLab`: effect of varying $\ell_{\min}$ and $\ell_{\max}$ . . . 105
4.4.1 Attempt 1: scaled $\ell_{\min}$ and $\ell_{\max}$ with an osmotic force present . 105
4.4.2 Attempt 2: scaled $\ell_{\min}$ and $\ell_{\max}$ without an osmotic force present 108
4.4.3 Attempt 3: plotting the actual values of $\ell_{\min}$ and $\ell_{\max}$ . . . 111
4.5 Glide and climb: a dual time step method . . . 112
4.5.1 Implementing the dual time step method . . . 113
4.5.2 Square prismatic loop under shear loading . . . 114
4.5.3 Circular prismatic loop under shear loading . . . 118
4.5.4 Calibrating the minimum plastic strain ratio η . . . 121
4.6 Concluding remarks . . . 122

5 Inclusions literature review 125
5.1 Introduction . . . 125
5.2 Inclusions . . . 125
5.2.1 Dispersion strengthening . . . 126
5.2.2 The stress field of a misfitting inclusion . . . 129
5.2.3 Oxide dispersion-strengthened steels . . . 130
5.2.4 Computational modelling of dislocation-inclusion interactions . . 133
5.3 Concluding remarks . . . 136

6 Code development and testing: inclusions 139
6.1 Introduction . . . 139

6.2 Impenetrable inclusions 140
6.2.1 Implementing spherical impenetrable inclusions 141
6.2.2 Isolated shear dislocation loop behaviour 142
6.2.3 Dislocation-inclusion test simulation: no applied load 144
6.2.4 Dislocation-inclusion test simulation: applied shear load 146
6.2.5 Dislocation-inclusion test simulation: applied compressive load . 148
6.2.6 Dislocation-inclusion test simulation: defect supersaturations present 150
6.3 Concluding remarks 151

7 Dislocation-inclusion simulation results 153
7.1 Introduction 153
7.2 Simulation setup and demonstrative behaviour 154
7.2.1 Simulation setup 154
7.2.2 Effect of applied σ_{13} shear load on pinning time 156
7.2.3 Demonstrative behaviour: applied σ_{12} shear load 158
7.2.4 Demonstrative behaviour: applied σ_{11} compressive load 162
7.2.5 Demonstrative behaviour: defect supersaturations present 164
7.3 Dislocation-inclusion unpinning time analysis 167
7.3.1 Dependence on applied σ_{13} shear load 167
7.3.2 Dependence on temperature 169
7.3.3 Dependence on applied load 171
7.3.4 Dependence on obstacle size 173
7.3.5 Dependence on defect supersaturation 175
7.4 Creep strain rate estimation from the unpinning time 180
7.5 Creep strain rate analysis 184
7.5.1 Dependence on temperature 184
7.5.2 Dependence on applied load 186
7.5.3 Dependence on obstacle size 188
7.5.4 Parametric dependences: obstacle size, number density and volume fraction 190

7.5.5 Dependence on defect supersaturation 200
7.6 Summary 204

8 Conclusions and further work **207**
8.1 Theoretical modelling of dislocation climb 207
8.2 3D DDD simulations of dislocation climb over obstacles 209
8.3 Further work 211

References **213**

A Climb via point defect bulk diffusion: calculations for tungsten **225**
A.1 Comparison of thermal and osmotic climb velocities 225
A.2 Supersaturation estimation from the transition temperature 227

B New original `DDLab` code **229**
B.1 Code added to existing scripts 229
B.1.1 An example `input_dd3d` script 229
B.1.2 The dual time step `main_dd3d` script 233
B.2 Code added to existing functions 237
B.2.1 `segforcevec` (excerpt) 237
B.2.2 `segforcevecInt` (excerpt) 240
B.2.3 `mobbcc0` 240
B.2.4 `mobbcc0Int` 244
B.2.5 `drndt` 247
B.3 New functions 248
B.3.1 `calcClimbDragVac` 248
B.3.2 `calcOsmoticForceVac` 249
B.3.3 `calcClimbDragInt` 249
B.3.4 `calcOsmoticForceInt` 250

Chapter 1

Introduction

In 2009 fossil fuels contributed to meeting 81% of the world's energy needs (IEA, 2011, p. 6). This is unsustainable for a number of reasons. In order to limit global temperature rise to no more than 2 °C a significant reduction in greenhouse gas emissions, and thus the use of fossil fuels, is required (Meinshausen et al., 2009). Furthermore, as fossil fuel resources become scarce and global energy demands rise, a new safe, cheap, and clean energy resource will be needed. Nuclear fusion energy is an appealing candidate to replace fossil fuels in the future (Ward and Dudarev, 2008).

1.1 Nuclear fusion energy

In a magnetic confinement fusion reactor, also called a tokamak, a deuterium-tritium (D-T) plasma is confined within a torus-shaped vacuum vessel by strong magnetic fields, and heated until D-T fusion reactions occur. A schematic representation of a tokamak is shown in figure 1.1(a). A single D-T reaction produces a 3.5 MeV ^{4}He ion, and a 14 MeV neutron. In a fusion power plant, (some of) the energy of these 14 MeV neutrons will be captured and converted into heat in the tokamak blanket (see figure 1.1(b)), which in turn is used to drive steam turbines and generate electricity (Gross, 1984).

Currently the world's largest operating experimental tokamak is the Joint European

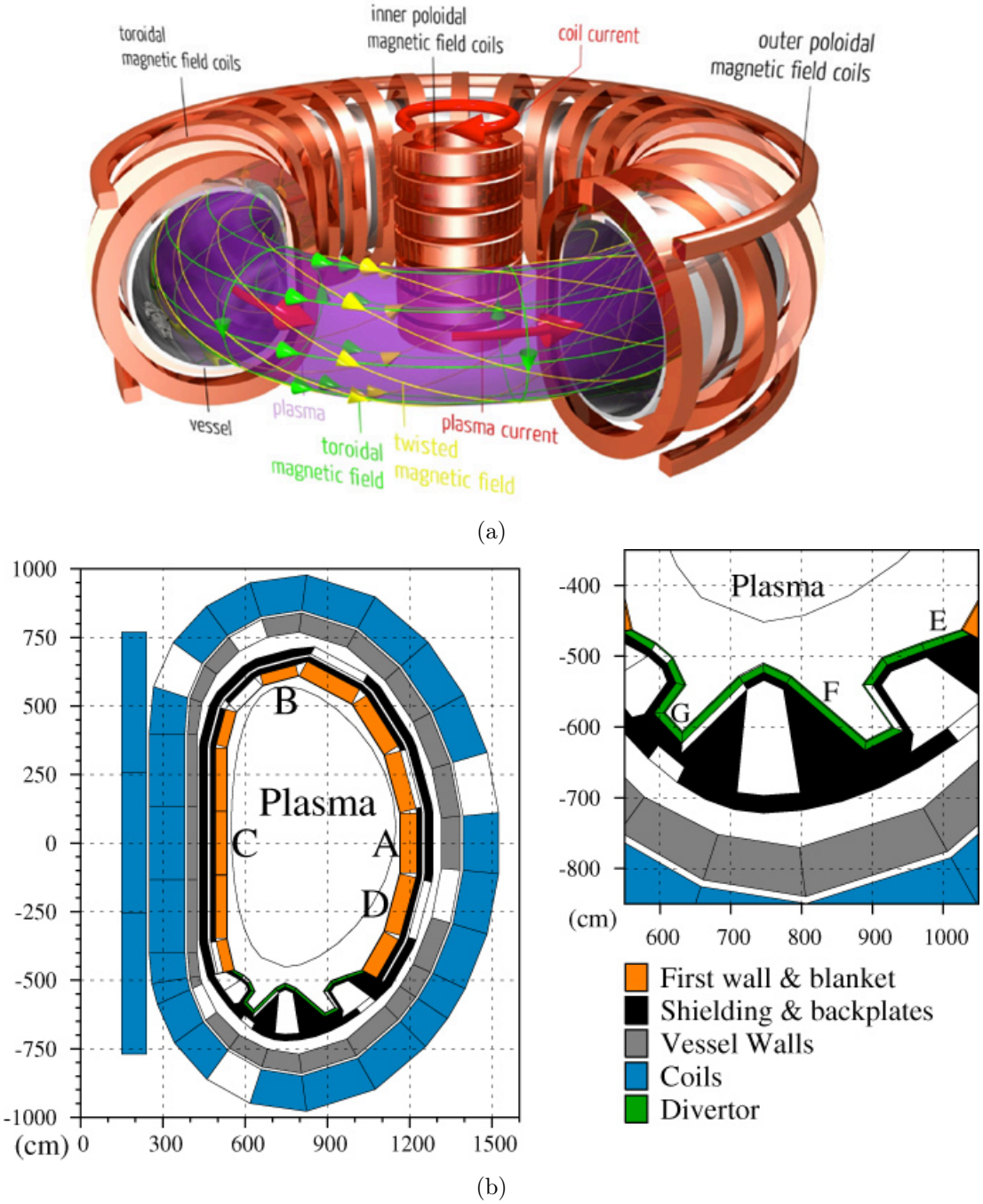


Figure 1.1: (a) A schematic representation of a tokamak. (b) A toroidal cross section through a model tokamak. This simplied model was used by Gilbert et al. in simulations to obtain neutron fluxes and spectra at various points A–D on the plasma-facing first wall and blanket (and points E–G on the divertor). *(a) from Hirsch (2014), (b) from Gilbert et al. (2012).*

Torus (JET) at the Culham Centre for Fusion Energy in Oxfordshire, UK (CCFE, 2012). An even larger experimental reactor, ITER, is currently under construction in Caderache, France, which is scheduled to produce its first plasma in 2020 (ITER, 2015). The performance of ITER will pave the way for the world's first demonstration nuclear fusion power plant, DEMO, which is in the conceptual design phase at present. It is hoped DEMO will begin operations in the early 2030s, and produce useable electricity as early as 2040.

The unprecedented amounts of neutron irradiation experienced by the first wall and blanket in a tokamak present a significant materials challenge (Schiller, 1993). The cascade damage (Ishino, 1996), transmutation damage (Seki et al., 1998), and hydrogen and helium accumulation (Gilbert et al., 2012) due to the neutron irradiation will occur at higher levels than in materials which are currently used similarly in the nuclear fission industry, due to the different — and on average, higher — energy spectra of the neutron fluxes[1]. In order to reduce long-lived radioactive waste upon reactor decomissioning, the materials' constituents are limited to low activation elements (Ward and Dudarev, 2008), such as iron, chromium and tungsten. The use of some common alloying elements, such as nickel, aluminium and niobium, is therefore ruled out (Gorley, 2014). Together with the high operating temperatures required by fusion reactor first wall/blanket materials (Bloom, 1998), these challenges mean that the development of advanced structural materials for use in a fusion reactor also has applications for future Generation IV (Gen IV) fission reactors (Zinkle and Was, 2013).

Due to the microscopic nature of these effects, understanding the physics of fusion reactor materials on the microscale, and how this affects their mechanical properties, is an essential part of making fusion energy a reality.

[1]There is also the fusion-specific problem of erosion due to the interaction between the plasma facing components and the plasma itself (Bolt et al., 2004). This is particularly important for the divertor (see figure 1.1(b)), where the plasma is deliberately brought into contact with the divertor plate, resulting in sputtering of the divertor material, and an extreme heat flux of the order of MWm^{-2}.

1.2 Research objectives

The aim of this thesis is to investigate some of the nanoscale physics which occurs in ferrous alloys, and their particle-reinforced counterparts, under both non-irradiation and irradiation conditions. This done using both theoretical modelling and computational simulations. The main questions this thesis seeks to answer are:

1. How does temperature and irradiation damage affect dislocation climb?
2. What can be learned from modelling irradiation-induced dislocation loop behaviour using temperature-dependent climb?
3. Is the creep response of particle-reinforced alloys caused by the climb of pinned dislocations over the strengthening particles?
4. How do the particle dispersion properties affect the creep response?
5. What can be learned from this modelling about the irradiation creep resistance of particle-reinforced alloys?

1.3 Thesis outline

This thesis is structured as follows:

Chapter 2 provides an introduction to the theory of point defects, dislocations, and irradiation damage, and the relevant literature. As ferrous alloys for nuclear applications are of particular interest, they are mentioned throughout.

Chapter 3 presents the results of the theoretical modelling of dislocation climb, both for thermal climb, and climb driven by non-equilibrium point defect supersaturations. The results are compared to the experimental characterisation of post-self-ion-irradiated bcc iron.

Chapter 4 describes the implementation of this theoretical climb model into an existing three-dimensional dislocation dynamics code, and subsequent code development.

Chapter 5 provides an introduction to the theory of particle-reinforced materials, and

discusses oxide dispersion-strengthened (ODS) ferrous alloys, together with the relevant literature.

Chapter 6 describes the implementation of three-dimensional obstacles which are impenetrable to dislocations into the dislocation dynamics code.

Chapter 7 presents and discusses the results of simulations of dislocation interactions with these impenetrable obstacles. The results are compared to experimental data on the thermal creep of ODS ferrous alloys, and predictions are made regarding the performance of these alloys under fusion reactor relevant irradiation conditions.

Chapter 8 summarises the conclusions of this work and suggests further avenues of research.

Chapter 2

Dislocations and irradiation literature review

2.1 Introduction

This literature survey is split into two main parts.

This first part provides an introduction to dislocations, the crystal defects which act as the carriers of plastic flow, and to irradiation damage. Dislocation motion, interactions, and sources are discussed, followed by the specifics of dislocations in bcc metals, and different approaches to modelling dislocations computationally. Irradiation damage is then reviewed, including some of the effects it has on mechanical properties, and some approaches to improving material resistance to these effects.

The second part, chapter 5, concerns inclusions — particularly nanoscale particles, or dispersoids — and their effects on material deformation behaviour. Particle-reinforced ferrous alloys for fusion applications, and attempts to model dislocations in such materials computationally, are also discussed.

To begin with however, the following section provides a brief introduction to point defects, as these are relevant to both dislocations and irradiation damage.

2.2 Point defects

In many solid materials, including metals and alloys, the atoms are arranged in a regular crystal structure. In a macroscopic sample, microscale single crystals — or grains — are fused together at grain boundaries. However, many of a material's mechanical properties are governed by the physical processes which take place within the single crystals.

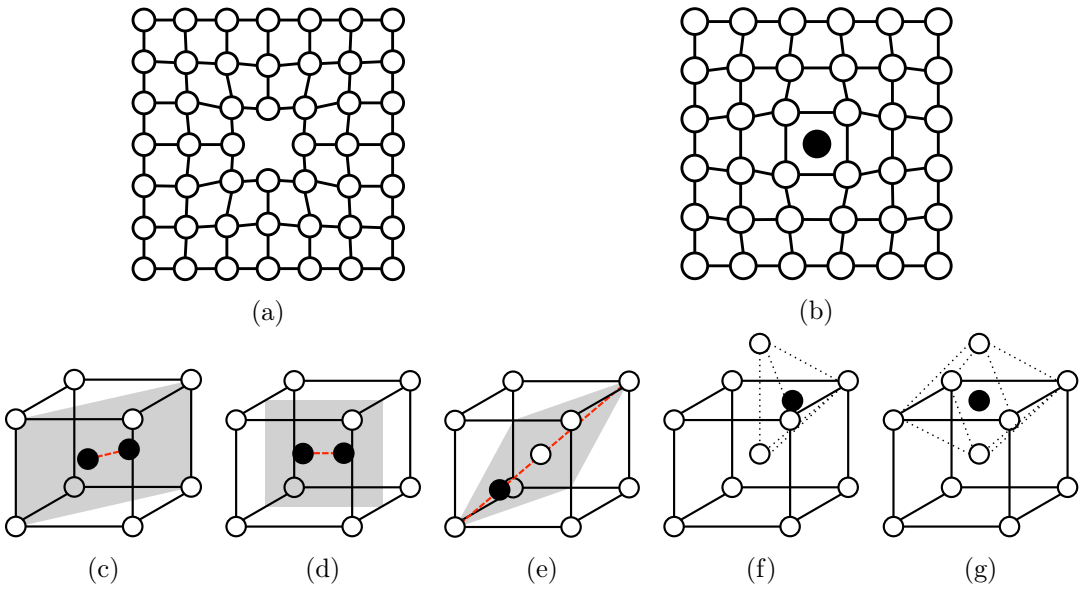


Figure 2.1: Different types of point defect: (a) vacancy, (b) interstitial; and different self-interstitial atom (SIA) configurations in a bcc lattice: (c) ⟨110⟩ dumbbell, (d) ⟨100⟩ dumbbell, (e) ⟨111⟩ crowdion, (f) tetrahedral, (g) octahedral. In (e), the incremental displacement of the extended 1D string of atoms in the ⟨111⟩ direction that make up the crowdion is not shown.

At non-zero temperatures, a single crystal is not a perfect lattice, but contains zero dimensional point defects (Hull and Bacon, 2011). There are two opposite types of point defects. The first is a lattice site which is not occupied by an atom, i.e. a gap in the crystal lattice (see figure 2.1(a)). Such a vacant lattice site is known as a vacancy point defect. The second type of point defect is an atom which occupies a non-lattice site, i.e. it is inserted into the matrix material at a location where an atom would not normally be found (figure (b)). This is known as a self-interstitial atom (SIA). Depending its position relative to the lattice structure, the SIA will have one of several possible configurations specific to the type of lattice. In bcc iron, the lowest energy SIA configuration is the ⟨110⟩ dumbbell configuration (Dudarev, 2013), but ⟨100⟩ dumbbell,

⟨111⟩ crowdion, tetrahedral and octahedral configurations are also found (figures (c)–(g)). Note that for dumbbell (and indeed crowdion) configurations it is impossible to identifiy which atom of the two (or many) which are displaced about their equilibrium positions is the original SIA.

Vacancies and SIAs are present in a material at concentrations determined by their formation energies and the temperature. The fractional thermodynamic equilibrium concentration c_0 of a point defect of formation energy E_f at temperature T is given simply by the Boltzmann factor:

$$c_0 = \exp\left(-\frac{E_\mathrm{f}}{k_\mathrm{B}T}\right), \tag{2.1}$$

where k_B is Boltzmann's constant. Hence the formation of point defects is a thermally-activated process: one which depends very strongly on temperature. As the formation energy of vacancies is generally lower than that of interstitials[2], the equilibrium population of vacancies is generally significantly larger than that of interstitials. A point defect population which is higher than c_0 at the given temperature is known as a supersaturation. For example, a supersaturation of vacancy defects is produced when a material undergoes quenching.

Point defects can diffuse through the lattice, obeying the local diffusion equation

$$\frac{\partial c}{\partial t} = D\nabla^2 c, \tag{2.2}$$

where $c = c(\mathbf{r}, t)$, and D is the diffusion coefficient given by

$$D = D_0 \exp\left(-\frac{E_\mathrm{m}}{k_\mathrm{B}T}\right), \tag{2.3}$$

where E_m is the migration energy of the given defect, and D_0 is the defect diffusion prefactor which characterises diffusion at very high temperatures[3] $> E_\mathrm{m}/k_\mathrm{B}$. If a vacancy

[2] In this work, SIAs are often referred to as simply "interstitials", although in general an interstitial atom need not be of the same atomic species as that of the matrix constituents, i.e. it can be an impurity atom.

[3] For realistic values of E_m, the material will likely melt before this temperature is reached, so this is an incomplete picture. Rather, D_0 is related to the attempt frequency of the defect escaping the local potential well it currently occupies, i.e. the Debye frequency, and the well width.

and interstitial get close enough to each other, they can mutually annihilate, restoring the perfect lattice structure in this region.

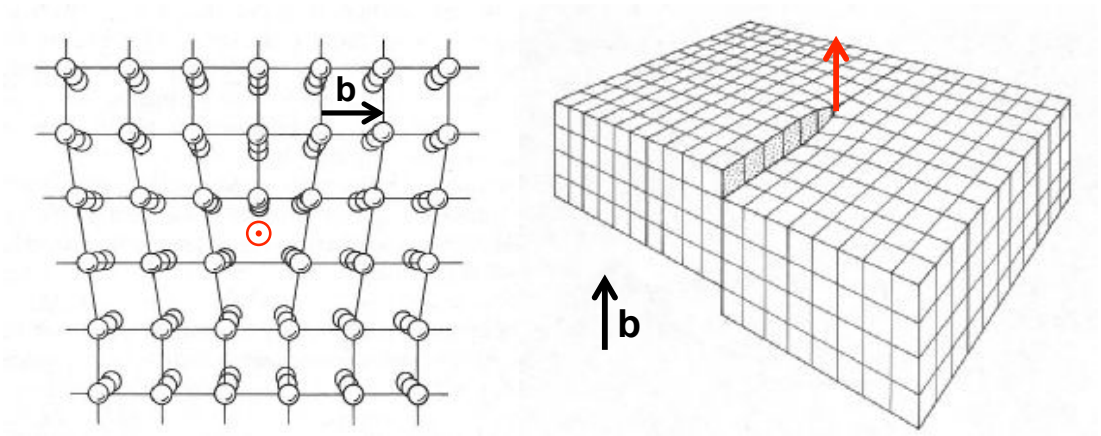
The migration energies of interstitials are generally lower than that of vacancies, allowing them to diffuse through the lattice more quickly. In particular, $\langle 111 \rangle$ crowdions are able to undergo rapid 1D motion along their close-packed lattice directions.

The diffusion of point defects transports matter through the material, and can lead to deformation in a plastic sense (as opposed to elastic deformation, which involves the stretching/shortening of inter-atomic bonds). However, plastic deformation is predominately governed by the formation and motion of dislocations.

2.3 Dislocations

Dislocations are one dimensional line defects which occur in crystalline solids (Volterra, 1907; Taylor, 1934). They act as the carriers of plastic flow, and so an understanding of their behaviour is extremely important when considering the way in which a material will deform. A good introduction to dislocations can be found in Hull and Bacon (2011).

A dislocation is characterised by its line direction, and (principally) its Burgers vector **b**, which describes the lattice disregistry caused by the presence of the dislocation, and is usually a lattice vector (Burgers, 1939). The sign of the Burgers vector is defined using a sign convention such as the right-hand/finish-start convention described by Hull and Bacon (2011, p. 18). The region of a few atomic spacings around the dislocation line is referred to as the dislocation core. There are two simple dislocation geometries, illustrated in figure 2.2.



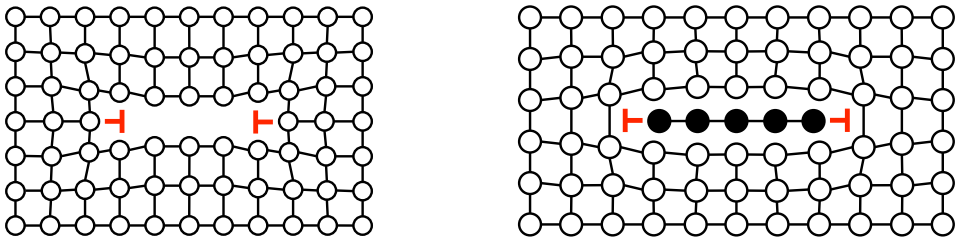
(a) (b)

Figure 2.2: Dislocations in a simple cubic crystal. The Burgers vector **b** is indicated, as is the line direction (in red). (a) An edge dislocation. (b) A screw dislocation. *From Hirth and Lothe (1982).*

An edge dislocation can be thought of as the result of inserting an extra half-plane of atoms mid-way through a crystal. The dislocation line is the inner edge of the extra half-plane, making the Burgers vector perpendicular to the dislocation line. A screw dislocation can be thought of as the result of making a cut part way through a crystal, displacing material on one side of the cut relative to the other, and joining the crystal together again. The crystal planes now have a spiral structure around the dislocation

line, the inner boundary of the cut, so the Burgers vector is parallel to the dislocation line. In general, straight dislocations have a mixed edge and screw character, i.e. their line direction lies at an arbitrary angle to their Burgers vector. The most general case is a curved dislocation, whose dislocation character varies along its line.

An important example of a curved dislocation is a dislocation loop. There are different types of dislocation loop. Shear dislocation loops have Burgers vectors which lie entirely in the plane of the loop. Conversely, prismatic dislocation loops — which are common in irradiation damage — have Burgers vectors which are entirely or partially perpendicular to the plane of the loop. A "pure" prismatic loop (one which has a Burgers vector entirely perpendicular to the plane of the loop) can be thought of as flat "pancake" of agglomerated vacancies (figure 2.3(a)) or SIAs (figure (b)).



(a) (b)

Figure 2.3: Prismatic dislocation loops: (a) vacancy, (b) interstitial. The edge dislocations which intersect the plane of the page are represented by the $\perp$ symbol.

2.3.1 Dislocation motion

In dislocation theory, the dislocations are treated as 1D interacting objects in an elastic continuum that represents the crystal. The fundamentals of dislocation dynamics and interactions can be found in Hirth and Lothe (1982). In this model, a dislocation experiences a force per unit length that depends on the local stress field $\boldsymbol{\sigma}$ as well as its line direction $\boldsymbol{\xi}$ and Burgers vector $\mathbf{b}$ given by

$$\mathbf{F} = (\boldsymbol{\sigma} \cdot \mathbf{b}) \times \boldsymbol{\xi}. \tag{2.4}$$

This general expression was developed by Peach and Koehler (1950), and derived in a different way by Nabarro (1951). Weertman (1965) suggested that a more natural

description of the forces on a dislocation is obtained if the stresses in (2.4) are replaced by the deviatoric stresses $\sigma'_{ij} \equiv \sigma_{ij} - \frac{1}{3}\delta_{ij}\sigma_{kk}$, the ordinary stresses with the hydrostatic part removed (δ_{ij} is the Kronecker delta). Subsequently Lewthwaite (1966) showed that Nabarro's derivation was in error, and when corrected Weertman's expression was reproduced. In § 2.3.6 the way in which the force on a dislocation causes it to move will be discussed, but first a description of the different types of dislocation motion is provided.

Since a dislocation is by definition a line defect, motion of the dislocation parallel to the local line direction is meaningless. There are two basic types of dislocation motion: glide and climb.

2.3.2 Glide

Glide is dislocation motion in the plane that contains both the dislocation's line direction and its Burgers vector, the so-called glide plane. A pure edge dislocation glides in the direction of its Burgers vector, and a mixed dislocation glides in the direction of the component of its Burgers vector which is perpendicular to its line direction. Pure screw dislocations do not have a defined glide plane. They will be discussed in § 2.3.4. Glide is also known as conservative motion, because the volume of the crystal remains constant, and it progresses via the successive breaking and reforming of atomic bonds at the dislocation core, so that in the case of a pure edge dislocation the position of the extra half-plane of atoms appears to move through the crystal, as illustrated in figure 2.4.

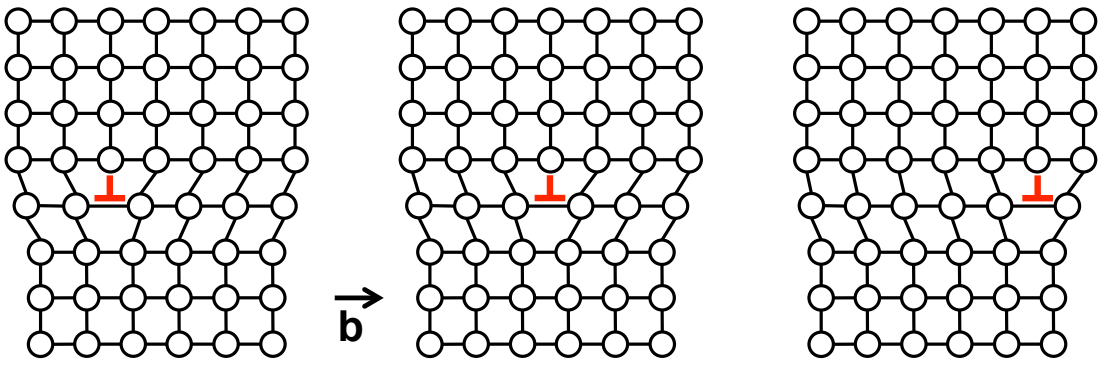


Figure 2.4: An edge dislocation (⊥) gliding from left to right.

For shear dislocation loops glide motion corresponds to the loop either shrinking or

expanding, whereas the glide plane of a prismatic dislocation loop is in fact a glide cyclinder whose axis is perpendicular to the plane of the loop.

Crystallographic slip, the most common form of plastic deformation, occurs when many dislocations on the same glide plane glide in the same direction[4], and results in the formation of slip steps on the surface of the crystal as the dislocations exit the crystal. The slip direction is necessarily parallel to the Burgers vectors of the gliding dislocations, as it is the accumulation of the lattice disregistry manifested by each dislocation, i.e. the Burgers vector, on the surface of the crystal that gives rise to the slip-step, and thus plastic deformation.

A slip system is defined by a slip plane (that is to say, a glide plane normal) and a slip direction (a Burgers vector). Because of the discrete nature of the crystal structure, slip planes and slip directions occur in specific crystallographic orientations, resulting in several possible slip systems. The slip planes are usually the planes with the widest spacing, and the slip directions are normally the close-packed directions.

The successive breaking and reforming of atomic bonds required for dislocation glide leads to a periodic potential energy surface experienced by the dislocation. In order for the dislocation to glide at 0 K, the dislocation must be subjected to a minimum shear stress, the Peierls stress, strong enough to allow the dislocation to overcome the Peierls energy barrier and progress to the next trench of minimum energy (Peierls, 1940; Nabarro, 1947). Atomic-scale computer simulations of metals calculate Peierls stresses orders of magnitude lower than the analytical calculation for a straight dislocation at 0 K. This is because as the temperature increases, the atoms in the lattice vibrate more, allowing segments of the dislocation line to progress to the next energy minimum. These different straight segments of dislocation in adjacent energy minima are connected by kinks which traverse the Peierls energy hump. Less energy is required for kinks to form and migrate than for the entire dislocation line to move rigidly from one energy minimum to the next, reducing the overall stress required for glide.

The critical resolved shear stress (CRSS) for slip is distinct from the Peierls stress. It

[4]Many dislocations on the same glide plane implies the existence of dislocation sources. These will be discussed in § 2.3.10.

is the minimum shear stress a slip system must be subjected to for dislocation sources to start to operate, multiplying the number of gliding dislocations and resulting in macroscopic plastic deformation. If a single crystal is subjected to an externally applied shear stress just large enough to produce slip, the CRSS can be calculated by multiplying the applied stress by the appropriate Schmid factor, a geometrical factor ≤ 0.5, required to resolve the applied stress onto the slip plane in the slip direction (Schmid, 1931).

2.3.3 Dislocation glide and mechanical properties

The CRSS is related to the yield strength, which is the applied tensile stress (rather than shear stress) at which a polycrystalline (rather than single crystal) material starts to deform plastically. A material's yield strength corresponds to the stress at which dislocations are able to glide easily from active sources, and depends on dislocation density, impurity levels, the presence of obstacles to dislocation glide, and temperature. It determines the maximum load a component manufactured out of such a material can withstand before plastic failure begins, and is empirically measured in constant strain rate tensile tests.

In ductile materials, once the load stress in such tests reaches the yield stress, the material starts to deform plastically, which continues as the load stress increases until finally failure via fracture occurs. The stress required for a material to continue to deform plastically at a given strain is known as the flow stress, a sort of "strain dependent yield stress". During yield, the increase in the flow stress with increasing strain is referred to as hardening, and is due to the dislocations requiring an increasing level of stress to continue to glide.

Moderate amounts of ductility can be useful, as plastic failure provides a safer soft failure mode, as opposed to the catastrophic failure of brittle materials when they fracture after undergoing very little plastic deformation. Whether a material is ductile or brittle at a given temperature also depends on whether the dislocations are able to glide substantially at that temperature (Tarleton and Roberts, 2009).

Material which is too ductile, or "soft", can be made less so by increasing its yield

strength, which is achieved by making it more difficult for dislocations to glide[5]. Strengthening mechanisms include: work hardening, grain size refinement, solid solution strengthening, precipitation strengthening, and dispersion strengthening (Hull and Bacon, 2011, § 10.7-9), which will be discussed in § 2.3.7.

2.3.4 Cross slip

Although pure screw dislocations do not have a defined glide plane, they can also undergo conservative motion. They tend to move in certain crystallographic planes, and can switch from one plane to another providing the new plane also contains the Burgers vector. This is called cross slip, and occurs when the local stress field experienced by the dislocation makes a switch of planes energetically favourable. Increasing the temperature makes cross slip more likely, as it is a thermally activated process which requires the dislocation core structure to reorganise. An example of cross slip is shown in figure 2.5.

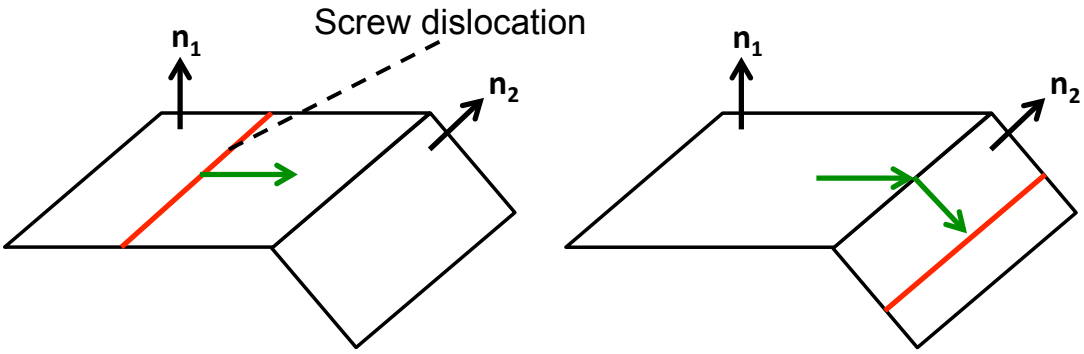


Figure 2.5: A screw dislocation undergoing cross slip.

At sufficently high temperatures cross slip events can happen so frequently that screw dislocations appear to move in a direction which does not lie in any crystallographic plane (Cai and Bulatov, 2004). The screw dislocations are in fact still restricted to in plane motion, but they are constantly undergoing cross slip between a subset of planes to produce this apparent motion. This process is known as pencil glide.

In some face-centred cubic (fcc) metals, dislocations can dissociate into two partial dislocations with a crystallographic plane stacking fault between them (Hull and Bacon,

[5]Hence strenghtening can also be thought of as making a material “harder”.

2011). This makes cross slip more difficult, because a dissociated screw dislocation must first constrict to form a pure screw in order to undergo cross slip. Cross slip is particularly difficult for fcc metals with low stacking fault energies, because the width of the dissociated dislocations increases with decreasing stacking fault energy, making constriction less likely. In fcc metals with high stacking fault energies, and in bcc metals in which dislocation dissociation does not occur, cross slip can be important.

2.3.5 Climb

Climb is dislocation motion out of the glide plane, i.e. perpendicular to both the line direction and the Burgers vector, so pure screw dislocations do not climb[6]. It is also known as non-conservative motion, because it is the result of the thermally activated diffusion of vacancies or interstitials to/from the dislocation line where they are absorbed/emitted at unit jogs on the dislocation line, as shown schematically in figure 2.6 (Arakawa et al., 2000). Thus, when a dislocation climbs, matter is transported either to or away from the dislocation core.

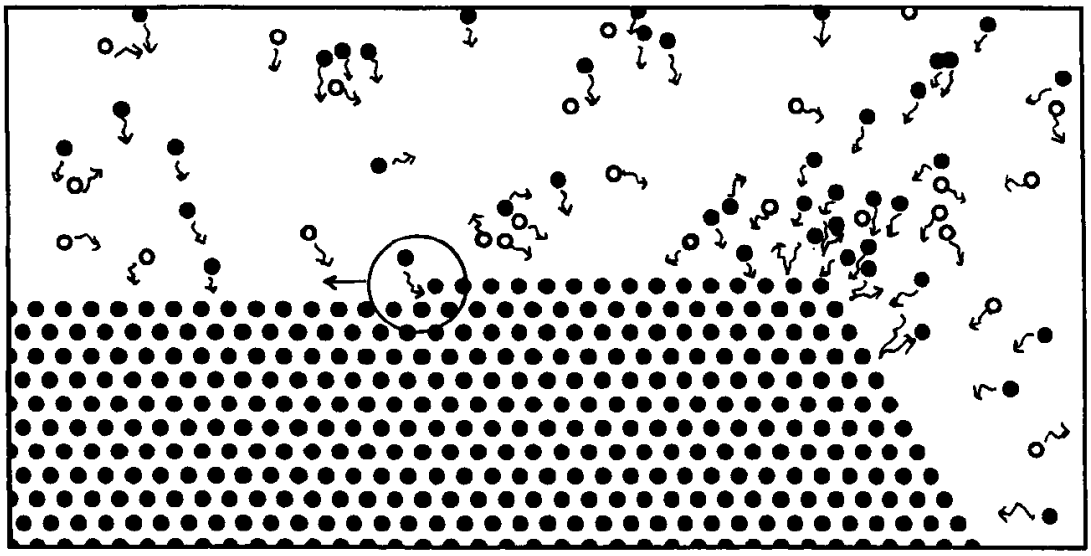


Figure 2.6: A schematic view of part of an interstitial dislocation loop growing via climb. The black dots represent interstitials, and the white dots represent vacancies. The 'step' in the encircled region is a unit jog. *From Arakawa et al. (2000).*

[6]Due to thermal fluctuations, parts of a pure screw dislocation can gain a slight edge component, which might then be able to climb. In certain situations screw dislocations form helical dislocations via this instability (Amelinckx et al., 1957; de Wit, 1959; Louchet and Kubin, 1975).

When defects diffuse to prismatic dislocation loops, the loops will incrementally grow or shrink depending on their type, and whether the defect is a vacancy or an interstitial. Hence growth (or shrinkage) of prismatic loops is a purely climb process.

Prismatic dislocation loops can also exhibit translational in-plane motion, and/or change their shape, without changing their overall area by undergoing another type of climb — known as conservative climb — but this is relatively uncommon (Kroupa and Price, 1961). Conservative climb is dislocation motion mediated by pipe diffusion: in the case of a dislocation loop undergoing conservative climb, this involves point defects from one side of the loop diffusing along the dislocation core to the other side. Such motion is clearly a climb only process, but it does not involve the diffusion of point defects to/from the loop, i.e. the number of point defects that constitute the loop is conserved, hence the name. Conservative climb only occurs when both the temperature and the stress on a dislocation loop are high enough, such as when two loops are very close together (Love, 1964).

Since climb is mediated by the thermal populations of point defects, and the thermal vacancy population is generally much larger than that of interstitials, climb is generally considered to be mediated by vacancies (Mordehai et al., 2008; Hull and Bacon, 2011; Bakó et al., 2011), with interstitials playing a significantly smaller role, if indeed any at all.

Bullough and Newman (1970) give a comprehensive review of the different interactions between point defects and dislocations that lead to point defect diffusion to dislocations and hence climb. The most important is the first-order size interaction. When a point defect is incorporated into the dislocation core it is removed from the bulk, resulting in a change in the overall volume of the crystal, as the lattice distortion caused by the point defect disappears. This distortion is characterised by an associated relaxation volume for the point defect. In bcc iron, this relaxation volume is -0.32 atomic volumes (Ω) for a vacancy, and 0.91Ω for a $\langle 110 \rangle$ interstitial (Wolfer, 1982, 2007, p. 411). This first-order size interaction is the interaction between the hydrostatic part of the long-range stress field of the dislocation and the relaxation volume of the point defect. Margvelashvili and Saralidze (1974) studied the effects of the stress field of a dislocation on the steady-

state diffusion fluxes of point defects during climb. Dislocation stress fields will be discussed in § 2.3.7. The inhomogeneity interaction is also important when considering vacancies. This is the second-order interaction due to the different elastic constants that characterise the bulk material and the point defect. Over the volume of a vacancy the elastic constants are zero, so they differ significantly from those of the bulk material. Other interactions include the second-order size interaction which takes in to account the third-order (non-linear) elastic properties of the crystal, and electrical and chemical interactions. However, representing the point defects which interact with dislocations as concentration mean fields allows dislocation climb to be modelled in a relatively straightforward manner.

When a dislocation climbs, the component of the Peach–Koehler (P–K) force in the climb direction F_{cl} (discussed in § 2.3.6) will make it energetically favourable for vacancies to be either absorbed or emitted from the dislocation core, and vice versa for interstitials. Which way round will depend on the relative geometry of the dislocation and the local stress state.

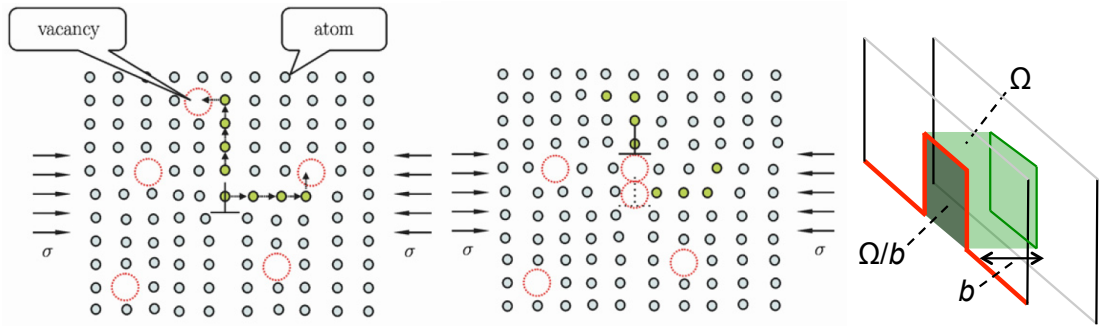


Figure 2.7: (a) An edge dislocation undergoing vacancy mediated climb due to a uniaxial compressive stress σ. The vacancies diffuse towards the dislocation via the successive jumping of adjacent atoms towards the vacancy site. (b) The dislocation has climbed up a distance of two atoms as a result of this diffusion. (c) Schematic diagram of a unit jog, illustrating that the area swept out by the dislocation when a single vacancy is absorbed is Ω/b, where Ω is the atomic volume. *(a) and (b) from Gao and Cocks (2009).*

For example, if the pure edge dislocation in figures 2.7(a) and (b) climbs up due to a uniaxial compressive stress σ as shown, the work done by the compressive load per atomic site on the dislocation line is $F_{\mathrm{cl}} = +\sigma b$ multiplied by the *area* swept out at the

atomic site, because the P–K force is a force *per unit length* of dislocation. Here $b \equiv |\mathbf{b}|$ is the magnitude of the Burgers vector. From geometric considerations this area must be equal to Ω/b, where Ω is the atomic volume, as illustrated in figure 2.7(c). Since $+F_{\mathrm{cl}}\Omega/b$ is the work done per atomic site, it is the work done per vacancy absorbed, i.e. destroyed. Thus the thermodynamic vacancy formation energy in the vicinity of the dislocation line is effectively increased by this amount of work (whereas the interstitial formation energy is effectively decreased by this amount). As a result of this chemical potential, the fractional vacancy concentration c^{v} close to the dislocation then becomes

$$c^{\mathrm{v}} = \exp\left(-\frac{E_{\mathrm{f}}^{\mathrm{v}} + F_{\mathrm{cl}}\Omega/b}{k_{\mathrm{B}}T}\right) \tag{2.5a}$$

$$= c_0^{\mathrm{v}} \exp\left(-\frac{F_{\mathrm{cl}}\Omega/b}{k_{\mathrm{B}}T}\right), \tag{2.5b}$$

where c_0^{v} is the (fractional) equilibrium vacancy concentration in a dislocation free crystal (2.1) given by[7] $c_0^{\mathrm{v}} = \exp(-E_{\mathrm{f}}^{\mathrm{v}}/k_{\mathrm{B}}T)$. In bcc iron, $E_{\mathrm{f}}^{\mathrm{v}}$ is between 1.6 and 2.2 eV (Derlet et al., 2007, p. 4). In this scenario vacancies will be depleted close to the dislocation ($c^{\mathrm{v}} < c_0^{\mathrm{v}}$), resulting in a concentration gradient and hence vacancy diffusion towards the dislocation. In steady-state quasi-equilibrium the chemical climb force due to this chemical potential balances the mechanical climb force F_{cl} (Turunen, 1976). Using appropriate boundary conditions for the fractional point defect concentrations, the rate of climb can be calculated from the diffusion flux of point defects to the dislocation. With some approximations, a linear mobility law (see § 2.3.6) for the climb rate of the form of (2.7b) can be reached (Hirth and Lothe, 1982; Nix et al., 1971; Mordehai et al., 2008; Bakó et al., 2011).

In the absence of a component of the P–K force in the climb direction, climb can still occur if there is point defect supersaturation in the bulk material (Silcox and Whelan, 1960). This affects the boundary conditions used for the point defect concen-

[7] Care needs to be taken when internal and/or external stresses are present in the crystal. For example, Raabe (1998) replaces $E_{\mathrm{f}}^{\mathrm{v}}$ in the expression for c_0^{v} with $[G_{\mathrm{f}}^{\mathrm{v}} + (\sigma_{\mathrm{h}} + p)\Delta V]$, where $G_{\mathrm{f}}^{\mathrm{v}}$ is the Gibbs free enthalpy of formation of a vacancy in a stress free crystal, σ_{h} is the external hydrostatic stress component, p is the internal hydrostatic stress component (a function of position), and ΔV is the externally measured volume change. See the discussion of Hirth and Lothe (1982, § 15-4).

trations when solving for the point defect diffusion flux, and results in an additional load-independent contribution to the rate of climb.

2.3.6 Dislocation mobility

Dislocations move at velocities which depend on their dislocation character, the applied shear stress, temperature and crystal purity. At low temperatures equilibrium point defect concentrations are negligible, and so in the absence of a supersaturation of point defects, very little climb can occur, and dislocations move almost exclusively by glide. At higher temperatures, dislocations are able to climb, but they do so with a small speed compared to their glide speed because the rate of climb is limited by the rates of point defect emission and diffusion (Whelan, 1966).

In order to obtain expressions for glide and climb velocities, the P–K force given by (2.4) needs to be resolved onto the glide and climb directions, which yields

$$F_{\mathrm{gl}} = [(\boldsymbol{\sigma} \cdot \mathbf{b}) \times \boldsymbol{\xi}] \cdot \mathbf{m}, \quad \text{and} \tag{2.6a}$$

$$F_{\mathrm{cl}} = [(\boldsymbol{\sigma} \cdot \mathbf{b}) \times \boldsymbol{\xi}] \cdot \mathbf{n}, \tag{2.6b}$$

where $\mathbf{m}$ and $\mathbf{n}$ are unit vectors in the glide and climb directions respectively, given by $\mathbf{n} \equiv \mathbf{b} \times \boldsymbol{\xi}/|\mathbf{b} \times \boldsymbol{\xi}|$ and $\mathbf{m} \equiv \mathbf{n} \times \boldsymbol{\xi}$. The glide and climb velocities $\mathbf{v}_{\mathrm{gl}} = v_{\mathrm{gl}}\mathbf{m}$ and $\mathbf{v}_{\mathrm{cl}} = v_{\mathrm{cl}}\mathbf{n}$ are then related to these forces by

$$v_{\mathrm{gl}} = M_{\mathrm{gl}} F_{\mathrm{gl}}, \quad \text{and} \tag{2.7a}$$

$$v_{\mathrm{cl}} = M_{\mathrm{cl}} F_{\mathrm{cl}}, \tag{2.7b}$$

where M_{gl} and M_{cl} are the glide and climb mobilities which are functions of the temperature, dislocation character, and, in the case of climb, point defect concentration. The equations (2.7) are called mobility laws. These linear mobility laws are a simplification, because in many materials dislocation velocity depends more strongly on stress[8].

In this model it is the dislocation velocity (not acceleration) which depends on the force

[8] $v_{\mathrm{gl}} \propto (F_{\mathrm{gl}})^n$, with $n > 1$.

on the dislocation, because at moderate (and above) temperatures, where it is easier for kinks to form, dislocations in some materials are observed to move at constant speed for a constant applied stress, i.e. they are subjected to a viscous drag and so move via over-damped motion (Prekel et al., 1968). For glide, this drag is due to the dislocation scattering lattice vibrations (phonons). The "drag" during climb is simply due to the rate limiting effects of point defect emission/absorption and diffusion to/from the dislocation line.

2.3.7 Dislocation interactions

Dislocation interactions with other dislocations as well as obstacles such as grain boundaries and hard precipitates/dispersoids play a significant role in the macroscopic strength of a material.

Dislocations produce their own stress fields since they can be represented by elastic displacements of the material. For example, a straight screw dislocation with its line direction and Burgers vector in the positive z-direction can be described by the displacement field (in cylindrical coordinates)

$$u_r = u_\theta = 0, \tag{2.8a}$$

$$u_z = \frac{b}{2\pi} \cdot \theta, \tag{2.8b}$$

which leads to the standard expressions for the stress due to a screw dislocation:

$$\sigma_{\theta z} = \frac{\mu b}{2\pi} \cdot \frac{1}{r}, \tag{2.9}$$

where μ is the shear modulus; with all other components equal to zero (Cottrell, 1953, p. 36). The non-zero stresses around an infinite straight edge dislocation with its line direction in the positive z-direction and Burgers vector in the positive x-direction — which result in plane strain in the x-y plane — are given by (also in cylindrical coordi-

nates)

$$\sigma_{rr} = \sigma_{\theta\theta} = -\frac{\mu b}{2\pi(1-\nu)} \cdot \frac{\sin\theta}{r}, \tag{2.10a}$$

$$\sigma_{r\theta} = \frac{\mu b}{2\pi(1-\nu)} \cdot \frac{\cos\theta}{r}, \tag{2.10b}$$

$$\sigma_{zz} = -\frac{\mu b\nu}{\pi(1-\nu)} \cdot \frac{\sin\theta}{r}, \tag{2.10c}$$

where ν is Poisson's ratio (Friedel, 1964, p. 21). These expressions were subsequently derived in a simple way by Eshelby (1966). It is important to note that these non-zero stress components exhibit a $1/r$ dependence. This leads to interaction energies between dislocations which depend on the logarithm of their separation, i.e. the interactions between dislocations are long-ranged. Therefore each dislocation in a single crystal interacts with every other dislocation. This is unlike, for example, electrostatic forces, which depend on $1/r^2$, resulting in interaction energies between charged particles which depend on $1/r$, and can hence be thought of as short-ranged. Furthermore, the $1/r$ dependence of the stress (and indeed strain) fields of straight dislocations approaches infinity close to the dislocation line. Clearly this is unphysical, and can be explained by the fact that the atomic displacements in the core of the dislocation are too large for linear elasticity theory to be valid. For this reason, elastic analyses of dislocations often neglect the effects of the dislocation core for r below some inner cut off radius r_c which is of the order of a few b.

Dislocations also interact with their own stress fields, leading to the so-called self-energy of a dislocation. For a mixed dislocation of character[9] θ, the self-energy per unit length $E(\theta)$ (neglecting the contribution from the dislocation core) is given by

$$E(\theta) = \frac{\mu b^2}{4\pi(1-\nu)} \ln\left(\frac{r_\infty}{r_\mathrm{c}}\right) \cdot \left[1 - \nu\cos^2\theta\right] \tag{2.11}$$

where r_c and r_∞ are the inner and outer integration cutoff radii: r_c corresponds to the radius of the dislocation core, and r_∞ is some outer cutoff radius of an appropriate lengthscale, for example, half the average dislocation separation (Cottrell, 1953, p. 51).

[9]Defined as $\theta \equiv \sin^{-1}(|\mathbf{b}\times\boldsymbol{\xi}|/b)$, where $\boldsymbol{\xi}$ is the dislocation's (unit) line direction. Hence $\theta = 0$ for a pure screw, and $\theta = \pi/2$ for a pure edge.

The self-energy of a dislocation is minimised by the dislocation remaining/becoming straight[10], for two reasons. Firstly, and trivially, the straight configuration has less overall line length, and thus less total self-energy than a longer curved line joining the same two points in the crystal. Secondly, non-zero line curvatures increase the self-stress felt by parts of the dislocation because of the angular dependence of the dislocation stress field of the other parts. This is captured by the line tension, or self-force, of a mixed dislocation segment $T(\theta)$, which is given by

$$T(\theta) = E(\theta) + \frac{\mathrm{d}^2 E(\theta)}{\mathrm{d}\theta^2}, \tag{2.12}$$

where $E(\theta)$ is given by (2.11) (Hull and Bacon, 2011, p. 75). It is these effects that keep a gliding dislocation straight as it is subjected to an applied shear stress.

Whether two dislocations are attracted to or repelled from each other depends on both the sign of their Burgers vectors and their relative position. For example, two co-planar edge dislocations with Burgers vectors of opposite sign will be attracted to each other, because when they come together they are able to annihilate by the two extra half-planes on different sides of the glide plane joining, leaving no dislocation behind. Similarly, two co-planar edge dislocations of like sign will repel each other due to the hydrostatic pressure each of the two extra half-planes on the same side of the glide plane feel due to the other. In a different scenario, two edge dislocations of opposite sign on parallel glide planes will glide until they reach a stable dislocation dipole configuration at an angle of 45° to each other due to the interaction of their stress fields (equations (2.10)). They might then be able to annihilate via a repeating process of small amounts of climb followed by subsequent glide to a new stable dipole configuration.

Dislocations with non-parallel Burgers vectors can still react with each other and can merge to form a new dislocation. The Burgers vector of this new dislocation is the sum of the Burgers vectors of the "parent" dislocations. In other words, dislocation interactions conserve Burgers vector in general[11], in an analogous way to Kirchoff's

[10] This is not always the case. See § 2.3.12.

[11] In certain specific scenarios, Burgers vector is not conserved. One example of this is the coalesence of two dislocation loops of different Burgers vector, where one loop is signficantly larger than the other. The smaller loop can be incorporated into the larger loop without its Burgers vector being conserved. Such an interaction involves the internal rearrangement of the point defects that constitute the smaller

laws for current-carrying wires.

2.3.8 Dislocations and strengthening mechanisms

The motion and interaction of dislocations during plastic deformation leads to strain, or work, hardening. Work hardening in single crystals of a range of materials exhibits three-stage behaviour with increasing strain (Hull and Bacon, 2011). Stage I corresponds to single slip, in which dislocations move on the slip system with the largest resolved shear stress. In stage I, the hardening rate is relatively low. Like dislocations on the same habit plane repel each other, and it is this mutual repulsion which leads the hardening. Whilst the dislocation sources are operating and the dislocations are multiplying (see § 2.3.10), the dislocations which are ahead of others exert stresses on those behind them in the opposite direction to the load which is causing them all to glide in the first place. If a leading dislocation is blocked from progressing any further, the resultant back stresses reduce the amount by which the dislocations behind are able to glide, and a dislocation pile-up is formed (Eshelby et al., 1951). There are a number of types of obstacle to dislocation motion, all of which can cause pile-ups. In stage II work hardening, or multiple slip, dislocations on additional slip systems move. The interactions of the dislocations on different slip systems produce additional barriers to motion, leading to a higher rate of hardening. Finally, in stage III, or dynamic recovery, the hardening rate decreases again, as dislocations are able to climb out of their original slip planes, thus overcoming the barriers to their motion.

Grain boundaries can also interact with dislocations. If the glide planes in two adjacent grains happen to meet along a common line, a dislocation in grain 1 with Burgers vector $\mathbf{b}_1$ can be transmitted through the boundary into grain 2 as a dislocation with Burgers vector $\mathbf{b}_2$, leaving behind a dislocation on the grain boundary with Burgers vector $(\mathbf{b}_1 - \mathbf{b}_2)$. If this mechanism is not possible due to the relative positions and orientations of the grains the dislocation can become pinned and hence lead to a pile-up. In scenarios like this, strengthening can be achieved by refining the grain size, and hence

loop, i.e. it is an atomistic scale process at a smaller length scale than that of either climb or glide dislocation motion.

decreasing the amount of glide which can occur before the dislocations are stopped by the pile-ups at the grain boundaries — this is known as the Hall–Petch effect (Hall, 1951; Petch, 1953).

When alloying elements are introduced into a metal matrix they can sometimes diffuse into the lattice and exist in a solid solution. These alloying atoms can have stress fields which interact with mobile dislocations and impede their motion, leading to solid solution strengthening. Atmospheres of impurities can also impede dislocation motion: in iron base alloys, for example, the segregation of impurities such as carbon and nitrogen to dislocation lines can pin the dislocations and lead to hardening (Cottrell and Bilby, 1949).

Dislocations interact with precipitates, regions of a material which are of a second phase to the matrix material inhabited by the dislocations. The precipitates can also prevent the glide of dislocations by blocking their motion at the precipitate-matrix interface, leading to precipitation hardening. An example of this is nickel base superalloys which are used for turbine blades, in which the cubic γ' phase precipitates form regular arrays, and the dislocations' glide motion is restricted to the narrow γ phase channels between the precipitates (Reed, 2008).

Lastly, dislocations can interact with the stress fields of nano-scale hard particles, or dispersoids, or become blocked at the particle-matrix interface in the same manner as grain boundaries and precipitates. Thus dispersoids also act as obstacles to dislocation motion, resulting in dispersoid strengthening. These particles, or inclusions, will be the focus of the literature review in chapter 5.

2.3.9 Creep

Grain boundaries, precipitates and dispersoids are all relevant to the process of creep. Creep is the deformation of metals under constant stress on relatively long timescales, and creep rates vary strongly on temperature (Caillard and Martin, 2003). This is because thermal creep involves the thermally-activated formation and diffusion of point defects to the grain boundaries, and to dislocations which are blocked by each other, or

pinned on precipitates and dispersoids, allowing them to climb over these obstacles and continue to glide. Another type of creep, irradiation creep, is also possible, and will be discussed in § 2.5.3.

Thermal creep exhibits three-stage behaviour with increasing time (Was, 2007). The first stage corresponds to strain hardening due to single and multiple slip, resulting in an initial decrease in the creep strain rate, and the during third stage localised deformation causes necking, increasing the creep strain rate at long times. The steady-state creep rate during the second stage is due to dynamic recovery, i.e. the unpinning[12] of dislocations from obstacles to their motion via climb.

In metals, creep depends primarily on applied stress as well as the temperature. At high temperatures, the creep strain rate is observed to exhibit a power law dependence on the applied stress, with an exponent which can vary from 4 to 8 (Keralavarma et al., 2012), but at high enough stresses this power law breaks down, and the creep rate increases exponentially with the applied stress (Was, 2007).

Steady-state creep is of practical importance since it occurs throughout the majority of a component's operational lifetime.

2.3.10 Dislocation sources

Significant dislocation populations are introduced into crystals during their growth due to pre-existing defects in "seed" crystals, and internal stresses. It is these dislocations that move and result in small amounts of plastic deformation at stresses lower than the CRSS. However, the macroscopic plastic deformation that occurs later, once the CRSS is reached, is due to the activation of dislocation sources in the crystal and subsequent dislocation multiplication. Real dislocation sources can be very complex, but they often have characteristics similar to the idealised Frank–Read source, which is illustrated in figure 2.8.

[12] Throughout this work, "pinned" is used in a general sense to describe a dislocation whose glide motion is blocked by an obstacle, rather than its more technical meaning for a dislocation which is held in place by e.g. a solute atmosphere.

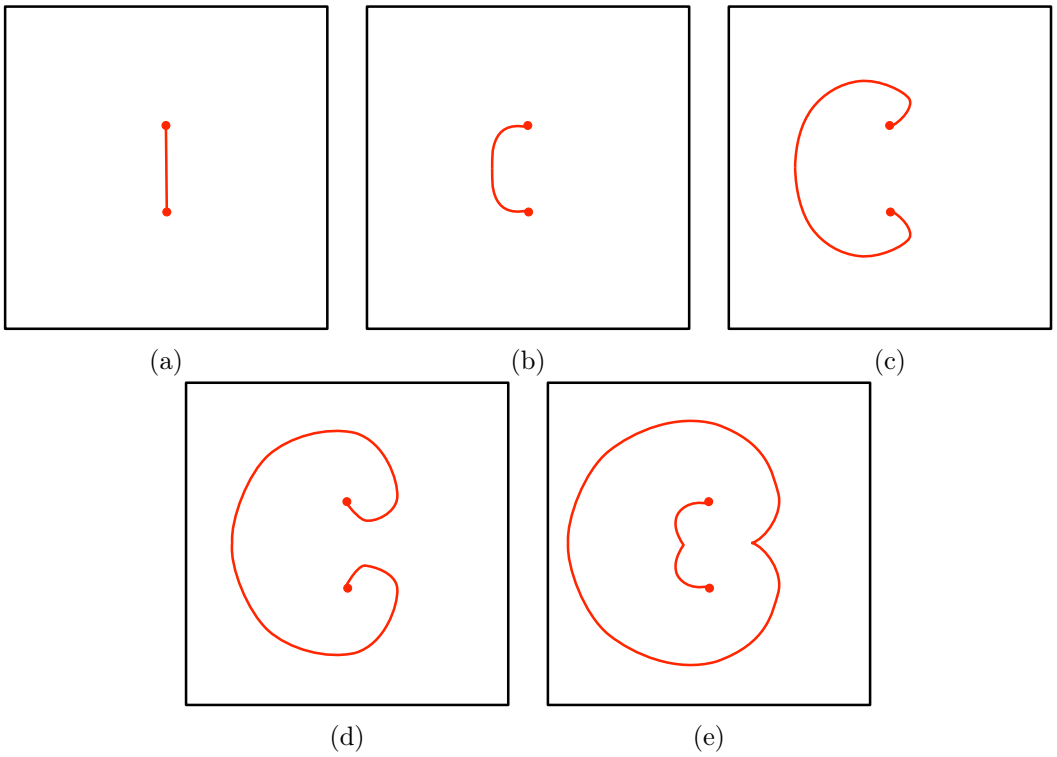


Figure 2.8: A schematic illustration of the operation of a Frank-Read source.

Frank and Read (1950) considered a segment of dislocation pinned at both ends. Such a situation can arise when a dislocation forms irregularly during crystal growth so that part of it lies in its glide plane whilst other parts lie in other planes. When subjected to a (resolved) applied shear stress the segment starts to bow out, as illustrated in figures 2.8(a) and (b). In this new geometry the dislocation self-stress acts against the applied stress so a stable equilibrium can be reached. However, if the resolved shear stress is large enough ($>$ CRSS), the segment bows out and then continues outwards in an unstable way, forming a kidney shape as shown in figures (c) and (d). Parts of the segment now lie behind the source and have the same Burgers vector but opposite line-senses, so they are attracted to each other. They annihilate, leaving an expanding loop with a pinned segment in the middle (figure (e)), allowing the process to repeat itself. In this way a single source can produce multiple dislocations. The CRSS is proportional to $1/L$, where L is the initial straight length of the source.

2.3.11 Dislocations in bcc metals

Understanding dislocation behaviour in bcc metals is particularly important for fusion applications, as a number of these metals will be incorporated into the design of such a reactor. These are discussed in § 2.5.5.

In bcc metals, the shortest lattice vectors lie in the ⟨111⟩ directions. Because of this, slip tends to occur in the ⟨111⟩ directions as the dislocations in bcc metals often have Burgers vectors of the type $\frac{1}{2}\langle 111\rangle$[13]. Dislocations with ⟨100⟩ Burgers vectors are also observed at higher temperatures (Yao et al., 2010). These are believed to form via the reaction of two $\frac{1}{2}\langle 111\rangle$ dislocations, for example:

$$\frac{1}{2}[1\bar{1}1] + \frac{1}{2}[11\bar{1}] \rightarrow [100]. \tag{2.13}$$

The crystallographic slip planes for $\frac{1}{2}\langle 111\rangle$ dislocations are {110}, {112} and {123}. A specific ⟨111⟩ direction intersects a total of twelve of these planes[14], so if appreciable cross slip is possible screw dislocations can move in an erratic way on several of these planes as favoured by the local stress. Temperature, crystal orientation, material composition and strain rate all affect this behaviour. For example, pure iron deformed at room temperature exhibits slip irrespective of crystal orientation (Keh, 1965), whereas iron alloyed with silicon or pure iron deformed at low temperatures only exhibits slip in the {110} planes (Low and Turkalo, 1962; Christian, 1983).

After low temperature deformation, electron microscopy of bcc metals reveals long screw dislocations (Louchet et al., 1979). This implies that the non-screw dislocations are significantly more mobile, as they have all glided out of the bulk to the grain surfaces, generating loops with long screw segments. Because of this[15], screw dislocations dictate the slip characteristics and yield stress of bcc metals. The high lattice resistance to glide of the screw dislocations which contributes to the strong temperature dependence of the yield stress is due to the particular non-planar character of the screw dislocation core

[13] In this work, Burgers vectors are given in units of a, the material's lattice parameter, e.g. $\mathbf{b} = \frac{1}{2}[111]$ is equivalent to $\mathbf{b} = \frac{1}{2}[111]a$.

[14] Three {110}, three {112}, and six {123} planes.

[15] Screw dislocations also have less self-energy per unit length than edge dislocations (Hirth and Lothe, 1982), so at a given temperature a higher density of screw dislocations is expected.

(Gilbert and Dudarev, 2010).

The atomic structure of the core of a screw dislocation with $\mathbf{b} = \frac{1}{2}[111]$ necessarily exhibits the same three-fold symmetry as the bcc lattice along the [111] direction. The result of molecular dynamics simulations (see § 2.4) of a $\frac{1}{2}[111]$ screw dislocation core in bcc molybdenum is shown in figure 2.9 (Vitek, 2004; Vitek et al., 2004; Mrovec et al., 2004; Vitek and Paidar, 2008). The circles in figure 2.9 represent the projection onto the plane of the paper of three adjacent (111) planes with an interplanar spacing of $b/3$. The shading distinguishes between the three successive (111) planes. The disregistry in the [111] direction of the atoms in the core is represented by the arrows drawn between neighbouring pairs of atoms. The length of the arrows is proportional to the difference in the displacement in the [111] direction of the two atoms, and is scaled so that arrows representing displacement differences of $b/3$ run from one atom to the other. If the displacement difference is between $b/2$ and b, it is reduced by b (and hence the arrow reverses direction). For the isotropic elastic solution (2.8), the length of the arrows would decrease reciprocally with radius from the core. As can be seen in the plot in figure 2.9, far from the dislocation core this behaviour is reproduced. However, taking into account the atomic structure of the core results in an anisotropic displacement distribution close to it, which exhibits the three-fold symmetry along the [111] direction.

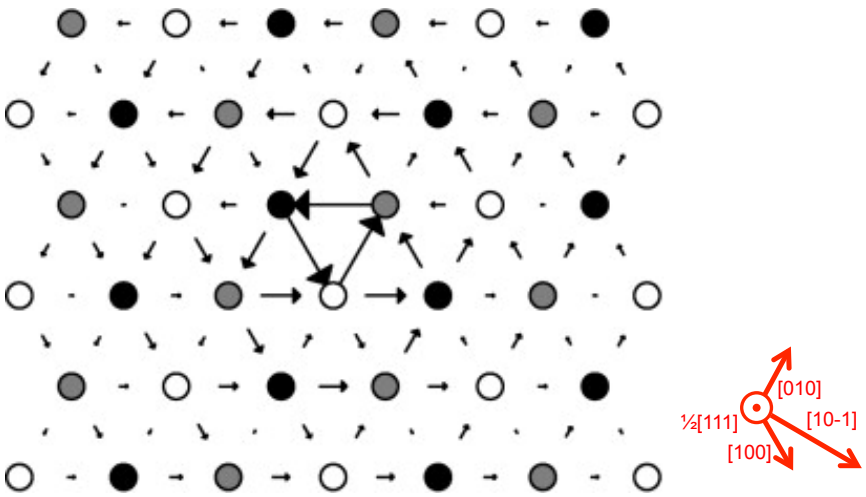


Figure 2.9: The result of molecular dynamics simulations of a $\frac{1}{2}[111]$ screw dislocation core in bcc molybdenum. See the main text for an explanation of what is shown. *From Vitek and Paidar (2008).*

The core structure shown in figure 2.9 is also invariant with respect to the two-fold symmetry of the $[10\bar{1}]$ direction, and is said to be a non-degenerate core structure. This six-fold symmetrical non-degenrate core structure has since been corroborated in bcc iron by Gilbert and Dudarev (2010) and Itakura et al. (2012). The high applied stress required for straight screw dislocations to glide due to their non-planar core structures result in glide via kink-pair nucleation, and hence the strong temperature dependence of the yield stress.

Like screw dislocations, the CRSS for slip of $\langle 100 \rangle$ edge dislocations is much larger than for other edge dislocations (Yao et al., 2010). In bcc iron the elastic energy of $\langle 100 \rangle$ dislocations decreases with increasing temperature due to the effects of anisotropic elasticity coming into play (see § 2.3.12.). Therefore edge dislocations with Burgers vectors of type $\langle 100 \rangle$ as well as screw dislocations play an important role in the high temperature plastic behaviour of bcc iron (Fitzgerald and Dudarev, 2009).

2.3.12 Effects of anisotropic elasticity in bcc iron

Up to this point, elastic isotropy has been assumed, for example in (2.10). More general anisotropic elasticity with applications to dislocation theory was considered by Eshelby et al. (1953), and Bacon et al. (1979). Anisotropic elasticity is relevant for bcc iron — also referred to as α-iron, or ferrite — at the high operating temperatures of a fusion reactor because of its α-γ phase transition at 912 °C (Hasegawa and Pettifor, 1983). At temperatures approaching 912 °C iron displays strongly temperature-dependent anisotropic elastic constants, and in particular 'softening' of the tetragonal shear modulus C' is observed. This is due to the lattice translations conducive to the phase transition becoming energetically favourable (Hasegawa et al., 1985).

Fitzgerald and Dudarev (2008, 2009) studied the effect of elastic anisotropy on dislocation pile-ups in bcc iron at high temperatures. Their results offer one explanation for the precipitous fall in tensile strength of ferritic steels at high temperature, as the softening of C' causes pile-ups of $\langle 100 \rangle \{001\}$-type dislocations to collapse, significantly reducing the stress required to initiate plastic deformation. In a crystal with appreciable

elastic anisotropy, the energy of certain dislocation line orientations drops considerably. Dislocations avoid the higher energy line orientations by forming angular loops, and even becoming jagged rather than remaining straight. Using an analytic line tension model with full anisotropic elasticity to reproduce the angular dislocation loops observed in high temperature bcc iron (an illustration of which is shown in figure 2.10), Fitzgerald (2010) argued that the critical stress required to initiate dislocation production at Frank–Read sources also falls dramatically with temperature, in agreement with experimental observation. This was corroborated by the work of Fitzgerald et al. (2012) which considered the numerical evaluation of the self-force on dislocation segments using anisotropic elasticity and compared the results to those of the analytic line tension model, showing good agreement (Fitzgerald and Aubry, 2010; Aubry et al., 2011).

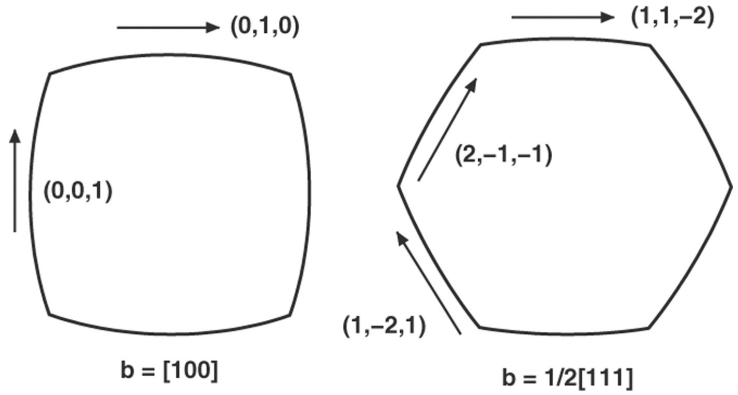


Figure 2.10: Predicted prismatic loop shapes for (highly anisotropic) iron at 900 °C. The loop sides align themselves along the lowest energy directions: (001) and (010) for [100](100) loops (left); and $(11\bar{2})$, $(2\bar{1}\bar{1})$, and $(1\bar{2}1)$ for $\frac{1}{2}[111](111)$ loops (right). *From Fitzgerald and Yao (2009).*

An appreciation of the strong effects of anisotropic elasticity is clearly important when considering the way in which dislocation behaviour affects the macroscopic mechanical properties of bcc iron at very high temperatures.

2.4 Computational modelling of dislocations

A comprehensive guide to the different approaches to computationally modelling dislocations is given by Bulatov and Cai (2006). There are two main types of model.

Atomistic models deal with the interactions and dynamics of the atoms themselves. First principles models such as density functional theory (DFT, also referred to as *ab initio*, or electronic structure) are used for the smallest scale simulations. DFT is based on quantum mechanics, but treats the electrons in an ensemble of atoms as a continuous field of electron density, significantly reducing the number of degrees of freedom. In general, DFT is time-independent, and captures the local equilibrium spatial configuration of the ensemble of atoms simulated[16]. Although DFT is limited to simulations of only a few hundred atoms (and hence lengthscales of a few nanometres) because of its high computational cost, it can nevertheless provide accurate information about, for example, crystal structure, SIA configurations, formation and migration energies of point defects and defect clusters (see § 2.5.2), and dislocation core structure.

Interatomic potentials informed by DFT calculations and/or experimental measurements are employed to model the potential energy landscape due to and felt by larger ensembles of atoms. These interatomic potentials attempt to capture the underlying quantum mechanics such as the short-range repulsion and long-range attraction of the atoms due to their electronic configurations, to varying degrees of precision whilst minimising computational cost. One such potential, the "hard-sphere" model, crudely captures the short range repulsion of the atoms by setting the potential equal to infinity when the interatomic separation is below the diameter of the atoms, and zero when the separation is above it. This is extremely simple, and hence computationally cheap, but fails to capture the long-range attraction of the atoms. On the other hand, the Lennard-Jones potential (Bulatov and Cai, 2006, p. 29) is more precise, smoothly interpolating between a short-range repulsive and long-range attractive atomic interaction, but is more computationally expensive. Embedded-atom model potentials such as the Finnis–Sinclair potential (Finnis and Sinclair, 1984) include additional terms in

[16] DFT can be extended to time-dependent DFT, which can provide information about excited states.

order to capture the collective many-body interaction between the atoms and the electrons in the material, further refining the model and increasing computational expense. Different interatomic potentials are valid to varying degrees depending on the material and the problem under consideration. They can never be fitted to all the properties of a material, for example accuracy in the vacancy formation energy could be improved at the expense of the accuracy in the calculated melting point (Bulatov and Cai, 2006, § 2.1).

Using a prescribed interatomic potential, molecular dynamics (MD) algorithms evolve the atomic configurations towards those that minimise the overall energy of the system. At each time step the forces on the atoms are calculated and the equation of motion is numerically integrated. Parts of one or two dislocations can be captured and used to investigate dislocation interactions by employing appropriate periodic boundary conditions. MD simulations are able to model $\sim 10^6$ atoms at a time (and hence lengthscales of ∼10–100 nanometres), although the majority of these do nothing — only those close to the dislocation(s) are displaced. The time step in MD simulations is of the order of a few 10^{-15} s, so the maximum amount of time that can be simulated is ∼100 ps. Though useful for examining the structure of dislocation cores (as in figure 2.9), or measuring the stress dependence of dislocation velocity at a given temperature, simulating a larger sample of material undergoing plastic deformation due to the dynamics of several dislocations within it becomes extremely computationally expensive. This is because the number of atoms required becomes unfeasibly large, and a timescale of at least $\sim 10^{-6}$ s is needed to observe micron-scale dislocation behaviour.

In order to simulate many interacting dislocations, and hence predict the resulting mechanical response, for example in the form of a stress-strain curve, or the microstructural evolution, continuum models are used. In such models — collectively known as dislocation dynamics (DD) models — the simulation box comprises of an elastic continuum in which dislocations are the interacting objects. In dislocation dynamics models it is the forces on the dislocations themselves which are calculated in order to integrate the equation of motion numerically at each time step. In this way lengthscales of several microns, and timescales of $>10^{-6}$ s, can be simulated.

Two-dimensional models of infinite straight dislocations in situations of plane strain are often used (van der Giessen and Needleman, 1995), and can be a powerful tool for simulating dislocation phenomena such as micro-mechanical size effects (Balint et al., 2006; Tarleton et al., 2015). Some attempts have also been made to incorportate climb into 2D DD simulations in order to model creep (Keralavarma et al., 2012; Ayas et al., 2014). However, their applications are somewhat limited as they cannot capture some important three-dimensional physics, including the behaviour of dislocation loops, and dislocation-obstacle interactions. More general curved dislocations in three-dimensional space can be described using discrete dislocation dynamics.

2.4.1 3D discrete dislocation dynamics (DDD)

In 3D discrete dislocation dynamics (DDD) simulations, a curved dislocation network is discretised into inter-connected straight dislocation segments joined together by discretisation (or physical) nodes, as illustrated in figure 2.11.

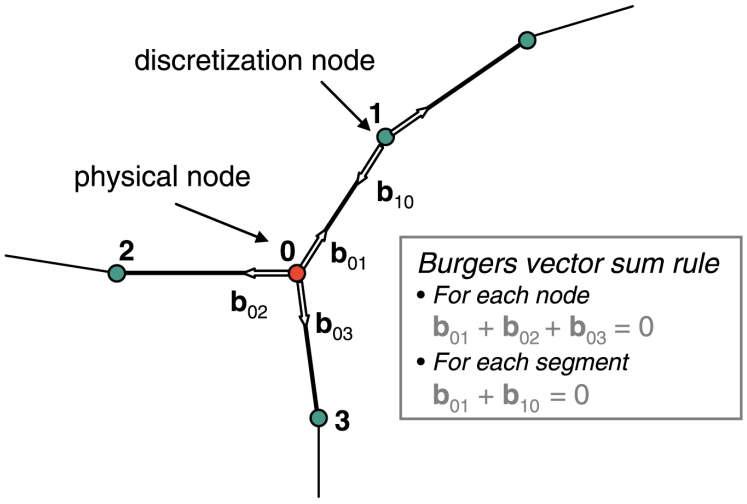


Figure 2.11: A schematic illustration of the discretisation of a dislocation network into inter-connected straight segments joined together by either discretisation or physical nodes. The white arrows represent the line directions over which the Burgers vectors are defined, not the Burgers vectors themselves. *From Arsenlis et al. (2007).*

The discretisation nodes connect two dislocation segments, whereas the physical nodes connect an arbitrary number of segments, and represent a physical dislocation junction. Burgers vector conservation is enforced at both types of nodes, and hence in order for

the discretised dislocation network to represent a topology which is not unphysical, the network must consist of closed loops, with no "dangling" nodes (this requirement is not illustrated in figure 2.11).

The stress field due to any straight dislocation segment can be evaluated without the need for integration using expressions such as those given by Cai et al. (2006, § B.2). Thus the stress field at any position in the simulation box can be computed by summing over the contributions from all segments of the dislocation network. DDD simulations are computationally expensive, because as described in § 2.3.7, the forces between dislocations are inversely proportional to their separation, so every dislocation segment in a simulation box interacts with every other segment. The force on each node is calculated by first using an analytic expression for the force on a straight dislocation segment to calculate the force on each of the segments to which the node is connected, and then performing a weighted sum of these forces using an appropriate shape function. At each time step the forces on the nodes are calculated, and nodal mobility laws are used to move the nodes.

Cai and Bulatov (2004) describe how simple nodal mobility laws can be implemented in DDD simulations when material specific mobility laws are available, for example from MD simulations. Short range interactions, such as the annihilation of two opposite segments and junction formation, are captured using constitutive rules such as those described by Rhee et al. (1998), and Bulatov and Cai (2006, § 10.4). Rhee et al. also give an example of a Monte Carlo (see section § 2.5.2) type analysis of cross slip. Using their code `3D-MICRO` Rhee et al. investigated single slip in bcc single crystals, and demonstrated the feasibility of such a DDD model predicting macroscopic hardening and the strain rate dependence of the flow stress, providing of course that dislocation mobilities, structures and pinning points are known. An example of cross slip in their simulations is shown in figure 2.12.

A simple way to discretise a curved dislocation is to reduce it to connected edge and screw segments only. This simplifies the expressions for the stress fields of the segments — reducing computational expense — and was done by Fivel (2008). The simulations carried out by Fivel predicted the formation of slip bands in fatigued steel, but again

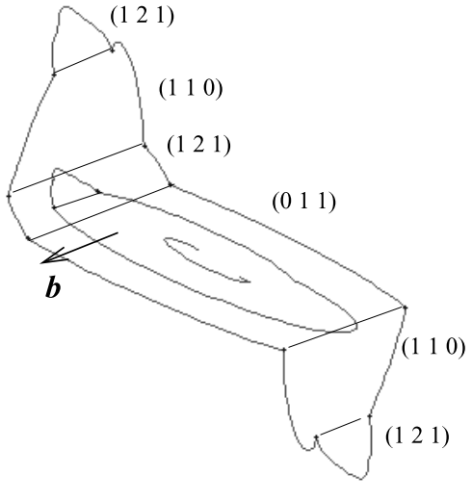


Figure 2.12: An example of cross slip in a bcc metal simulated using `3D-MICRO`. The operating edge Frank–Read source lies on the (011) plane, with a Burgers vector **b** in the $[1\bar{1}1]$ direction. *From Rhee et al. (1998).*

required significant input from MD simulations for dislocation mobilities and local interaction rules.

Novokshanov and Roberts (2009) studied the interaction of a mobile dislocation with a $\frac{1}{2}[111]$ prismatic loop in bcc iron using the `MicroMegas` code developed at LEM-ONERA, Paris (Devincre et al., 2001). This code discretises the dislocations into straight edge, screw, and two possible orientations of "mixed" segments. Novokshanov and Roberts also used a Monte Carlo method to simulate cross slip, and observed a complicated 3D interaction resulting in the mobile dislocation bowing around the loop, and subsequently either leaving it behind unchanged or reacting with it. The simulations were carried out at room temperature[17], and the mobility laws used were fitted to the available experimental data for dislocation velocity in bcc iron from 77 to 373 K.

The existing `DDLab` and `ParaDiS` codes developed at LLNL, California, are based on the non-singular DDD formulation described by Arsenlis et al. (2007) (see § 4.2). `DDLab` was written in `MATLAB` and used to assist in the development of `ParaDiS` which was written in `C`/`C++`. `ParaDiS` uses the fast multipole method (LeSar and Rickman, 2002), and can perform massively parallel simulations. The codes use isotropic elasticity, but since they are written in a modular way they can be made anisotropic by implementing

[17] Indeed, this is true whichever way you look at it.

such code and incorporating it into the modular framework (Yin et al., 2012). The non-singular theory used to avoid divergent interaction energies does so by distributing the Burgers vector smoothly and continuously over the dislocation core with a spreading parameter, and is described by Cai et al. (2006). The linear glide and climb mobilities are input parameters. A study of the interactions between dislocations and stacking-fault tetrahedra in fcc copper using both MD simulations and `ParaDiS` was carried out by Marian et al. (2009), a snapshot of which is shown in figure 2.13. They used the smaller scale MD results to inform the faster, larger scale DDD simulations. Their work shows broad agreement with irradiation hardening measurements in copper, and highlights the predictive power of such hierarchal multi-scale modelling.

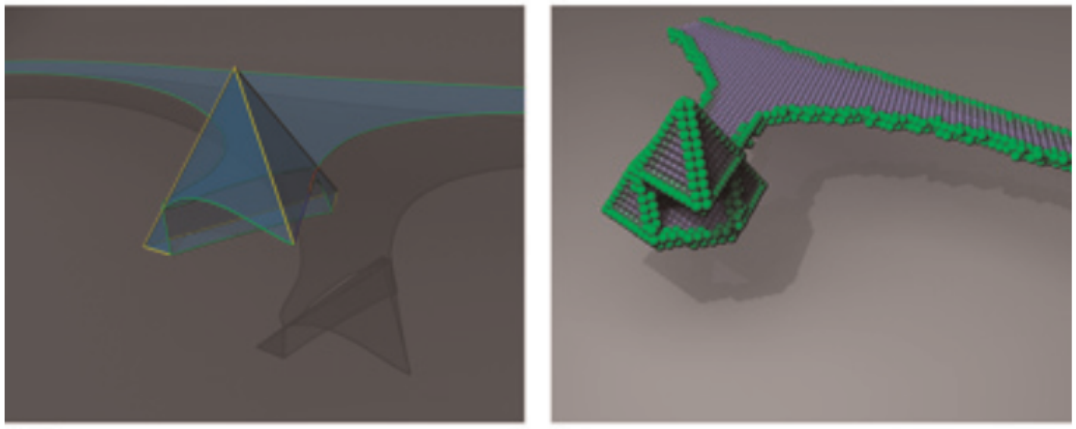


Figure 2.13: A snapshot of a `ParaDiS` (left) and MD (right) simulation of the interaction between a dislocation and a stacking-fault tetrahedron in fcc copper. *From Marian et al. (2009).*

All of the simulations discussed so far have been for the case of isotropic elasticity. A method for implementing dislocation stress fields using anisotropic elasticity is given by Rhee et al. (2001), and they suggest that whilst anisotropic elasticity is important for short-range interactions, which can differ from the isotropic case by as much as 15%, long-range interactions can be approximated using isotropic elasticity. However, Rhee et al. did not consider highly anisotropic materials, such as bcc iron at very high temperatures (close to ∼900 °C). Recently, Yin et al. (2012) have described a method for computing dislocation stress fields in an anisotropic elastic medium using fast multipole expansions. Their method reduces the computational cost of each simulation step from

$\mathcal{O}(N^2)$ to $\mathcal{O}(N)$ for N discretised dislocation segments[18].

2.4.2 Modelling climb in DDD

In order to model climb using DDD, simple linear climb mobilities are often implemented in the same manner as glide, i.e. as an input parameter (this is the case for `DDLab`). For example, Hafez-Haghighat et al. (2013) used `ParaDiS` to study creep in γ'-strengthened nickel base superalloys using an ad hoc climb mobility which takes the value of 10^{-1}, 10^{-2} or 10^{-3} times that of glide. However, some attempts have been made to incorporate the temperature-dependent diffusion of point defects into the dislocation climb mobility law. The work of Kabir et al. (2010) is an example of atomistic modelling of climb in this way.

Raabe (1998) outlined a concept for incorporating climb into DDD models. The non-conservative motion is introduced by using (2.5a), which describes how the climb force affects the local vacancy concentration, coupled with the diffusion equation (2.2), to calculate the diffusion flux of vacancies (but not interstitials) to/from the dislocation. Using the same reasoning, Mordehai et al. (2008) derived the following expression for the climb velocity for a pure edge dislocation of the form

$$v_{\mathrm{cl}} = A\left[\exp\left(\frac{F_{\mathrm{cl}}\Omega/b}{k_{\mathrm{B}}T}\right) - \frac{c_{\infty}^{\mathrm{v}}}{c_0^{\mathrm{v}}}\right], \tag{2.14}$$

where

$$A = \frac{2\pi D^{\mathrm{v}} c_0^{\mathrm{v}}}{b\ln(r_{\infty}/r_{\mathrm{c}})}. \tag{2.15}$$

Here, c_0^{v} is the (fractional) equilibrium vacancy concentration in a dislocation free crystal (2.1) given by $c_0^{\mathrm{v}} = \exp(-E_{\mathrm{f}}^{\mathrm{v}}/k_{\mathrm{B}}T)$, and c_{∞}^{v} is the vacancy concentration in the bulk material far from the dislocation. The vacancy diffusion coefficient D^{v} (2.3) is given by $D^{\mathrm{v}} = D_0^{\mathrm{v}}\exp(-E_{\mathrm{m}}^{\mathrm{v}}/k_{\mathrm{B}}T)$. r_{c} and r_{∞} are again the inner and outer integration cutoff radii — the dislocation core radius, and some outer radius far from the dislocation core — respectively. c_{∞}^{v} can be set to be equal to c_0^{v} in order to capture thermal climb

[18]The bottleneck in simulations however is still the $\mathcal{O}(N^2)$ operations needed to calculate the close-range interactions which aren't handled by the fast multipole method.

behaviour, or, in the $c_\infty^{\mathrm{v}} > c_0^{\mathrm{v}}$ case, it corresponds to a vacancy supersaturation due to e.g. quenching.

Away from surfaces and grain boundaries the dislocations are the only sources and sinks for point defects, and so assuming that during climb — that is, the generation or destruction of point defects at the dislocation line — the vacancies in the bulk reach a steady-state concentration instantaneously, the time evolution of the vacancy bulk concentration is governed by the equation

$$\frac{\mathrm{d}c_\infty^{\mathrm{v}}}{\mathrm{d}t} = \frac{b}{V}\frac{\mathrm{d}S}{\mathrm{d}t}, \tag{2.16}$$

where V is the volume of the crystal, and S is the area swept by the loops during this vacancy mediated climb (Bakó et al., 2011). If a dislocation segment of length $\delta\ell$ climbs a distance $v_{\mathrm{cl}}\Delta t$, the corresponding swept area is given by $\delta S = v_{\mathrm{cl}}\Delta t\delta\ell$. Using this model, dislocation vacancy loop coarsening solely by climb (i.e. without glide), has been captured in DDD simulations (Mordehai et al., 2008, 2009; Bakó et al., 2011). Larger dislocation loops are seen to grow at the expense of the smaller ones, some of which disappear completely — a process known as Ostwald ripening. This is illustrated in figure 2.14.

Bakó et al. (2011) combined glide with this climb model in order to investigate the effects glide has on loop coarsening. Using the 3D DDD code `Numodis` developed at CEA-Saclay and the University of Grenoble, France, they observed faster loop coarsening than in the climb only case. This was attributed to the attractive elastic interaction of dislocation loops which possess intersecting prismatic glide cylinders causing them to glide towards each other faster than the vacancy bulk diffusion process. Once in contact with each other they can then merge by diffusion-limited climb. This whole process is illustrated in figure 2.15.

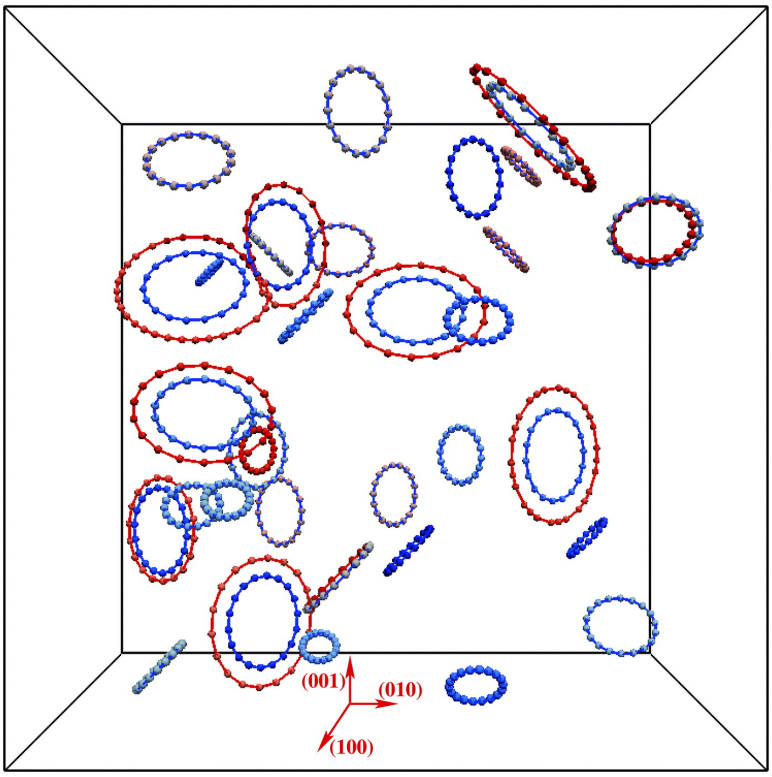


Figure 2.14: Dislocation vacancy loop coarsening by climb, when glide is not included, in fcc aluminium at 600 K. Blue lines represent the loops at $t = 0$, and red lines at some time later. The larger loops grow at the expense of the smaller ones, some of which disappear completely (the loops shown in blue only). *From Bakó et al. (2011).*

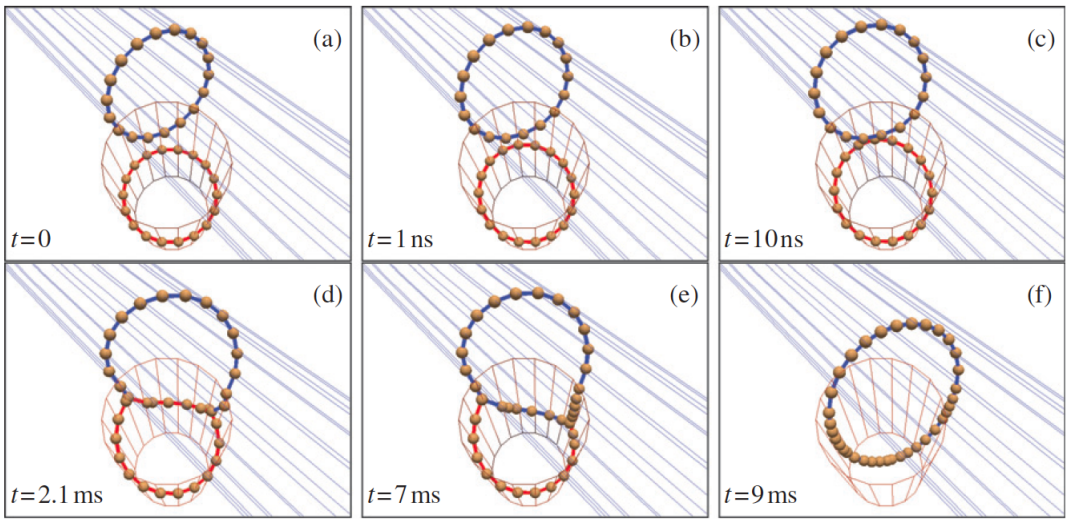


Figure 2.15: The merging of two attracting dislocation loops in fcc aluminium at 600 K. First the loops glide along their prismatic glide cylinders, and subsequently they undergo climb. The initial glide cylinders of both loops are indictated by the faint lines. *From Bakó et al. (2011).*

An alternative thermodynamic variational approach to modelling climb is given by Gao and Cocks (2009). The variational principle states that the rate of evolution of a system is given by the stationary value of the functional

$$\Pi = \dot{G} + \Psi, \tag{2.17}$$

where $\dot{G}$ is the rate of change of Gibbs free energy of the system, which provides the thermodynamic driving forces for the system, and Ψ is the dissipation rate potential of the system, which contains contributions from the full range of kinetic processes in the evolution of the system. Mathematically, this implies

$$\delta\Pi = \delta\left(\dot{G} + \Psi\right) = 0. \tag{2.18}$$

Gao and Cocks derive expressions for $\dot{G}$ and Ψ in the case of (a) a defect free region of crystal subjected to an external hydrostatic pressure, and (b) a region containing a climbing edge dislocation subjected to an external traction. By applying the variational principle they present governing equations for cases (a) and (b). In the case of a climbing edge dislocation with a dislocation core bounded by the surface Γ in a region of crystal B bounded by the surface ∂B, three governing equations are needed: one on Γ, one on ∂B, and one in B^*, the crystal region B excluding the dislocation core.

This alternative approach is interesting, but it is not studied in this work.

2.5 Irradiation damage

The energy of the high flux of neutrons resulting from the deuterium-tritium reactions in a fusion reactor will be converted into useful heat energy in the blanket of the reactor wall. The energetic neutrons travel through the first wall and blanket materials, scattering off the lattice atoms and transferring their kinetic energy to the material, ultimately resulting in heating. However, this necessarily displaces the lattice atoms, infliciting significant amounts of displacement damage on the first wall/blanket materials. In a commerical fusion reactor, the first wall/blanket materials will be subjected to up to 200 atomic displacements per atom (dpa) during their operational lifetimes (Odette et al., 2008). This is also true of the in-core structural materials in a number of Gen IV fission reactor concepts (Zinkle and Was, 2013).

The neutron bombardment also results in transmutation, or burn-up, occuring within the structural materials of a reactor. Changes in the materials' chemical composition necessarily lead to changes in their mechanical properties, and the formation of long-lived radioactive isotopes has implications for both nuclear reactor safety during operation, and clean, safe storage after decommisioning. In iron (and metals and alloys in general), the production of gas atoms, for example hydrogen from n + ^{56}Fe $\rightarrow$ ^{1}H + ^{56}Mn reactions, and helium from n + ^{56}Fe $\rightarrow$ ^{4}He + ^{53}Cr reactions, can have particularly severe consequences (Gilbert et al., 2012).

Clearly, an understanding of neutron irradiation damage and its effects is extremely relevant when considering materials for nuclear applications. A comprehensive review of the science of irradiation damage can be found in Was (2007).

2.5.1 Displacement cascades

When a high energy neutron scatters off a lattice atom, it transfers some of its kinetic energy to the atom, which becomes a primary knock-on atom (PKA). Subsequently, the high energy PKA scatters off other lattice atoms, creating a chain of additional knock-on atoms, as illustrated schematically in figure 2.16. In this way a single incident neutron results in the displacement of multiple atoms, known as a displacement cascade. The entire displacement cascade take place on a timescale of $\sim 10^{-13}$ s (Kinchin and Pease, 1955).

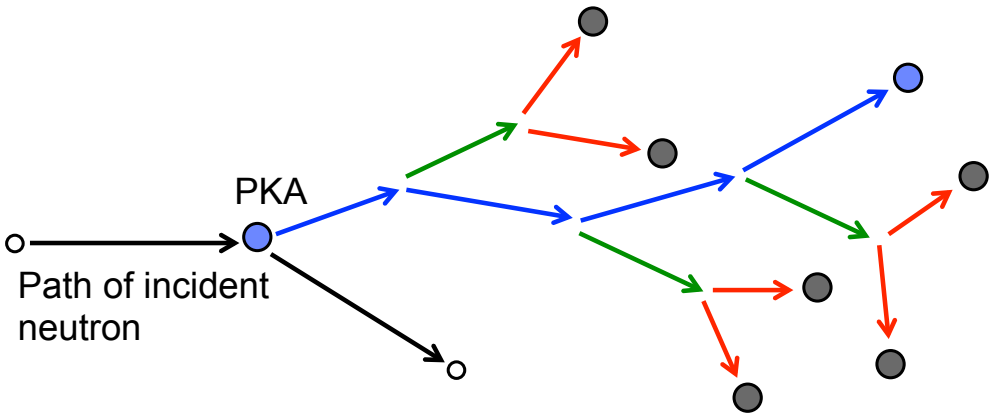


Figure 2.16: A schematic representation of a displacement cascade.

The minimum amount of kinetic energy an atom needs to receive in order to be (permanently) displaced from its lattice site is know as the threshold displacement energy (E_d). This energy must be at least the formation energy of a Frenkel pair in the material (one vacancy and one SIA, see § 2.5.2), of the order of a few eV. In reality E_d is somewhat larger than this, as a *stable* Frenkel pair must be produced rather than an instantaneous one. Furthermore, if the energy transferred is greater than some minimum threshold displacement energy $E_{\mathrm{d,min}}$, the atom will not necessarily be displaced, but rather there is a probability of displacement which increases to 1 at some higher E_d. This spread in E_d depends on the orientation of the displacement trajectory with respect to the lattice, atomic vibrations due to the temperature, and impurity atoms. In iron, the accepted values of $E_{\mathrm{d,min}}$ and E_d are 20 and 40 eV respectively (Was, 2007, p.83).

Conversely, the maximum amount of kinetic energy an atom of mass M can receive from an incident particle of mass m and kinetic energy E_i is given by $E_\mathrm{i} \times 4mM/(m+M)^2$.

This expression follows from (non-relativistic) energy and momentum conservation. For an incident neutron interacting with an iron atom this comes to $0.07E_{\mathrm{i}}$, so fusion neutrons with a maximum energy[19] of 14 MeV will produce PKAs with a maximum energy of 970 keV in iron. For iron-iron interactions the maximum energy transferred is simply equal to the energy of the incident iron atom (the $4mM/(m+M)^2$ factor is equal to 1).

A simple model to estimate the average number (N) of atoms displaced in a cascade due to a PKA of energy E_{PKA} was developed by Kinchin and Pease (1955). They assumed (amongst other things) that a cascade involves a sequence of two-body elastic collsions, and that if E_{PKA} is greater than some cutoff energy E_{c} no further atomic displacements occur until the PKA energy has reduced to E_{c}. The cutoff energy is E_{c} attributed to electronic stopping. The results of the Kinchin–Pease (K–P) model are as follows:

- When $E_{\mathrm{PKA}} < E_{\mathrm{d}}$, the threshold displacement energy, $N(E_{\mathrm{PKA}}) = 0$.
- When $E_{\mathrm{d}} < E_{\mathrm{PKA}} < 2E_{\mathrm{d}}$, $N(E_{\mathrm{PKA}}) = 1$.
- When $2E_{\mathrm{d}} < E_{\mathrm{PKA}} < E_{\mathrm{c}}$, $N(E_{\mathrm{PKA}}) = E_{\mathrm{PKA}}/2E_{\mathrm{d}}$. In this regime N increases proportionally with E_{PKA}.
- When $E_{\mathrm{PKA}} \geq E_{\mathrm{c}}$, $N(E_{\mathrm{PKA}}) = E_{\mathrm{c}}/2E_{\mathrm{d}}$. This specifies a maximum value for N for a given E_{PKA}.

For PKAs of 970 keV in iron, $N(970\ \mathrm{keV}) = 1.2\text{–}2.4 \times 10^4$, depending on which value of E_{d} is used, and assuming 970 keV $< E_{\mathrm{c}}$ in iron.

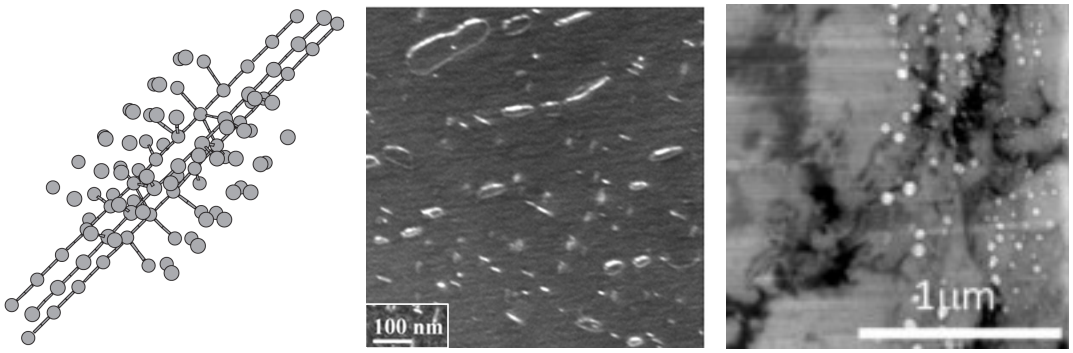
Various modifications and improvements to the K–P model exist, such as the NRT model (Norgett et al., 1975), but nevertheless it is still widely used. The Stopping and Range of Ions in Matter (SRIM) software package uses models such as these to simulate the resultant displacement damage due to ion irradiation (Ziegler et al., 1985, 2010), and Stoller et al. (2013) recommend that when direct comparisons between ion and neutron dpa data are required, the K–P option of SRIM should be selected.

[19] Roughly 20% of the neutrons which reach the blanket have an energy of 14 MeV, but the other ∼80% will have a spectrum of lower energies similar to that of fission neutrons due to scattering events in the first wall.

The large number of atoms which are displaced in a cascade result in point defects in the lattice structure.

2.5.2 Damage defects

When an atom is displaced from its lattice site, both a vacancy and an SIA are produced. Such a vacancy-SIA pair is known as a Frenkel pair. During a displacement cascade, large numbers of Frenkel pairs are produced, and the energy spike leads to localised melting. Over the course of the $\sim 10^{-11}$ s immediately after a cascade, this energy dissipates, heating the surrounding material, and many of the Frenkel pairs undergo spontaneous recombination, resulting in a smaller number of stable Frenkel pairs. Nearby defects of the same type are able to cluster, forming structures such as those shown in figure 2.17: (a) multi-crowdion clusters (Dudarev, 2003), (b) prismatic dislocation loops (Yao et al., 2010), and, in the case of vacancies, (c) three-dimensional voids (Shao et al., 2014). This cascade damage evolution can be modelled using MD simulations, providing information about the populations of different point defects after their initial recombination, and the types and numbers of defect clusters formed (Björkas and Nordlund, 2007; Sand et al., 2014).



(a) (b) (c)

Figure 2.17: Defect clusters in bcc iron. (a) The result of modelling a cluster of three $\langle 111 \rangle$ crowdions, (b) a micrograph of prismatic dislocation loops obtained using transmission electron microscopy (TEM), (c) a TEM micrograph of voids. *(a) from Dudarev (2003), (b) from Yao et al. (2010), (c) from Shao et al. (2014).*

On timescales $>10^{-8}$ s, the remaining point defects (and, to some extent, the defect clusters) are able to move around by thermal diffusion. In this way further recombi-

nation can occur, as well as the formation of more damage loops and voids via the agglomeration of like point defects (Was, 2007). Existing loops and voids can grow and coalesce by absorbing point defects, and absorption can also occur at other defect sinks such as threading dislocations, grain boundaries and precipitates/dispersoids. Futhermore, gas atoms produced by nuclear reactions can themselves diffuse, forming gas bubbles at these sinks.

The thermally-activated diffusion of these point defects and defect clusters can be modelled using Monte Carlo (MC) methods for timescales of up to ∼1 s (Bulatov and Cai, 2006, § 9), and rate theory for timescales much longer than ∼1 s (Was, 2007, § 5). Whereas MD simulations are deterministic[20], and so temperature can only be taken into account by randomising the initial conditions and conducting multiple simulations, MC is inherently stochastic. In an MC algorithm, the system evolves based on the probability that atoms[21] will transition from one state to another, and these transitions are treated as rare events, so knowledge of the rates of the processes being simulated is required. MC simulation can be made more efficient, and capable of capturing longer timescales, by using a kinetic Monte Carlo (KMC) algorithm, which does not have a time step that is fixed by the (reciprocal of the) fastest rate in the simulation. For example, atomistic KMC simulations were performed by Kabir et al. (2010) in order to model dislocation climb in vacancy supersaturated bcc iron, and hence predict power law creep exponents. Their results were quantitatively consistent with experiment. Furthermore, this lattice KMC method can be made even more efficient by using an object kinetic Monte Carlo (OKMC) method instead, in which the diffusion of defects and defect clusters is captured by treating these defects — rather than the much larger number of atoms — as the simulated objects themselves (Mason et al., 2014). Again, in order to perform OKMC simulations all the relevant rates, such as those of defect/defect cluster diffusion, must be known. These can be obtained from DFT calculations and/or MD simulations.

The presence of these microscopic defects has significant consequences at the macroscale.

[20] Unmodified DDD methods are also deterministic.
[21] Or dislocations, as in Rhee et al. (1998), and Novokshanov and Roberts (2009).

2.5.3 Effects on mechanical properties

Neutron irradiation damage can have a number of effects on the mechanical properties of a material, including hardening, embrittlement, volumetric swelling, and irradiation creep.

The populations of damage loops, voids and bubbles impede the motion of gliding dislocations, leading to hardening. The interaction of mobile dislocations with defect clusters such as interstitial loops can be investigated using both MD (Marian et al., 2003), and DDD simulations[22] (Novokshanov and Roberts, 2009). The resulting loss of ductility, together with the diffusion of the damage defects — notably voids and gas atoms such as helium — to grain boundaries leads to embrittlement, and hence an increase in the likelihood of catastrophic failure (Bloom, 1998). Helium embrittlement particularly reduces the operational lifetime of e.g. steels, as above some critical radius the helium bubbles no longer require more helium to diffuse to them in order to grow (Bloom et al., 2007). Instead they grow via the biased absorption of vacancies, thus accelerating their growth.

Volumetric swelling at the macroscale is accompanied by the formation of voids on the microscale. The presence of voids within a material implies that on average matter has been transported outwards, away from the voids, necessarily resulting in expansion. Hence volumetric swelling is often referred to as void swelling, despite the fact that when considered in isolation a void clearly has a negative relaxation volume.

Swelling is observed in (fcc) austenitic stainless steel which has been subjected to neutron irradiation at temperatures and doses relevant to Gen IV fission and fusion reactor conditions. Such steels are used in current fission reactor fuel cladding, but the expansion observed is beyond the operational tolerance for advanced nuclear applications (Odette et al., 2008).

[22] In the case of MD both the loops and the dislocations are captured by the appropriate atomic configurations, and in DDD by dislocation lines. However, DD simulations in which the loops are captured by non-dislocation simulation objects, whose interaction rules with mobile dislocations are (partially) derived from MD simulations, are also possible. A simple example of this is the 2D DD framework of van der Giessen and Needleman (1995), which incorporates point-like obstacles to dislocation glide.

2.5.4 Irradiation creep

The excess point defects produced by irradiation can lead to a significant increase in the rate of creep. Irradiation creep does not depend strongly on temperature like thermal creep, but instead on the rate of displacement damage — via the steady-state supersaturations of vacancies and interstitials produced during irradiation (Was, 2007). Because of this, appreciable irradiation creep can occur at relatively low temperatures, at which thermal creep rates are negligible. Irradiation creep rates in excess of 10^{-6} s^{-1} are possible in fission reactor core conditions, resulting in a time to 1% strain[23] of the order of a few hours.

A number of processes can contribute to irradiation creep. The stress-induced preferential nucleation of interstitial/vacancy loops on planes perpendicular/parallel to an applied tensile stress can account for some of the increase in the observed creep rate, as can the stress-induced preferential absorption (SIPA) of supersaturated interstitials at dislocations which are aligned with the stress direction. The origin of SIPA is the elastic interaction between the long-range stress field of the dislocations and the defects. As both these processes are diffusional, the creep strain accumulated from them is relatively small.

SIPA does however gives rise to glide due to preferential absorption, in which dislocations are able to overcome obstacles to their glide motion via the climb which occurs as a result of SIPA. Thus appreciable creep strain can be accumulated — strain which would not otherwise occur in the absence of irradiation. Finally, the absorption of supersaturated interstitials at all the dislocations (regardless of their alignment) also leads to appreciable creep strains, even in the absence of an applied stress, via the same climb and glide process. This is thought to be necessarily accompanied by void swelling, in order to account for the supersaturated vacancies (Was, 2007). However, in chapter 3 it is argued this does not need to be the case, as the *thermodynamic* preferential absorption of interstitials at dislocations is to be expected.

In order to mitigate irradiation creep, the effects of irradiation on a material's mechan-

[23]Time to 1% strain is a measure commonly used when interpreting strain rates. In many situations 1% strain essentially constitutes mechanical failure.

ical properties, and the transmutation production of long-lived radioactive isotopes, irradiation resistant materials are required.

2.5.5 Irradiation resistant materials

A number of properties need to be incorporated when designing irradiation resistant materials. Low activation is required for minimising long-lived radioactive waste, which limits the deliberate use — and occurrence of impurities — of certain elements, including nickel, which is commonly used in (austenitic) stainless steels. Materials with a bcc structure, such as ferritic and martensitic steels, and tungsten[24], exhibit reduced amounts of volumetric swelling during neutron irradiation compared to their fcc counterparts (Odette, 1988; Garner et al., 2000; Wolfer, 2007). As a result of this, reduced activation ferritic/martensitic steels (RAFM) have been developed for use in fission reactors (Klueh, 2005).

In addition to their irradiation resistant properties, RAFM steels have high thermal conductivities and exhibit low thermal expansion, which is beneficial at their high operating temperatures. As with conventional stainless steels, their chromium content of ∼12–20% weight percentage (wt%) in solution leads to corrosion resistance, which is important for RAFM steels used in water-moderated reactors.

Typical yield stresses of RAFM steels vary from 450–650 MPa at room temperature. However, this drops sharply from about ∼500 °C, making RAFM steels somewhat unsuitable for use at fusion reactor blanket operating temperatures of ∼650 °C (Ukai and Fujiwara, 2002). Nevertheless, the planned baseline structural material for the blanket is currently EUROFER RAFM steel (Stork et al., 2014). Other issues with EUROFER include its low creep strength (Yu et al., 2005), and its lack of resistance to irradiation embrittlement at lower operating temperatures.

Oxide dispersion strengthed (ODS) RAFM steels offer some improvements over non-ODS RAFM steels, such as increased yield and creep strengths, and enhanced irradiation

[24]Tungsten is a promising candidate material for the divertor plate of a fusion reactor, because its thermal properties allow it to withstand the extreme heat loads of the order of MWm^{-2} to which the divertor will be subjected.

resistance. Because of this they are promising candidate structural materials for use in fusion (and fission) reactors. They will be discussed later in chapter 5.

Chapter 3

Theory and modelling of dislocation climb

3.1 Introduction

Dislocation climb is usually mediated by the diffusion of the thermal vacancy population, leading to the strong temperature dependence of thermal creep. However, under irradiation conditions the large supersaturations of both vacancies and interstitials increase the rate of dislocation climb, resulting in irradiation creep, which does not depend strongly on temperature, but does depend on the irradiation dose rate (Was, 2007). Higher irradiation dose rates naturally lead to larger point defect supersaturations. During continuous irradiation, a steady-state will be reached in which the defect[25] supersaturations remain constant, as the rate of increase of the defects due to the ongoing irradiation is balanced by defect losses via recombination, and to sinks such as grain boundaries, threading dislocations, and damage defect clusters such as dislocation loops and voids. This leads to changes in the microstructure, such as the unpinning of pinned dislocations from obstacles, and the growth or shrinkage of irradiation-induced damage loops.

Using a vacancy bulk diffusion model of climb, Mordehai et al. (2008) derived an expres-

[25] In this chapter, and those that follow, point defects will often be referred to as simply "defects".

sion, given in (2.14), for the climb velocity of a pure edge dislocation. In this chapter, vacancy *and interstitial* diffusion is taken into account in order to model dislocation climb. In § 3.2 an expression for the climb velocity of an edge dislocation in the presence of coupled vacancy and interstitial concentration mean fields is derived in much the same way as in the presence of vacancies only, as in Mordehai et al. (2008), and Bakó et al. (2011). This model is then applied to bcc iron and compared to experimental data in § 3.3. Analysis of the expression for the climb velocity leads to an explanation for the experimentally observed dominance of interstitial-type irradiation damage loops over vacancy-type loops in bcc iron. The model also predicts an absence of damage loops altogether at high enough temperatures, and for low enough irradiation dose rates.

3.2 Dislocation climb via point defect bulk diffusion

The coupled diffusion equations for vacancy and interstitial point defects are given by

$$\frac{\partial c^{\mathrm{v}}}{\partial t} = D^{\mathrm{v}}\nabla^2 c^{\mathrm{v}} + K_0^{\mathrm{v}} - K_{\mathrm{r}} c^{\mathrm{v}} c^{\mathrm{i}}, \tag{3.1a}$$

$$\frac{\partial c^{\mathrm{i}}}{\partial t} = D^{\mathrm{i}}\nabla^2 c^{\mathrm{i}} + K_0^{\mathrm{i}} - K_{\mathrm{r}} c^{\mathrm{i}} c^{\mathrm{v}}, \tag{3.1b}$$

where c^{v} and c^{i} are the fractional atomic concentrations, D^{v} and D^{i} are the diffusion coefficients, and K_0^{v} and K_0^{i} are the (effective) production rates of vacancies and interstitials respectively; and K_{r} is their (uncorrelated) recombination rate (Was, 2007, p. 192). The point defect concentration fields are functions of position $\mathbf{r}$, and time t, i.e. $c^j = c^j(\mathbf{r}, t)$, where j indicates either vacancies (v) or interstitials (i). The diffusion coefficients D^j depend on temperature T, and defect migration energy E_{m}^j, and are given by the expression in (2.3).

The coupled diffusion equations given in (3.1) assume that the defect diffusion coefficients D^j do not depend on position. Furthermore, the presence of defect sinks, such as an edge dislocation, is not captured by (3.1). Instead, the presence of an edge dislocation will be incorporated by using an appropriate boundary condition.

In the steady-state, (3.1) become

$$D^{\mathrm{v}}\nabla^2 c^{\mathrm{v}}(\mathbf{r}) + K_0^{\mathrm{v}} - K_{\mathrm{r}} c^{\mathrm{v}}(\mathbf{r}) c^{\mathrm{i}}(\mathbf{r}) = 0, \tag{3.2a}$$

$$D^{\mathrm{i}}\nabla^2 c^{\mathrm{i}}(\mathbf{r}) + K_0^{\mathrm{i}} - K_{\mathrm{r}} c^{\mathrm{i}}(\mathbf{r}) c^{\mathrm{v}}(\mathbf{r}) = 0. \tag{3.2b}$$

Subtracting (3.2b) from (3.2a) yields

$$D^{\mathrm{v}}\nabla^2 c^{\mathrm{v}}(\mathbf{r}) - D^{\mathrm{i}}\nabla^2 c^{\mathrm{i}}(\mathbf{r}) + K_0^{\mathrm{v}} - K_0^{\mathrm{i}} = 0. \tag{3.3}$$

By defining the *diffusion-weighted concentration difference field* $u(\mathbf{r})$ as

$$u(\mathbf{r}) \equiv D^{\mathrm{v}} c^{\mathrm{v}}(\mathbf{r}) - D^{\mathrm{i}} c^{\mathrm{i}}(\mathbf{r}), \tag{3.4}$$

and the production rate difference ΔK_0 as $\Delta K_0 \equiv K_0^{\mathrm{v}} - K_0^{\mathrm{i}}$, (3.3) can be re-written as

$$\nabla^2 u(\mathbf{r}) = -\Delta K_0. \tag{3.5}$$

Hence $u(\mathbf{r})$ obeys the Poisson equation, and in the case of equal defect production, i.e. $\Delta K_0 = 0$, the Laplace equation.

The general solution for $u(\mathbf{r})$, assuming cylindrical geometry and a radial field $u(\mathbf{r}) = u(r)$, is given by

$$u(r) = k_1 + k_2 \ln(r) - \frac{1}{4}\Delta K_0 r^2, \tag{3.6}$$

where k_1 and k_2 are constants to be determined from the boundary conditions on $u(r)$.

If a straight edge dislocation is located at $r = 0$, and we assume that the vacancy and interstitial concentrations are both independently in local equilibrium with the (climbing) dislocation core, the first boundary condition on $u(r)$ becomes

$$u(r = r_{\mathrm{c}}) = u_{\mathrm{eq}} \equiv D^{\mathrm{v}} c_{\mathrm{eq}}^{\mathrm{v}} - D^{\mathrm{i}} c_{\mathrm{eq}}^{\mathrm{i}}, \tag{3.7}$$

where r_c is the dislocation core radius, and c^v_{eq} and c^i_{eq} are given by

$$c^j_{eq} = \exp\left(-\frac{E^j_f \pm F_{cl}\Omega/b}{k_B T}\right), \tag{3.8}$$

which is, in essence, the same expression as (2.5a). The only difference is the $\pm$ sign, which indicates that the change in the effective defect formation energy in the vicinity of the dislocation core (the $F_{cl}\Omega/b$ term) corresponds to either an increase or a decrease in the formation energy of vacancies, and *vice versa for interstitials*. Which way round depends on the relative orientation of the dislocation's Burgers vector and the climb force, i.e. it depends on the sign of F_{cl} — whether it induces "up-climb" or "down-climb" of the edge dislocation.

As in (2.5b), the equilibrium concentration (3.8) can be re-written as

$$c^j_{eq} = c^j_0 \exp\left(\mp\frac{F_{cl}\Omega/b}{k_B T}\right), \tag{3.9}$$

where $c^j_0 = \exp(-E^j_f/k_B T)$ is the usual thermal equilibrium concentration of the given point defect. Again, the $\mp$ sign is realised one way for vacancies, and the opposite way for interstitials, but which way round is unknown at this point.

Assuming that $F_{cl}\Omega/b \ll k_B T$, which will be the case unless extremely large climb forces are present, the exponential in (3.9) can be expanded in powers of $F_{cl}\Omega/bk_B T$. Keeping only terms of $\mathcal{O}(1)$ and $\mathcal{O}(F_{cl}\Omega/bk_B T)$, the expression for c^j_{eq} then becomes

$$c^j_{eq} = c^j_0\left(1 \mp \frac{F_{cl}\Omega/b}{k_B T}\right). \tag{3.10}$$

For the second boundary condition on $u(r)$, consider the value $u(r)$ takes at some outer cut-off radius r_∞ far from the dislocation core:

$$u(r = r_\infty) = u_\infty \equiv D^v c^v_\infty - D^i c^i_\infty. \tag{3.11}$$

Here c^v_∞ and c^i_∞ are the vacancy and interstitial concentrations far from the dislocation in the bulk of the material. If these concentrations are larger than their corresponding

thermal equilibrium values $c_0^j(T)$, then they represent defect supersaturations at the given temperature.

Inserting the boundary conditions (3.7) and (3.11) into the general solution (3.6) yields

$$u(r) = u_\infty + \frac{1}{4}\Delta K_0 r_\infty^2 + \frac{(u_\infty - u_{\mathrm{eq}} + \frac{1}{4}\Delta K_0(r_\infty^2 - r_{\mathrm{c}}^2))}{\ln(r_\infty/r_{\mathrm{c}})}\ln(r/r_\infty) - \frac{1}{4}\Delta K_0 r^2. \quad (3.12)$$

The rate of vacancies emitted $\delta\dot{N}^{\mathrm{v}}$ added to the rate of interstitials absorbed $-\delta\dot{N}^{\mathrm{i}}$ by an infinitesimal edge segment of length $\delta\ell$ is given by

$$\delta\dot{N}^{\mathrm{v}} - \delta\dot{N}^{\mathrm{i}} = -\frac{2\pi r_{\mathrm{c}}}{\Omega}\delta\ell D^{\mathrm{v}}\frac{\partial c^{\mathrm{v}}}{\partial r}\bigg|_{r=r_{\mathrm{c}}} + \frac{2\pi r_{\mathrm{c}}}{\Omega}\delta\ell D^{\mathrm{i}}\frac{\partial c^{\mathrm{i}}}{\partial r}\bigg|_{r=r_{\mathrm{c}}} \quad (3.13a)$$

$$= -\frac{2\pi r_{\mathrm{c}}}{\Omega}\delta\ell\frac{\partial u}{\partial r}\bigg|_{r=r_{\mathrm{c}}}. \quad (3.13b)$$

The full solution for $u(r)$ given in (3.12) can be differentiated and evaluated at $r = r_{\mathrm{c}}$ to give

$$\frac{\partial u}{\partial r}\bigg|_{r=r_{\mathrm{c}}} = \frac{u_\infty - u_{\mathrm{eq}}}{r_{\mathrm{c}}\ln(r_\infty/r_{\mathrm{c}})} + \Delta K_0\left(\frac{r_\infty^2 - r_{\mathrm{c}}^2(2\ln(r_\infty/r_{\mathrm{c}}) + 1)}{4r_{\mathrm{c}}\ln(r_\infty/r_{\mathrm{c}})}\right), \quad (3.14)$$

and sustituting this expression into (3.13b) yields

$$\delta\dot{N}^{\mathrm{v}} - \delta\dot{N}^{\mathrm{i}} = -\frac{2\pi r_{\mathrm{c}}}{\Omega}\delta\ell\left(\frac{u_\infty - u_{\mathrm{eq}}}{r_{\mathrm{c}}\ln(r_\infty/r_{\mathrm{c}})} + \Delta K_0\left(\frac{r_\infty^2 - r_{\mathrm{c}}^2(2\ln(r_\infty/r_{\mathrm{c}}) + 1)}{4r_{\mathrm{c}}\ln(r_\infty/r_{\mathrm{c}})}\right)\right). \quad (3.15)$$

The rate of climb of the infinitesimal segment is given by

$$v_{\mathrm{cl}} = (\delta\dot{N}^{\mathrm{v}} - \delta\dot{N}^{\mathrm{i}})\frac{\Omega}{b\,\delta\ell}, \quad (3.16)$$

as the distance it climbs when it absorbs/emits a defect is $\Omega/b\,\delta\ell$ (see figure 2.7(c)). Inserting (3.15) into this expression yields

$$v_{\mathrm{cl}} = \frac{2\pi}{b\ln(r_\infty/r_{\mathrm{c}})}\left(u_{\mathrm{eq}} - u_\infty - \frac{1}{4}\Delta K_0\left(r_\infty^2 - r_{\mathrm{c}}^2(2\ln(r_\infty/r_{\mathrm{c}}) + 1)\right)\right). \quad (3.17)$$

Replacing the diffusion-weighted concentration difference fields evaluated at the boundaries, u_{eq} and u_∞, with their expressions in terms of c_{eq}^j and c_∞^j given by (3.7) and (3.11),

leads to

$$v_{\mathrm{cl}} = \frac{2\pi}{b\ln(r_\infty/r_\mathrm{c})}\left(D^\mathrm{v}(c^\mathrm{v}_\mathrm{eq} - c^\mathrm{v}_\infty) - D^\mathrm{i}(c^\mathrm{i}_\mathrm{eq} - c^\mathrm{i}_\infty) - \frac{1}{4}\Delta K_0\left(r^2_\infty - r^2_\mathrm{c}(2\ln(r_\infty/r_\mathrm{c}) + 1)\right)\right). \tag{3.18}$$

Finally, substituting in the linearised expression for c^j_eq given by (3.10) results in the following expression for the edge dislocation's climb velocity:

$$\begin{aligned} v_{\mathrm{cl}} = {} & \frac{2\pi\Omega}{b^2\ln(r_\infty/r_\mathrm{c})}\frac{D^\mathrm{v}c^\mathrm{v}_0}{k_\mathrm{B}T}\left(F_\mathrm{cl} \pm^\mathrm{v} \frac{bk_\mathrm{B}T}{\Omega}\left(1 - \frac{c^\mathrm{v}_\infty}{c^\mathrm{v}_0}\right)\right) \\ & + \frac{2\pi\Omega}{b^2\ln(r_\infty/r_\mathrm{c})}\frac{D^\mathrm{i}c^\mathrm{i}_0}{k_\mathrm{B}T}\left(F_\mathrm{cl} \mp^\mathrm{i} \frac{bk_\mathrm{B}T}{\Omega}\left(1 - \frac{c^\mathrm{i}_\infty}{c^\mathrm{i}_0}\right)\right) \\ & - \frac{\pi}{2b\ln(r_\infty/r_\mathrm{c})}\Delta K_0\left(r^2_\infty - r^2_\mathrm{c}(2\ln(r_\infty/r_\mathrm{c}) + 1)\right). \end{aligned} \tag{3.19}$$

Again, the realisation of the $\pm^\mathrm{v}$ and $\mp^\mathrm{i}$ signs will either be $+^\mathrm{v}$ and $-^\mathrm{i}$, or $-^\mathrm{v}$ and $+^\mathrm{i}$, depending on the orientation of F_cl relative to the Burgers vector, i.e. the sign of F_cl.

The rather unwieldy expression in (3.19) can be rewritten in the simple form

$$\begin{aligned} v_{\mathrm{cl}} = {} & M^\mathrm{v}_\mathrm{cl}\left(F_\mathrm{cl} + F^\mathrm{v}_\mathrm{os}\right) \\ & + M^\mathrm{i}_\mathrm{cl}\left(F_\mathrm{cl} + F^\mathrm{i}_\mathrm{os}\right) \\ & + v^\mathrm{prod}_\mathrm{cl}(\Delta K_0), \end{aligned} \tag{3.20}$$

where M^v_cl and M^i_cl are the dislocation mobilites for vacancy and interstitial mediated climb respectively, F^v_os and F^i_os are the so-called "osmotic forces" driving dislocation climb due to a supersaturation of vacancies and of interstitials respectively, and $v^\mathrm{prod}_\mathrm{cl}(\Delta K_0)$ is the contribution to the climb velocity caused by a difference in the (effective) rate of production of defects in the material, i.e. a non-zero ΔK_0.

The osmotic force

$$F^j_\mathrm{os} = \pm\frac{bk_\mathrm{B}T}{\Omega}\left(1 - \frac{c^j_\infty}{c^j_0}\right), \tag{3.21}$$

is the thermodynamic driving force which captures the reduction of the total free energy of the system when supersaturated defects are incorporated into the dislocation line, which is assumed to be a perfect sink for these defects. The osmotic force due to a su-

persaturation of vacancies acts in the opposite direction to one due to a supersaturation of interstitials, as implied by the $\pm$ sign.

The dislocation mobilities for vacancy and interstitial mediated climb are given by

$$M_{\mathrm{cl}}^{j} = \frac{2\pi\Omega}{b^2 kT \ln(r_\infty/r_{\mathrm{c}})} D^j c_0^j, \tag{3.22}$$

and the contribution to the climb rate due to a difference in the (effective) production rates of vacancies and interstitials is given by

$$v_{\mathrm{cl}}^{\mathrm{prod}}(\Delta K_0) = -\frac{\pi}{2b\ln(r_\infty/r_{\mathrm{c}})} \Delta K_0 \left(r_\infty^2 - r_{\mathrm{c}}^2(2\ln(r_\infty/r_{\mathrm{c}}) + 1)\right). \tag{3.23}$$

The expression for the climb velocity (3.20) has a number of interesting qualities:

1. The simple linear form of (3.20) allows the magnitude and sign of the five different terms which contribute to dislocation climb to be compared to each other directly, in order to examine which effects dominate under different circumstances.

2. The osmotic force (3.21) has identical forms for vacancies and interstitials, and acts in the opposite direction for the two different types of defect. An osmotic force is only present when there is a non-equilibrium defect concentration in the bulk, i.e. when $c_\infty^j \neq c_0^j$, and osmotic forces can be present *in the absence of any other climb forces*, that is to say, when $F_{\mathrm{cl}} = 0$.

3. In deriving (3.20), vacancy and interstitial recombination *everywhere* has been taken into account via the recombination rate K_{r} in (3.1). Since the dislocation climb velocity v_{cl} depends on the gradient of the diffusion-weighted concentration difference field $u(r)$ evaluated at the dislocation core, and the steady-state diffusion equation for $u(r)$ (3.5) does not involve K_{r}, recombination does not appear in the expression for v_{cl} (3.20).

4. The effective production rates of vacancies and interstitials have also been taken into account. The production rate term (3.23) is directly proportional to the difference in the production rates ΔK_0. When these two rates are the same, i.e. $K_0^{\mathrm{v}} = K_0^{\mathrm{i}}$, and so $\Delta K_0 = 0$, the production rate term becomes zero, and the

rate of climb ceases to have any explicit dependence on the the defect production rates K_0^j.

5. The free parameters in the expression for the dislocation climb velocity (3.20) are temperature T, defect supersaturations c_∞^{v} and c_∞^{i}, and the difference in the effective defect production rates ΔK_0 if it is non-zero. However, the choice of c_∞^{v} and c_∞^{i} should take the defect production rates K_0^{v} and K_0^{i} into account, and so an alternative set of free parameters is T, K_0^{v}, K_0^{i}, and ΔK_0 if it is non-zero, provided a relationship between the effective defect production rates and the defect supersaturations is known.

3.3 Calculations for bcc iron

In this section, a number of the important quantities in (3.20) are calculated for bcc iron over a range of temperatures. The results of these calculations are discussed, and compared qualitatively to experimental observations.

3.3.1 Thermal point defect concentrations

In bcc iron, the vacancy formation energy $E_{\mathrm{f}}^{\mathrm{v}}$ is about 2 eV (de Schepper et al., 1983; Fu et al., 2005; Derlet et al., 2007; Wen et al., 2013), and that of the $\langle 110 \rangle$ dumbbell SIAs which dominate the interstitial population[26], $E_{\mathrm{f}}^{\mathrm{i}}$, is about 4 eV (Fu et al., 2005; Derlet et al., 2007). The thermal equilibrium concentrations c_0^j, given by (2.1), of these two defects are shown on an Arrhenius plot for the temperature range 200–900 °C in figure 3.1.

At all the temperatures shown, the thermal vacancy concentration is several orders of magnitude larger than that of the interstitials. This is to be expected given the lower formation energy of vacancies compared to interstitials.

[26] In the other bcc transition metals, the SIA population is instead dominated by $\frac{1}{2}\langle 111 \rangle$ crowdions (Dudarev, 2013).

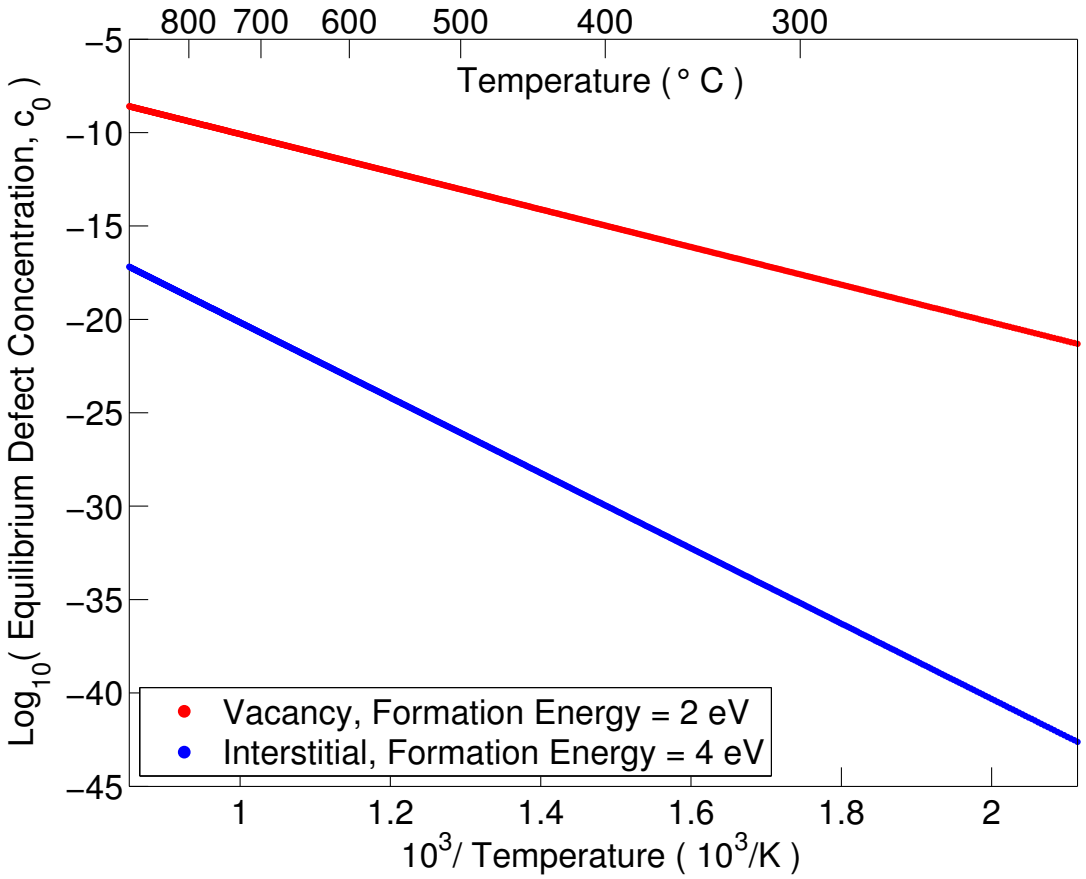


Figure 3.1: Thermal point defect concentrations (in units of fractional atomic concentration). At all the temperatures shown, the thermal vacancy population is several orders of magnitude larger than that of the interstitials.

3.3.2 Dislocation climb mobilities

In bcc iron, the vacancy migration energy $E_{\mathrm{m}}^{\mathrm{v}}$ is about 0.6 eV (Takaki et al., 1983; Fu et al., 2005; Derlet et al., 2007; Wen et al., 2013). The $\langle 110 \rangle$ dumbbell SIAs are able to undergo 3D motion with a migration energy $E_{\mathrm{m}}^{\mathrm{i}}$ of about[27] 0.3 eV (Takaki et al., 1983; Fu et al., 2005). The climb mobility

$$M_{\mathrm{cl}}^{j} = \frac{2\pi\Omega}{b^2 kT \ln(r_\infty / r_{\mathrm{c}})} D^j c_0^j, \tag{3.24}$$

is shown on an Arrhenius plot for the same temperature range of 200–900 °C in figure 3.2.

[27] In the other bcc transition metals, the $\frac{1}{2}\langle 111 \rangle$ crowdions are able to undergo much faster 1D motion, i.e. they have a lower migration energy. However, they can reorient their $\langle 111 \rangle$ direction, and do so even on MD timescales. This reorientation also has an associated energy barrier, leading to net 3D motion with an effective migration energy which is not significantly lower than those of other SIA configurations.

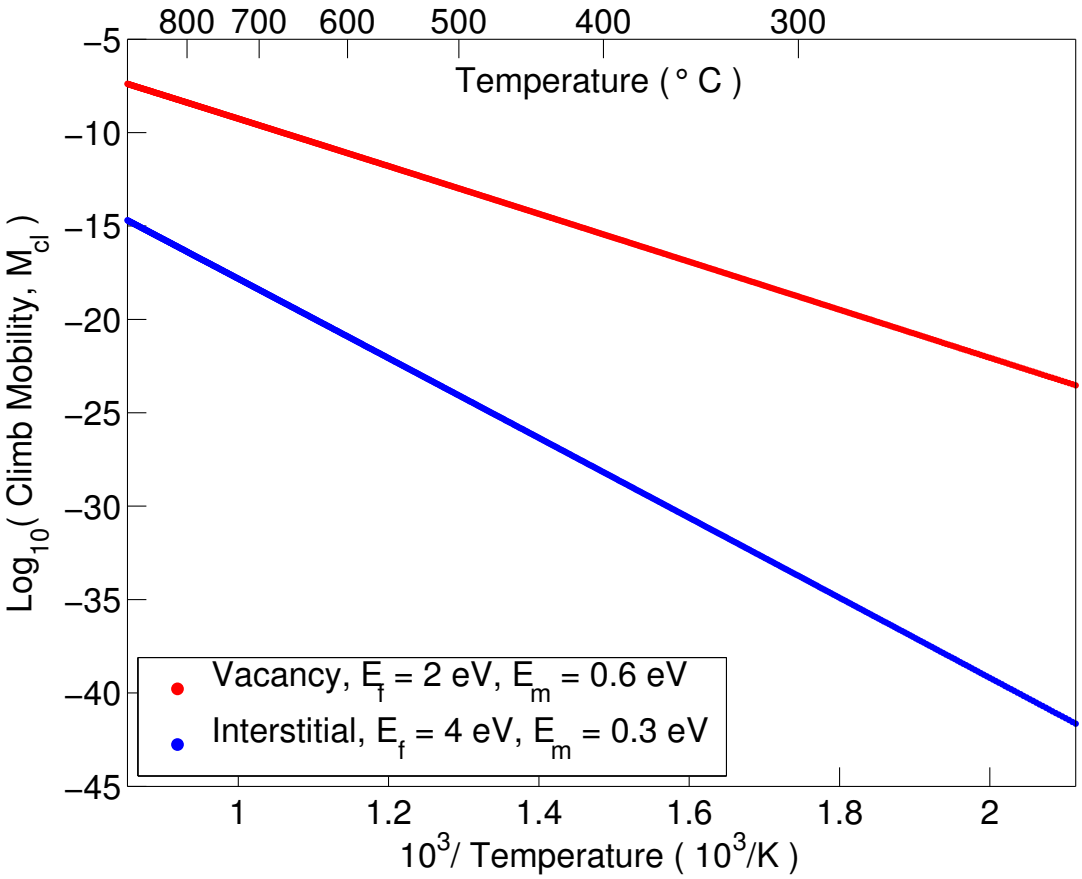


Figure 3.2: Dislocation climb mobilities (in units of $\mathrm{m^2 s^{-1} N^{-1}}$). At all the temperatures shown, the mobility for vacancy mediated climb is several orders of magnitude larger than the mobility for interstitial mediated climb. This is due to the significantly larger population of thermal vacancies at any given temperature (figure 3.1).

For this plot (and those that follow), the Burgers vector magnitude b is chosen to be equal to the lattice parameter a, which for bcc iron is 0.287 nm. The atomic volume Ω in bcc iron is 0.0118 $\mathrm{nm^3}$. The values of r_c and r_∞ are chosen to be $5b$ and $10^4 b$ respectively, making $r_\infty / r_\mathrm{c} = 2000$. The dislocation core radius is chosen to be $5b$ as below a few Burgers vectors from the dislocation line linear elasticity breaks down, and the (linear) dislocation stress reaches the theoretical limit of the material. The outer cutoff radius can be represented by half the average distance between dislocations, which for an isolated dislocation can be $\sim 10^4 b$ (Hirth and Lothe, 1982). However, the resulting climb mobilities are relatively insensitive to the exact choice of r_c and r_∞, as they appear in the logarithm. The defect diffusion pre-factor D_0 in (2.3) is the same for both vacancies and interstitials, and is assumed to be given by $D_0 / a^2 = 10^{13}$ Hz.

This is the widely accepted value (Fu et al., 2005), and is at least of the expected order of magnitude (Takaki et al., 1983).

In figure 3.2 the climb mobility is orders of magnitude larger for vacancies than for interstitials at all the temperatures plotted. Despite the thermal interstitials being more mobile (as they have a lower migration energy), the vacancies still dominate the climb behaviour of the dislocations. This is a direct result of the fact that at any given temperature there is a significantly larger thermal population of vacancies than of interstitials, as shown explicitly in figure 3.1.

These calculations confirm that in the absence of any defect supersaturation, the climb of dislocations due to the climb component of the Peach–Koehler force F_{cl} acting on them will be mediated by the diffusion of vacancies.

3.3.3 Osmotic forces

Defect supersaturations are now introduced, which result in non-zero osmotic forces. In what follows, the vacancy and interstitial supersaturations in the bulk are assumed to be the same, and the difference in the effective production rates of vacancies and interstitials ΔK is assumed to be zero.

The osmotic force due to a supersaturation of defects

$$F_{\mathrm{os}}^{j} = \pm \frac{b k_{\mathrm{B}} T}{\Omega} \left(1 - \frac{c_{\infty}^{j}}{c_{0}^{j}} \right), \tag{3.25}$$

is shown on an Arrhenius plot in figure 3.3, for three different demonstrative supersaturations. The osmotic forces due to vacancies and interstitials result in dislocation climb in opposite directions, which is not explictly shown.

The osmotic force due to an interstitial supersaturation of 10^{-12} fractional atomic concentration of defects, or 10^{-6} parts per million (ppm), is initially very large, but drops by twenty-five orders of magnitude as the temperature is increased from 200 to 900 °C. This is due to the value of the interstitial supersaturation *relative* to the thermal interstitial concentration — the $c_{\infty}^{\mathrm{i}}/c_{0}^{\mathrm{i}}$ factor in the osmotic force (3.25) — decreasing as

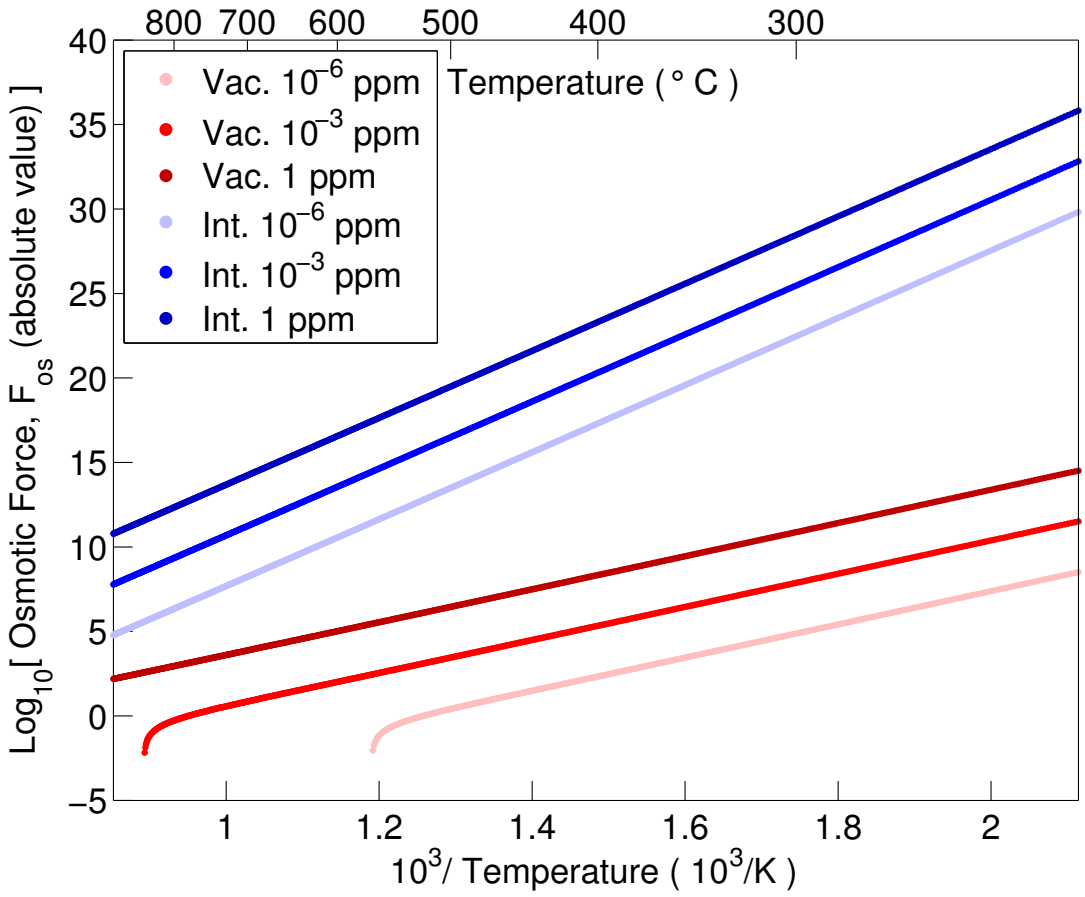


Figure 3.3: Osmotic forces (in units of Nm^{-1}) for three demonstrative bulk defect concentrations. At all the temperatures shown, the osmotic force due to the supersaturation of interstitials dominates, as the relative supersaturation of interstitials is larger than that of vacancies.

c_0^{i} increases with temperature. This leads to a positive gradient on the Arrhenius plot, corresponding to a negative activation energy.

In the case of a vacancy supersaturation of 10^{-12} defects, or 10^{-6} ppm, the osmotic force is up to twenty-two orders of magnitude smaller than in the case of the interstitial supersaturation, and it also decreases with temperature. Again, this is due to the dependence of the osmotic force on the ratio of the vacancy supersaturation to the thermal vacancy concentration at the given temperature. The much larger thermal concentrations of vacancies mean that the relative supersaturation, and thus the osmotic force, is much smaller. In fact, above roughly 570 °C the osmotic force for this vacancy supersaturation of 10^{-6} ppm drops to zero. This is because the thermal vacancy population at this temperature has reached the same value as the bulk concentration, i.e. the

bulk concentration no longer amounts to a supersaturation at all, and hence there is no osmotic force.

In these calculations, and subsequently in this work, bulk defect concentrations which are *below* their corresponding thermal concentrations are considered to be unphysical, as such a "subsaturation" would quickly increase to the thermal equilibrium value. In cases where $c_\infty^j < c_0^j$, the bulk concentration is set to be equal to the thermal concentration instead.

For a supersaturation of 10^{-9} (10^{-3} ppm), the osmotic forces are higher in general than the 10^{-12} (10^{-6} ppm) case, and the osmotic force due to the vacancy supersaturation now drops to zero at a higher temperature of about 850 °C, but otherwise the general trends are the same. The increase in the forces of three orders of magnitude is exactly as expected from the form of (3.25). Finally, the 10^{-6} (1 ppm) case shows further increases, again as expected, and the osmotic force due to the vacancy supersaturation now does not drop to zero at any point over this range of temperatures.

3.3.4 Osmotic climb velocities

The climb velocity of a dislocation due purely to the presence of a supersaturation of a particular defect is simply the product of the dislocation mobility for climb mediated by that defect, and the osmotic force due to the supersaturation of that defect, i.e.

$$v_{\mathrm{os}}^j = M_{\mathrm{cl}}^j F_{\mathrm{os}}^j. \tag{3.26}$$

The magnitude of these osmotic climb velocities is plotted in figure 3.4 over a range of temperatures for the same three demonstrative defect supersaturations as used previously. These velocities are in opposite directions for vacancies and interstitials. At all temperatures and for all three supersaturation values considered, the osmotic climb velocity due to an interstitial supersaturation is 1–3 orders of magnitude higher than the corresponding osmotic climb velocity due to a vacancy supersaturation of the same size. In fact, for the lower bulk concentrations, at a high enough temperature the vacancy

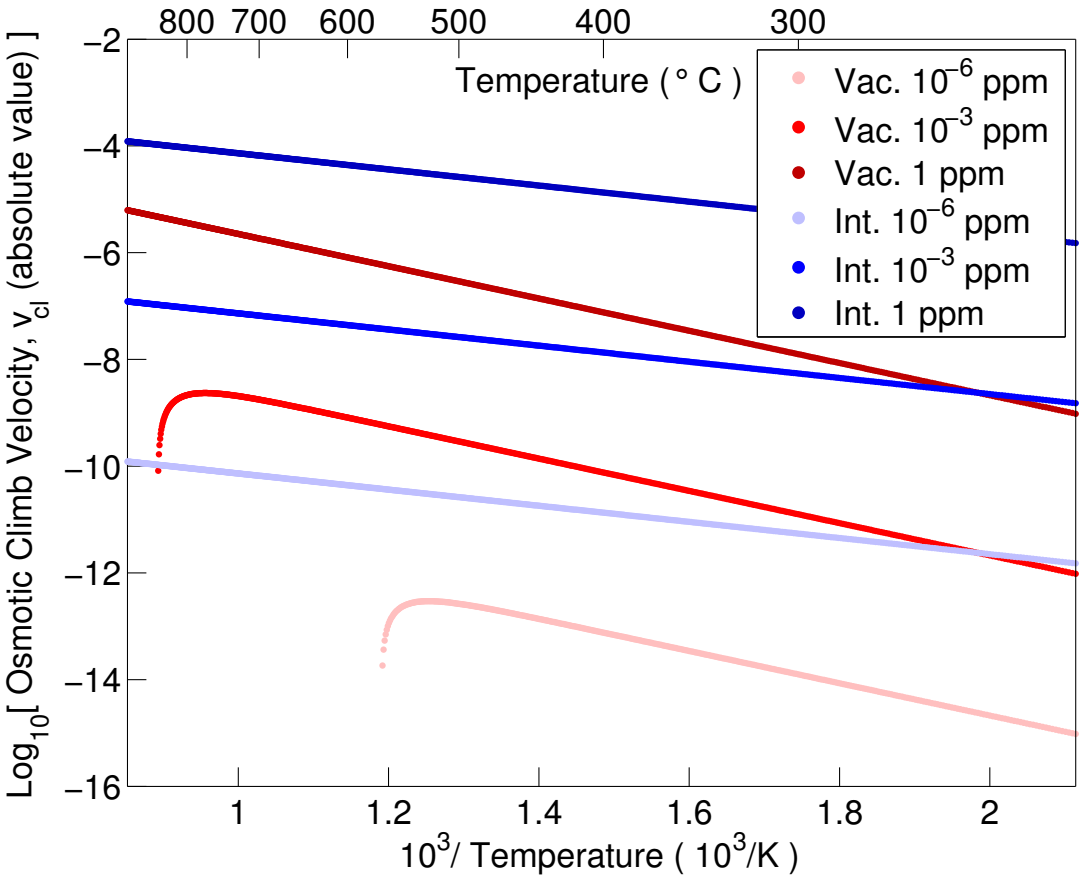


Figure 3.4: Osmotic climb velocities (in units of ms^{-1}) for the same three demonstrative bulk defect concentrations as used previously. For a given c^j_∞, the osmotic climb velocity is 1–3 orders of magnitude larger for the interstitial supersaturation than for the vacancy supersaturation.

bulk concentration is unable to produce an osmotic climb velocity at all.

It is clear that the (osmotic) climb of dislocations caused by the presence of equal supersaturations of vacancy and interstitial defects will be dominated by the interstitial defects, and so will proceed in the direction of climb favoured by the absorption of interstitial defects at the dislocations.

3.3.5 Comparison of thermal and osmotic climb velocities

Figure 3.5 compares the osmotic climb velocities shown in figure 3.4 with the climb velocity of an edge dislocation subjected to a 1 GPa compressive load, mediated by either thermal vacancies or interstitials. A load of 1 GPa roughly equates to the self-force felt by a prismatic dislocation loop of width ∼5 nm acting to shrink it. This size

is approximately consistent with the real irradiation damage loops observed in situ in bcc iron undergoing self-ion irradiation by Xu (2013). These loops were all indentified as interstitial-type. The observations of Xu, and their relationship to this work, will be discussed further in § 3.3.8.

The loop width of ∼5 nm is estimated from the loop self-stress σ_{loop} of –1 GPa using the simple expression

$$F_{\text{loop}}(R) = \sigma_{\text{loop}}(R)b = -\frac{\mu b^2}{4\pi(1-\nu)}\frac{1}{R}, \tag{3.27}$$

where R is the loop radius, μ is the shear modulus, and ν is Poisson's ratio. For bcc iron, μ and ν are taken to be 82 GPa and 0.305 respectively. The sign convention used in (3.27) is that forces acting radially outward are postive, whereas those acting radially inward are negative.

The simple expression for the loop self-force (3.27) is found by taking the energy of a circular prismatic loop of radius R (Hirth and Lothe, 1982, p. 169, (6-52)), given by

$$E_{\text{loop}}(R) = 2\pi R\frac{\mu b^2}{4\pi(1-\nu)}\left[\ln\left(\frac{4R}{r_{\text{c}}}\right) - 1\right], \tag{3.28}$$

dividing it by $2\pi R$ to get the energy of the loop per unit length, and then differentiating this energy per unit length with respect to R to get (minus) the force per unit length. The validity of (3.27) will be discussed shortly.

In figure 3.5, when the bulk defect concentration is 10^{-12} defects (10^{-6} ppm), the osmotic climb due to the absorption of interstitials dominates at temperatures below 700 °C, i.e. an interstitial loop of width ∼5 nm would grow under these conditions. However, at temperatures above 700 °C, climb mediated by thermal vacancies takes over, as indicated by the dotted line further to the right. In this case, an interstitial loop would shrink and disappear via the absorption of thermal vacancies. For the larger defect supersaturations, the osmotic climb due to the interstitial supersaturation dominates at all the temperatures shown.

Furthermore, the osmotic climb velocities exhibit a much weaker temperature depen-

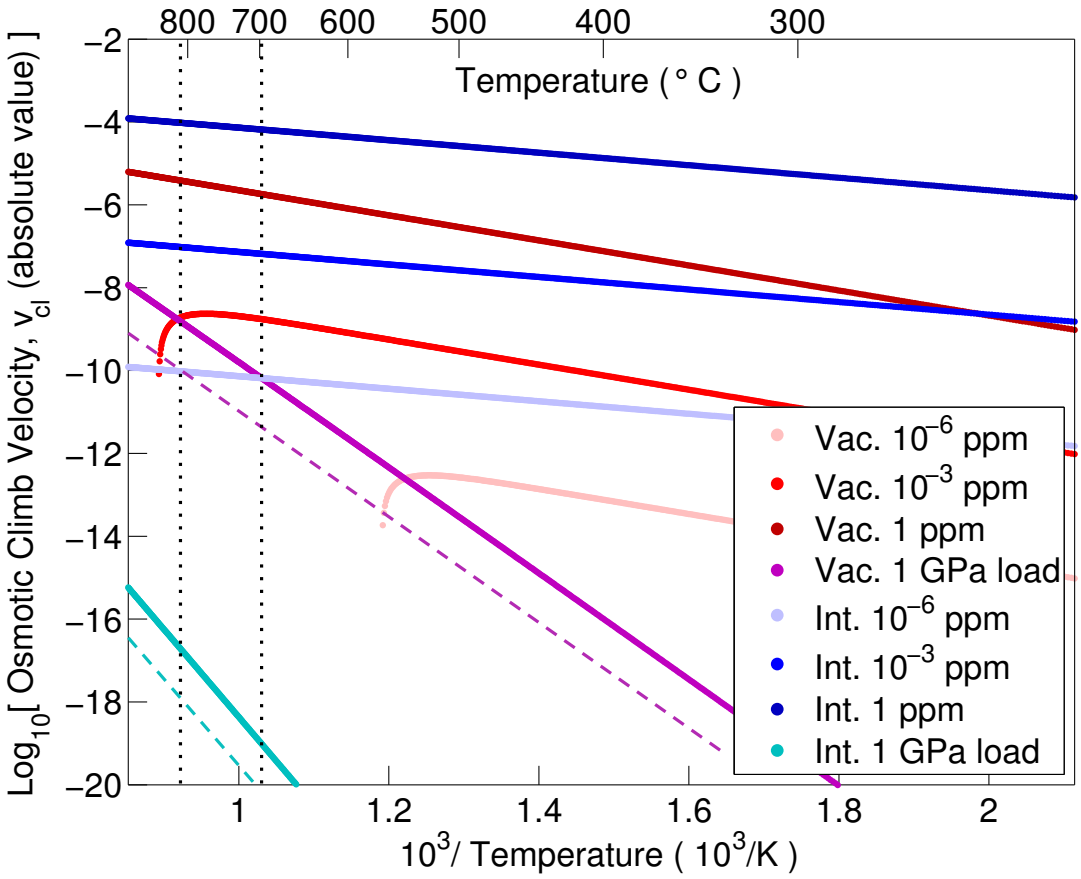


Figure 3.5: Comparison between thermal and osmotic climb velocities (in units of ms^{-1}), for a 1 GPa compressive load in the thermal case. The osmotic climb due to supersaturated interstitials dominates the behaviour, except at high enough temperatures together with a low enough supersaturation. In this case, thermal vacancy mediated climb dominates instead. The dashed lines indicate the 0.1 GPa compressive load case, and the dotted lines indicate the temperature at which the loop behaviour transitions.

dence than those of thermal climb. Thermal vacancy mediated climb becomes negligible at the lower temperatures, dropping by over ten orders of magnitude as the temperature decreases from 900 to 200 °C, and thermal interstitial mediated climb is negligible at all the temperatures shown. On the other hand, the osmotic climb due to supersaturated interstitials drops by only one order of magnitude over this temperature range (and osmotic climb due to supersaturated vacancies drops by only three orders of magnitude). This is because although the mobility decreases with temperature, the osmotic force increases, somewhat mitigating the effect of the lower mobility.

These calculations imply that interstitial loops of width ∼5 nm should grow in the presence of equal vacancy and interstitial supersaturations at temperatures <700 °C, as

the osmotic climb due to the absorption of the supersaturated interstitials dominates. However, if the temperature is high enough, and the steady-state defect supersaturations are low enough, the interstitial loops should shrink and disappear via thermal vacancy mediated climb instead.

This assumes that the climb velocity of an infinite straight edge dislocation derived in § 3.2 can be applied to a nanoscale prismatic loop. Put more precisely, the derivation considers a straight edge segment of infinitesmal length, but assumes the defect concentration mean fields have a cyclindrically symmetric geometry. It is the difference between this cylindrical geometry and the approximately spherically symmetric geometry of the mean fields far from a prismatic loop that could lead to a difference in the precise form of (3.20) were it to be re-derived assuming spherically symmetric defect concentration fields. However, the strong temperature dependence, the linear nature of the mobility laws, and the linear dependence of the osmotic forces on the relative supersaturation for a given temperature would all be reproduced, the differences being restricted to geometric prefactors. Hence the comparison of the terms in the climb velocity (3.20) is considered to be broadly applicable to nanoscale loops.

In this way these calculations can explain why interstitial loops are seen in post-irradiation characterisation of irraditiated bcc metals, but vacancy loops are not (Eyre and Bullough, 1965). It is important to bear in mind that the defect supersaturations considered in this model correspond to the in situ irradiation steady-state values, which depend on the large amounts of cascade damage which is continually produced, and the ongoing loss of the defects to dislocations and other sinks, on timescales much greater than that of individual cascades. The calculations using the present model suggest any loops formed during irradiation provide sinks for the steady-state defect supersaturations, but the absorption of interstitials will dominate the loop behaviour[28]. Hence, during irradiation, the interstitial loops grow, and the vacancy loops disappear. At high enough temperatures, and for low enough irradiation doses (as this implies the steady-state defect supersaturations are low enough), the interstitial loops should disappear as

[28]This model does not capture the formation of proto-loops — i.e. defect clusters — nor their initial growth to the point where they can be considered to be loops of dislocation line. However, qualitatively the mechanism is the same: these defect clusters act as sinks for further defects, and the absorption of interstitials could feasibly dominate their behaviour.

well.

Furthermore, the temperature at which the interstitial loops are no longer seen in either in situ or post-irradiation TEM should indicate the approximate value of the steady-state interstitial supersaturation (and hence the vacancy supersaturation, as these are assumed to be the same). This provides a method of estimating the steady-state interstitial supersaturation if the interstitial loop behaviour transition temperature is known, which is investigated further in § 3.3.6.

The choice of the value of the compressive load (which is directly related to the loop width via (3.27)) has a relatively small effect on the resulting climb velocity in these plots. Decreasing the load to 0.1 GPa — which is equivalent to increasing the loop width by one order of magnitude, to ∼50 nm — shifts the thermal climb trends shown in figure 3.5 down by one order of magnitude, as indicated by the dashed lines. This leads to an increase of ∼100 °C in the transition temperature (the dotted line further to the left). Because of this, provided the interstitial loop population is comprised of loops with widths that are of the same order of magnitude, the temperature at which *all* the loops appear to shrink and disappear instead of grow should indicate the value of the interstitial supersaturation, with an error of a few tens of °C. Hence, the approximate interstitial supersaturation could be found experimentally by this method, without relying on observing loops of a specific size.

Lastly, the present model could be verified by comparing this estimated steady-state interstitial supersaturation with a theoretical value for what the steady-state supersaturation should be. Both K–P-type calculations using, for example, SRIM, and MD simulations can shed some light on the defect supersaturations that form as a result of individual cascades. However, as the defect supersaturations in this model are the in situ irradiation steady-state values, which depend on the ongoing occurence of large numbers of cascades (together with the ongoing loss of the defects produced to dislocations and other sinks) over timescales much greater than that of individual cascades, it is very difficult to accurately predict the steady-state supersaturations using these methods. KMC methods show more promise in this field (Soisson et al., 2010).

3.3.6 Defect supersaturation estimation from the interstitial loop behaviour transition temperature

The behaviour of the interstitial damage loops will transition from growing to shrinking — and hence the loops will disappear altogether — when the magnitude of the climb velocity acting to grow the loop $v^{\mathrm{i}}_{\mathrm{os}}$ (via the osmotic absorption of supersaturated interstitials) becomes equal to that of the climb velocity acting to shrink the loop v_{cl} (via the absorption of thermal vacancies), i.e. when

$$v^{\mathrm{i}}_{\mathrm{os}} = -v_{\mathrm{cl}}, \tag{3.29}$$

$$\Rightarrow M^{\mathrm{i}}_{\mathrm{cl}} F^{\mathrm{i}}_{\mathrm{os}} = -M^{\mathrm{v}}_{\mathrm{cl}} F_{\mathrm{loop}}. \tag{3.30}$$

Expressions for the mobilities $M^{\mathrm{v}}_{\mathrm{cl}}(T)$ and $M^{\mathrm{i}}_{\mathrm{cl}}(T)$ are given by (3.22), and the osmotic force due to supersaturated interstitials $F^{\mathrm{i}}_{\mathrm{os}}(T, c^{\mathrm{i}}_{\infty})$ by (3.21). Substituting these expressions into (3.30), and rearranging it in order to make the interstitial supersaturation c^{i}_{∞} the subject, leads to the following expression for the interstitial supersaturation as a function of the temperature at which the interstitial loop behaviour transition occurs, T_{t}:

$$c^{\mathrm{i}}_{\infty}(T_{\mathrm{t}}) = \left(1 - \frac{F_{\mathrm{loop}}\Omega/b}{k_{\mathrm{B}}T_{\mathrm{t}}} e^{-\Delta E/k_{\mathrm{B}}T_{\mathrm{t}}}\right) c^{\mathrm{i}}_{0}(T_{\mathrm{t}}), \tag{3.31}$$

where $\Delta E = E^{\mathrm{v}}_{\mathrm{f}} + E^{\mathrm{v}}_{\mathrm{m}} - E^{\mathrm{i}}_{\mathrm{f}} - E^{\mathrm{i}}_{\mathrm{m}}$. Incidentally, this interstitial supersaturation is equal to the vacancy supersaturation, since they are assumed to be the same in this model.

The estimated interstitial supersaturation in (3.31) is plotted for loops of width 5, 10 and 20 nm over a range of possible behaviour transition temperatures in figure 3.6. The simple expression for F_{loop} given in (3.27) is used for this initial estimation.

As can been seen from the plot, a transition temperature of 700 °C leads to a predicted supersaturation of roughly 10^{-12} (10^{-6} ppm), which is correct given the location of the crossing points of the thermal vacancy mediated climb curve with the curve for osmotic climb due to 10^{-6} ppm interstitials in figure 3.5. For a given transition temperature, there is a spread of about one order of magnitude in the predicted supersaturation, depending on which loop size is considered. Hence the estimated supersaturation is fairly

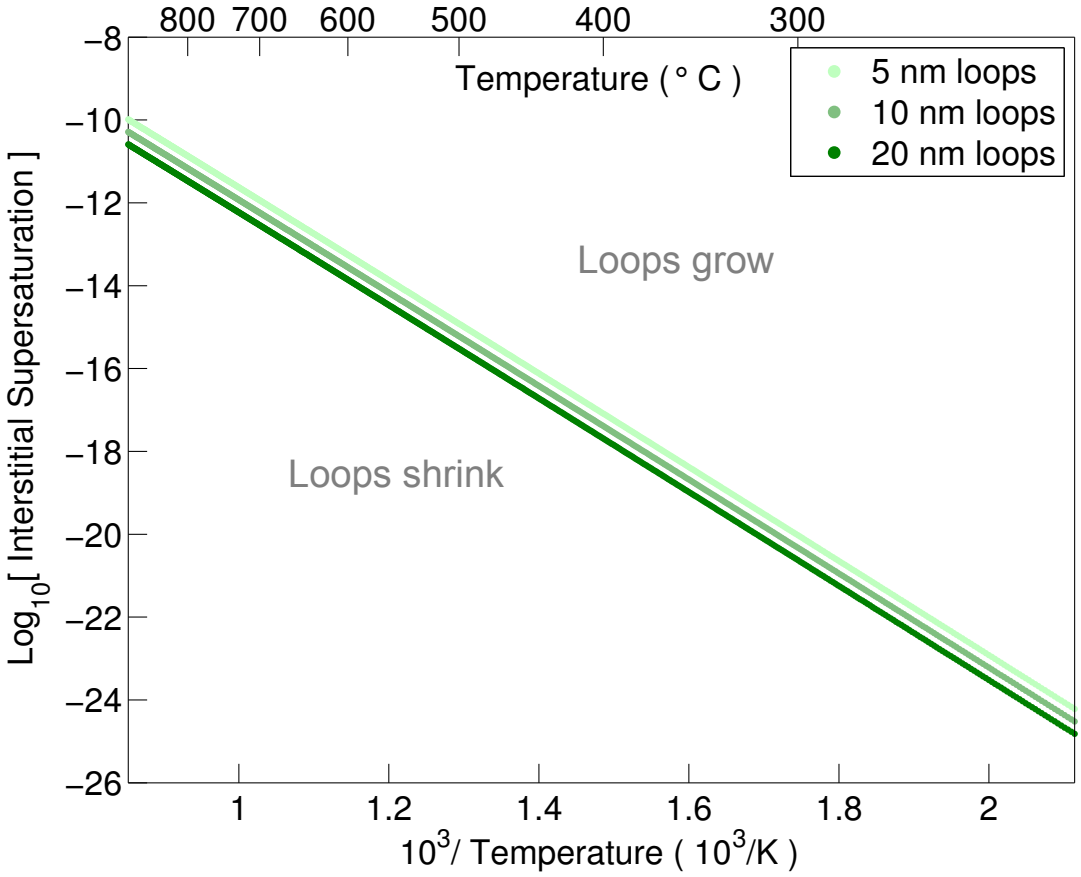


Figure 3.6: Interstitial supersaturation (and hence vacancy supersaturation — they are equal) dependence on loop behaviour transition temperature (3.31). Expression (3.27) is used to calculate F_{loop}.

weakly dependent on the size of the loops studied, as previously argued. Conversely, for a given supersaturation, there is a spread of up to about 100 °C (at the higher temperatures) in the predicted transition temperature depending on loop size.

Interstitial loop behaviour transition temperatures could be observed experimentally, provided high enough temperatures can be reached in such in situ irradiation experiments. If the present model is correct, then such transition temperatures provide a measurement of the steady-state defect supersaturations during irradiation. KMC simulations could also capture the transition temperature, provided they can accurately represent the steady-state defect supersaturations.

3.3.7 Circular prismatic loop self-force

The expression for the self-force acting to shrink a circular prismatic loop F_{loop} given in (3.27) is not the only possible such expression. Gavazza and Barnett (1976, (5.6)), after Kroupa (1960), give the contribution to the self-force of a prismatic loop which neglects the contribution from the dislocation core as

$$F_{\text{cut}} = -\frac{\mu b^2}{4\pi(1-\nu)}\frac{1}{R}\left[\ln\left(\frac{8R}{r_{\text{c}}}\right) - 1\right], \tag{3.32}$$

where r_{c} is the dislocation core radius. Gavazza and Barnett (1976, (6.7) onwards) also give the contribution due to the dislocation core as

$$F_{\text{tube}} = -\frac{\mu b^2(3-2\nu)}{16\pi(1-\nu)^2}\frac{1}{R}. \tag{3.33}$$

Hence, the total self-force on a prismatic loop, $F_{\text{loop}} = F_{\text{cut}} + F_{\text{tube}}$, is given by

$$F_{\text{loop}} = -\frac{\mu b^2}{4\pi(1-\nu)}\frac{1}{R}\left[\ln\left(\frac{8R}{r_{\text{c}}}\right) - 1 + \frac{(3-2\nu)}{4(1-\nu)}\right]. \tag{3.34}$$

Note that this expression is just the simple expression given previously in (3.27) multiplied by the sum of two terms. The first term depends only logarithmically on the loop radius R, and the second term is a constant of $\mathcal{O}(1)$.

If we choose $r_{\text{c}} = 5a$, as has been chosen here previously, we can evaluate the "full" self-force in (3.34) for the three loop widths of interest. These self-forces are compared with the simple ones used in figure 3.6 in table 3.1. The multiplicative factors by which these full self-forces are larger than the corresponding simple ones (the term in square brackets in (3.34)) are also shown explicitly.

Loop width, $2R$ (nm)	Simple F_{loop} (3.27) (Nm^{-1})	Full F_{loop} (3.34) (Nm^{-1})	Multiplicative factor
5	-0.309	-0.770	2.50
10	-0.154	-0.492	3.19
20	-0.0772	-0.300	3.88

Table 3.1: Prismatic loop self-force values.

From table 3.1 it can be seen that the full loop self-forces are larger than the simple ones by a factor of ∼2–4. This will shift the curves in figure 3.6 up slightly, but on such an Arrhenius plot the change will be relatively small. Furthermore, the relative variation between the three full self-forces is smaller than for the simple ones, which will serve to move the curves in figure 3.6 closer together, leading to a small error in the estimated supersaturation. The resulting interstitial supersaturations using these full self-forces are shown in figure 3.7, and the curves are indeed slightly higher up the plot, and slightly closer together.

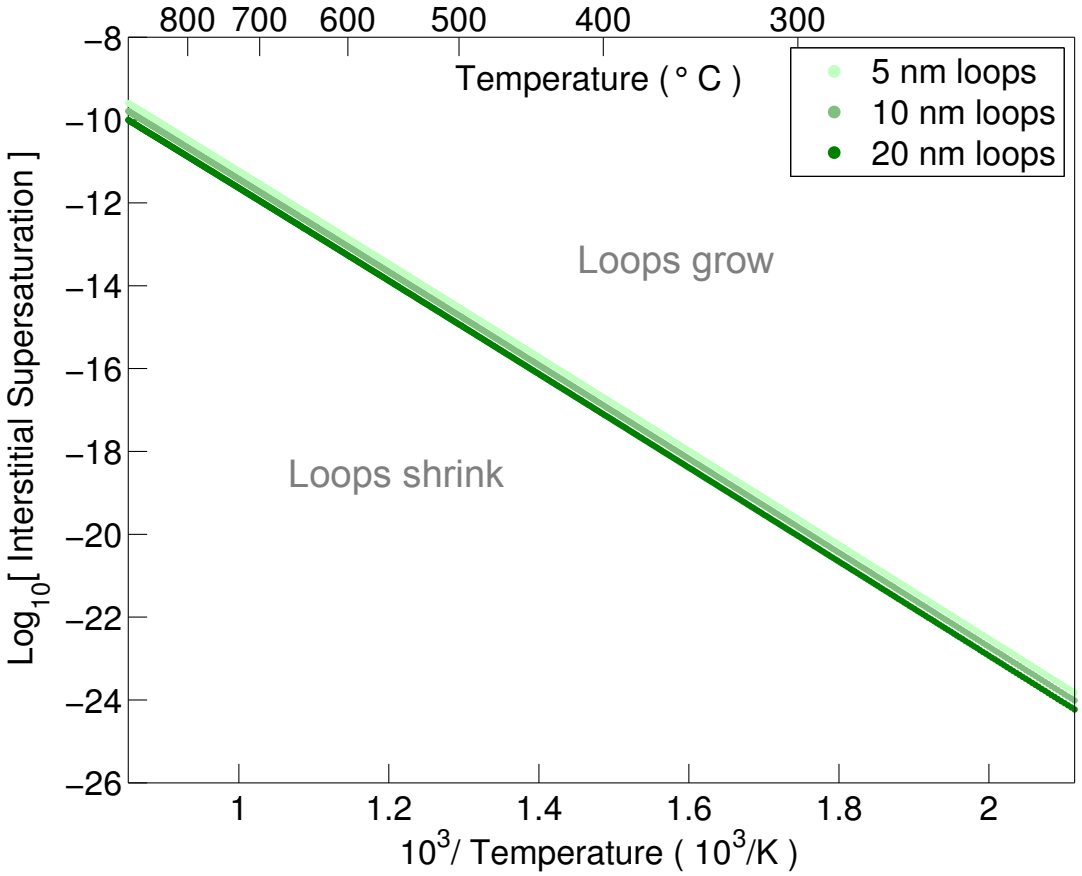


Figure 3.7: Interstitial supersaturation dependence on loop behaviour transition temperature (3.31), using the full expression (3.34) to calculate F_{loop}.

The overall spread between the curves in figures 3.6 and 3.7 when both figures are taken together is still less than two orders of magnitude. However, the estimated defect supersaturations vary by more than ten orders of magnitude over the 200–900 °C temperature range, and so using this methodology a measured — or simulated — interstitial loop behaviour transition temperature can still be used to provide a reasonable estimate of

the order of magnitude of the steady-state defect supersaturations.

3.3.8 Comparison with experiment

Self-ion irradiation-induced damage loops of width >5 nm have been observed in situ in bcc iron undergoing irradiation at several temperatures up to 460 °C by Xu (2013). During these observations, the vacancy and interstitial supersaturations are constantly replenished by the irradiation.

All the damage loops produced were identified as interstitial type. As the irradiation dose rate was increased from 3×10^{-5} to 6×10^{-4} dpa/s (calculated using SRIM), both the size and density of the loops increased. This is consistent with the larger interstitial supersaturations produced by the higher dose rates leading to both the formation of more interstitial clusters (loop embryos), and faster loop growth. Furthermore, as the irradiation temperature was increased, the size of the loops increased, whilst the density of the loops decreased. This is consistent with the higher temperatures leading to an increase in the formation of finger loops (which were also observed at the higher temperatures). These finger loops form when existing loops coalesce, a process which involves glide motion followed by some — but relatively small amounts of — climb motion. The growth of loops accompanied by a reduction in the loop density which proceeds via the coalescence of existing loops in this way is known as loop coarsening.

Importantly, it appears Xu did not perform irradiations at a high enough temperatures/low enough dose rates to observe a disappearance of interstitial damage loops as predicted by this model. In these experiments it appears the transition temperature was not reached, and hence if indeed there is a transition temperature, it must be above 460 °C. In this case, this would imply a lower limit on the interstitial supersaturation of $\sim 10^{-16}$ defects ($\sim 10^{-10}$ ppm). This is many orders of magnitude lower than the displacements per second — i.e. Frenkel pairs per second — predicted by SRIM for these irradiation conditions, which is to be expected, as a large fraction of the Frenkel pairs predicted by SRIM undergo spontaneous recombination in reality. Nevertheless, the SRIM calculations suggest that steady-state defect populations larger than, and indeed

much larger than, 10^{-16} defects are feasible for Xu's irradiation conditions.

3.4 Summary

In § 3.2, an expression for the climb velocity of an edge dislocation was derived using a bulk diffusion model which incorporates both vacancies and interstitials. The calculations for bcc iron in § 3.3 using this model provide a number of insights:

1. In the absence of any defect supersaturation, the climb of dislocations due to the climb component of the Peach–Koehler force acting on them will be mediated by the bulk diffusion of vacancy defects.

2. The osmotic climb of dislocations caused by the presence of equal steady-state supersaturations of vacancy and interstitial defects will instead be dominated by the interstitial defects, and hence will proceed in the direction of climb favoured by the absorption of interstitial defects at the dislocations. Steady-state defect supersaturations are expected under fusion neutron irradiation conditions, although they are not necessarily equal.

3. Experimentally, interstitial loops are usually observed in in situ and post-irradiation characterisation of irraditiated materials, but vacancy loops are not. It is argued that any proto-loops formed provide sinks for both the vacancy and interstitital supersaturations, but the absorption of the interstitials dominates the behaviour of the loops. Hence the interstitial loops grow, and the vacancy loops disappear. At high enough temperatures, and for low enough irradiation dose rates, interstitial loops should not been seen either.

4. If this model is correct, the experimentally measured temperature at which the behaviour of interstitial loops of a given size transitions from growth to shrinkage should provide a measurement of the steady-state defect supersaturations under irradiation conditions.

5. Comparison of the model with the available experimental data provides a lower bound of $\sim 10^{-16}$ for the steady-state defect supersaturations. Were irradiation

experiments to be performed at progressively higher temperatures than 460 °C in bcc iron in order to observe the transition temperature, the value of the transition temperature would indicate the order of magnitude of the steady-state defect supersaturations.

6. This model could then be verified by comparing the steady-state supersaturation calculated from the experimentally measured transition temperature with a theoretical value for what the supersaturation should be at the transition temperature. However, finding such a theoretical value for the steady-state defect supersaturation under irradiation conditions is very challenging.

Finally, similar calculations to those performed in § 3.3 are carried out for tungsten — a promising candidate material for the divertor plate of a fusion reactor — in appendix A.

Chapter 4

Code development and testing: dislocation climb

4.1 Introduction

In this work, the deformation characteristics of particle-reinforced ferrous alloys at the high operating temperatures — and under the irradiation conditions — of a fusion reactor is investigated by modelling the dislocations in such alloys computationally. This is done by conducting 3D DDD simulations using the existing `DDLab` code. In order to capture temperature and defect supersaturation effects, development of the `DDLab` code was required.

In section § 4.2 the functionality of `DDLab` as released is briefly discussed, particularly the mobility law function for bcc metals which is provided with the code. Then, in section § 4.3, the temperature-dependent climb model derived in chapter 3 is implemented, tested, and compared to theory. The results of some unforeseen but necessary calibration of `DDLab` are discussed in § 4.4. Finally, § 4.5 discusses the implementation, testing and calibration of a glide and climb dual time step method.

4.2 DDLab functionality as released

A detailed discussion of the line dislocation dynamics methodology used by DDLab can be found in Bulatov and Cai (2006, § 10), and a discussion of DDLab's performance and capabilities in Arsenlis et al. (2007). As described in § 2.4.1, DDLab is a 3D DDD code which uses the non-singular analytical expressions developed by Cai et al. (2006, § B.2) to compute the stress field due to a network of straight dislocation segments.

In an elastically isotropic medium, the components of the stress field $\boldsymbol{\sigma}(\mathbf{r})$ at position $\mathbf{r}$ generated by a general curved dislocation network C are given by the following line integral (Peach and Koehler, 1950; Hirth and Lothe, 1982, p. 105):

$$\begin{aligned}\sigma_{\alpha\beta}(\mathbf{r}) = &-\frac{\mu}{8\pi}\oint_C b_m\epsilon_{im\alpha}\frac{\partial}{\partial r'_i}\nabla'^2 R\mathrm{d}r'_\beta - \frac{\mu}{8\pi}\oint_C b_m\epsilon_{im\beta}\frac{\partial}{\partial r'_i}\nabla'^2 R\mathrm{d}r'_\alpha \\ &-\frac{\mu}{4\pi(1-\nu)}\oint_C b_m\epsilon_{imk}\left(\frac{\partial^3 R}{\partial r'_i\partial r'_\alpha\partial r'_\beta} - \delta_{\alpha\beta}\frac{\partial}{\partial r'_i}\nabla'^2 R\right)\mathrm{d}r'_k, \qquad (4.1)\end{aligned}$$

where $R \equiv |\mathbf{r}-\mathbf{r}'|$, $\mathbf{b}$ is the Burgers vector at location $\mathbf{r}'$ on the dislocation network C, and ϵ_{ijk} is the Levi-Civita symbol. Each line integral $\oint_C$ is taken over the entire dislocation network exactly once. As $R \to 0$, i.e. as $\mathbf{r}$ approaches anywhere which is part of the dislocation network C, some (if not all) of the components of $\boldsymbol{\sigma}(\mathbf{r})$ diverge. This is unphysical, and is due to the assumption that the Burgers vector is a delta function located on C. It is this singular behaviour which Cai et al. eliminated using their non-singular theory. The Burgers vector is spread smoothly over a radius $\sim a_{\mathrm{ns}}$ — the non-singular spreading parameter — about the dislocation line C. Thus a_{ns} provides an alternative definition of the dislocation core radius.

At each DDLab simulation time step, the stress field due to the network of straight dislocation segments is evaluated using the analytical expressions of Cai et al.. Together with the externally applied stress, this stress field is used to compute the Peach–Koehler-type forces (per unit length) on the segments. These segment forces are integrated along the segments using a simple linearly-weighted shape function in order to evaluate the net forces on the discretisation nodes themselves. A mobility law such as the one for bcc metals described in § 4.2.1 is then used to compute the nodal velocities from these nodal

forces (a mobility function for fcc metals is also provided). In this way the equation of motion of the nodes is numerically integrated at each time step. Different integrator functions are provided, including explicit Euler-forward and implicit trapezoid schemes. Dislocation reactions are handled by the `separation` and `collision` functions, and the nodal discretisation is managed by the `meshcoarsen` and `meshrefine` functions.

4.2.1 Mobility law for bcc metals

In `DDLab`'s bcc mobility law function `mobbcc0`, the nodal velocities $\mathbf{v}_\mathrm{n}$ are evaluated using the following expression:

$$\mathbf{v}_\mathrm{n} = \mathbf{D}_\mathrm{n}^{-1} \cdot \mathbf{F}_\mathrm{n}, \tag{4.2}$$

where $\mathbf{F}_\mathrm{n}$ is the force on node n, and the 3×3 matrix $\mathbf{D}_\mathrm{n}$ is given by[29]

$$\mathbf{D}_\mathrm{n} = \sum_i \left(\mathbf{B}_i(\boldsymbol{\xi}_i) \cdot \frac{L_i}{2} \right), \tag{4.3}$$

where the sum is taken over all the dislocation segments to which node n is connected, $\mathbf{B}_i(\boldsymbol{\xi}_i)$ is the 3×3 orientation-dependent drag coefficient matrix of segment i which depends on its line direction $\boldsymbol{\xi}_i$, and L_i is the length of segment i.

The i subscripts are now dropped for clarity. $\mathbf{B}(\boldsymbol{\xi})$ combines the drag coefficents for pure edge dislocation glide B_eg, pure screw glide B_sg, and pure edge climb B_cl, together with the line drag coefficient B_li, in such a way as to orient them correctly in 3D space relative to the segment's arbitrary line direction $\boldsymbol{\xi}$ in 3D space.

The dislocation drag coefficients B_eg, B_sg and B_cl are related to the dislocation mobilities defined in § 2.3.6 — they are simply the inverse of these quantities, although here pure edge and pure screw dislocations are considered seperately, allowing their drag coefficients to differ. The line drag coefficient B_li is included in order to allow nodal velocities to have a component parallel to the line directions of the segments to which the

[29] Note that (4.3) is implemented incorrectly in the `mobbcc0` function of `DDLab`. The $L_i/2$ factor is implemented as $2L_i$, which has the effect of erroneously increasing the magnitude of all the drag coefficents by a factor of 4. For example: currently, if the screw glide drag coefficient `Bscrew` is set to 1×10^{-4} Pa·s by the user in the `input` script, it has actually been set to 4×10^{-4} Pa·s.

nodes are connected, which is required to avoid partially pinning the nodes artificially. As the nodes should be relatively free to move parallel to the segment line directions, B_{li} should be much smaller than the other drag factors. The directions in which these different drag factors act are illustrated in figure 4.1.

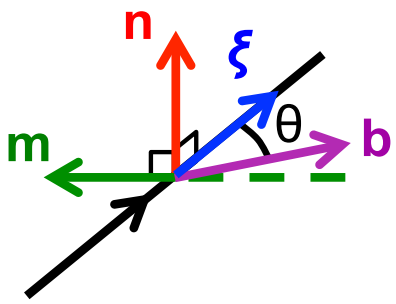


Figure 4.1: The arrangement of a mixed dislocation's Burgers vector $\mathbf{b}$, and line $\boldsymbol{\xi}$, climb $\mathbf{n}$, and glide $\mathbf{m}$ directions. The dislocation character angle θ is also shown.

For a pure screw segment, which in bcc metals can undergo pencil-glide isotropically in any direction perpendicular to its line direction (provided the temperature is high enough), $\mathbf{B}(\boldsymbol{\xi}) = \mathbf{B}_{\mathrm{s}}(\boldsymbol{\xi} \parallel \mathbf{b})$, which is given by

$$\mathbf{B}_{\mathrm{s}}(\boldsymbol{\xi} \parallel \mathbf{b}) = B_{\mathrm{sg}}[\mathbf{I} - (\boldsymbol{\xi} \otimes \boldsymbol{\xi})] + B_{\mathrm{li}}(\boldsymbol{\xi} \otimes \boldsymbol{\xi}), \tag{4.4}$$

where $\mathbf{I}$ is the 3×3 identity matrix. The first term allows nodes connected to pure screw dislocations to move in any direction which lies in the plane perpendicular to $\boldsymbol{\xi}$ subject to the screw glide drag, and the second term allows them to move parallel to $\boldsymbol{\xi}$ subject to the line drag.

Conversely, for a pure edge segment, which can glide in the $\mathbf{m}$ direction and climb in the $\mathbf{n}$ direction[30], $\mathbf{B}(\boldsymbol{\xi}) = \mathbf{B}_{\mathrm{e}}(\boldsymbol{\xi} \perp \mathbf{b})$, which is given by

$$\mathbf{B}_{\mathrm{e}}(\boldsymbol{\xi} \perp \mathbf{b}) = B_{\mathrm{eg}}(\mathbf{m} \otimes \mathbf{m}) + B_{\mathrm{cl}}(\mathbf{n} \otimes \mathbf{n}) + B_{\mathrm{li}}(\boldsymbol{\xi} \otimes \boldsymbol{\xi}). \tag{4.5}$$

The line drag term — the last one in (4.5) — is present again, and first and second terms allow nodes connected to pure edge dislocations to move parallel to the glide and climb directions subject to the edge glide and climb drags respectively.

[30] These are defined by $\mathbf{n} \equiv \mathbf{b} \times \boldsymbol{\xi}/|\mathbf{b} \times \boldsymbol{\xi}|$, and $\mathbf{m} \equiv \mathbf{n} \times \boldsymbol{\xi}$, as in § 2.3.6.

Finally, for a mixed dislocation, DDLab uses the following smooth interpolation between these two limiting cases:

$$\mathbf{B}_{\text{mix}}(\boldsymbol{\xi}) = B_{\text{gl}}(\mathbf{m} \otimes \mathbf{m}) + B'_{\text{cl}}(\mathbf{n} \otimes \mathbf{n}) + B_{\text{li}}(\boldsymbol{\xi} \otimes \boldsymbol{\xi}), \tag{4.6}$$

where

$$B_{\text{gl}} = \left[\frac{|\mathbf{b} \times \boldsymbol{\xi}|^2}{B_{\text{eg}}^2} + \frac{(\mathbf{b} \cdot \boldsymbol{\xi})^2}{B_{\text{sg}}^2} \right]^{-\frac{1}{2}}, \quad \text{and} \tag{4.7a}$$

$$B'_{\text{cl}} = \sqrt{B_{\text{cl}}^2 |\mathbf{b} \times \boldsymbol{\xi}|^2 + B_{\text{sg}}^2 (\mathbf{b} \cdot \boldsymbol{\xi})^2}. \tag{4.7b}$$

As $\boldsymbol{\xi} \times \mathbf{b} \to \mathbf{0}$ the expression in (4.6) tends to that in (4.4).

4.3 Temperature-dependent climb

The dislocation drag coefficients described in § 4.2.1 are input parameters for DDLab simulations. Glide drag factors[31] can be measured experimentally under some circumstances or determined from MD or KMC simulations. However, an ad hoc approach is often taken for the choice of climb drag factor, as mentioned in § 2.4.2.

In this work, temperature-dependent climb is incorporatated into DDLab using the climb drag factors for both vacancies and interstitials derived from the bulk point defect diffusion model derived in chapter 3, together with the osmotic forces which also resulted from the model. In this way the dislocation climb not only depends realistically on temperature, but also on the bulk defect concentrations, which allows for the incorporation of bulk defect supersaturations arising from irradiation into the simulations.

4.3.1 Implementing thermal vacancy mediated climb

In order to implement temperature-dependent climb, new original code needed to be developed for DDLab. Climb mediated by the bulk diffusion of only one type of defect was implemented first, as this was relatively straightforward to incorporate into the existing

[31] Edge and/or screw.

code. Vacancies were chosen, in order to simulate and test thermal climb scenarios, before adding the effect of a vacancy supersaturation only[32].

To begin with, new blocks of code were added to the `input_dd3d` script, and a new function `calcClimbDragVac`, which evaluates the temperature-dependent drag factor for vacancy mediated climb $B_{\mathrm{cl}}^{\mathrm{v}}(T)$, was written. This climb drag factor is simply the reciprocal of the climb mobility $M_{\mathrm{cl}}^{\mathrm{v}}$ defined for a pure edge dislocation in (3.22), with one caveat. For a general, mixed dislocation segment, the factors of b in (3.22) must be replaced with $b \sin\theta$, where θ is the dislocation character angle. This is because it is only the edge component of a mixed dislocation's Burgers vector which undergoes climb. In terms of code implementation, this proved troublesome, as $B_{\mathrm{cl}}^{\mathrm{v}}(T)$ now needed to be evaluated for each individual segment depending on its Burgers vectors and line direction, whereas the drag factor input parameters act on the nodal forces after they have been evaluated by iterating through the segment list. This issue was ultimately dealt with by changing some lines of code in the mobility law function `mobbcc0`.

The `DDLab` scripts and functions which had blocks of code changed and/or added to them — together with the entirely new functions — mentioned throughout this chapter, and the subsequent code development and testing in chapter 6, are included in appendix B.

4.3.2 Square prismatic loop

A simple test case of a square prismatic vacancy loop is used to test the implementation $B_{\mathrm{cl}}^{\mathrm{v}}(T)$, in the absence of an osmotic force due to a vacancy supersaturation. The input parameters for bcc iron, and the simulation free parameters, used to calculate $B_{\mathrm{cl}}^{\mathrm{v}}(T)$ are listed in table 4.1. The temperature is set to 700 °C.

The initial configuration of the test loop at simulated time $t = 0$ is shown in figure 4.2(a). The loop has a width of $100a$ (28.7 nm) and its Burgers vector is $\mathbf{b} = [100]$ (the line-sense is defined to be clockwise about [100]). The view is down the $[1\bar{1}1]$ direction. There is no applied load. From this initial configuration the only forces on the loop are due to the loop's interaction with its own stress field. These forces act to shrink

[32] The subsequent implementation of interstitial mediated climb is described in § 4.3.11, and climb mediated by both vacancies and interstitials is tested in § 4.3.12.

Properties of bcc iron	
Shear modulus, μ	82 GPa
Lattice parameter, a	0.28665 nm
Atomic volume, Ω	0.0118 nm^3
Vacancy formation energy, $E_{\mathrm{f}}^{\mathrm{v}}$	2 eV
Vacancy migration energy, $E_{\mathrm{m}}^{\mathrm{v}}$	0.6 eV
Point defect self-diffusion pre-exponent, D_0	2×10^4 m^{2}s^{-1}
Simulation free parameters	
Dislocation core radius, r_{c}	$5a$
Outer cut-off radius, r_∞	$10^4 a$

Table 4.1: Temperature-dependent climb test simulation input parameters for bcc iron. See § 3.3 for more details.

the loop and round the sharp corners to smooth curves. The vacancy mediated climb should allow the loop to round and shrink before disappearing.

Figure (b) shows an intermediate snapshot after 0.778 s of simulated time (after 36 time increments). The loop has both rounded and shrunk via climb as expected. Figure (c) shows the loop at the moment it ceases to exist — after 1.36 s of simulated time. A timescale of the order of ∼1 s for this nanoscale loop to shrink down to nothing via thermal vacancy mediated climb does not seem unreasonable for the relatively high temperature in bcc iron of 700 °C, as thermal creep lives observed in tensile creep testing of RAFM steels at the lower temperature of 550 °C are ∼1000 s (Yu et al., 2005).

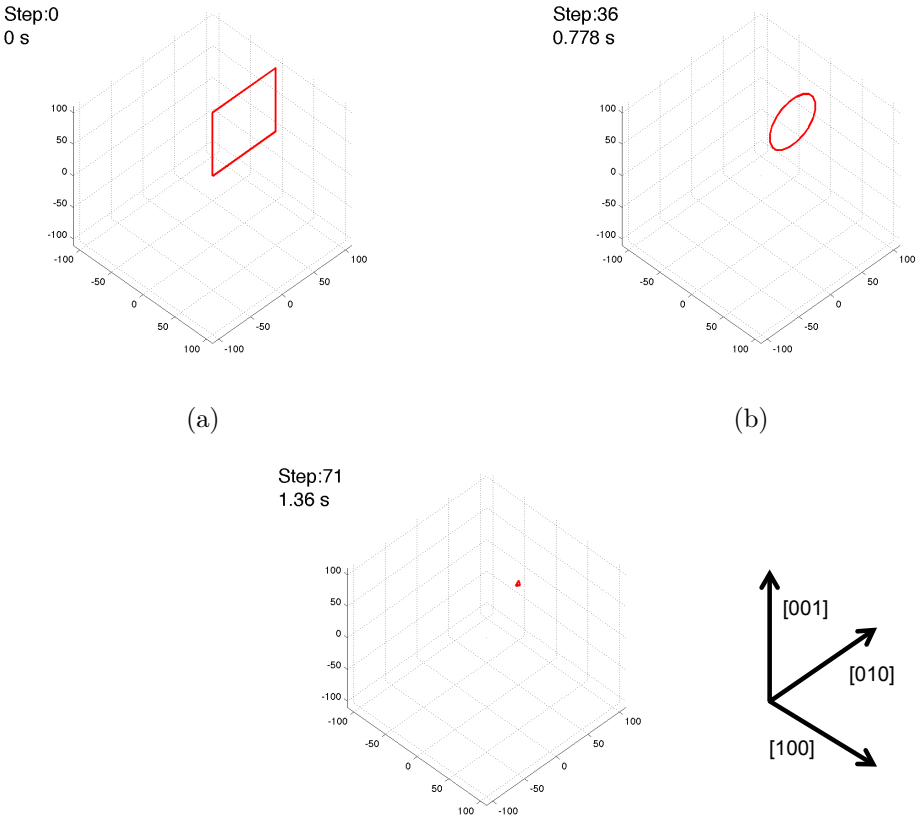


Figure 4.2: An initially square pure prismatic vacancy loop shrinking via climb under zero applied load. The loop has a width of $100a$ (28.7 nm) and its Burgers vector is $\mathbf{b} = [100]$ (the line-sense is defined to be clockwise about [100]). The temperature is set to 700 °C. The view is down the $[1\bar{1}1]$ direction.

4.3.3 Effect of introducing a compressive load

If a compressive load is applied parallel to the vacancy loop's Burgers vector, this should provide an additional force acting to shrink the loop, and hence it should take less time for the loop to shrink and disappear.

Figure 4.3 shows the loop shrink time for a number of σ_{11} compressive loads. As the size of the compressive load increases the loop shrink time decreases as expected. A load of 82 MPa causes only a small reduction in the loop shrink time, but as this load is increased up to 82 GPa the shrink time drops by over one order of magnitude. During the simulations themselves, it can be seen that for relatively large compressive loads, the loop retains its initial square shape as it shrinks, rather than first rounding before

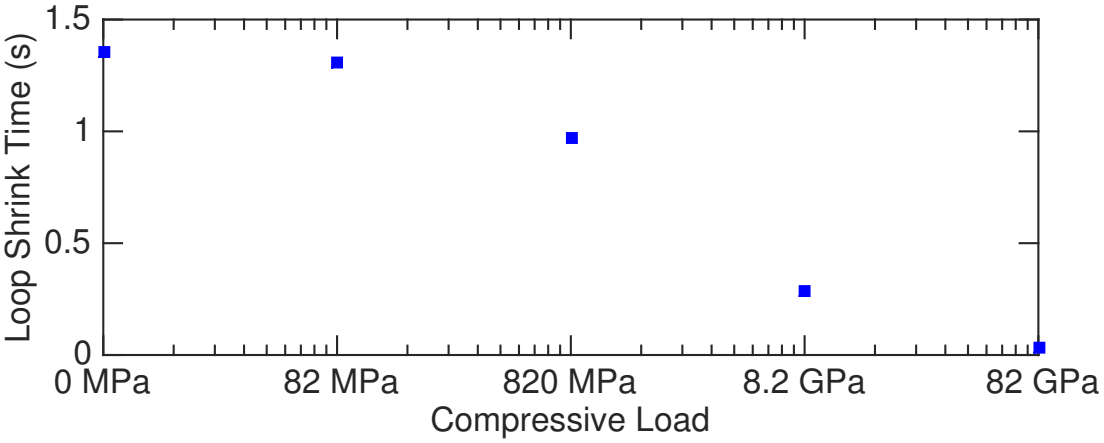


Figure 4.3: Vacancy loop shrink time as a function of applied σ_{11} compressive load.

shrinking down to nothing. This behaviour also seems reasonable as such large loads are close to the theoretical strength of the crystal lattice itself.

4.3.4 Kinetics of a circular prismatic dislocation loop

In order to assess the validity of these square loop shrink times quantitatively, a theoretical model of what the shrink time should be is needed. In what follows, a *circular* loop is considered, as this is more straightforward to model analytically.

The first step in finding an analytical expression for the time it takes a circular prismatic dislocation of initial radius R_0 to shrink down to nothing is to setup a differential equation for the radius of the loop $R(t)$ as a function of time t. The rate of change of the area A of the loop is given by

$$\frac{dA}{dt} = \frac{d}{dt}(\pi R^2) = 2\pi R \frac{dR}{dt}. \tag{4.8}$$

The rate of change of the area of the loop is also given by

$$\frac{dA}{dt} = -\frac{1}{B_{\mathrm{cl}}(T)} \frac{\mu b^2}{2(1-\nu)} \ln\left(\frac{8R}{a_{\mathrm{ns}}}\right), \tag{4.9}$$

where a_{ns} is the core spreading parameter in the non-singular theory used by `DDLab` (Cai et al., 2006, (43)).

Setting (4.8) and (4.9) equal to each other yields

$$\frac{R}{\ln(8R/a_{\mathrm{ns}})}\frac{dR}{dt} = -\frac{1}{B_{\mathrm{cl}}(T)}\frac{\mu b^2}{4\pi(1-\nu)}. \tag{4.10}$$

This can be integrated using separation of variables:

$$\int_{R_0}^{0} \frac{R}{\ln(8R/a_{\mathrm{ns}})} dR = -\frac{1}{B_{\mathrm{cl}}(T)}\frac{\mu b^2}{4\pi(1-\nu)}\int_0^t dt', \tag{4.11}$$

which gives the time t it takes a loop of initial radius R_0 to shrink down to nothing as

$$t = \frac{\pi a_{\mathrm{ns}}^2(1-\nu)B_{\mathrm{cl}}(T)}{16\mu b^2}\ \mathrm{li}\left(\frac{64R_0^2}{a_{\mathrm{ns}}^2}\right), \tag{4.12}$$

where $\mathrm{li}(x)$ is the logarithmic integral function of x.

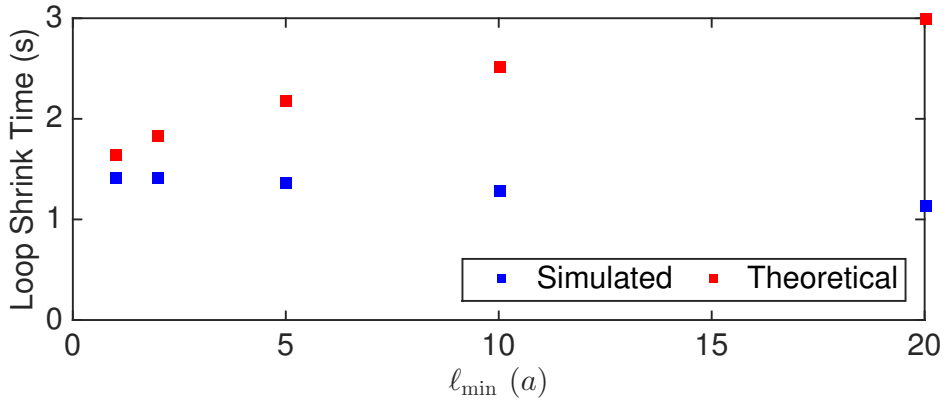
Using expression (4.12), theoretical calculations of the shrink times for circular loops of various initial radii R_0 can be compared to the shrink times for loops simulated by `DDLab`, albeit loops which are initially square.

4.3.5 Comparison between simulation and theory: effect of varying minimum segment length

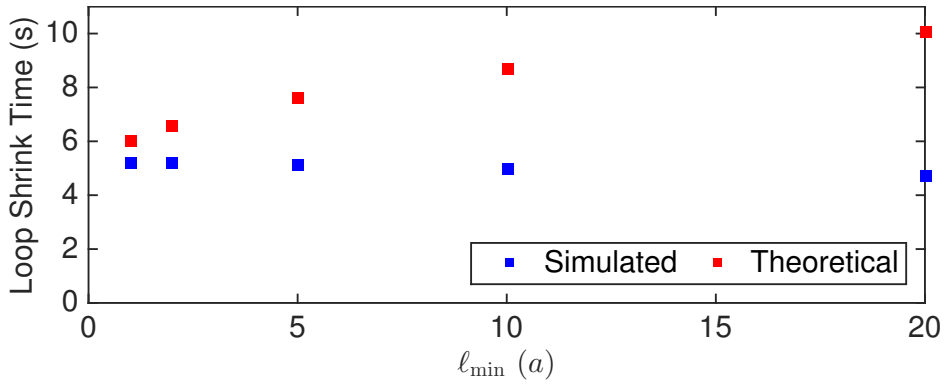
The theoretical loop shrink time (4.12) depends on the core spreading parameter a_{ns}. In the `DDLab` simulations, a_{ns} is defined as

$$a_{\mathrm{ns}} = \frac{\ell_{\mathrm{min}}}{2\sqrt{3}}, \tag{4.13}$$

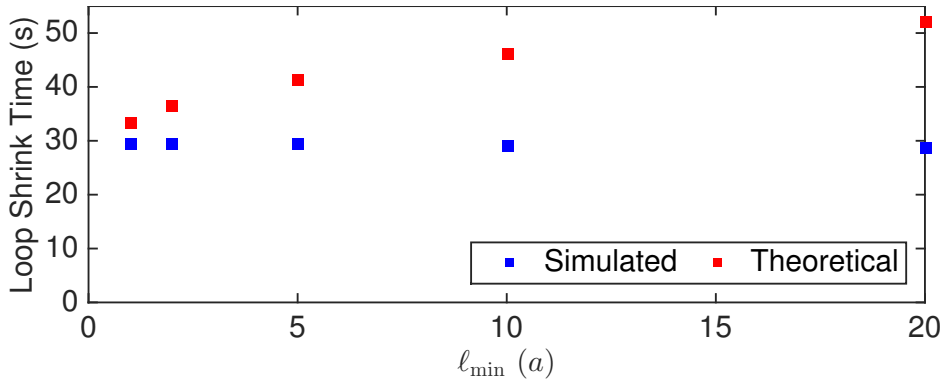
where ℓ_{min} is the minimum dislocation segment length. ℓ_{min} is a free parameter in the `DDLab` simulations, and in the preceding simulations it has always been set to be equal to $5a$. Figure 4.4 shows the effect of varying ℓ_{min}, and thus a_{ns} via (4.13), on both the simulated and theoretical loop shrink times, for three different initial square loop widths w. In order to compare the simulated square loop shrink times with the theoretical ones for circular loops, the theoretical circular loops are chosen to have the same initial area as the simulated square ones, i.e. $R_0 = w/\sqrt{\pi}$. The temperature is again set to 700 °C.



(a) Square loop width $w = 100a$ (28.7 nm).



(b) Square loop width $w = 200a$ (57.3 nm).



(c) Square loop width $w = 500a$ (143 nm).

Figure 4.4: Simulated shrinkage time for a square vacancy loop of width w, compared with the theoretical values for a circular loop of the same area, as a function of minimum segment length $\ell_{\min}$. The temperature is set to 700 °C.

As can be seen in figure 4.4, the `DDLab` simulations consistently underestimate the loop shrink times by about 10% to 50% as $\ell_{\min}$ increases from $1a$ to $20a$. Furthermore, different trends in the loop shrink times are seen between the simulated and the theoretical values as $\ell_{\min}$ increases — the simulated values remain fairly constant (decreasing very

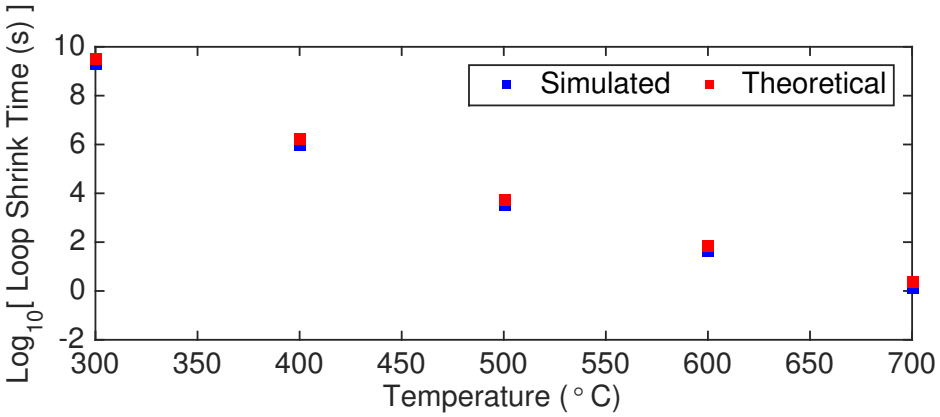
slightly), whereas the theoretical values steadily increase.

In § 4.4 it is argued that the small $\ell_{\min}$ regime is preferable for more accurate dislocation behaviour. Encouragingly, the small $\ell_{\min}$ regime is when the discrepancy between the simulated and the theoretical values in figure 4.4 is smallest.

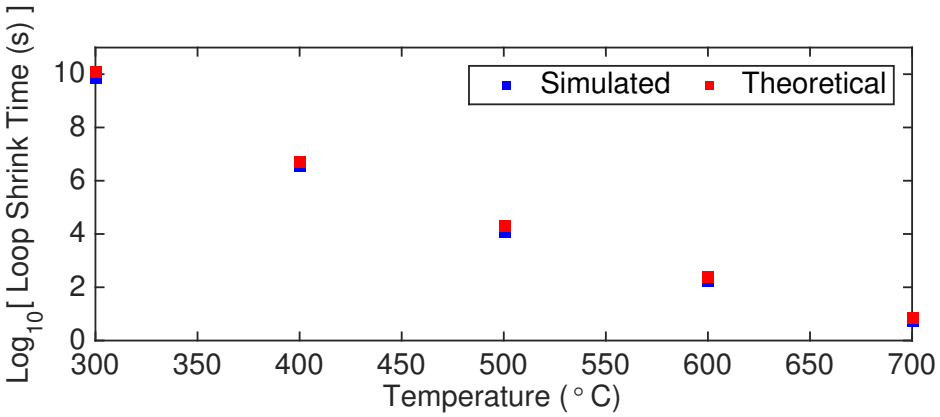
The simulations and the theoretical values are reasonably similar, particularly for the smaller values of $\ell_{\min}$. The loop shrink times only differ by a factor of 0.1–0.5. Furthermore, it is expected that the simulations will underestimate the loop shrink times to some extent, because of the additional inward force provided by the corners of the simulated square loops, which leads to the faster initial shrinkage of the square loops as they round. This effect is exacerbated as $\ell_{\min}$ increases, because the coarser discretisation of the loops makes them more angular, and hence prone to shrinking, explaining the increase in the discrepancy between the simulated and the theoretical loop shrink times for larger values of $\ell_{\min}$.

4.3.6 Comparison between simulation and theory: effect of varying temperature

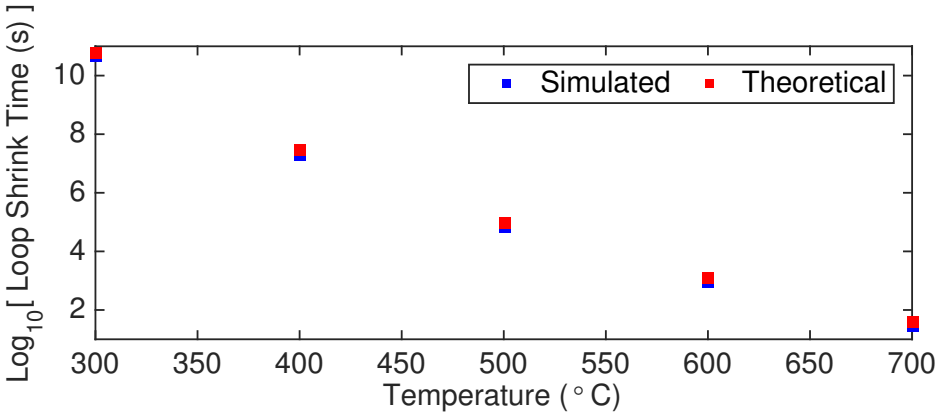
Figure 4.5 shows the effect of varying the temperature on both the simulated and theoretical loop shrink times, as this affects the value of $B_{\mathrm{cl}}^{\mathrm{v}}(T)$. $\ell_{\min}$ is again set to be equal to $5a$. The loop shrink times are shown on a logarithmic scale because the climb rate is strongly temperature-dependent. As the temperature is increased from 300 °C to 700 °C, the loop shrink times drop by about 10 orders of magnitude. Apart from the systematic underestimation of the loop shrink times by the simulations compared with the theoretical values already discussed, a good correspondence between the two can be seen. Thus the erroneous factor of 0.1–0.5 can be thought of as only a small "error" in the simulated temperature.



(a) Square loop width $w = 100a$ (28.7 nm).



(b) Square loop width $w = 200a$ (57.3 nm).

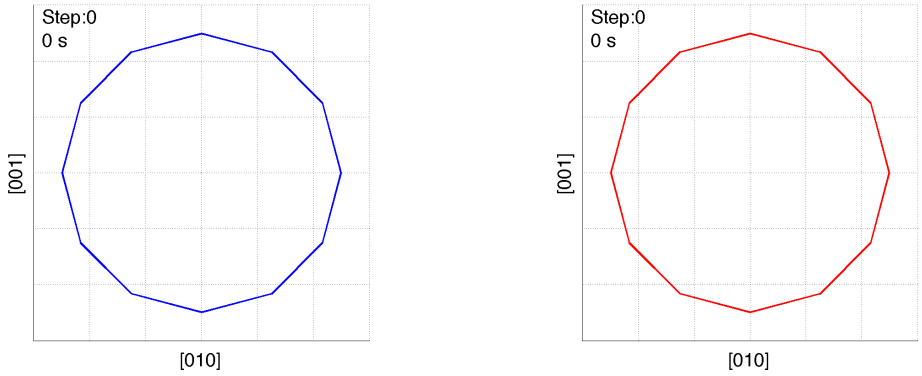


(c) Square loop width $w = 500a$ (143 nm).

Figure 4.5: Simulated shrinkage time for a square vacancy loop of width w, compared with the theoretical values for a circular loop of the same area, as a function of temperature.

4.3.7 Circular prismatic loop

In order to make a better comparison between simulation and theory, a circular test loop is now considered.



(a) (b)

Figure 4.6: The initial dislocation configuration of a "circular" prismatic loop of radius $50a$ (14.3 nm) — it is actually a twelve-sided polygon. (a) The Burgers vector is in the [100] direction — pointing out of the page. The line-sense is defined to be anti-clockwise, making this an interstitial loop. (b) The Burgers vector is in the $[\bar{1}00]$ direction — pointing into the page. The line-sense is defined to be anti-clockwise, making this a vacancy loop.

Figure 4.6 shows the initial dislocation configuration of a "circular" loop of radius $50a$ (14.3 nm). Because of the discretisation of the dislocation network, the geometry is actually that of a twelve-sided polygon. In figure (a) the Burgers vector is in the [100] direction — pointing out of the page. The line-sense is defined to be anti-clockwise about [100], making this an interstitial loop. In figure (b) the Burgers vector is in the $[\bar{1}00]$ direction — pointing into the page. The line-sense is again defined to be anti-clockwise about [100], making this a vacancy loop.

Figure 4.7 shows the interstitial loop in figure 4.6(a) shrinking via climb under zero applied load at 700 °C. The view is down the $[1\bar{1}1]$ direction. Figure (a) shows the initial configuration at simulated time $t = 0$. Figure (b) shows an intermediate snapshot after 0.74 s of simulated time (after 23 time increments). The loop has shrunk, keeping its circular shape, as expected. Finally, figure (c) shows the loop at the moment it ceases to exist — after 1.06 s of simulated time.

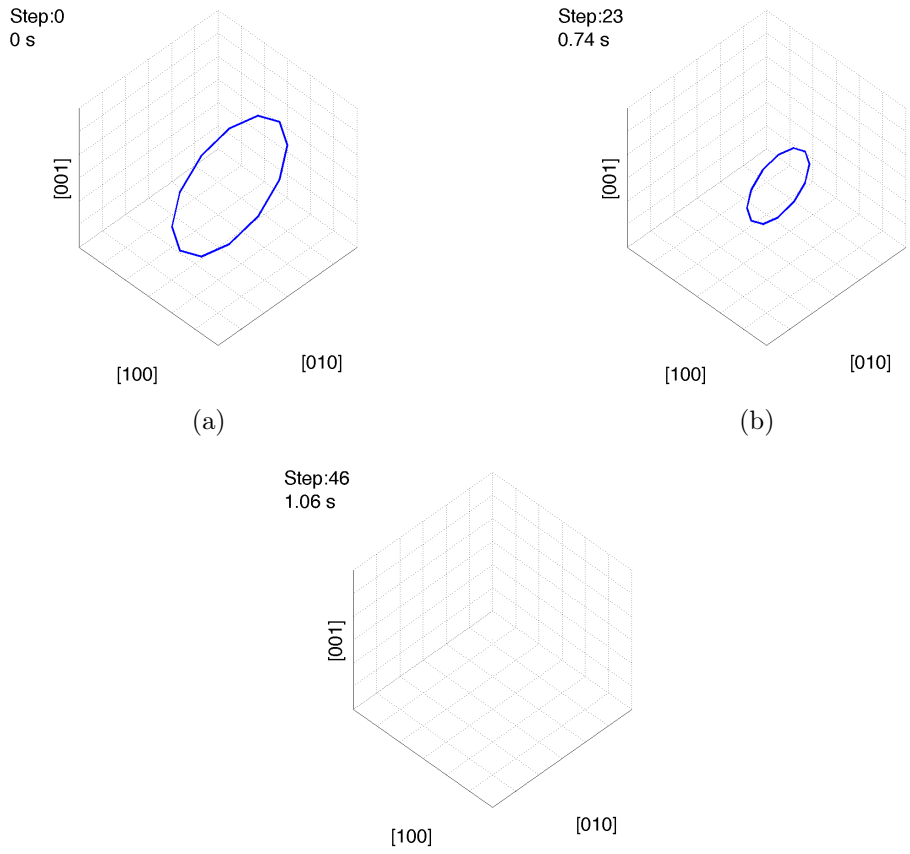
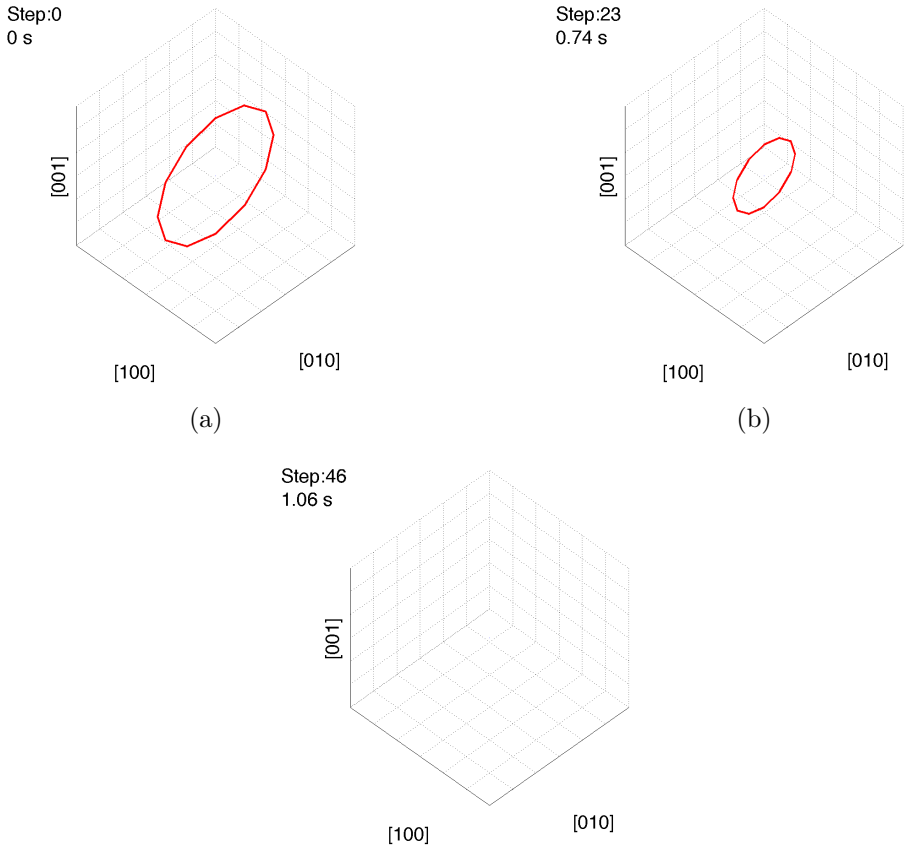


Figure 4.7: An initially circular pure prismatic interstitial loop shrinking via climb under zero applied load. The Burgers vector of the loop $\mathbf{b} = [100]$. The view is down the $[1\bar{1}1]$ direction. The temperature is set to 700 °C.

Figure 4.8 shows the vacancy loop in figure 4.6(b) shrinking via climb under zero applied load at 700 °C. The vacancy loop shrinks in exactly the same way as the interstitial loop in figure 4.7, as expected.

The simulated circular loop shrink time is 1.06 s, whereas the theoretical one calculated using (4.12) is 1.75 s. Again, $\ell_{\text{min}} = 5a$ is used for this comparison. The simulation underestimates the loop shrink time by 39%. This is very similar to the factors of underestimation seen in figure 4.4 for an initially square loop for $\ell_{\text{min}} = 5a$. The difference between simulating an initially circular loop and an initially square one — and then comparing this to the theoretical shrink time for a circular loop — is negligible, at least when using $\ell_{\text{min}} = 5a$. In § 4.3.5 it was argued that this underestimation could be explained by the relatively coarse discretisation of the loop when $\ell_{\text{min}} = 5a$, particularly



(a) (b) (c)

Figure 4.8: An initially circular pure prismatic vacancy loop shrinking via climb under zero applied load. The Burgers vector of the loop $\mathbf{b} = [\bar{1}00]$. The view is down the $[1\bar{1}1]$ direction. The temperature is set to 700 °C.

as the underestimation was seen to decrease for smaller values of $\ell_{\min}$.

4.3.8 Implementing an osmotic force due to supersaturated vacancies

Using the model described in chapter 3, point defect supersaturations can be included in the implementation of climb. These supersaturations lead to osmotic forces on the dislocations F^j_{os} of the form of (3.21).

An osmotic force due to a supersaturation of vacancies only was implemented by first writing a new function `calcOsmoticForceVac`, which computes F^{v}_{os} for a given vacancy defect supersaturation c^{v}_{∞} (defined in the `input_dd3d` script). Again, this calculation does not include the factor of b in (3.21), as this must be replaced with $b \sin\theta$, which is specific to each dislocation segment. Secondly, this osmotic force function needed

to be incorportated into the `segforcevec` function, which computes the different contributions to the segment forces and combines them appropriately. A new subroutine was added to `segforcevec`, which includes the missing $b \sin\theta$ factor for each segment. The relevant lines of code in `segforcevec`, and `calcOsmoticForceVac`, are included in appendix B.

In what follows, the implementation of the osmotic force due to supersaturated vacancies in `DDLab` is tested.

4.3.9 Effect of an osmotic force due to supersaturated vacancies

Different defect supersaturations need to be chosen in order to vary the osmotic force. For a given defect supersaturation c_∞, the resulting osmotic force will differ by orders of magnitude at different temperatures due to the strong temperature dependence of the equilibrium defect concentration $c_0(T)$. To begin with, in order to make the comparison between osmotic forces at different temperatures easier, the temperature *independent* defect supersaturation *ratio* c_∞/c_0 is varied, rather than the absolute defect supersaturation. The defect supersaturation ratio is a helpful measure of the defect supersatuation relative to the thermal background defect concentration at a given temperature. By choosing to vary the defect supersaturation ratio, the osmotic forces at different temperatures will vary in a simple linear way with temperature for a given defect supersaturation ratio according to (3.21).

Figure 4.9 shows the effect that varying the vacancy supersaturation ratio has on the loop shrink time of square vacancy and interstitial loops of width $100a$ (28.7 nm) at 600 °C and 700 °C. When the vacancy supersaturation ratio is equal to 1, and hence the osmotic force is zero, the loop shrinks in 42.7 s at 600 °C and 1.36 s at 700 °C due to its own line tension regardless of whether it is a vacancy or interstitial type loop. This is the same behaviour as seen previously, and the difference in shrink times at the different temperatures is because of the temperature dependence of the climb mobility (3.22).

The presence of a vacancy supersaturation ratio >1 produces a non-zero osmotic force on the vacancy loops in the opposite direction to the line tension, and should inhibit their

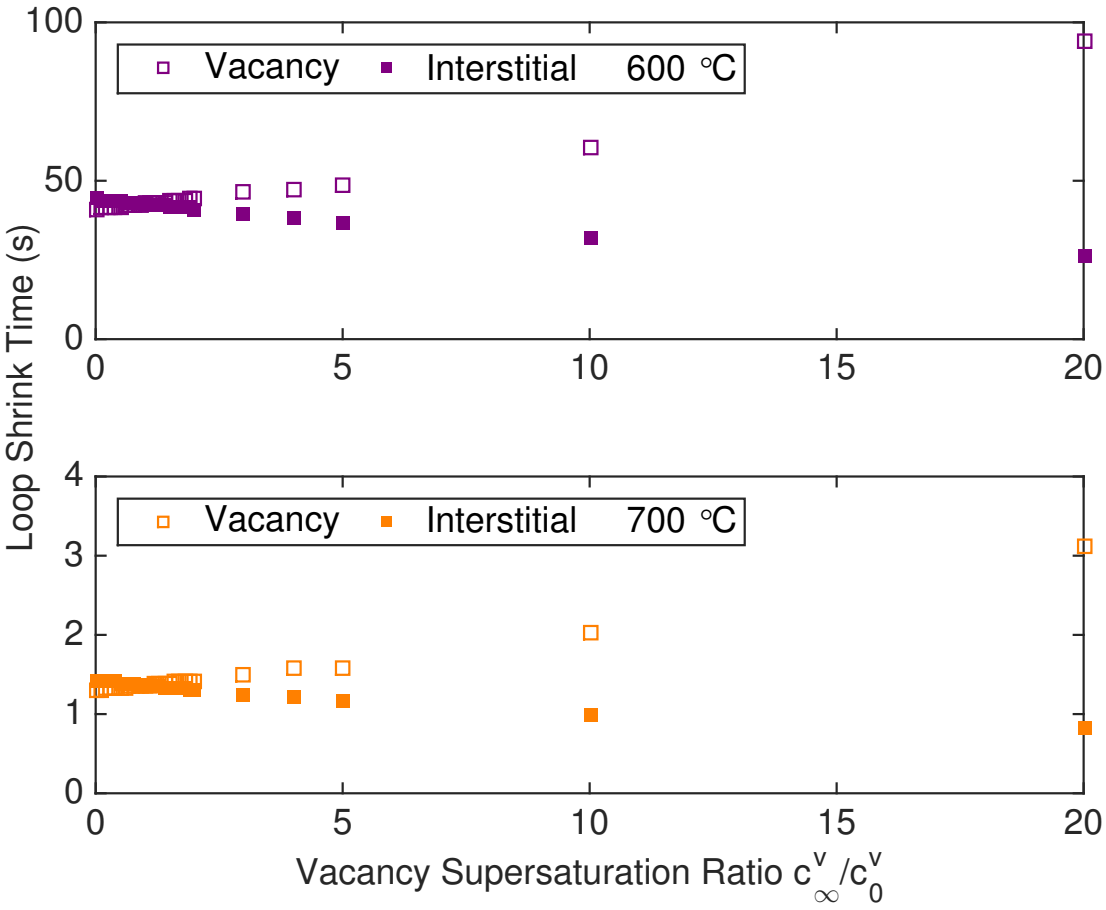


Figure 4.9: The simulated time taken for square vacancy and interstitial loops of width $100a$ (28.7 nm) to shrink and disappear, as a function of the vacancy supersaturation ratio, at 600 °C and 700 °C.

shrinkage, leading to progressively larger shrink times as the supersaturation ratio is increased. This is because it is energetically unfavourable for the loop to shrink and add more vacancies to the already overpopulated bulk. This behaviour is indeed captured by the simulations and shown in figure 4.9. Increasing the vacancy supersaturation eventually leads to the loop growing instead of shrinking (this is not shown in the figure), and this is also expected. In this case there are so many vacancies in the bulk that it is energetically favourable for some of these to condense onto the loop and for the loop to grow. Similarly, a vacancy subsaturation (a supersaturation ratio <1) is seen to lead to a faster shrink time, as it is energetically favourable for the vacancies to evaporate from the loop and add to the underpopulated bulk. However, as discussed in chapter 3, such a vacancy subsaturation is unphysical.

With the interstitial loops, the opposite behaviour to the vacancy loops is seen, as ex-

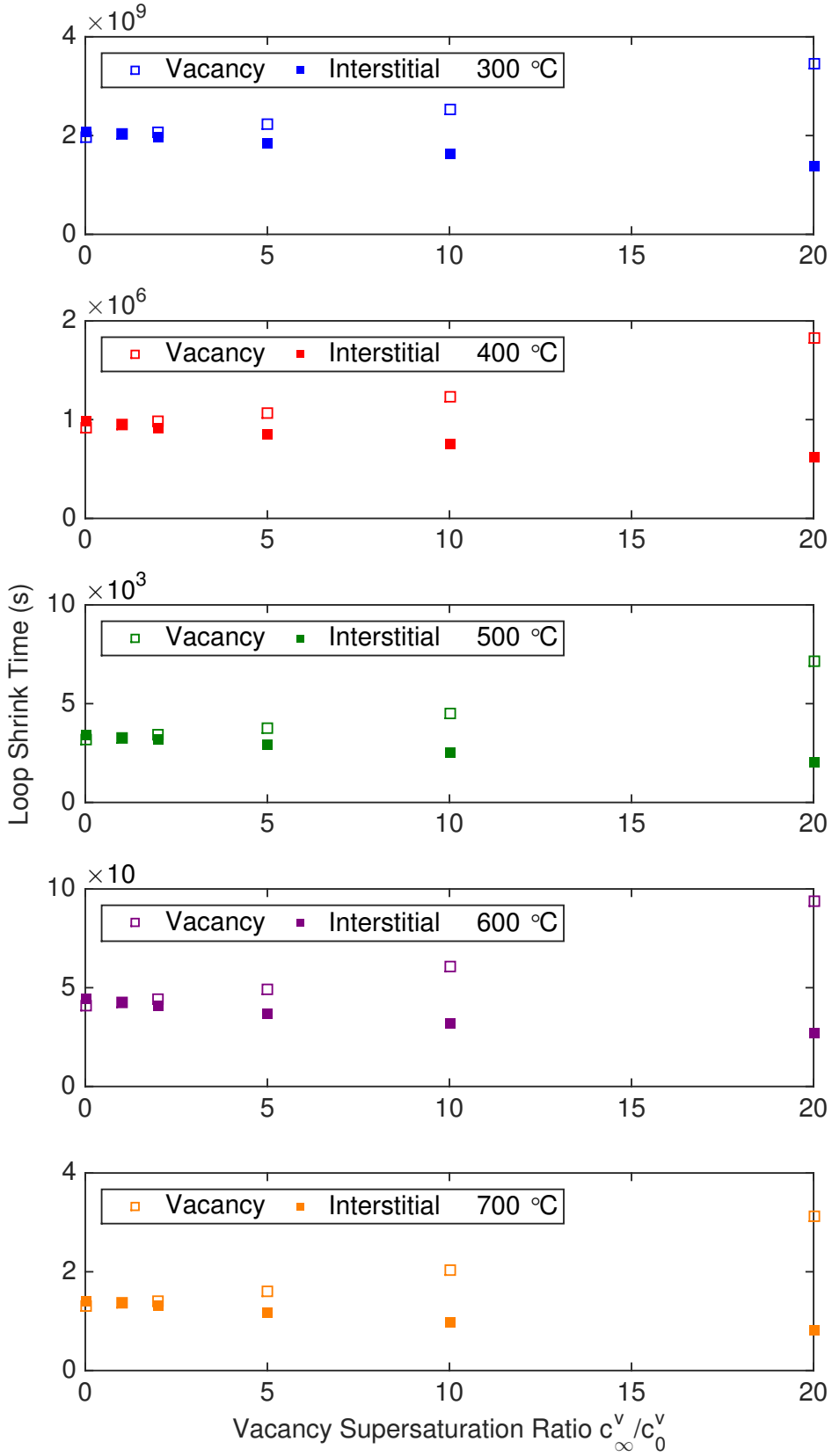


Figure 4.10: The simulated time taken for square vacancy and interstitial loops of width $100a$ (28.7 nm) to shrink and disappear, as a function of the vacancy supersaturation ratio, at a range of temperatures between 300 °C and 700 °C.

pected. A vacancy supersaturation leads to smaller loop shrink times, as it is favourable for interstitial point defects to leave the loop and reduce the vacancy supersaturation in the bulk by annihilating with the vacancies. A vacancy undersaturation leads to larger loop shrink times as such vacancy-interstitial annihilations would exacerbate the subsaturation of vacancies in the bulk.

Figure 4.10 compares the data in figure 4.9 with further data at three additional, lower temperatures. From 300 °C to 700 °C a difference in loop shrink times of about ten orders of magnitude is seen once more, i.e. at 300 °C it takes tens of years for a loop to shrink, whereas at 700 °C it takes merely seconds. In the presence of the non-zero osmotic forces shown, the loop shrink times at each temperature differ by factors of the order of unity in the same manner as in figure 4.9.

4.3.10 Threshold vacancy supersaturation for vacancy loop growth

A vacancy loop will grow rather than shrink if the vacancy supersaturation is large enough. The minimum value of the vacancy superaturation at which loop growth occurs will depend on both the initial size of the loop, and the temperature. This is due to the competition between the two forces on the loop governing the resulting behaviour: the line tension force acting to shrink it, which depends on the loop's size; and the osmotic force acting to grow it, which depends on the vacancy supersaturation and the temperature.

This threshold vacancy supersaturation for vacancy loop growth is shown in figure 4.11 for a number of square loops of different initial widths at three different temperatures. Note that again it is the vacancy supersaturation *ratio* $c^{\mathrm{v}}_{\infty}/c^{\mathrm{v}}_{0}$ that is plotted. At each of the temperatures the threshold vacancy supersaturation ratio increases with loop size, i.e. the larger the loop, the larger the supersaturation needed to halt loop shrinkage. For progressively larger loops the size of this incremental increase in the threshold supersaturation ratio decreases. Additionally, the threshold vacancy supersaturation ratios are consistently higher the lower the temperature. This is due to the simple proportionality between osmotic force and temperature (provided the osmotic force is

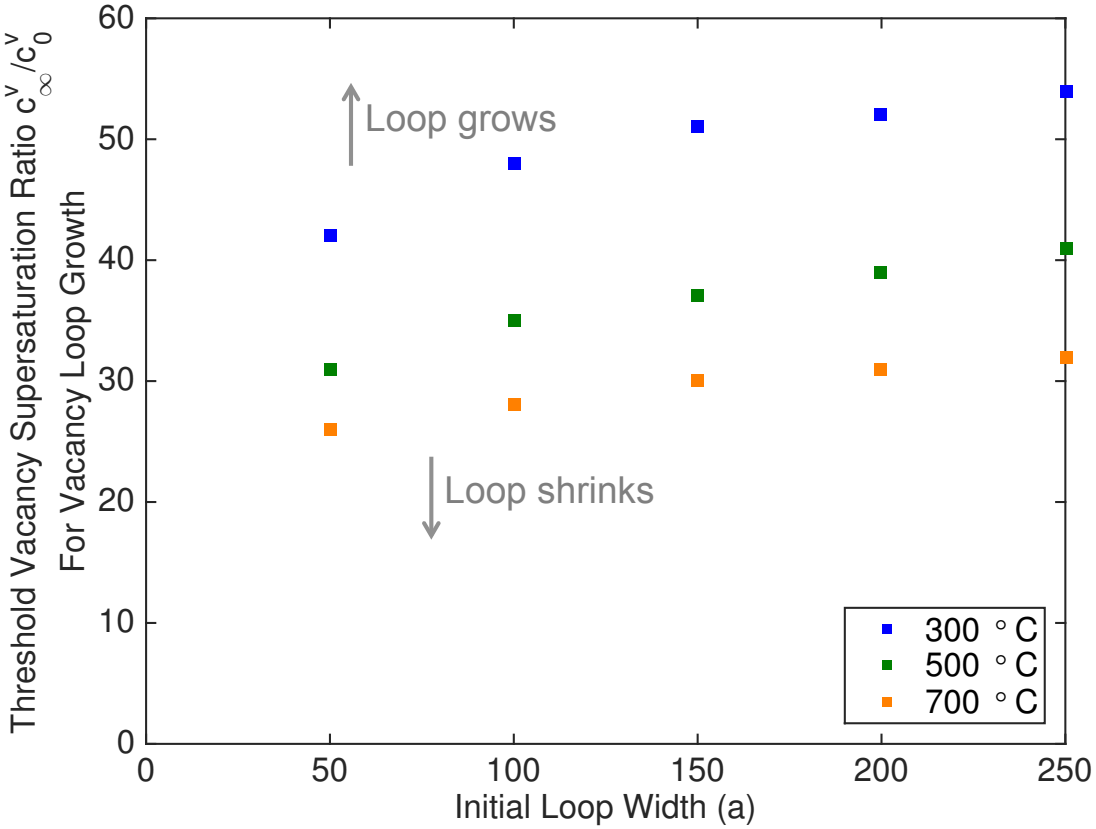


Figure 4.11: Threshold vacancy supersaturation for square vacancy loop growth as a function of initial loop width at 300 °C, 500 °C and 700 °C.

evaulated as a function of the temperature independent supersaturation ratio, as is the case here).

The force acting to shrink the loops should ultimately decrease to zero as they get larger, because the dislocation segments on opposite sides of the loop which attract each other get further apart. Indeed, (3.34) gives the force acting to shrink a *circular* loop of radius R as proportional to $\ln(R)/R$, which does tend to zero as R tends to infinity. Hence the osmotic force required to drive the loop to grow should decrease at the larger loop widths, and with it the threshold supersaturation ratio should tend to one.

This expected behaviour is consistent with the simulation results shown in figure 4.11, even though a decrease in the threshold vacancy supersaturation ratio at larger loop widths is not seen. The loop widths shown still approximate to a $\ln(w)/w$ regime (where w is the width of the initially square loops), provided w is relatively small. Hence the

trend shown is increasing and flattening, rather than decreasing at the larger loop widths. Further simulations at larger loop widths are exepcted to yield this decreasing trend in the threshold supersaturation ratios.

For the simulations shown in figure 4.11, the minimum dislocation segment length ℓ_{min} was chosen to be equal to $w/20$ for each of the loops of initial width w. Similarly, the maximum dislocation segment length ℓ_{max}, another of `DDLab`'s free parameters, was chosen to be equal to $w/2$ for each loop. This scaling of ℓ_{min} and ℓ_{max} was used to ensure each loop was discretised to the same level of fineness. The effect of using fixed, unscaled values of ℓ_{min} and ℓ_{max} is compared to scaled data at 600 °C in figure 4.12.

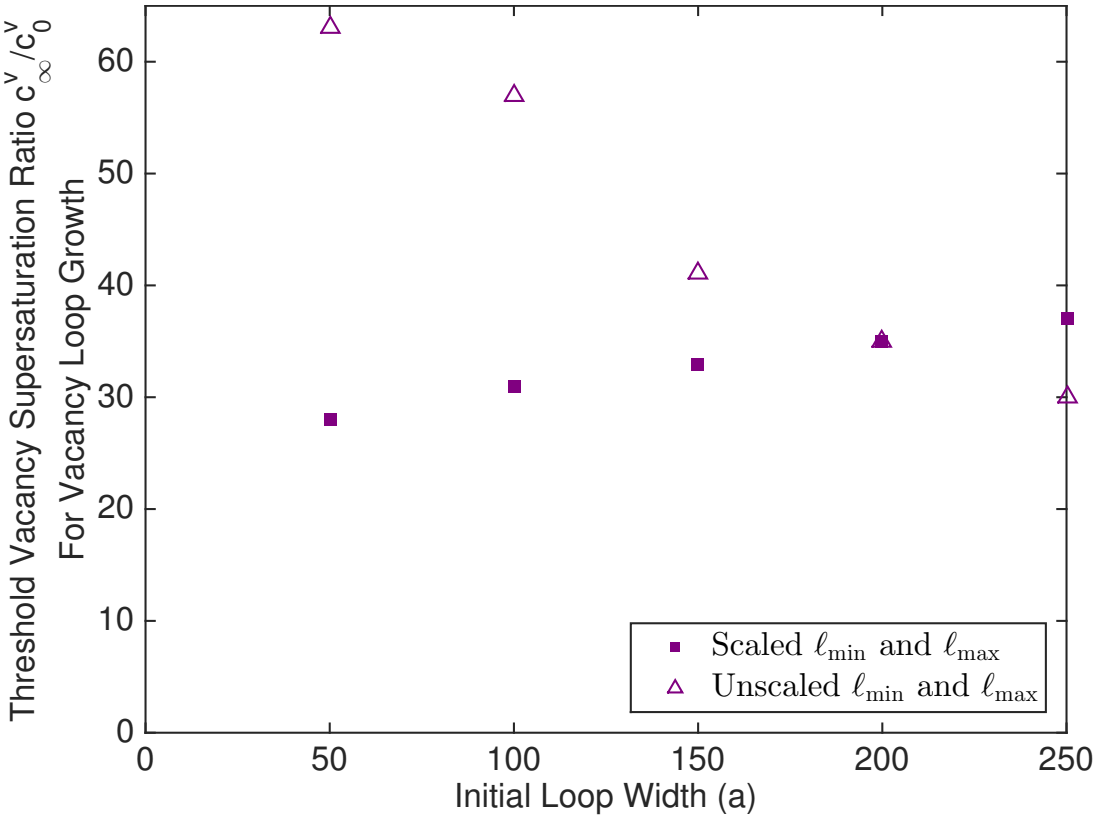


Figure 4.12: Threshold vacancy supersaturation for square vacancy loop growth as a function of initial loop width at 600 °C. Results using scaled and unscaled values for ℓ_{min} and ℓ_{max} are shown.

Fixing the value of ℓ_{min} to $10a$ and ℓ_{max} to $100a$ has a strong effect compared to the results when using scaled values of these two parameters. Both sets of data coincide for the $200a$ loop, as this is when the $\ell_{\text{min}} = w/20$ and $\ell_{\text{max}} = w/2$ scaling used matches up with the fixed, unscaled values.

The unscaled loops with widths less than $200a$ are less well discretised than the scaled ones, i.e. they are more angular. The presence of these sharper corners artificially introduces stronger inward forces and hence the loop is more prone to shrinking. This leads to a much larger threshold supersaturation ratio for loop growth. The effect of the coarse discretisation of the loop is overpowering the $\sim\ln(w)/w$ trend seen in figure 4.11.

Conversely, the unscaled $250a$ loop actually has a finer discretisation than the scaled one. It is clear that this finer discretisation produces a more physical result, because such a discretisation is a closer approximation to the curved dislocation loop. Loops with a coarse discretisation will be artificially angular, and shrink faster due to their sharp corners. Hence we can infer that the curves in figure 4.11 should all lie somewhat lower on the vertical scale, and a finer discretisation than the one used here — at least for the larger loops — is required. However, making the dislocation segments smaller will increase the number of segments that need to be simulated, and thus the computation time of the simulations, so some convergence optimisation is needed. This is done in § 4.4, but first the implementation of interstitial mediated climb — together with the osmotic force due to supersaturated interstitials — is described, and tested by investigating the behaviour of a single prismatic loop in the presence of supersaturations of both vacancies and interstitials.

4.3.11 Implementing interstitial mediated climb

Implementing interstitial mediated climb in addition to the vacancy mediated climb already incorporated into `DDLab` proved significantly more involved. Writing the new functions `calcClimbDragInt` and `calcOsmoticForceInt` was straightforward, but the requirement that the two different drag factors $B^{\mathrm{v}}_{\mathrm{cl}}(T)$ and $B^{\mathrm{i}}_{\mathrm{cl}}(T)$ act on two different combinations of forces, namely $(F_{\mathrm{cl}} + F^{\mathrm{v}}_{\mathrm{os}})$ and $(F_{\mathrm{cl}} + F^{\mathrm{i}}_{\mathrm{os}})$ respectively, was problematic[33]. This was because the `segforcevec` function evaluates the total force on each of the dislocation segments, and the drag matrix in `mobbcc0` then acts on these total forces. Instead, partial forces and partial drag matrices are needed during the mobility function call, in order to compute the nodal climb velocities due to vacancy mediated

[33] This is illustrated for the mobility coefficients (rather than for the drag coefficients) in (3.20).

and interstitial mediated climb correctly.

The first part of the solution to this problem was to create a new `segforcevecInt` function, which computes the partial segment forces ($F_{\text{cl}} + F_{\text{os}}^{\text{i}}$), to complement the `segforcevec` function, which had already been developed to compute ($F_{\text{cl}} + F_{\text{os}}^{\text{v}}$). The `drndt` function, which evaluates the nodal velocities by calling `mobbcc0` with the computed segment forces as an argument, was developed to compute these two different sets of segment forces, and then call `mobbcc0` twice — once with each set of segment forces as an argument. The two resulting sets of nodal velocities are then added together, thus correctly capturing the total nodal climb velocities due to thermal vacancies and interstitials, and supersaturations of these defects.

However, the double-counting of the glide and line velocities in the total nodal velocities described was not accounted for in `drndt`. To remedy this, a new mobility function `mobbcc0Int` was created, which only returns the nodal velocity contributions due to interstitial climb. `drndt` was altered again, so that is calls `mobbcc0` with the `segforcevec` segment forces as an argument, followed by `mobbcc0Int` with the `segforcevecInt` segment forces as an argument, before computing the total nodal velocities, thus eliminating the double-counting issue.

In this way the full point defect bulk diffusion model for both vacancies and interstitials was successfully implemented in `DDLab`.

4.3.12 Supersaturations of both vacancies and interstitials

The implementation described in the previous section was tested using similar isolated prismatic loop simulations to those done previously. The circular loops simulated have radii of $18a$ (5.2 nm). The minimum dislocation segment length ℓ_{min} is set to $4a$, as this is argued to be the optimum value in § 4.4, and the maximum segment length ℓ_{max} is set to $8a$. For this value of ℓ_{min}, the core spreading parameter a_{ns} becomes $1.15a$, and so to reflect this, the dislocation core radius r_{c} used in the climb calculations is set to $2a$. The outer cut-off radius r_{∞} is changed to $4000a$, so that r_{∞}/r_{c}, which appears in the logarithm in the climb drag factors, remains 2000 as before. However, as argued in

§ 3.3.2, the value of r_∞/r_c chosen has a relatively small effect on the climb drag factors because it appears in the logarithm. The interstitial formation and migration energies, E_f^i and E_m^i, are set to 4 eV and 0.3 eV for bcc iron (see § 3.3). The temperature is set to 700 °C.

Vacancy loop shrink time (s)			
Supersaturation c_∞	Vacancies only	Interstitials only	Both vacancies and interstitials
None ($c_\infty = c_0$)	0.236	0.236	0.236
10^{-12}	0.236	0.225	0.225
10^{-11}	0.236	0.162	0.162
10^{-10}	0.255	0.0454	0.0500
10^{-9}	Expands	9.72×10^{-3}	9.86×10^{-3}
10^{-8}	Expands	5.19×10^{-3}	5.21×10^{-3}
10^{-7}	Expands	4.72×10^{-3}	4.72×10^{-3}
10^{-6}	Expands	5.81×10^{-6}	5.98×10^{-6}

Table 4.2: Circular vacancy loop shrink times for a range of supersaturations of vacancies only, interstitials only, and of both defects. The loop has a radius of $18a$ (5.2 nm), and the temperature is 700 °C.

In these simulations the absolute vacancy supersaturation c_∞ is varied (rather than the supersaturation ratio). The vacancy loop shrink times for a range of supersaturations of vacancies only, interstitials only, and of both defects are shown in table 4.2. In the absence of any supersaturation the loop shrinks in 0.236 s. A vacancy supersaturation of 10^{-12} or 10^{-11} atomic fraction of vacancies has a negligible effect on this shrink time, but for a supersaturation of 10^{-10} vacancies it increases to 0.255 s, and for supersaturations of 10^{-9} vacancies and above the loop expands instead of shrinking. This is the same qualitative behaviour as seen in § 4.3.9 for the square vacancy test loop.

On the other hand, an interstitial supersaturation of as little as 10^{-12} interstitials is able to reduce the loop shrink time appreciably. As the interstitial supersaturation is increased to 10^{-6} interstitials, the loop shrink time continues to decrease, and by 10^{-6} interstitials it is four orders of magnitude smaller than the supersaturation-free case. This behaviour is expected: the supersaturated interstitials drive the loop to shrink faster by being absorbed at the dislocation line, and larger supersaturations result in a

faster overall climb rate. Such a large increase in the rate of climb over this range of supersaturations of several orders of magnitude is expected from the linear dependence of the osmotic force (3.21) on the defect supersaturation at a given temperature.

Finally, when equal supersaturations of both types of defect are simulated, the loop shrink times are all remarkably similar to those for an interstitial supersaturation only. The interstitial supersaturation completely dominates over that of the vacancies, as is expected from the climb velocity calculations in § 3.3.4. This is because the osmotic climb velocities are proportional to the defect supersaturation ratios. For equal vacancy and interstitial supersaturations at a given temperature, the interstitial supersaturation ratio is significantly larger than that of vacancies.

Interstitial loop shrink time (s)			
Supersaturation c_∞	Vacancies only	Interstitials only	Both vacancies and interstitials
None ($c_\infty = c_0$)	0.236	0.236	0.236
10^{-12}	0.236	0.248	0.248
10^{-11}	0.236	0.512	0.512
10^{-10}	0.219	Expands	Expands
10^{-9}	0.107	Expands	Expands
10^{-8}	0.0206	Expands	Expands
10^{-7}	6.55×10^{-3}	Expands	Expands
10^{-6}	4.85×10^{-3}	Expands	Expands

Table 4.3: Circular interstitial loop shrink times for a range of supersaturations of vacancies only, interstitials only, and of both defects. The loop has a radius of $18a$ (5.2 nm), and the temperature is 700 °C.

Table 4.3 shows similar results for an interstitial loop. In the absence of any supersaturation the loop shrinks in 0.236 s, exactly the same as in the vacancy loop case. This is expected, as the shrinkage of the loops is enabled via thermal vacancy mediated climb, which in the vacancy loop case amounts to (thermal) vacancy emission at the dislocation line, and (thermal) vacancy absorption in the interstitial loop case.

In the presence of a vacancy supersaturation only, the interstitial loop shrink time decreases with increasing supersaturation, but again the change in the shrink time is only non-negligible for supersaturations of 10^{-10} vacancies and larger. At a supersatura-

tion of 10^{-6} vacancies, the shrink time of this interstitial loop (which is identical in every other way to the previous vacancy loop) has decreased by less than two orders of magnitude compared to the supersaturation-free case. Hence the effect of a vacancy supersaturation of 10^{-6} vacancies is significantly smaller than that of an equal interstitial supersaturation under equivalent circumstances.

For an interstitial supersaturation only, the interstitial loop shrink time increases with increasing supersaturation, and again the effect is more pronounced than in the equivalent vacancy loop and supersaturation case. A supersaturation of 10^{-12} interstitials is enough to increase the shrink time appreciably, and 10^{-10} interstitials is enough to cause the loop to grow (compared to 10^{-10} and 10^{-9} vacancies respectively in the corresponding vacancy case).

Lastly, supersaturations of both types of defect have an indistinguishable effect from that of an interstitial supersaturation only, again as expected.

4.4 Calibrating **DDLab**: effect of varying $\ell_{\min}$ and $\ell_{\max}$

In what follows, three successive attempts are made to investigate the effect of varying the minimum dislocation segment length $\ell_{\min}$, and the maximum segment length $\ell_{\max}$, both of which are free parameters of the simulations.

4.4.1 Attempt 1: scaled $\ell_{\min}$ and $\ell_{\max}$ with an osmotic force present

Figure 4.13 shows the vacancy loop shrink times of two square loops of initial widths w of $100a$ (28.7 nm) and $200a$ (57.3 nm), for various values of both $\ell_{\min}$ and $\ell_{\max}$. Three values of $\ell_{\max}$ are shown for each loop: $w/10$, $w/5$ and $w/2$. In these simulations the vacancy supersaturation ratio $c_\infty^{\mathrm{v}}/c_0^{\mathrm{v}} = 10$. Hence there is an osmotic force present, acting outwardly (in the direction of loop growth). There is no interstitial supersaturation.

The plots for the two loop widths are strikingly similar. When $\ell_{\max} = w/2$ (i.e. $\ell_{\max} = 50a$ in figure (a), and $100a$ in figure (b)), the choice of $\ell_{\min}$ has a relatively small effect on the shrinkage time, although there is a clear trend: smaller minimum segment lengths

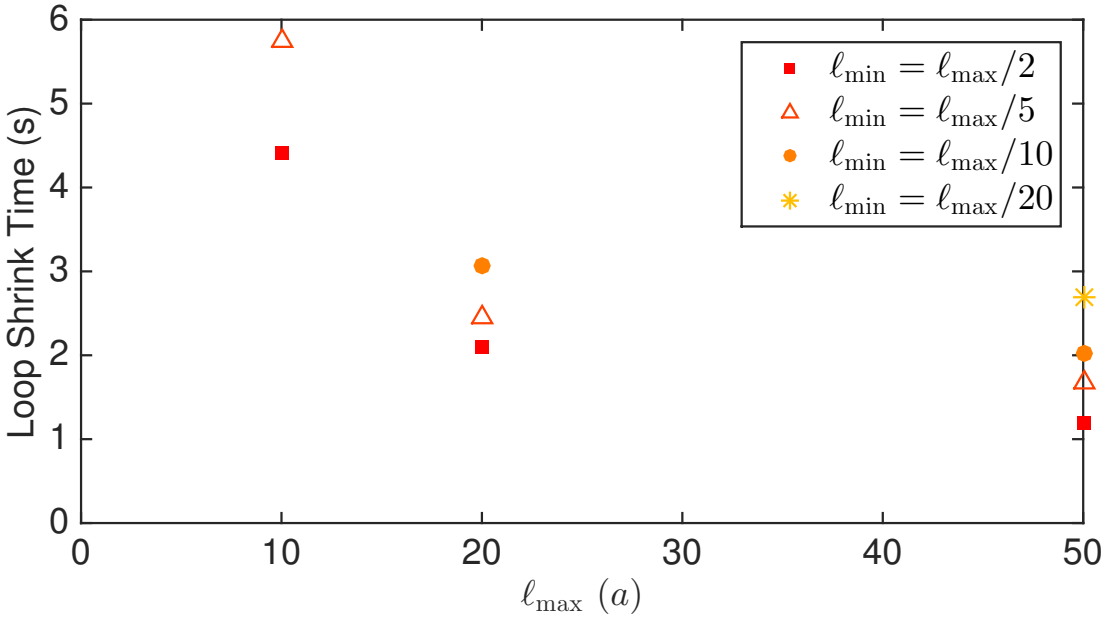
lead to larger shrink times. This is due to the finer discretisation of the circular loop allowed by the presence of smaller segments. There are more segments, all of which are shorter, and hence they have shallower angles between them. This leads to a smaller inward force on the nodes at either end of each segment, i.e. the line tension is effectively reduced by the smoother discretisation regime.

This trend of increasing shrink time with decreasing ℓ_{min} for fixed ℓ_{max} is repeated across both plots for the different values of ℓ_{max} considered. The decrease in the loop shrink times seen as ℓ_{max} is increased is also explained by the overall presence of larger segments and more angular corners which increases the line tension (contributing to the loop shrinking in the first place). This leads to an interesting conclusion: as you increase the number of dislocation segments discretising your circular loop by making them smaller, you reduce the line tension until this force eventually disappears completely in the limit of an infinite number of straight segments making up the circular loop. This is an incorrect result, as an infinitely smooth curve still has curvature, and therefore line tension causing it to shrink. Clearly this curvature disappears as the straight segments making up the loop get smaller and smaller. However, in this limit the segment-segment forces still drive the loop to shrink, albeit at a slower rate.

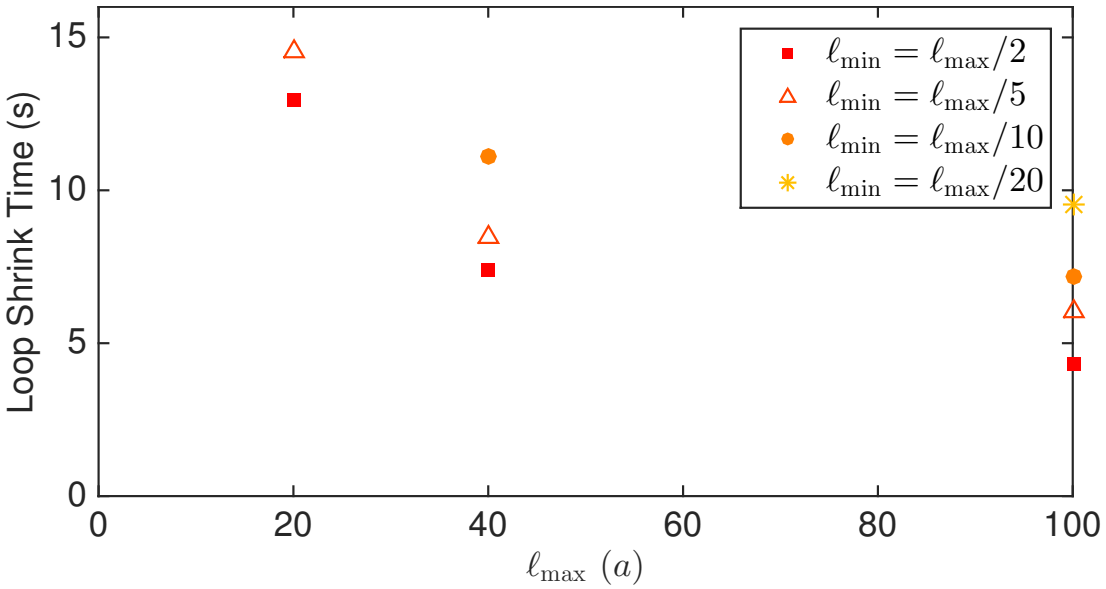
The data shown imply that the shrink times are likely to flatten off as ℓ_{max} increases beyond $50a$ in (a), and $100a$ in (b). This would be reasonable, because eventually ℓ_{max} will become bigger than the initial loop width itself, and cease to be a relevant parameter for these simulations whatsoever.

When $\ell_{\text{max}} = 10a$ in (a), the absolute value of ℓ_{min} appears to have a relatively larger effect. In figure (a) these values of ℓ_{min} are $2a$ and $5a$, and in figure (b) they are $4a$ and $10a$. The smaller absolute values appear to cause a relatively large increase in the shrink time. Note also the "missing" data points for $\ell_{\text{min}} = \ell_{\text{max}}/20$ and $\ell_{\text{min}} = \ell_{\text{max}}/10$ on both plots. These are absent because the loop actually grew in these cases. These missing data points are again for relatively small absolute values of ℓ_{min}, of the order of a.

An interpretation of this is that the presence of very small segments with lengths of the



(a) Loop of width $100a$ (28.7 nm).



(b) Loop of width $200a$ (57.3 nm).

Figure 4.13: The effect of varying $\ell_{\min}$ and $\ell_{\max}$ on the shrinkage time of a square vacancy loop of width w. Three values of $\ell_{\max}$ are shown for each loop: $w/10$, $w/5$ and $w/2$. The non-zero osmotic force due to the presence of a vacancy supersaturation ratio $c_\infty^{\mathrm{v}}/c_0^{\mathrm{v}} = 10$ acts outwardly (in the direction of loop growth). The temperature is 700 °C.

order of a is unphysical. This also seems reasonable: a dislocation segment should not have a length of the order of the atomic spacing, as on this length scale the approximations of linear elasticity, and indeed an elastic continuum, break down. Furthermore, the calculations of the forces between dislocation segments use the dislocation core spreading parameter $a_{\text{ns}} = \ell_{\text{min}}/2\sqrt{3}$. When $\ell_{\text{min}} < 4a$, $a_{\text{ns}} \leq a$, and so the dislocation core is also spread over a region with a width of the order of a, potentially leading to inaccurate calculations. The existence of these small length scales of the order of a in the code indicate that dislocation segment lengths as small as this cannot be used without major assumptions of the model breaking down and the results becoming unstable and inaccurate.

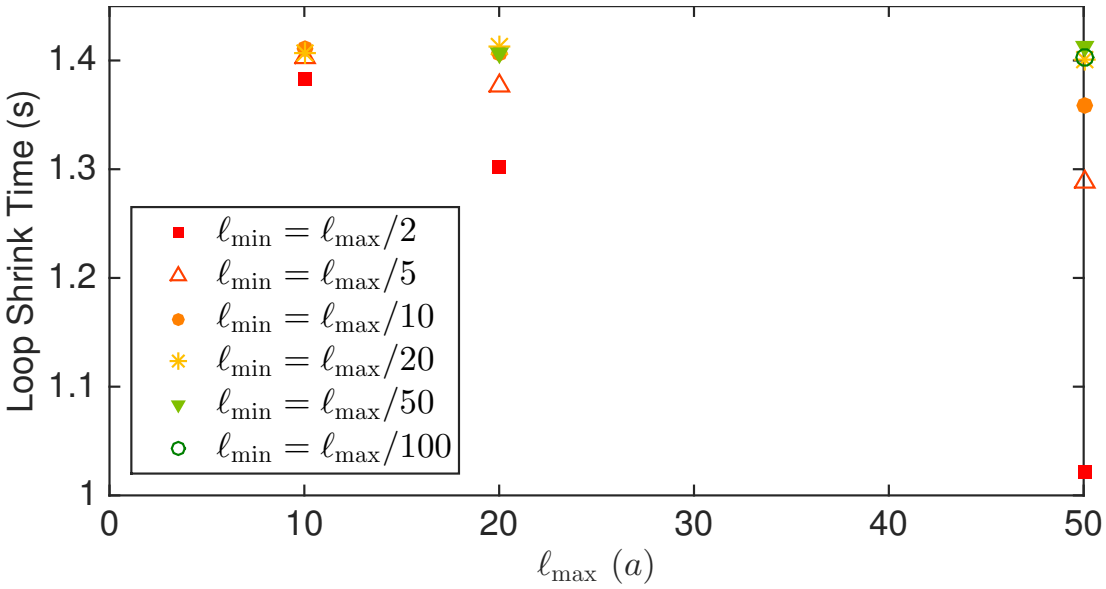
The non-zero osmotic force is responsible for the loop expanding in the extreme cases. In order to make the situation under consideration less complicated, this should be removed by setting the vacancy supersaturation ratio $c_{\infty}^{\text{v}}/c_{0}^{\text{v}} = 1$.

4.4.2 Attempt 2: scaled ℓ_{min} and ℓ_{max} without an osmotic force present

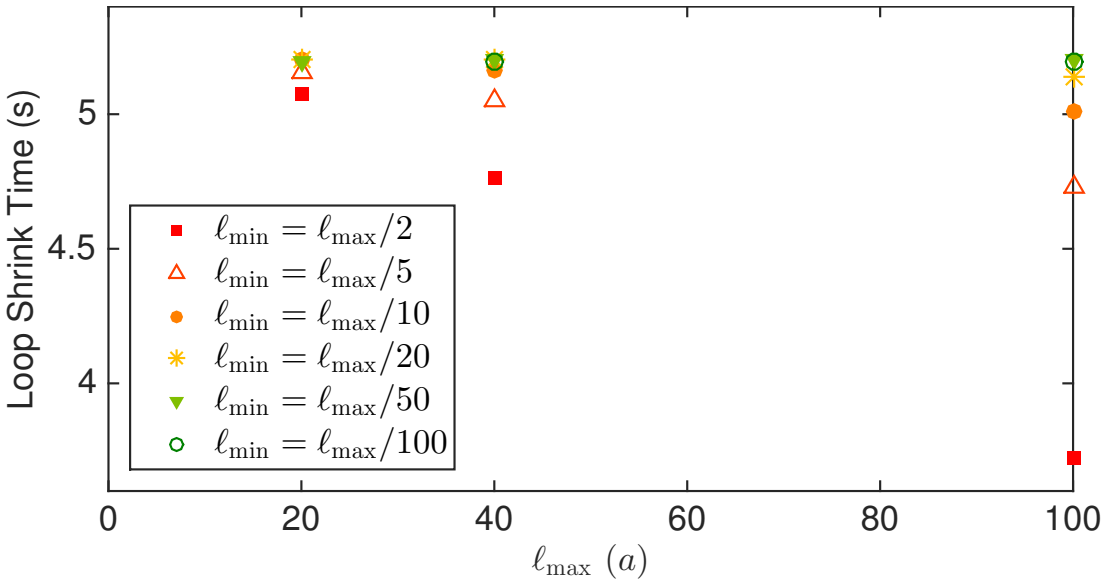
Figure 4.14 shows that removing the osmotic force by setting $c_{\infty}^{\text{v}}/c_{0}^{\text{v}} = 1$ reveals how the choice of ℓ_{min} and ℓ_{max} affects the simulated loop shrink times in a much clearer way than previously in figure 4.13.

The loop shrink times on both plots in figure 4.14 are much less spread out than in figure 4.13. Furthermore, the loop shrink times converge as ℓ_{min} decreases down to the order of a. The loop becomes unstable at about $\ell_{\text{min}} = 0.2a$. In the $\ell_{\text{min}} =$ 1–5a regime, the value of ℓ_{max} has very little effect. It is only when ℓ_{min} is relatively large that smaller values of ℓ_{max} yield more accurate results.

The plots in both figures 4.13 and 4.14 do not clearly indicate the actual values of ℓ_{min}, as ℓ_{min} is always defined as a variable fraction of ℓ_{max} in order to investigate such scaling regimes. However, it would be even clearer to plot the actual values of both ℓ_{min} and ℓ_{max}, as in figure 4.15.

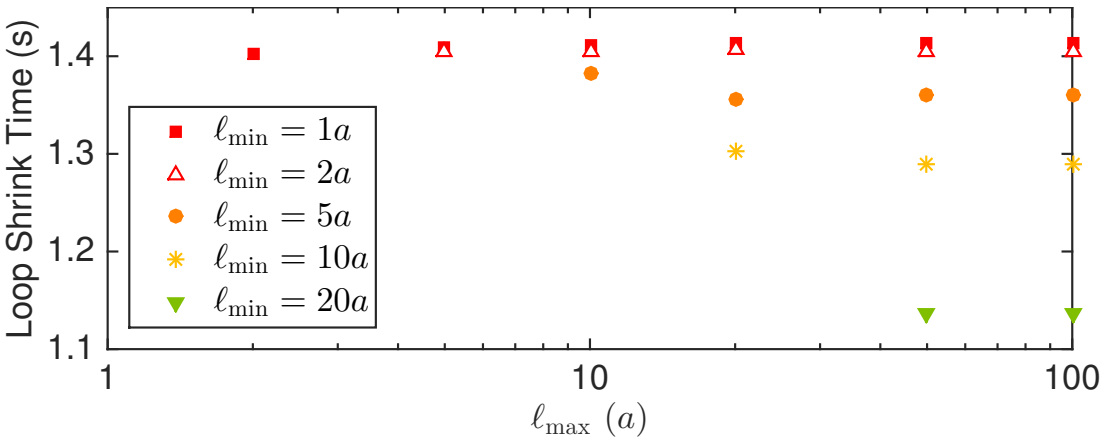


(a) Loop of width $100a$ (28.7 nm).

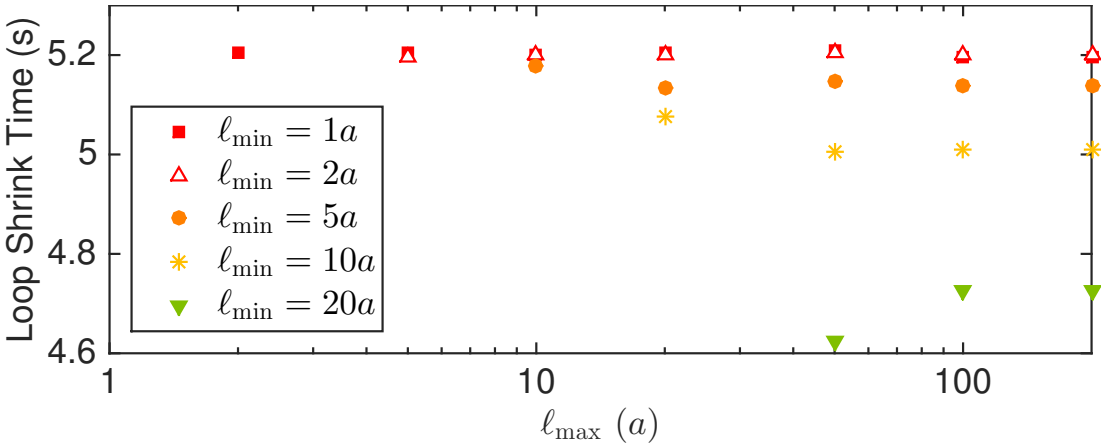


(b) Loop of width $100a$ (57.3 nm).

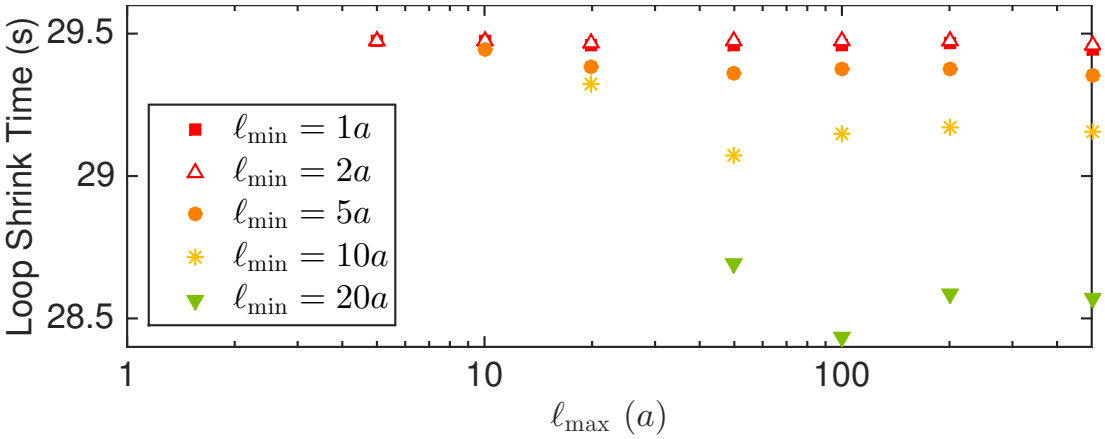
Figure 4.14: The effect of varying $\ell_{\min}$ and $\ell_{\max}$ on the shrinkage time of a square vacancy loop of width w. Three values of $\ell_{\max}$ are shown for each loop: $w/10$, $w/5$, and $w/2$. There is no vacancy supersaturation (i.e. $c_\infty^{\mathrm{v}}/c_0^{\mathrm{v}} = 1$) and hence no osmotic force on the loop. The temperature is 700 °C.



(a) Loop of width $100a$ (28.7 nm).



(b) Loop of width $200a$ (57.3 nm).



(c) Loop of width $500a$ (143 nm).

Figure 4.15: The effect of varying $\ell_{\min}$ and $\ell_{\max}$ on the shrinkage time of a square vacancy loop of width w. There is no vacancy supersaturation (i.e. $c_\infty^{\mathrm{v}}/c_0^{\mathrm{v}} = 1$) and hence no osmotic force on the loop. The temperature is 700 °C.

4.4.3 Attempt 3: plotting the actual values of ℓ_{min} and ℓ_{max}

The plots in figure 4.15 show the loop shrink times for several combinations of the actual values of ℓ_{min} and ℓ_{max} for loops of three different sizes (unlike the previous figures 4.13 and 4.14).

The loop shrink times converge as ℓ_{min} decreases to about 1–2 a. In this regime of small ℓ_{min}, the choice of ℓ_{max} has virtually no effect on the simulated loop shrink time (however in the larger ℓ_{min} regime, there is small amount of variation for intermediate values of ℓ_{max}). This trend is seen for all three loop sizes simulated.

In conclusion, choosing ℓ_{min} to be small yields accurate results, but it should not be less than $\sim 4a$ so as to ensure $a_{\text{ns}} > a$, as otherwise this would be unphysical, and lead to inaccurate results. Hence $\ell_{\text{min}} = 4a$ is considered to be optimal.

In these loop shrinking tests, ℓ_{max} is free to be anything larger than ℓ_{min}, but if it is bigger than the loops themselves it becomes irrelevant. Also, it is feasible that in other, different situations the choice of ℓ_{max} could affect the result, such as simulating the time it takes a circular interstitial loop to expand to e.g. two times its initial radius for a fixed interstitial supersaturation. Because of this it is suggested that ℓ_{max} should be no more than a factor of 2–5 larger than ℓ_{min}.

4.5 Glide and climb: a dual time step method

Even at higher temperatures when the rate of dislocation climb is relatively fast, glide motion is still many orders of magnitude faster. Because of this, running `DDLab` simulations in which both glide and climb occur is somewhat challenging. If the simulations are run with relatively small time increments, glide motion is captured accurately, but virtually no climb motion is able to progress over such a short amount of simulated time. Conversely, if relatively large time increments are used, appreciable amounts of climb are able to occur, but huge amounts of glide are able to occur in every single time step, resulting in highly unstable and inaccurate dislocation behaviour.

In order to tackle this problem the dual time step method described by Bakó et al. (2011) is employed. During each step of the `DDLab` simulations, the dislocation motion is restricted to one of two regimes:

1. *"Glide only" motion*, which is characterised by a small time increment. Climb is still occurring, but only very small amounts, since the time increment is relatively small and the climb drag is significantly larger than the glide drag. This is the default behaviour of `DDLab`.

2. *"Climb only" motion*, which is characterised by a much larger time increment. The glide drag factor is artifically, and unphysically, set to be equal to that of climb. Hence non-negligible amounts of climb are able to occur — glide motion, which otherwise has a much smaller drag factor, no longer dominates. Note that a little glide is still occurring, but at a rate no faster than that of climb. This is so as not to pin the dislocation segments artificially.

At the end of each step which of the two regimes is used for the next step is decided as follows.

The simulations begin with glide only steps. These progress until the dislocation network has reached quasi-equilibrium with respect to glide only motion, that is to say until

$$\left| 1 - \frac{\sqrt{\mathrm{tr}[\varepsilon_\mathrm{p}(t+\Delta t)^\mathrm{T}\varepsilon_\mathrm{p}(t+\Delta t)]}}{\sqrt{\mathrm{tr}[\varepsilon_\mathrm{p}(t)^\mathrm{T}\varepsilon_\mathrm{p}(t)]}} \right| < \eta, \tag{4.14}$$

where t is the simulated time at the n^{th} time step, $(t + \Delta t)$ is the simulated time at the $(n+1)^{\text{th}}$ time step, and $\varepsilon_{\text{p}}(x)$ is the accumulated plastic strain tensor at simulated time x. η is the minimum plastic strain ratio from one time increment to the next, and is a number $\ll 1$. It is a free parameter of the simulations which controls at what point the glide-climb switch occurs (Bakó et al., 2011). When the condition in (4.14) is met, a small number of climb only steps are carried out. The simulation then switches back to glide only steps and the process begins again. In this way occasional bursts of climb are simulated, and in between these climb only bursts the dislocation network is able to "relax" with respect to glide only motion.

4.5.1 Implementing the dual time step method

In order to implement the dual time step method in `DDLab`, more original code development was required, as Bakó et al. only provided a brief outline of the method, rather than any detailed algorithms.

The `main_dd3d` script was developed first to perform the glide-to-climb switch check — whether the condition in (4.14) has been met — at the end of each time step (except the first one, as in this case the left hand side of (4.14) cannot be evaluated). Three different approaches to evaluating the plastic strains needed for this glide-to-climb switch check were implemented, and their behaviour is investigated in § 4.5.4.

After some unsuccessful attempts, blocks of code were added to (or altered in) the `mobbcc0`, `mobbcc0Int` and `drndt` functions, such that glide only and climb only motion are both captured correctly, depending on which type of time step is currently active. The Euler-forward integration scheme was chosen to complement this implementation, in order to limit the maximum distance any node moves in a single time step, whether it is a glide or a climb one, to one lattice parameter.

In the next section, the implementation of this dual time step method in `DDLab` is tested using an applied shear load on a square test loop, and on a circular test loop in § 4.5.3.

4.5.2 Square prismatic loop under shear loading

Table 4.4 shows various input parameters relevant to these dual time step test simulations. The drag factors are as described in § 4.2.1, although the edge and screw glide drag factors are assumed to be equal, i.e. $B_{\mathrm{eg}} = B_{\mathrm{sg}} = B_{\mathrm{gl}}$, which is chosen to be equal to 4×10^{-4} Pa·s. This is the correct order of magnitude for bcc iron (Gilbert et al., 2011). In reality B_{eg} and B_{sg} are not equal, and both depend on temperature and applied stress. However, as the climb drag $B_{\mathrm{cl}}(T)$ comes to 6.64×10^{7} Pa·s at 700 °C[34], which is over eleven orders of magnitude larger than 4×10^{-4} Pa·s, the precise values of B_{eg} and B_{sg} have a negligible effect on the simulation outcome.

Temperature, T	700 °C	
Applied shear load, σ_{12}	410 MPa	
Minimum plastic strain ratio, η	10^{-3}	
	Glide step	Climb step
Glide drag, B_{gl}	4×10^{-4} Pa·s	6.64×10^{7} Pa·s
Climb drag, $B_{\mathrm{cl}}(T)$	6.64×10^{7} Pa·s	6.64×10^{7} Pa·s
Line drag, B_{li}	$10^{-4} \times B_{\mathrm{gl}}$	$10^{-4} \times B_{\mathrm{cl}}(T)$

Table 4.4: Dual time step test simulation input parameters.

Notice that for climb steps, B_{gl} is set to be equal to $B_{\mathrm{cl}}(T)$, and that the dislocation line drag B_{li} also needs to be set to different values for the two different regimes: in this case 10^{-4} multiplied by whichever of the glide and climb drag factors is the smallest.

Figure 4.16(a) shows the initial configuration of the square vacancy test loop. This is exactly the same simulation setup as in figure 4.2(a), but now an applied σ_{12} shear load of 410 MPa is introduced. The loop has a width of $100a$ (28.7 nm) and its Burgers vector is $\mathbf{b} = [100]$ (the line-sense is defined to be clockwise about [100]). The view is down the $[1\bar{1}1]$ direction. Figure (b) shows the loop after only 7.78×10^{-11} s of simulated time has passed (after 111 time increments of glide only motion). The loop has deformed around its glide "cylinder" via glide motion due to the applied shear load, and appears somewhat rotated and elongated, such that it now lies in (approximately) the $(1\bar{1}0)$ plane. This motion has been colloquially referred to as "rubber-banding".

[34] At temperatures lower than 700 °C, $B_{\mathrm{cl}}(T)$ is even larger than 6.64×10^{7} Pa·s.

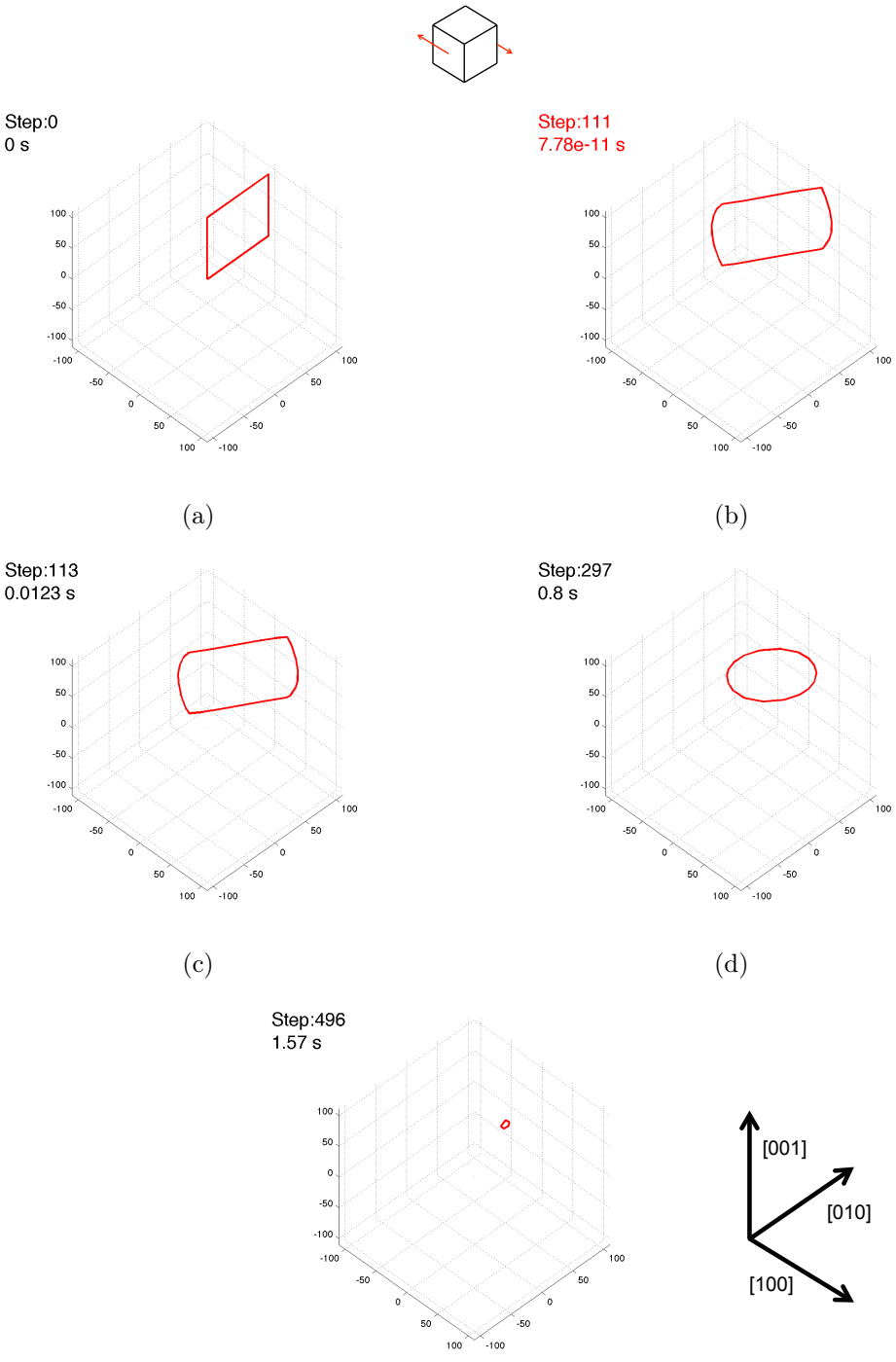


Figure 4.16: An initially square pure prismatic vacancy loop undergoing both glide and climb under an applied σ_{12} shear load of 410 MPa. The loop has a width of $100a$ (28.7 nm) and its Burgers vector is $\mathbf{b} = [100]$ (the line-sense is defined to be clockwise about [100]). The view is down the $[1\bar{1}1]$ direction.

The red text in the figure indicates that the dislocation network has reached quasi-equilibrium with respect to glide only motion. The dislocation motion now switches to the climb only regime for 2 time increments. Figure (c) shows the loop after these 2 climb steps. It is difficult to see in the figure, but some climb has occurred. Note that a much larger amount of simulated time has passed in these 2 climb steps: the clock now reads 0.0123 s. The black text in the figure indicates that the simulation will now return to the glide only regime. This process then continues: the loop "relaxes" with respect to glide only motion until the relative change in the plastic strain tensor drops below the prescribed value η in (4.14). Once this quasi-equilibrium is reached, 2 climb steps are carried out, and then the simulation returns to glide only relaxation.

Figure (d) shows the loop after 0.8 s of simulated time has passed (after 297 time increments). The majority of these are small time increment glide only steps, but some are the larger time increment climb only steps. The loop has rounded and shrunk overall via climb, and rotated and elongated via glide.

Finally, figure (e) shows the loop at the moment it ceases to exist — after 1.57 s of simulated time. This is slightly longer than 1.36 s for the zero load loop in figure 4.2, but of the same order of magnitude.

Figure 4.17 shows the same simulation setup as in figure 4.16, but with the sign of the σ_{12} shear load reversed. The simulation progresses in exactly the same way as the one shown in figure 4.16, with the exception of the specific geometry of the rubber-banding, which occurs in the opposite direction as expected, with the intermediate loop this time lying in (approximately) the (110) plane. Indeed, the five snapshots shown match up exactly with the five in figure 4.16, both deliberately in terms of which steps are displayed, but also in terms of the simulated time that has passed at each of the steps. The loop takes the same total simulated time to shrink. Figures (b)–(d) demonstrate the rotation and elongation of the loop due to the applied shear load particularly clearly.

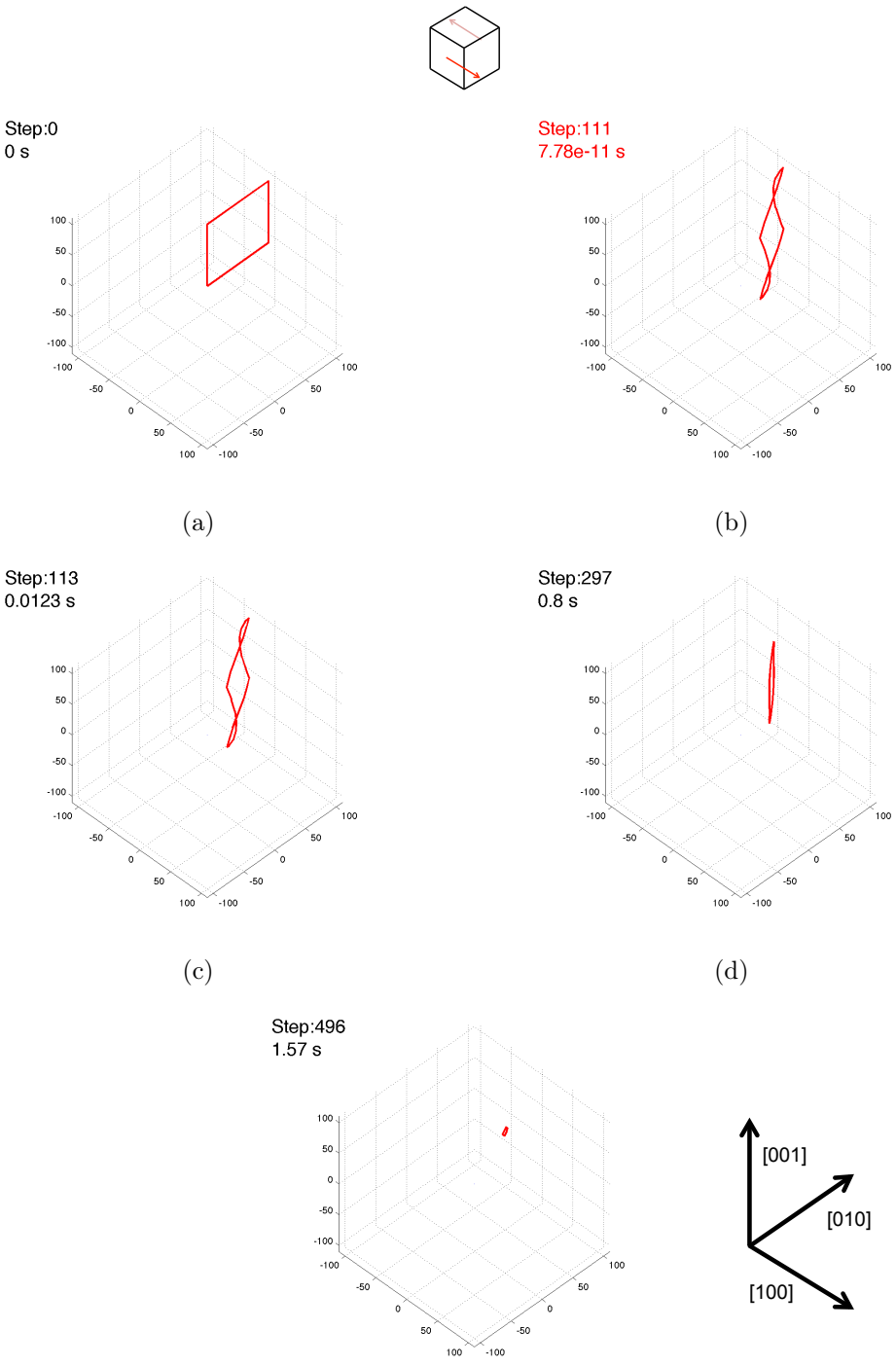


Figure 4.17: The same simulation setup as in figure 4.16, but with the sign of the σ_{12} shear load reversed. The five snapshots shown match up exactly with the five in figure 4.16, both deliberately in terms of which steps are displayed, but also in terms of the simulated time that has passed at each of the steps.

4.5.3 Circular prismatic loop under shear loading

Figure 4.18(a) shows the initial configuration of the circular interstitial test loop. This is exactly the same simulation setup as in figure 4.7, but now a σ_{12} shear load of 410 MPa is applied. As in the square loop simulations in the previous section, the loop exhibits a combination of glide mediated rubber-banding along its glide cylinder, and climb mediated shrinkage perpendicular to its Burgers vector. The intermediate loop lies in (approximately) the $(1\bar{1}0)$ plane. The glide motion occurs on a timescale of $\sim 10^{-11}$ s, whereas the climb motion occurs on a timescale of $\sim 10^{-2}$ s, resulting in a shrink time of 1.18 s. This is only marginally longer than the 1.06 s shrink time in the absence of an applied σ_{12} shear load, as expected.

Figure 4.19 shows the same simulation setup as in figure 4.18, but for a vacancy loop instead of an interstitial one. The sign of the σ_{12} shear load is kept the same. Again, the rubber-banding directions are reversed (because the Burgers vector is now equal to $[\bar{1}00]$, and hence the intermediate loop lies in (approximately) the $(\bar{1}\bar{1}0)$ plane), but otherwise the simulation progresses in the same manner as it did for the vacancy loop, and the shrink time is 1.18 s as before.

These square and circular loop test simulations are encouraging. The glide mediated deformation of the loops has very little effect on the amount of time it takes for them to shrink via climb, which should be the case given the hugely different timescales for these two processes. In fact, under shear loading it takes slightly longer for the loops to disappear, which seems reasonable given the initial elongation (and hence growth) of the loops in these simulations.

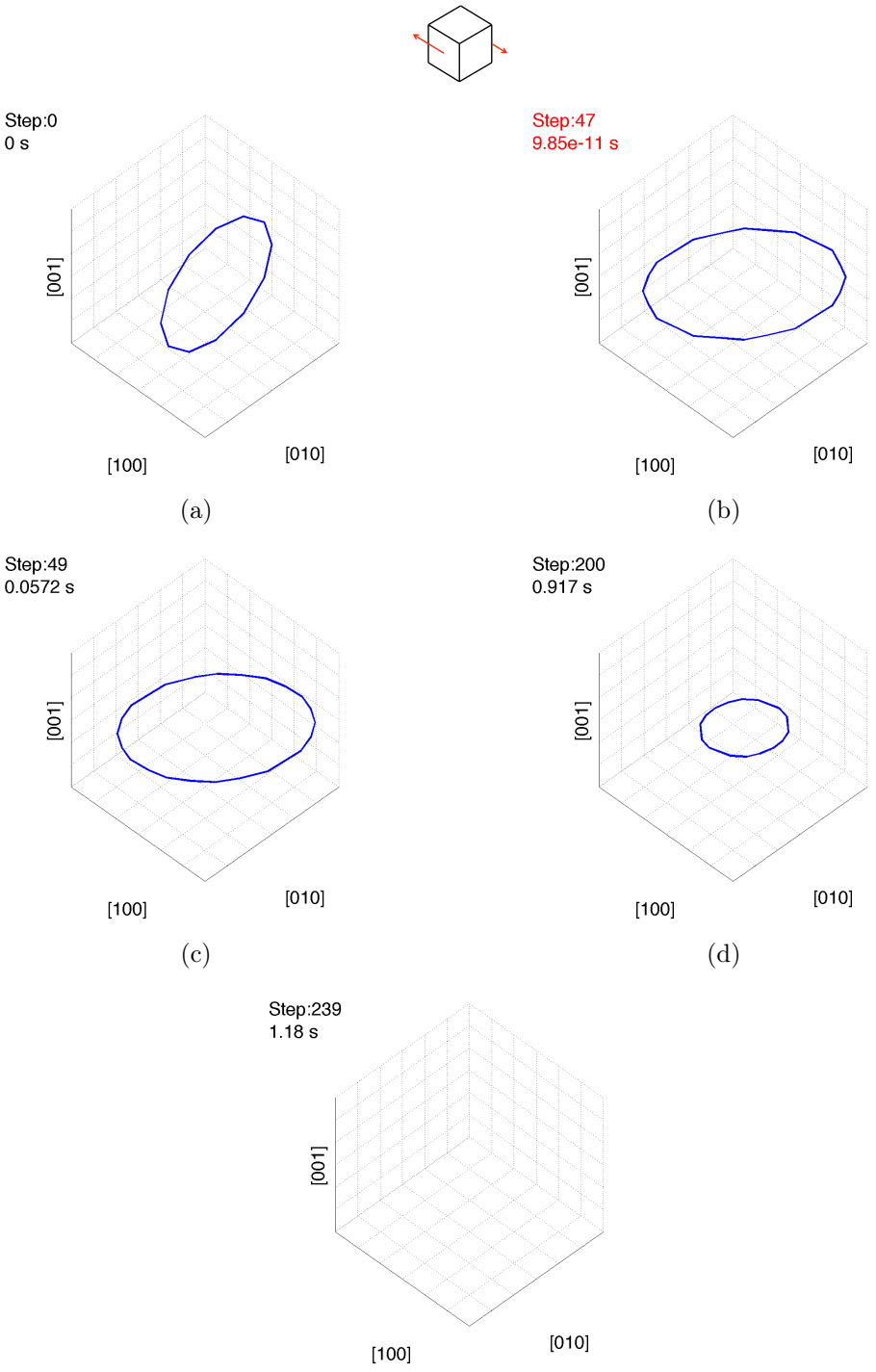


Figure 4.18: A circular intersitial loop undergoing both glide and climb under an applied σ_{12} shear load of 410 MPa. The loop has a radius of $50a$ (14.3 nm), and its Burgers vector is $\mathbf{b} = [100]$ (the line-sense is defined to be anti-clockwise about [100]). The view is down the $[1\bar{1}1]$ direction.

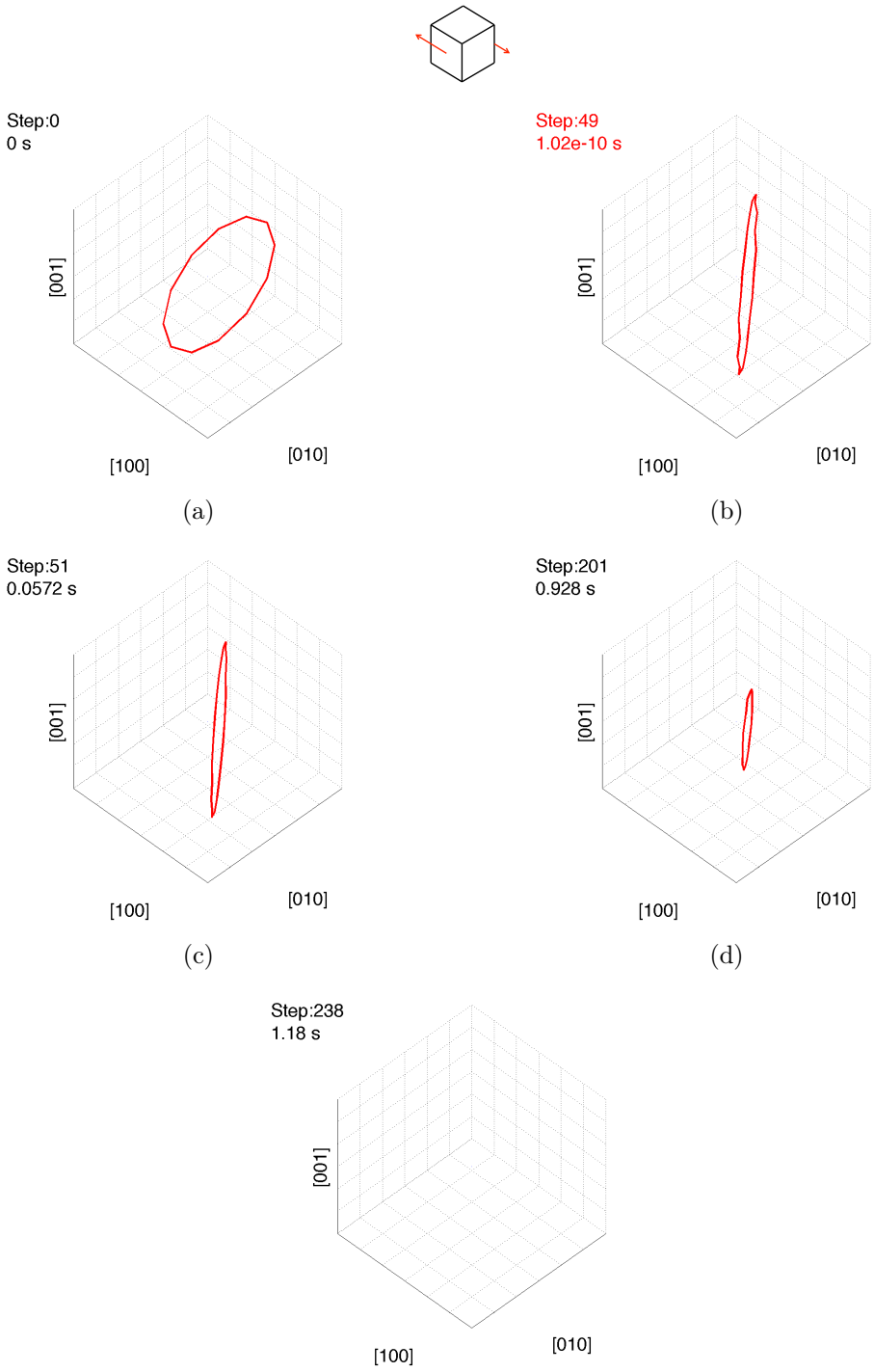


Figure 4.19: The same simulation setup as in figure 4.18, but for a vacancy loop instead, subjected to the same σ_{12} shear load of 410 MPa. The loop takes the same amount of simulated time to shrink as the intersitital loop in figure 4.18.

4.5.4 Calibrating the minimum plastic strain ratio η

In this section, the effect of varying the minimum plastic strain ratio η — which determines the glide to climb switching condition (4.14) — in the circular interstitial loop subjected to an applied σ_{12} shear load test simulation (shown in figure 4.18) is investigated, in order to find an optimal value for η.

Three different schemes of evaluating the glide to climb switching condition (4.14) are compared. The first one, (a), involves updating the accumulated total plastic strain tensor every time step, regardless of whether the time step is a glide or a climb one. Hence the accumulated plastic strain tensor used in (4.14) contains the plastic strain as a result of both the glide and climb motion of the dislocations. Scheme (b) mimics scheme (a), the difference being only deviatoric plastic strains are included in the calculation of the accumulated plastic strain tensor. Lastly, scheme (c) involves updating the accumulated total plastic strain tensor after glide steps only. When using this scheme — it turns out — there is no difference between only using deviatoric plastic strains, and using total plastic strains. This seems reasonable, as during the glide only time steps, the plastic strain which arises is solely due to dislocation glide, which by definition induces pure shear strain.

Figure 4.20 shows the effect of varying η over a range of values from 10^{-4} to 0.5 on the loop shrink time. For relatively large values of η, the loop takes the shortest time to shrink. This is due to the relatively small amounts of glide which need to occur before climb is able to set in. Hence glide motion is unphysically suppressed by the larger values of η.

The three different sets of data shown have coincident data points for the five largest values of η. Only when $\eta \leq 10^{-2}$ is there some scatter in the data between the three schemes of evaluating (4.14). There are some slight differences between the data points of schemes (a) and (b) for the intermediate and low values of η, but they are relatively small.

Using scheme (c) however has a notable effect for intermediate values of η, although the maximum discrepancy is only $\sim$10%, when $\eta = 10^{-2}$. Furthermore, as η decreases from

10^{-2}, the size of this discrepancy decreases, and the shrink times when using all three schemes appear to be converging to the same value. Data points for $\eta = 1$ and 2×10^{-4} for scheme (c) are absent from the plot because in these cases the loop was unable to shrink down to nothing and disappear. Instead the few remaining nodes became artificially pinned once the loop had shrunk down to a relatively small size.

Good convergence in the shrink times is seen for values of $\eta \leq 10^{-3}$. However, the number of computation steps required for the loop to shrink and disappear increases rapidly as η is reduced from 10^{-3}, as shown in figure 4.21. In order to reduce computational expense, and mitigate the potential for artificial node pinning, the value of $\eta = 10^{-3}$ is suggested for further simulations. Incidentally, 10^{-3} is the value of η used by Bakó et al. in their loop coarsening simulations (Bakó et al., 2011).

It is also suggested that the total plastic strains (rather than the deviatoric ones) for all time steps are used to evaluate the glide to climb switching condition (4.14), i.e. scheme (a), as this scheme appears to be more stable than scheme (c), and does not exhibit significant differences to the results from scheme (b) (which also appears to be stable).

4.6 Concluding remarks

The point defect bulk diffusion model of climb has been successfully implemented in `DDLab`, together with a dual time step method of capturing glide and climb behaviour in the same simulation — both of which required original code development.

In chapter 5 the literature relevant to particle-reinforced materials is reviewed, and in chapter 6 the implementation of obstacles which are impenetrable to dislocations in `DDLab` is described.

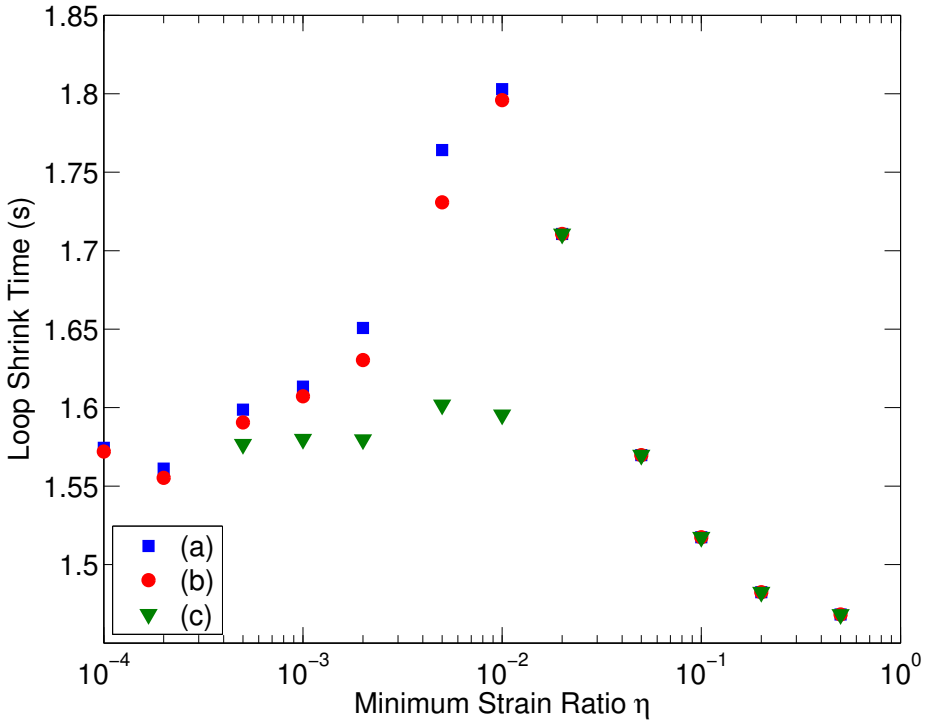


Figure 4.20: Loop shrink time as a function of minimum strain ratio η. (a) Total plastic strain increments, for both glide and climb steps. (b) Only deviatoric plastic strain increments, for both glide and climb steps. (c) Plastic strain increments (total and deviatoric exhibit no difference), for glide steps only.

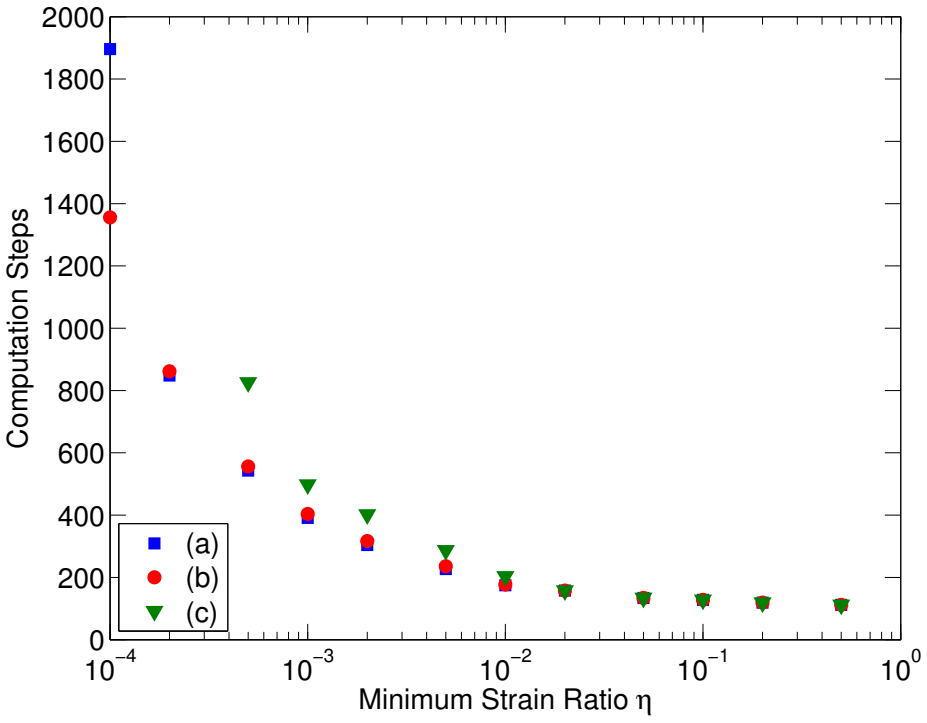


Figure 4.21: Number of computation steps as a function minimum strain ratio η. See figure 4.20, and the main text, for the interpretation of the data points (a), (b) and (c).

Chapter 5

Inclusions literature review

5.1 Introduction

This second literature survey concerns inclusions — particularly nanoscale particles, or dispersoids — and their effects on a material's deformation behaviour. Dispersion strengthening is discussed, before moving on to the specifics of RAFM oxide dispersion-strengthened (ODS) steels for fusion applications, and the results of attempts to model dislocation-inclusion interactions computationally.

5.2 Inclusions

In an elastic continuum, an inclusion is a region which is differentiated from the rest of the continuum — the "matrix" — for some reason. If a region in the continuum has changed its form, leaving the surrounding matrix in a state of internal stress, then this region is a misfitting inclusion. A region with different elastic constants to the surrounding matrix is also an inclusion, such as a precipitate of a second phase of the matrix material, or an insoluble particle of a different material altogether. Such precipitates and particles can also produce misfit stresses in the surrounding matrix.

These inclusions can interact with gliding dislocations, and can hinder dislocation motion by acting as pinning obstacles, leading to hardening (Dieter, 1986, p. 212). In steels

at high temperatures, any carbide and nitride precipitates present become soluble in the matrix, leading to the loss of the precipitation strengthening induced by these precipitates (Arzt, 1988). Dispersoids, however, are often composed of an entirely different material to that of the matrix, such as non-base metal oxides, which has a high insolubility in the matrix. Because of this, dispersoids are relatively insoluble particles[35], even at higher temperatures, making oxide dispersions a viable means of strengthening ferrous alloys for fusion applications (Alinger, 2004). Understanding how the distribution, size and composition of these particles affects mechanical behaviour is important if dispersion strengthening is to be incorporated into ferrous alloys for this purpose.

5.2.1 Dispersion strengthening

Dispersoids can be semi-coherent with the surrounding matrix, and thus partially shearable (i.e. partially penetrable) by gliding dislocations; or they can be incoherent particles, and thus impenetrable to dislocations[36]. In these cases, dislocations can become pinned at the particle-matrix interface, or within the particle itself. The stress fields of misfitting particles can also interact with gliding dislocations, and hence impede their motion without the dislocations coming into direct contact with the particles.

When a gliding dislocation approaches an obstacle which intersects its glide plane, it becomes pinned and bows around either side of the obstacle. In the presence of a distribution of obstacles in the matrix, at a certain applied shear stress the dislocations only glide a certain amount before becoming pinned (i.e. blocked, or impeded), which leads to hardening. At higher applied shear stresses, the dislocations remain pinned, but bow out further around the particles, leaving trailing tails. At a critical unpinning stress, the dislocations are able to loop around the obstacles and pinch off, continuing their glide motion whilst leaving behind dislocation loops encircling the particles. This is known as the Orowan mechanism (Orowan, 1947), and is illustrated schematically in figure 5.1.

[35] It also possible, however, for oxide particles in ODS alloys to be formed from supersaturated solutions (Odette et al., 2008).

[36] In some cases, precipitates can be fully coherent with the surrounding matrix, and dislocations are able to pass through the precipitate by shearing through it. This has implications for precipitation strengthening (Martin, 1968).

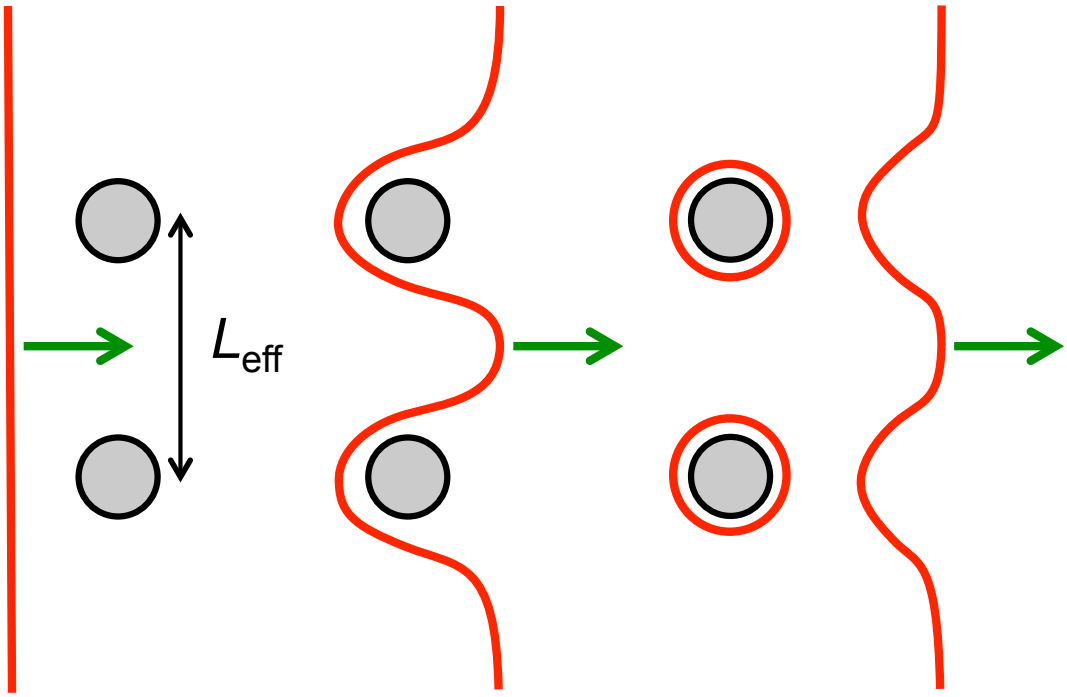


Figure 5.1: A schematic illustration of a gliding dislocation unpinning from impenetrable particles via the Orowan mechanism. Orowan dislocation loops are left encircling the particles.

The critical unpinning stress is also known as the Orowan stress, and is given by the expression:

$$\sigma_{\text{Orowan}} = \frac{\mu b}{L_{\text{eff}}}, \tag{5.1}$$

where L_{eff} is the average effective obstacle separation in the 2D glide plane[37]. This average effective separation is distinct from the average separation in *3D* space, and is discussed in more detail in § 7.4. Nevertheless, it is clear that increasing the number density of obstacles, and hence decreasing their average effective separation, will lead to an increase in the Orowan stress, i.e. an increase in the dispersion strengthening effect. The expression in (5.1) is sometimes multiplied by a barrier strength coefficient, which for a random distribution of impenetrable obstables is ∼0.8 (Cunningham, 2008).

Bacon et al. (1973) studied the effect that including the dislocation self-interaction has on the Orowan stress for a collinear array of non-misfitting, impenetrable circular obstacles. As the ratio of obstacle size to effective spacing decreases, the area swept

[37] (5.1) is an approximation: if L_{eff} is not very large in comparison with the size D of the obstacles in the 2D glide plane, then L_{eff} in (5.1) must be replaced by L'_{eff}, which is given by $L'_{\text{eff}} = L_{\text{eff}} - D$ (Hull and Bacon, 2011). This is done in the modified expression in (5.2).

swept out by the bowing dislocations is suppressed, leading to an increase in the flow stress, i.e. hardening. These results were used to develop an approximate form for the flow stress of a random distribution of impenetrable obstacles, given by

$$\sigma_{\text{random}} = \left(\frac{\ln D}{\ln L'_{\text{eff}}}\right)^{\frac{1}{2}} \frac{\mu b}{L'_{\text{eff}}} \frac{\ln D}{2\pi}, \tag{5.2}$$

where D is the average obstacle diameter (in the 2D glide plane), and L'_{eff} is simply given by $L'_{\text{eff}} = L_{\text{eff}} - D$. Note that quantities with dimensions of length in (5.2) are normalised to units of a dislocation "core radius" cut-off parameter, which can be thought of as $\sim r_{\text{c}}$. Scattergood and Bacon (1975) went on to consider the case of anisotropic elasticity, in which the bow out becomes asymmetric at higher stresses, reducing the flow stress compared to the isotropic elasticity case.

At applied stresses below the Orowan stress, pinned dislocations can still unpin from obstacles by climbing over them. Because thermal climb velocities increase rapidly with temperature, dislocation-inclusion unpinning via climb can occur relatively quickly at high temperatures. This has implications for thermal creep, as the rate of plastic flow in dispersion-strengthened materials depends on the rate at which dislocations are able to overcome the strengthening obstacles. In such situations, the overall strain rate $\dot{\varepsilon}$ is given by

$$\dot{\varepsilon} = \rho b v, \tag{5.3}$$

where ρ is the mobile dislocation density, and v is the average dislocation velocity. The faster the rate of dislocation-inclusion unpinning, the faster the average dislocation velocity. (5.3) is known as the Orowan equation (Hull and Bacon, 2011).

Under irradiation conditions, dislocation-inclusion unpinning has the potential to occur at even faster rates, due to the osmotic climb caused by the induced point defect supersaturations. Higher irradiation dose rates lead to more osmotic climb, and hence to faster dislocation-inclusion unpinning rates.

Understanding the role dislocation-inclusion unpinning via climb plays in the temperature-dependent creep response of dispersion-strengthened steels for fusion applications is clearly important.

5.2.2 The stress field of a misfitting inclusion

Eshelby (1957, 1959) developed expressions in terms of elliptic integrals for the stress field both inside and outside a single misfitting ellipsoidal inclusion with elastic constants different from the infinite medium in which it lies. The Eshelby solutions have been applied successfully to a number of different physical situations: for example, they have been used to model the elastic constants of short fibre composite materials by treating the fibres as aligned prolate spheroids (Tandon and Weng, 1984; Weng, 1992). In the simple case of a spherical inclusion of radius R which is fitted in to a smaller hole in an isotropic elastic medium with radial misfit δ, the stress in the matrix outside the inclusion in spherical coordinates is given by:

$$\sigma_{rr} = -\frac{4\mu_{\mathrm{m}}C}{r^3}, \quad \sigma_{\theta\theta} = \sigma_{\phi\phi} = \frac{2\mu_{\mathrm{m}}C}{r^3}, \tag{5.4}$$

where

$$C = \frac{\delta\nu}{4\pi\left(1 + \frac{4\mu_{\mathrm{m}}}{3K_{\mathrm{i}}}\right)}, \quad \text{and} \quad K_{\mathrm{i}} = \lambda_{\mathrm{i}} + \frac{2\mu_{\mathrm{i}}}{3}, \tag{5.5}$$

where $\delta\nu = 4\delta\pi R^2$ is the (assumed small) misfit volume between the particle and the hole, λ is Lame's constant, K is the bulk modulus, and the 'i' subscripts indicate inclusion quantities whereas the matrix quantities have 'm' subscripts (Khraishi et al., 2004, after Eshelby, 1957). The expressions in (5.4) are only valid outside the inclusion, and hence they are insufficient to describe the situation where a semi-coherent inclusion intersects the glide plane of the dislocation with which it is interacting.

In the case of an anisotropic elastic medium, no such simple solutions exist for a similar spherical centre of dilatation. However, Barnett (1972) describes how the dilatation field due to a spherical volumetric strain in a cubic anisotropic medium is equal to the second derivative of the elastic Green's function tensor, and he gives a method for accurately calculating this by numerical integration. It exhibits the expected $1/r^3$ radial dependence for a centre of dilatation in an isotropic medium (Eshelby, 1954), with a non-trivial angular dependence due to the different values of the triagonal and tetragonal shear moduli. Again, when used to describe an inclusion of non-zero radius,

this expression is only valid outside the inclusion.

5.2.3 Oxide dispersion-strengthened steels

RAFM oxide dispersion-strengthened (ODS) steels are promising candidate structural materials for use in fusion (and Gen IV fission) reactors for a number of reasons. A comprehensive review of their typical compositions, microstructures, and mechanical properties is given by Odette et al. (2008).

Yttrium oxide (yttria) is often used as the base material for the insoluble oxide dispersoids, as Y_2O_3 particles exhibit high thermal stability in ferrite (Ukai and Fujiwara, 2002), but other oxide compositions such as TiO_2 and $Y_2Ti_2O_7$ are also used (Hoelzer et al., 2007; Zhong et al., 2012). Typical weight percentages of yttrium incorporated into ODS steels range from 0.1 to 0.5% (Bartsch et al., 1999; Gorley, 2014). The oxide particles have diameters of ∼5 nm and less, and number densities of the order of 10^{23}–10^{24} m^{-3} (Gorley, 2014).

Grain refinement is observed in ODS alloys, with a bi-modal distribution of grain sizes — mostly relatively small grains accompanied by a small number of relatively large ones — is often seen (Hoelzer et al., 2007; Odette et al., 2008). The grain refinement is thought to be due to the pinning of the grain boundaries by the oxide particles, and the bi-modal distribution of grain sizes is consistent with the abnormal grain growth — in which a small number of grains overcome their pinning particles during annealing, and hence quickly assimilate nearby grains — seen in nickel base superalloys (Decker et al., 1956).

In ODS alloys, an increase in the room temperature yield strength compared to similar non-ODS RAFM steels is observed (Klueh et al., 2005). Yield strengths ranging from 600 to 1200 MPa are seen (Kasada et al., 2007), meaning this increase can be of almost 100%. However, at higher temperatures significant softening is seen, and the strengthening benefits can disappear entirely by temperatures which range from 600–900 °C (Klueh et al., 2005; El-Genk and Tournier, 2005). An example of this is shown in figure 5.2

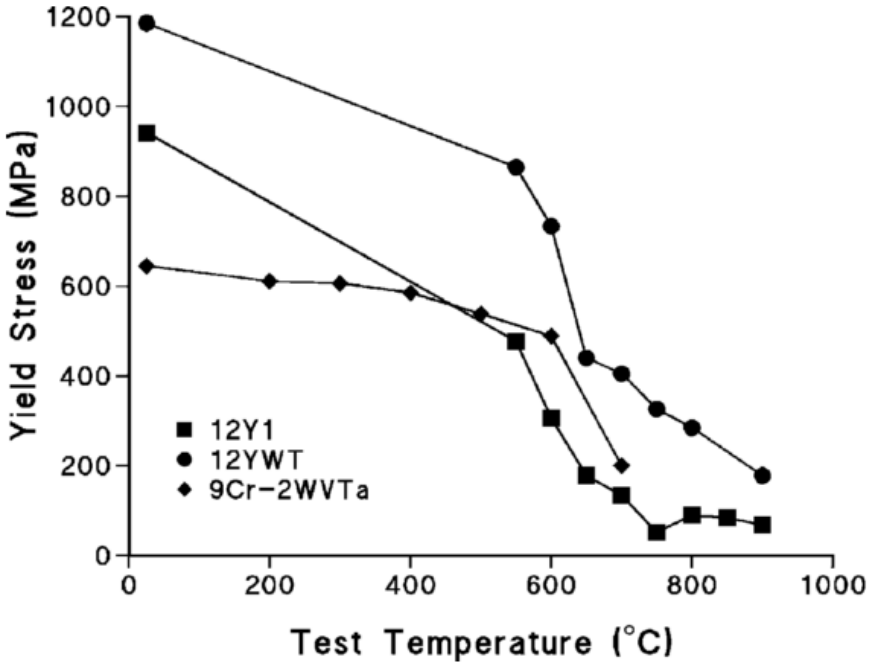


Figure 5.2: Comparison of experimental data for the yield stress of two RAFM ODS alloys (12Y1 and 12YWT) with a simular non-ODS alloy (9Cr-2WVTa) at a range of temperatures. The ODS alloys are extemely strong at room temperature, but exhibit significant softening at high temperatures. *From Klueh et al. (2005).*

The strengthening in ODS alloys has been attributed to Orowan strengthening (Alinger, 2004), but also to the grain size refinement (Klueh et al., 2005). This is consistent with the observation that different ODS-alloys with similar dispersion properties (oxide particle composition, size, number density), but which have been processed in different ways, can exhibit different yield strengths (Kasada et al., 2007). The high temperature softening mechanism is poorly understood.

ODS alloys also exhibit improved creep strength compared to their non-ODS counterparts (Klueh et al., 2002; Ukai and Fujiwara, 2002), as illustrated in the Larson–Miller parameter plot shown in figure 5.3 (since at a given temperature and stress, the logarithm of the creep life is larger — i.e. further to the right — for the ODS alloys than the non-ODS EUROFER 97).

Some examples of the high temperature creep life of ODS alloys are 9 and 29 hours at 650 °C for applied stresses of 200 and 160 MPa respectively in an ODS EUROFER 97

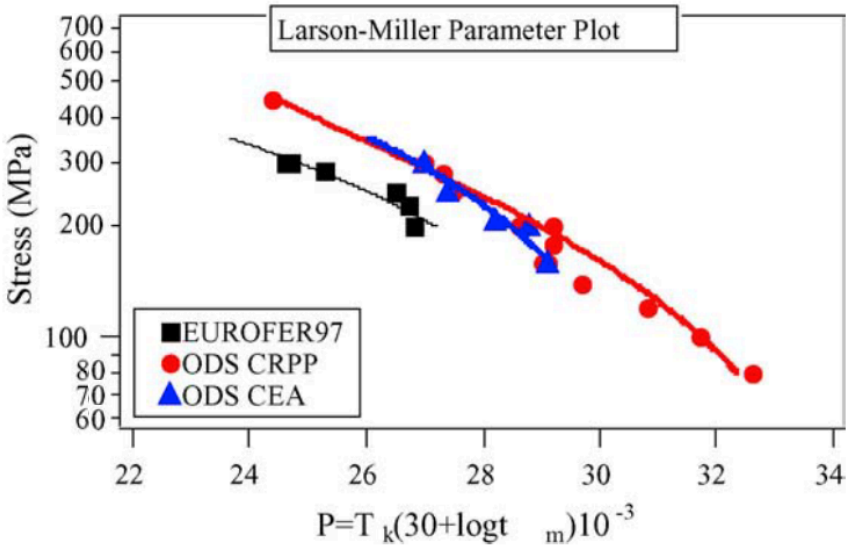


Figure 5.3: Larson–Miller parameter (P) plot (Larson and Miller, 1952) for non-ODS EUROFER 97, and two ODS EUROFER 97 alloys. In the formula for P given at the bottom of the figure, T_k is the temperature in Kelvin, and t_m is the creep life in hours. *From Yu et al. (2005).*

alloy (Yu et al., 2005), and 8–29 days[38] at 800 °C for an applied stress of 250 MPa in an ODS 14YWT alloy (Hayashi et al., 2008). This is an improvement on the 1 and 2 hour creep lifes observed in EUROFER 97 at 550 °C for applied stresses of 300 and 285 MPa respectively by Yu et al..

The high creep strength of ODS alloys has been attributed to Orowan strengthening, and the temperature and stress dependent creep response to the climb of dislocations at the oxide particles allowing them to overcome these obstacles (Yu et al., 2005). In order to investigate the mechanisms by which dislocations are able to overcome the oxide particles, in situ straining experiments can also be performed, in which dislocation-inclusion unpinning can be observed directly using high voltage TEM. By carrying out such experiments, Bartsch et al. (1999) and Wasilkowska et al. (2003) found a strong temperature dependence on which effects dominated the dislocation behaviour. Contrary to Yu et al., they asserted that "the importance of oxide dispersions becomes relevant at higher temperatures (above 900 °C)", but from 400 to 900 °C dislocation drag due to point defect and solute atmospheres might dominate the overall dislocation motion. Again, the physics behind the temperature and stress dependent creep be-

[38] Depending on the different annealing conditions prior to the creep test.

haviour of ODS alloys is poorly understood, with some disagreement in the literature.

In addition to their high strength and creep resistance, ODS steels exhibit resistance to neutron irradiation-induced microstructural changes, which is attributed to the oxide particles acting as sinks for the point defect supersatuations which arise as a result of the cascade damage (Akasaka et al., 2004; Zinkle and Snead, 2014), as well as gases such as hydrogen and helium (Kurtz et al., 2007; Hsiung et al., 2010). Williams et al. (2011) found that manganese segregation to dislocations in ODS EUROFER 97 after heavy ion irradiation is significantly reduced in regions of high oxide particle density compared to regions of high particle density. This suggests that under irradiation conditions the oxide particles can act as sinks for solute atoms such as manganese as well. Importantly, the oxide particles themselves remain very stable when irradiated, as the yttrium atoms are very insoluble in iron, and so any ballistic damage done to the particles quickly reverses itself (Certain et al., 2013; Ribis and Lozano-Perez, 2014).

Irradiation creep resistance after neutron irradiation which persists up to temperatures of 600 °C has been observed in ODS MA957 steel (Toloczko et al., 2012), but in situ heavy/self-ion irradiation creep data is lacking in the literature. Some in situ irradiation creep data is available for helium implantation in ODS steels, for example Chen and Hoffelner (2009). Over the temperature range of 300–500 °C they observed irradiation creep dominating over thermal creep, but interestingly no creep dependence on the size and distribution of the oxide dispersoids.

5.2.4 Computational modelling of dislocation-inclusion interactions

In this section various attempts to model dislocation-inclusion interactions are discussed.

Xiang and Srolovitz (2006) investigated the interaction between a single dislocation and a single particle when the dislocation is driven against the particle, particularly focusing on the role climb played in determining the mechanism by which the dislocation eventually bypasses the particle. Their model included the effects of dislocation-inclusion elastic interactions, glide, cross slip (via a simple isotropic screw dislocation mobility), and climb (via a linear climb mobility input parameter). Rather than DDD, they

used 3D level-set dislocation dynamics simulations, as described by Xiang et al. (2003). They observed some interesting qualitative behaviour, such as a pure screw dislocation wrapping round an impenetrable, misfitting particle several times to form a helical dislocation for the case of appreciable climb, as shown in figure 5.4.

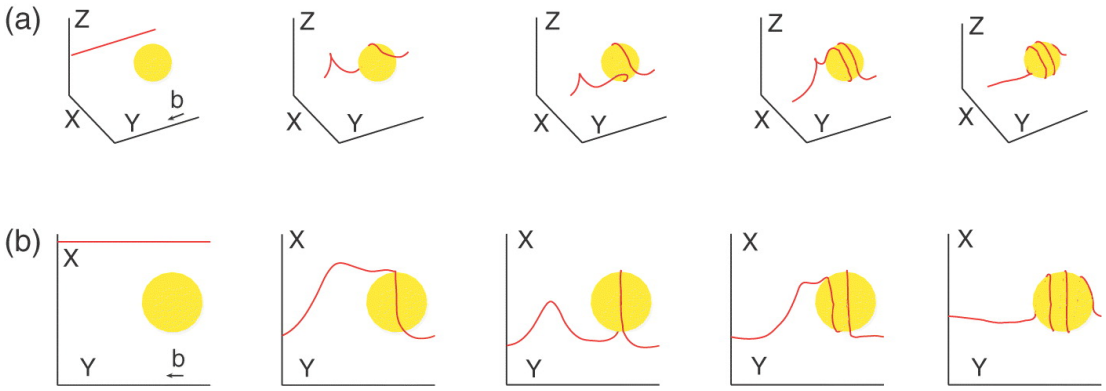


Figure 5.4: An initially pure screw dislocation driven against an impenetrable, misfitting particle with a small applied stress for the case of appreciable climb. The simulation box side length is 143 nm, and the particle radius is 29 nm. (a) 3D view. (b) View from above. *From Xiang and Srolovitz (2006).*

However, though their work provides insights into the conditions under which different particle bypass mechanisms operate, it does not provide quantitative information on the changes in the resultant strain rate due to a distribution of such particles under a range of conditions.

Khraishi et al. (2004) have simulated the interaction of gliding dislocations with inclusions which did not intersect the dislocations' glide planes, using DDD. Unlike Xiang and Srolovitz they considered a number of particles (up to 16), and because their simulations were initialised with a Frank–Read source above and offset from the particle(s), multiple dislocations were generated over the course of the simulations. Figure 5.5 shows the observed dislocation storage, in the form of pile-ups of dislocation loops above the particles, as part of the stress relief. In turn these pile-ups exert a back stress on upcoming gliding dislocations, resulting in an increase in the calculated flow stress — which was ∼20 MPa for the case of no particles present — of ∼5 MPa for 2 particles (on the left of the figure) and ∼15 MPa for 4 particles (on the right).

Khraishi et al. used their simulations of different numbers of particles to show a linear

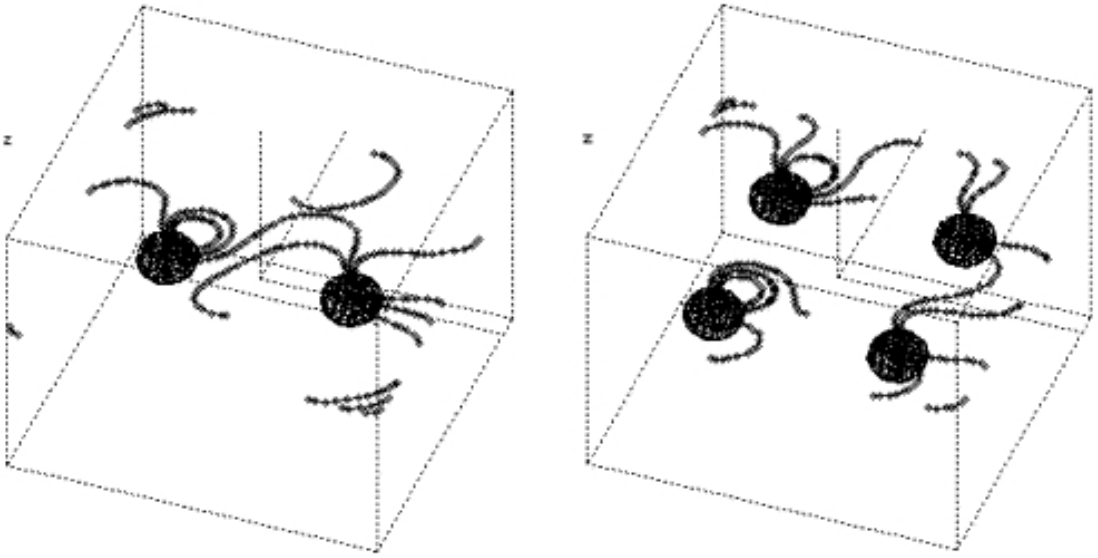


Figure 5.5: Time frames from two different simulations illustrating dislocation storage, in the form of dislocation pile-ups, in the source's glide plane above the particle. The simulation box side length is 2.86 μm, and the particle radii are 229 nm. *From Khraishi et al. (2004).*

increase in the flow stress of 4.6–16.6 MPa with increasing particle volume fraction of ∼0.2–0.8%, which they compared to typical experiment results of 5 MPa. The flow stress was also seen to be sensitive to other microstructural features, such increasing linearly with the particle radius, and decreasing linearly before leveling off with distance between the dislocations' glide plane and the particles. However, these simulations neglected climb, so these results are less insightful when considering higher temperature situations.

DDD simulations of an entire grain containing both oxide particles and irradiation loops were carried out by Gururaj and Robertson (2011). Their model included a thermally activated cross slip mechanism, but no climb. The details of how the irradiation loops and oxide particles were represented are unclear. In the cases of irradiation only and an oxide dispersion only, strain localisation and hardening compared to the pure ferritic matrix were observed. A bimodal distribution of irradiation loops and oxide particles reduced this effect. They concluded that their results are consistant with the reported evidence that ODS alloys can be more resistant to post-irradiation loss of ductility than their non-ODS counterparts.

Bakó et al. (2007) carried out 3D DDD simulations of Y_2O_3 dispersoids in bcc single

crystal PM2000, a commerical alloy, using the code developed by Weygand et al. (2001). The dispersoid distribution they used was derived from experimental TEM observations of PM2000, allowing for better comparison between their simulations and the experimental data. They implemented a phenomenological repulsive force profile due to the immobile impenetrable obstacles which acted against the resolved shear stresses due to the externally applied stress field. This force profile was given by:

$$f(\mathbf{r}) = \sum_{i=0}^{N_d} \frac{1}{1 + \exp[(|\mathbf{r}_i - \mathbf{r}| - 0.995R_i)^2]}, \tag{5.6}$$

where $N_d \sim 10^4$ is the number of dispersoids, $\mathbf{r}$ is the position of the centre of the dislocation segment, and R_i and $\mathbf{r}_i$ are the radius and position of the centre of dispersoid i respectively. Their simulations were initialised with an initially straight pure screw dislocation, and a linear mobility law

$$M(\theta) = M_\mathrm{s} \cos^2\theta + M_\mathrm{e} \sin^2\theta, \tag{5.7}$$

was used for glide as usual. Here M_s and M_e are the mobilities for pure screw and pure edge dislocation segments respectively, and θ describes the dislocation character and is defined as the angle between Burgers vector and the line direction of the segments. The values used for M_s and M_e are not discussed, and cross slip and climb appear to have been neglected. Bakó et al. observed Orowan loop formation, as shown in figure 5.6.

The CRSS of 240 MPa they calculate was found to be only slightly lower than the experimentally determined value of 246 MPa, and they conclude that this implies the dispersoids are the main source of hardening.

5.3 Concluding remarks

The 3D modelling of dislocation motion in the presence of obstacles found in the literature has concentrated on predicting the strengthening effect of these obstacles, and shows some promising consistency with experimental measurements. However, these investigations have necessarily focussed on accurately capturing dislocation glide, and

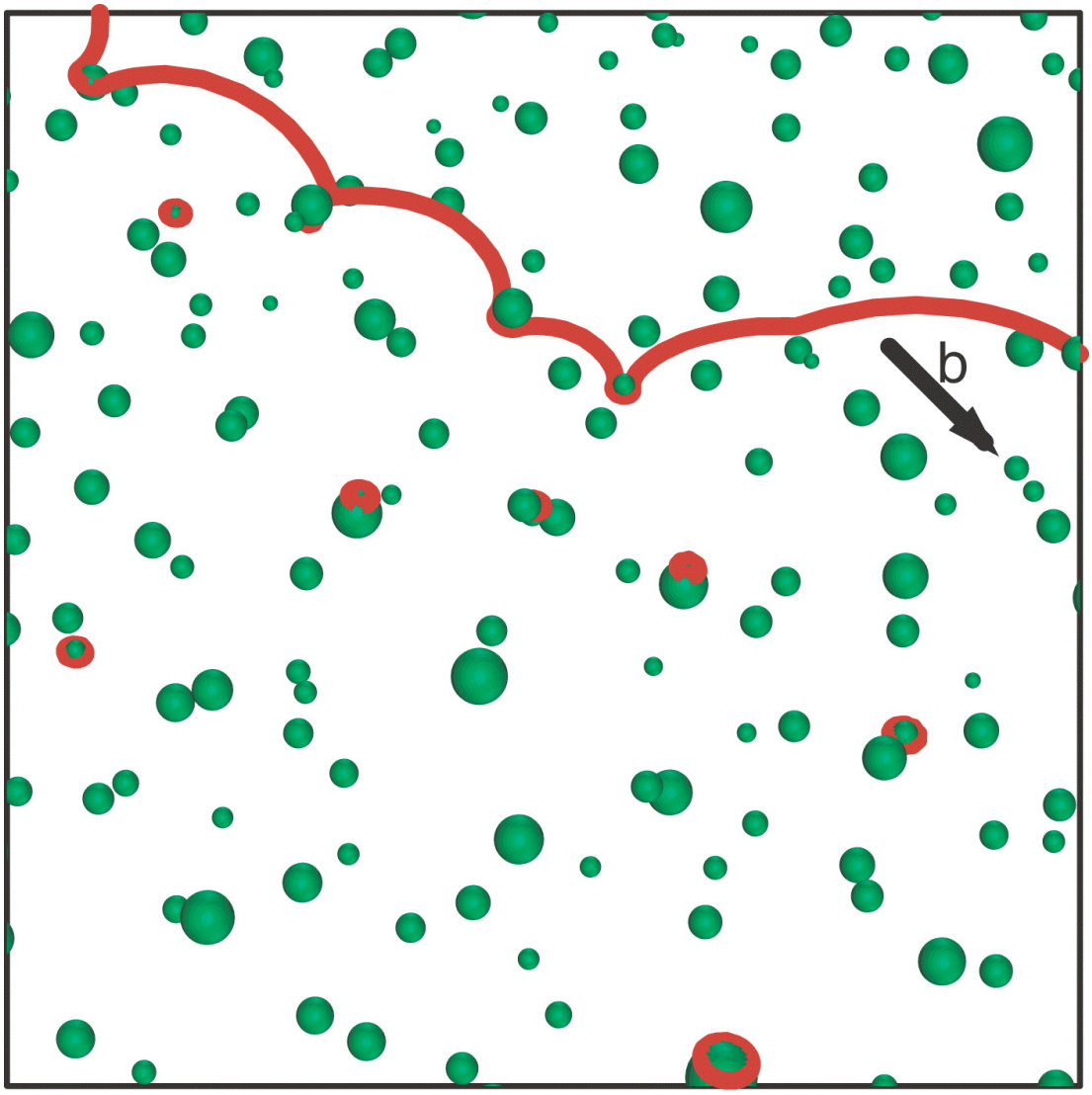


Figure 5.6: Orowan loop formation, and a typical pinned dislocation line, when the external stress is just slightly less than the critical value for the given random configuration. The simulation box dimensions are $3 \times 6 \times 3$ μm^3. *From Bakó et al. (2007).*

very little progress seems to have been made towards quantitatively capturing dislocation climb, and hence predicting the creep response of particle-reinforced alloys. Irradiation effects have also been neglected.

In chapter 7, the results of such simulations of dislocation climb over obstacles are presented and discussed. A quantitative comparison with the experimental data on the thermal creep of ODS ferrous alloys is made, and predictions are made regarding the performance of these alloys under fusion reactor relevant irradiation conditions.

First, however, chapter 6 describes the implementation and testing of the three-dimensional obstacles which are impenetrable to dislocations required for such simulations in `DDLab`.

Chapter 6

Code development and testing: inclusions

6.1 Introduction

In order to use `DDLab` to computationally model dislocation-obstacle unpinning in particle-reinforced ferrous alloys at the high operating temperatures — and under the irradiation conditions — of a fusion reactor, the capability of representing such inclusions needs to be implemented into the `DDLab` code.

In this chapter, the details of incorporating impenetrable spherical inclusions into the dual time step method described in chapter 4 are discussed, and the implementation of these inclusions is tested using a number of simple demonstrative simulations. These involve gliding dislocations in the form of a shear dislocation loop in the presence of a single impenetrable inclusion.

6.2 Impenetrable inclusions

Impenetrable inclusions are chosen because they offer a straightforward approach to capturing the pinning (i.e. blocking), and subsequent bowing out, of gliding dislocations at such obstacles, as well as the potential unpinning of these dislocations by climbing over the inclusions. In this work the inclusions considered are not misfitting, and so do not produce stress fields which interact with the gliding dislocations. However, misfit stresses could be added to these impenetrable inclusions using the expressions given in (5.4).

After some unsuccessful attempts at incorporating a spherical impenetrable inclusion into the dual time step method in `DDLab` (see § 6.2.1), the following scheme was devised:

- Glide only steps:
    1. The forces on the dislocation nodes are evaluated in the usual manner.
    2. The components of the nodal forces in the climb direction are all set to zero. Components due to pure screw segments are unaffected.
    3. The nodal velocities are then computed for these glide only nodal forces.
    4. A check is performed: if the distance between a dislocation node and the centre of an inclusion is less than the capture radius for that inclusion — defined by the sum of the inclusion's radius r_i and the dislocation core radius r_c — then the component of the node's velocity in the glide direction is set to zero.
    5. The positions of all the nodes are updated by numerically integrating their equations of motion in the usual manner. The glide pinned nodes are unable to move, and remain pinned during the following glide steps.
- Climb only steps:
    1. The forces on the dislocation nodes are evaluated in the usual manner.
    2. The components of the nodal forces in the glide direction are all set to zero, with the exception of components due to pure screw segments.

3. The nodal velocities are then computed for these climb (and screw glide) only nodal forces.

4. A different check to the one used for glide only steps is performed: if the distance between a dislocation node and the centre of an inclusion is below the capture radius for that inclusion, then the predicted position of the node is evaluted, and if the new distance between the node and the inclusions centre would be less than r_{i}, then the node's velocity is set to zero in order to prevent it from penetrating the inclusion in this way.

5. The positions of all the nodes are updated by numerical integration. The climb pinned nodes are unable to move, and remain pinned for the subsequent duration of the simulation.

6.2.1 Implementing spherical impenetrable inclusions

In the first attempt to implement a spherical impenetrable inclusion, the `drndt` function was developed to perform the glide step check described in § 6.2 — whether the distance between a dislocation node and the centre of an inclusion is less than the capture radius for that inclusion — and if this condition is met, to set that node's velocity to zero. In the climb only steps all the nodal velocities, even those of nodes which are within an inclusion's capture radius, were left unaltered. This method was unsuccessful, as during the climb only steps the dislocations were able to penetrate the inclusions in some dislocation-inclusion arrangements, either by climbing up/down into them, or by the small amounts of glide which still occurred during the climb only steps. To remedy this, it was clear that the new code which captures the impenetrable inclusions would require access to the climb and glide directions of the individual segments.

In the second attempt, the `mobbcc0` and `mobbcc0Int` functions were developed to remove *all* climb motion in the glide only steps, and *all* (non-screw) glide motion in the climb only steps. Altering the nodal velocities after they had been evaluted within the mobility functions was tried, but this was unsuccessful, as the glide pinned dislocation nodes would become fully pinned, i.e. permanently stuck, due to subtleties in

DDLab's implementation. Finally, the scheme described in § 6.2, in which the nodal forces are altered *before* they are used to evaluate the nodal velocities, was formulated and implemented successfully in the `mobbcc0` and `mobbcc0Int` functions.

In what follows, simple test simulations of a shear dislocation loop shrinking via glide and becoming pinned on a single impenetrable inclusion are used to test this implementation in DDLab. To begin with, however, the behaviour of a shear loop in isolation is briefly discussed.

6.2.2 Isolated shear dislocation loop behaviour

Figures 6.1(a) and (b) show the initial configuration of the circular, pure shear loop used in these test simulations. The view is down the $[1\bar{1}1]$ direction in figure (a), and down the [001] direction in figure (b). The loop is centred on the origin, lies in the (001) plane, has a radius of $18a$ (5.2 nm for bcc iron), and has a clockwise line-sense about the [001] direction — hence its Burgers vector is [100]. This Burgers vector is chosen for the mobile dislocations (captured here by the shear loop) instead of the usual $\frac{1}{2}\langle 111\rangle$ Burgers vectors found in bcc iron in order to emulate the high temperature dislocation population, in which [100] dislocations are expected to dominate due to their lower energies at higher temperatures (see § 2.3.11, and Fitzgerald and Dudarev (2009)). However, as the bcc mobility law model used by DDLab does not take different slip systems into account, the only differences between choosing to simulate mobile dislocations with $\langle 100\rangle$ and $\frac{1}{2}\langle 111\rangle$ Burgers vectors amount to geometric factors of the order of unity.

With no applied load present, this loop is expected to shrink and disappear via pure glide motion due to its own stress field. The edge and screw drag factors are assumed to be equal, and set to 4×10^{-4} Pa·s, as in § 4.5.2. Hence the shrink time should be roughly of the order of picoseconds. The minimum and maximum dislocation segment lengths ℓ_{min} and ℓ_{max} are set to their optimal values of $4a$ and $8a$ respectively, as was the case in the test simulations in § 4.3.12.

Figures (c) and (d) show a snapshot of this loop shrinking, after 0.792 ps of simulated

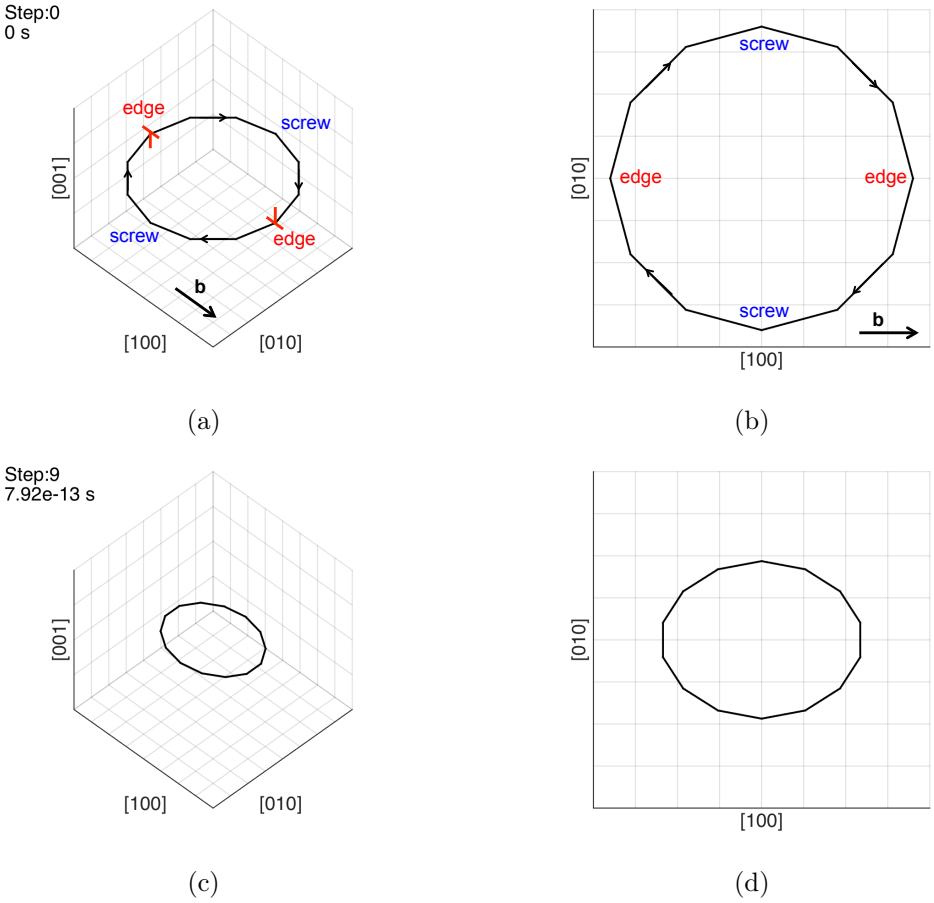


Figure 6.1: A pure shear loop of radius $18a$ (5.2 nm) shrinking due to its self-force via glide. The figures on the left are viewed down the $[1\bar{1}1]$ direction, and those on the right down the [001] direction. The intermediate elliptical shape seen is due to the slightly different forces on the edge and screw segments. The loop takes 1.18 ps to shrink completely.

time has elapsed. The intermediate elliptical shape seen is due to the slightly different forces on the edge and screw parts of the shear loop leading to slightly different glide velocities. The loop takes 1.18 ps of simulated time to shrink and disappear entirely — the expected order of magnitude.

6.2.3 Dislocation-inclusion test simulation: no applied load

An impenetrable inclusion with a radius of $8a$ (2.3 nm) is now placed at the origin, so that it lies concentric with the encircling shear dislocation loop. This set up is shown in figure 6.2. In these test simulations the minimum strain ratio for glide-to-climb switching η (see § 4.5) is set to 10^{-3} — the optimal value discussed in § 4.5.4 — and the dislocation core radius r_c, which is used in the dislocation-inclusion pinning checks, to $2a$.

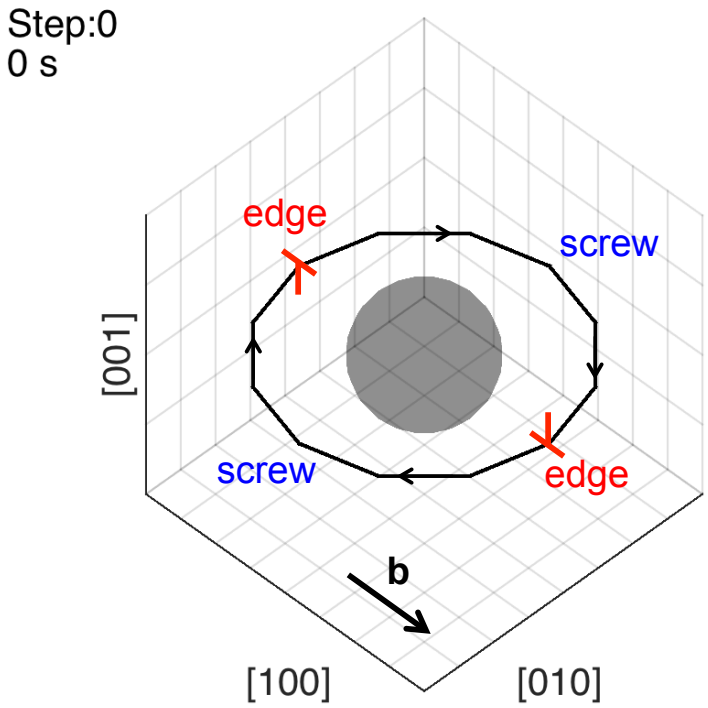


Figure 6.2: The dislocation-inclusion test simulation set up. The cubic simulation box has side length $40a$ (11 nm). The impenetrable inclusion of radius $8a$ (2.3 nm) lies concentric with the encircling shear dislocation loop from figures 6.1(a) and (b).

In the absence of an applied load (and with no defect supersaturations present), the loop shrinks due to its self-force as before, but becomes fully glide pinned after 1.03 ps, as shown in figure 6.3(a). During the following climb steps the loop does not undergo any further motion, as there are no out of plane forces on the dislocations (the self-force of the loop acting to shrink it lies entirely in the plane of the loop). This final pinned

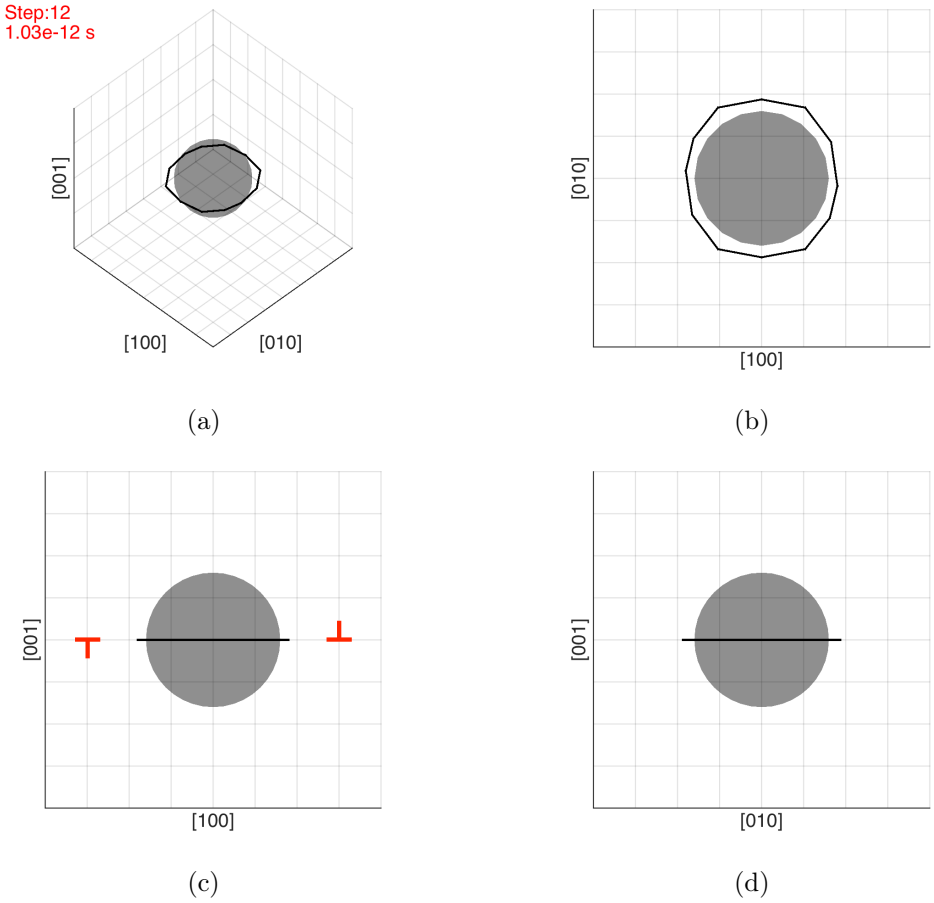


Figure 6.3: The glide pinned configuration after 1.03 ps of simulated time, viewed from multiple angles. The cubic simulation box has side length $40a$ (11 nm).

configuration is viewed down the [001] axis in figure (b), the $[0\bar{1}0]$ axis in figure (c), and the [100] axis in figure (d). The dislocation nodes have become pinned because they are within the capture radius $r_\mathrm{i} + r_\mathrm{c}$ of the centre of the inclusion, and they have not been able to penetrate into it, as can clearly be seen in figure (b).

6.2.4 Dislocation-inclusion test simulation: applied shear load

In this simulation, a constant σ_{12} shear load of 410 MPa (which corresponds to $\mu/200$) is applied to the simulation box. This results in an out of plane force in the [001] direction which acts on the screw part of the dislocation segments, as (6.1) shows. This force acts in opposite directions for dislocation segments whose screw parts are of opposite sign.

$$\mathbf{F} = (\boldsymbol{\sigma} \cdot \mathbf{b}) \times \boldsymbol{\xi} = \left[\begin{pmatrix} 0 & \sigma_{12} & 0 \\ \sigma_{12} & 0 & 0 \\ 0 & 0 & 0 \end{pmatrix} \cdot \begin{pmatrix} b \\ 0 \\ 0 \end{pmatrix} \right] \times \begin{pmatrix} \xi_\mathrm{s} \\ \xi_\mathrm{e} \\ 0 \end{pmatrix} = \begin{pmatrix} 0 \\ \sigma_{12} b \\ 0 \end{pmatrix} \times \begin{pmatrix} \xi_\mathrm{s} \\ \xi_\mathrm{e} \\ 0 \end{pmatrix} = \begin{pmatrix} 0 \\ 0 \\ -\sigma_{12} b \xi_\mathrm{s} \end{pmatrix} \tag{6.1}$$

During the simulation, the dislocations become glide pinned as before, and then they start to undergo thermal climb out of their glide plane. This is shown after 1.86 s of simulated time in figure 6.4(a) looking down the usual $[1\bar{1}1]$ direction, and in figures (b)–(d) from three different angles as was done previously in figure 6.3. The near-screw segments on the far side of the inclusion in figure (a) have climbed in the [001] direction due to the applied σ_{12} shear load, whereas the near-screw segments on the near side of the inclusion have climbed in the $[00\bar{1}]$ direction, as is expected from their opposite signs.

Note that although these segments are close to screw, and screw parts are able to cross slip out of the current glide plane, the fact that they are near-screw, i.e. mixed dislocations, means that some climb is required for out of plane motion. As this climb rate is much slower than that of glide (in a cross slip direction), it is the climb rate that governs the overall motion.

The dislocation configuration shown in figure 6.4 is actually the stable, final configuration, i.e. the dislocations climb no further than they already have in the figure. This is because as the near-screws segments climb up/down out of the glide plane, the loop elongates in the [001] direction (figure (d)), resulting in a net tilt of the plane of the loop. The screw parts of the dislocation segments have all moved either up or down out of the glide plane by roughly the same amount, as indicated by figure (c). This is contrary to the edge parts in figure (d), which steadily tilt in order to accommodate the

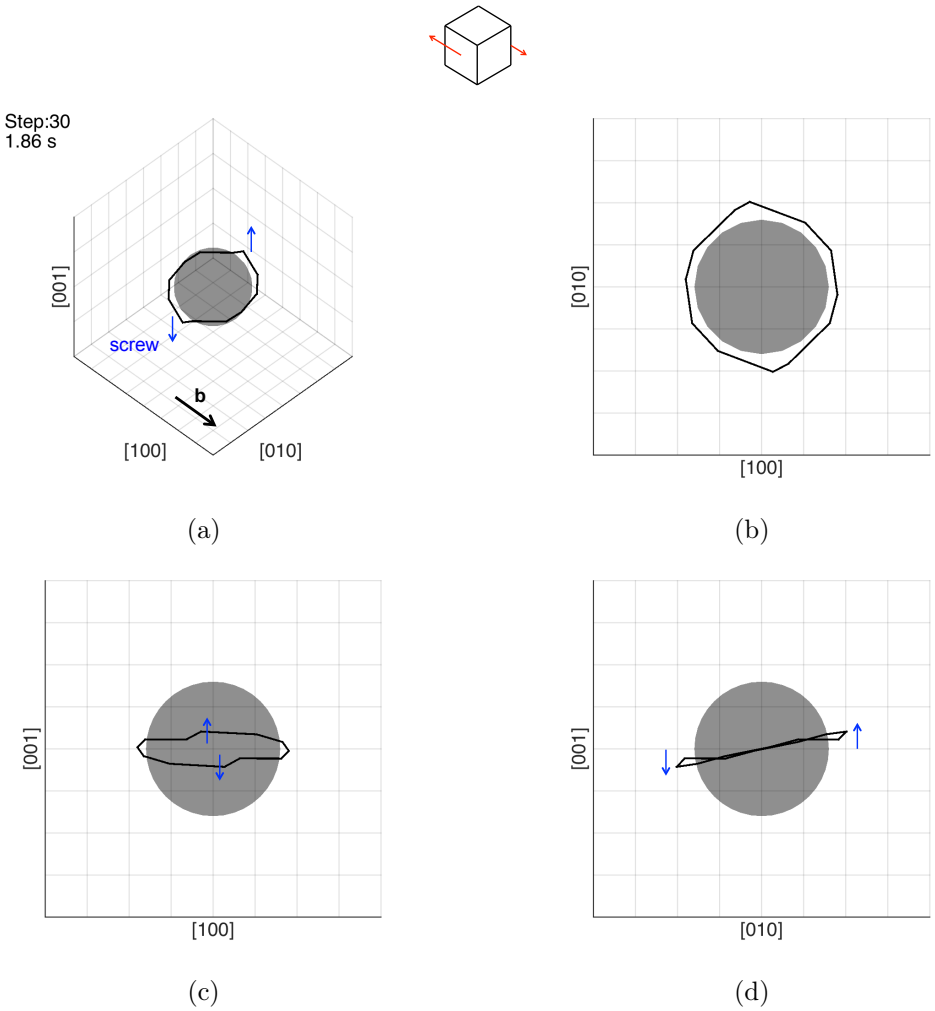


Figure 6.4: The stable configuration reached during applied σ_{12} shear loading of 410 MPa. After 1.86 s of simulated time the out of plane forces due to this applied load are balanced by the restoring force due to the self-force of the tilted loop. The temperature is once again set to 700 °C. The cubic simulation box has side length $40a$ (11 nm).

out of plane motion of the screw parts. One way of thinking of this is as deformation of the loop along its "climb cylinder", but again bearing in mind that in between the climb only steps glide can occur, which effectively changes the radius of this climb cylinder. The self-force of the tilted loop now has a component in the climb directions, acting to drive the loop back down/up onto the original habit plane. Eventually, this restoring force balances the out of plane forces caused by the applied load, resulting in the stable configuration shown in figure 6.4.

This stable configuration is reached after 1.86 s of simulated time. As the temperature is once again set to 700 °C, this seems reasonable as it is the same order of magnitude

as the simulated time in the test simulations which involved thermal climb processes conducted in chapter 4.

6.2.5 Dislocation-inclusion test simulation: applied compressive load

Instead of an applied σ_{12} shear load, a σ_{11} compressive load of 820 MPa is now applied. This also results in an out of plane force in the [001] direction, but this time it acts on the edge part of the dislocation segments, as (6.2) shows. Similarly to before, this force acts in opposite directions for dislocation segments whose edge parts are of opposite sign.

$$\mathbf{F}^{\mathrm{PK}} = (\boldsymbol{\sigma} \cdot \mathbf{b}) \times \boldsymbol{\xi} = \left[\begin{pmatrix} \sigma_{11} & 0 & 0 \\ 0 & 0 & 0 \\ 0 & 0 & 0 \end{pmatrix} \cdot \begin{pmatrix} b \\ 0 \\ 0 \end{pmatrix} \right] \times \begin{pmatrix} \xi_{\mathrm{s}} \\ \xi_{\mathrm{e}} \\ 0 \end{pmatrix} = \begin{pmatrix} \sigma_{11} b \\ 0 \\ 0 \end{pmatrix} \times \begin{pmatrix} \xi_{\mathrm{s}} \\ \xi_{\mathrm{e}} \\ 0 \end{pmatrix} = \begin{pmatrix} 0 \\ 0 \\ \sigma_{11} b \xi_{\mathrm{e}} \end{pmatrix} \tag{6.2}$$

After the dislocations become glide pinned as before, the applied σ_{11} compressive load drives the near-edge components, rather than the near-screw ones, to undergo thermal climb out of their glide plane. This is shown after 1.5 s of simulated time in figure 6.5. The near-edge segments on the near side of the inclusion in figure (a) have climbed in the [001] direction due to the applied σ_{11} compressive load, whereas the near-edge segments on the far side of the inclusion have climbed in the $[00\bar{1}]$ direction, as is expected from their opposite signs.

The dislocation configuration shown in figure 6.5 is also the stable, final configuration. The edge parts of the dislocation segments have moved either up or down out of the glide plane by smoothly varying amounts, as seen in figure (d). This is similar to the screw parts in figure (c), which exhibit some steady tilting in order to accommodate the out of plane motion of the edge parts, but also some net out of plane motion. An explanation for this compound out of plane motion could be that after the initial climb of the edge parts, the resulting restoring force due to the loop's self-force has a σ_{12} shear component, which produces some out of plane motion of the screw parts.

Nevertheless, a stable configuration is still reached after 1.5 s of simulated time, which

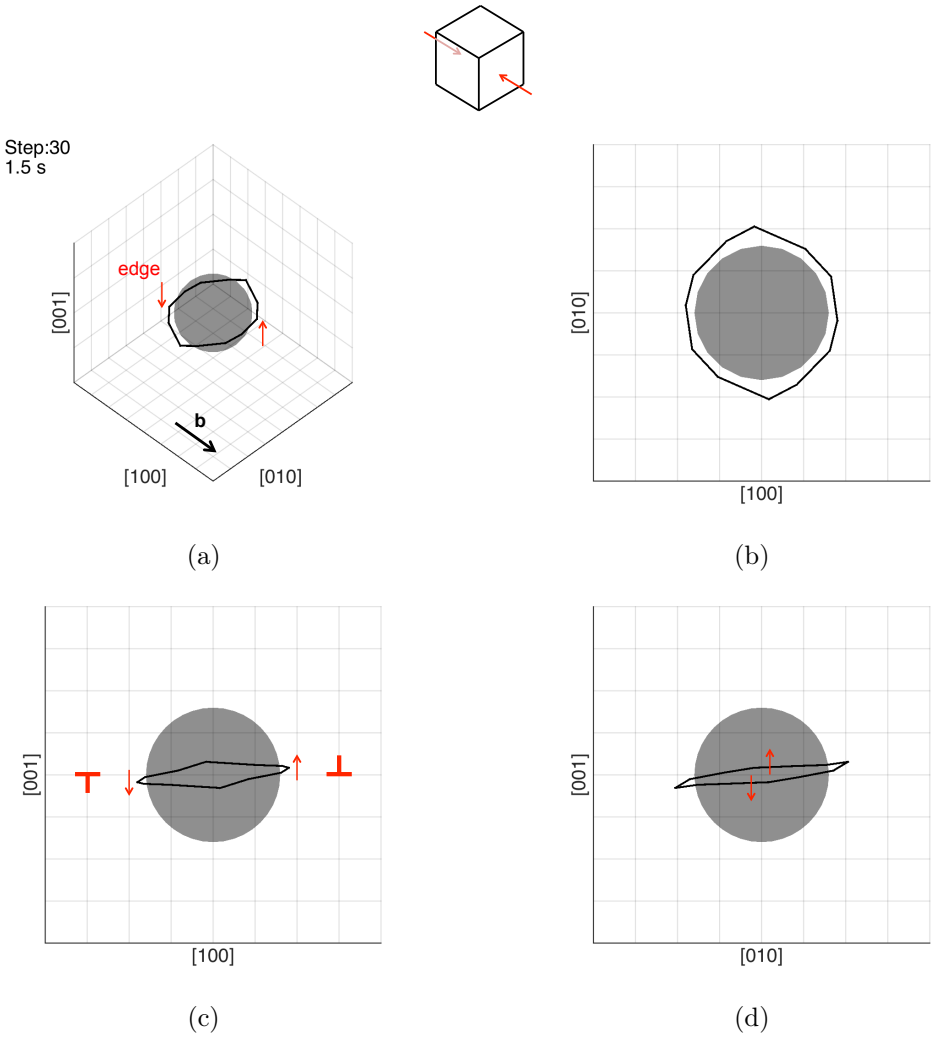


Figure 6.5: The stable configuration reached during applied σ_{11} compressive loading of 820 MPa. After 1.5 s of simulated time the out of plane forces due to this applied load are balanced by the restoring force due to the self-force of the tilted loop. The temperature is set to 700 °C. The cubic simulation box has side length $40a$ (11 nm).

again seems reasonable for the temperature of 700 °C, as the thermal vacancy mediated shrinkage of the nanoscale prismatic loop simulated in § 4.3.2 took ∼1 s at this temperature.

6.2.6 Dislocation-inclusion test simulation: defect supersaturations present

The last test simulation, in which there is no applied load, but there are equal vacancy and interstitial supersaturations of 10^{-9} defects (fractional atomic concentration) present in the simulation box, is shown in figure 6.6. These defect supersaturations result in out of plane osmotic forces in the [001] direction, which act on the edge part of the dislocation segments. Again, these forces act in opposite directions for dislocation segments whose edge parts are of opposite sign.

After the dislocations become glide pinned as before, the osmotic forces drive the near-edge components to undergo osmotic climb out of their glide plane. The resulting stable configuration is shown after 1.22 s of simulated time in figure 6.6. The near-edge segments on opposite sides of the inclusion in figure (a) have climbed up/down in the [001] direction, as they did in the case of an applied σ_{11} compressive load, but with the directions of climb reversed. Thus an overall tensile strain is produced, rather than a compressive one as was the case previously.

Futhermore, the climb is more pronounced, as can clearly be seen in figures (c) and (d). This indicates that the defect supersaturations of 10^{-9} defects induce a stronger osmotic climb response than the thermal climb response due to an applied σ_{11} compressive load of 820 MPa.

The edge parts of the dislocation segments have all moved either up or down out of the glide plane by roughly the same amount, as indicated by figure (d). This is contrary to the screw parts in figure (c), which tilt fairly steadily in order to accommodate the out of plane motion of the edge parts. A slight variation in the amounts of screw motion is seen, as was the case previously (indicated by the slight offset between the front and back screw segments in figure (c)), but the large amounts of osmotic climb dominate.

The stable, final configuration is shown after 1.22 s of simulated time. However, a relatively stable configuration — at which the restoring force due to the loop's self-force balances the osmotic forces — is reached after much less time ($\sim$0.01 s), as is expected for osmotic climb due to 10^{-9} defects at 700 °C from the prismatic loop shrink time

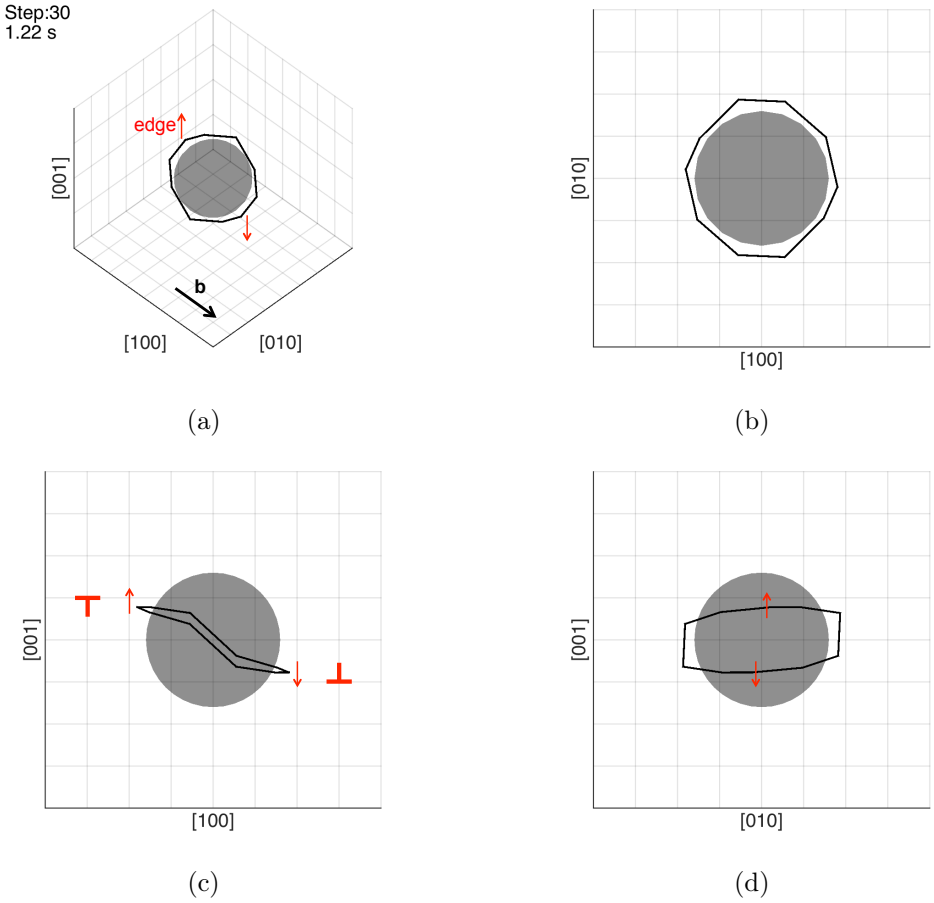


Figure 6.6: The stable configuration reached under no applied load, but with defect supersaturations of 10^{-9} defects present. After ∼0.01 s of simulated time the out of plane forces due to the defect supersaturations are balanced by the restoring force due to the self-force of the tilted loop (this is not shown). Subsequently, thermal climb up 1.22 s, as a result of the tilted loop's self-force, takes place. The temperature is set to 700 °C. The cubic simulation box has side length $40a$ (11 nm).

of 0.00986 s under these conditions in table 4.2. The subsequent dislocation motion to simulated time ∼1 s is attributed to thermal climb due to the σ_{11} compressive stress component of the loop's self-force produced by the loop's tilt after the osmotic climb has taken place.

6.3 Concluding remarks

The spherical impenetrable inclusion developed and tested in this chapter appears to capture the blocking of mobile dislocations by the obstacle successfully, together with

the subsequent climb of these dislocations in the obstacle's vicinity. In chapter 7, simulations involving four of these obstacles are peformed, in order to capture the climb over — and subsequent glide away from — these inclusions, and investigate the various factors which affect this unpinning behaviour.

Chapter 7

Dislocation-inclusion simulation results

7.1 Introduction

In this chapter, the results of simulations of dislocation-inclusion unpinning from impenetrable obstacles are presented and discussed.

In § 7.2 the initial setup of the simulations is described, and the three types of unpinning simulation which are conducted are discussed in detail. The effects of varying the temperature, applied load, obstacle size, and defect supersaturation on the simulated dislocation-inclusion unpinning time are then analysed and discussed in § 7.3. A simple model for estimating the creep strain rate from the simulated dislocation-inclusion unpinning time data is described in § 7.4, and this is applied to the data in § 7.5. In addition to temperature, applied load and defect supersaturation, the effects of varying obstacle size, number density and volume fraction parametrically with each other are investigated using the strain rate estimation. The results are compared to some experimental data on the thermal creep of RAFM ODS alloys, and predictions are made regarding the creep response of these alloys under fusion reactor relevant irradiation conditions.

7.2 Simulation setup and demonstrative behaviour

7.2.1 Simulation setup

The initial simulation setup is shown in figure 7.1. The cubic simulation box has size length of $130a$ (37 nm), although the box boundary conditions are simply that of in an infinite medium. A shear dislocation loop of radius $64a$ (18 nm) with a Burgers vector in the [100] direction is placed with its centre at the origin. The habit plane of the loop, which is also its glide plane, is the (001) plane. Hence the climb direction is [001]. The initial dislocation density in the box ρ is 2.2×10^{15} m^{-2}.

The simulation box also contains four impenetrable spherical inclusions, each with a radius of $8a$ (2.3 nm), which are encircled by the shear dislocation loop. Their centres are arranged in a square of side length 24 nm lying in the same (001) plane as the dislocation loop. The 24 nm side length of the square of inclusions corresponds to the

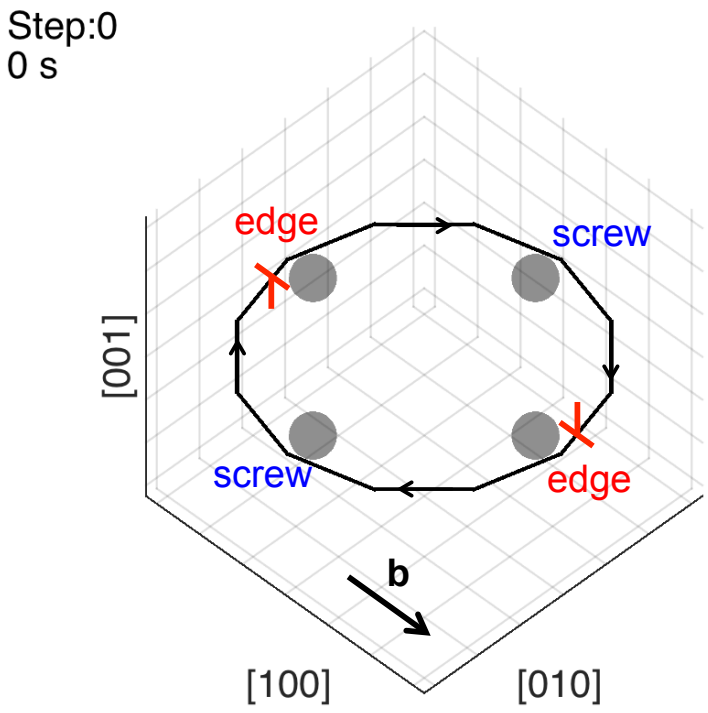


Figure 7.1: The initial simulation setup, viewed down the $[1\bar{1}1]$ direction. The cubic simulation box has size length of $130a$ (37 nm).

effective obstacle separation on this 2D plane L_{eff} (see § 5.2.1). An expression which relates the obstacle radius and the 3D obstacle number density to L_{eff} is found in § 7.4. Using this expression, given by (7.7), the inclusion number density captured by the simulation can be estimated using the value of L_{eff} and the inclusion radius: it comes to 3.7×10^{23} m^{-3}. Hence the inclusion volume fraction is 1.9%, and the corresponding yttrium weight percentage (wt%) for a matrix of pure iron with inclusions composed entirely of pure Y_2O_3 would be 0.94%[39].

This initial configuration is chosen in order to examine the dislocation-inclusion interaction between four such pairs in each simulation: two involving a near-edge dislocation and two involving a near-screw dislocation, as illustrated in figure 7.1. The self-force of the loop acts to shrink it, providing the force to drive the dislocations against the impenetrable inclusions in the absence of any applied load or osmotic forces due to a defect supersaturation.

The full dislocation climb velocity for climb mediated by both vacancies and interstitials — and the osmotic climb due to supersaturations of these defects — derived in chapter 3 is used in these simulations. The edge and screw glide drag factors are assumed to be equal, and set to 4×10^{-4} Pa·s. The temperature is set to 700 °C, unless otherwise stated.

Figure 7.2(a) shows the dislocation configuration after 101 simulation steps, with no applied load or defect supersaturation present. The dislocations have been driven against the inclusions and bowed around them. At this point the dislocation network has become glide pinned — the minimum strain ratio η is again set to 10^{-3}. This pinning takes 17.1 ps of simulated time. There are no out of plane forces, as the self-force of the loop acting to shrink it is in the (001) plane only, and hence there is no subsequent climb motion. In other words, the dislocation network has become fully pinned. Figures 7.2(b)–(d) show this glide-pinned configuration from a further three different

[39]The yttrium wt% is calculated from the inclusion volume fraction V_{frac} using the expression

$$\text{Y wt\% } (V_{\text{frac}}) = \frac{2A(\text{Y})}{2A(\text{Y}) + 3A(\text{O})} \times \frac{\rho(\text{Y}_2\text{O}_3)V_{\text{frac}}}{\rho(\text{Fe})(1 - V_{\text{frac}}) + \rho(\text{Y}_2\text{O}_3)V_{\text{frac}}}, \tag{7.1}$$

where A is the relative atomic mass, and ρ is the density, of the element/material in parenthesis. The values used for the calculation are $A(\text{Y}) = 89$, $A(\text{O}) = 16$, $\rho(\text{Y}_2\text{O}_3) = 5.010$ g/cm^3, and $\rho(\text{Fe}) = 7.874$ g/cm^3.

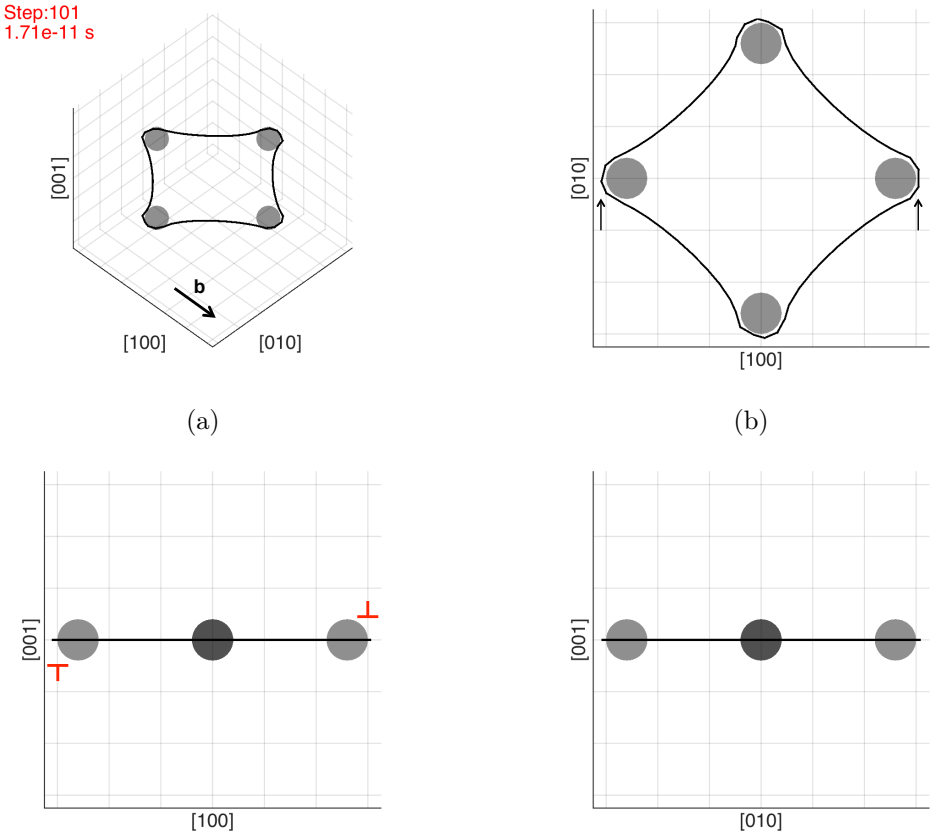


Figure 7.2: The glide pinned dislocation network after 17.1 ps of simulated time, under zero applied load, viewed from several different angles. The black arrows in (b) indicate discretisation asymmetry.

angles.

7.2.2 Effect of applied σ_{13} shear load on pinning time

When a non-zero σ_{13} shear load is applied to the initial configuration, the subsequent glide motion is affected by the resulting in plane forces, but there are still no out of plane forces in the [001] direction (and hence there is no climb), as (7.2) shows.

$$\mathbf{F} = (\boldsymbol{\sigma} \cdot \mathbf{b}) \times \boldsymbol{\xi} = \left[\begin{pmatrix} 0 & 0 & \sigma_{13} \\ 0 & 0 & 0 \\ \sigma_{13} & 0 & 0 \end{pmatrix} \cdot \begin{pmatrix} b \\ 0 \\ 0 \end{pmatrix} \right] \times \begin{pmatrix} \xi_{\mathrm{s}} \\ \xi_{\mathrm{e}} \\ 0 \end{pmatrix} = \begin{pmatrix} 0 \\ 0 \\ \sigma_{13} b \end{pmatrix} \times \begin{pmatrix} \xi_{\mathrm{s}} \\ \xi_{\mathrm{e}} \\ 0 \end{pmatrix} = \begin{pmatrix} -\sigma_{13} b \xi_{\mathrm{e}} \\ \sigma_{13} b \xi_{\mathrm{s}} \\ 0 \end{pmatrix} \tag{7.2}$$

The variation in the glide pinning time as a function of applied σ_{13} shear load is shown in figure 7.3. There appears to be a negligible trend in the data given the spread in the values. This spread is due to subtle differences in the discretisation of the initial dislocation loop, which in turn depends on the choice of the maximum dislocation segment length $\ell_{\max}$. A clear example of this discretisation asymmetry can be seen when comparing the near-edge dislocations (indicated by the black arrows) in figure 7.2(b). The simulations using $\sigma_{13} = 82$, 328 and 410 MPa were performed again using values of $\ell_{\max}$ other than $8a$ to investigate this sensitivity to the discretisation. The additional data points do not have a significant effect on the average glide pinning time of 17.8 ps calculated from the $\ell_{\max} = 8a$ results.

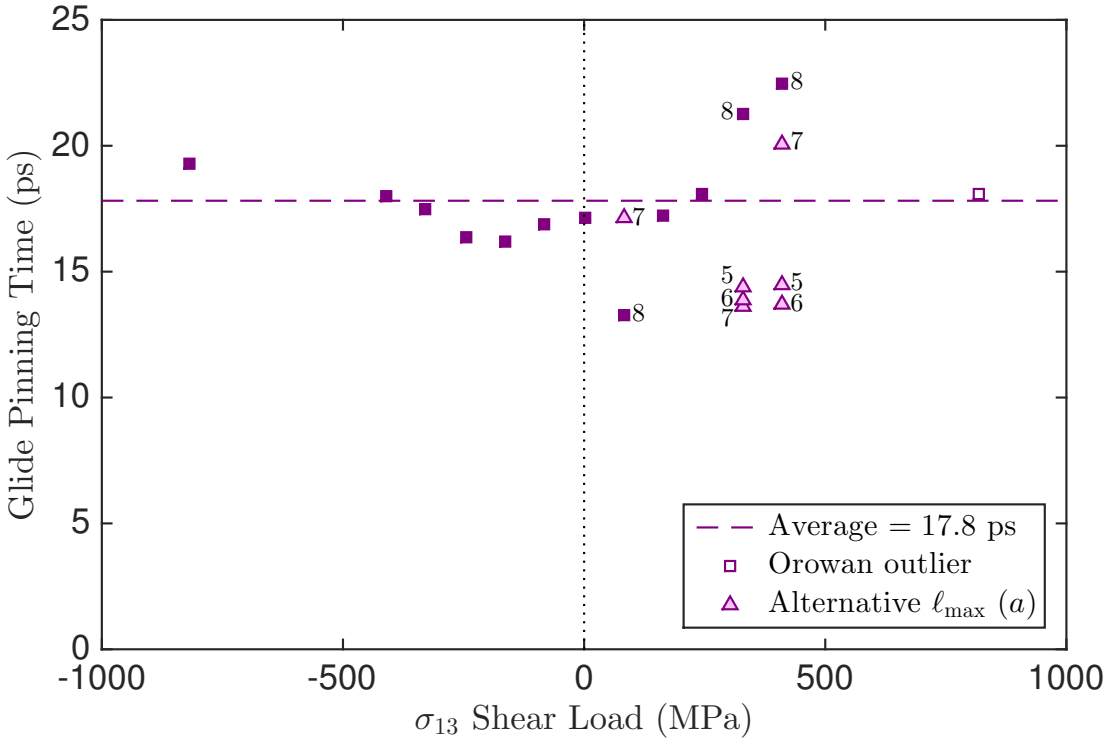


Figure 7.3: The effect of varying the applied σ_{13} shear load on the glide pinning time of the initial dislocation loop. There seems to be a negligible trend given the spread in the data.

The pinning time when $\sigma_{13} = 820$ MPa is not included in the calculated average (despite agreeing with it remarkably well), because in this particular simulation each of the near-screw dislocations glided around their inclusion entirely, pinched off, and left a dislocation loop encircling the inclusion, thus unpinning from their inclusion via the Orowan mechanism without the need for any climb to occur. Clearly the combination

of the applied σ_{13} shear load of 820 MPa and the initial loop's self-force acting to shrink it is greater than or equal to the Orowan stress for this effective obstacle separation. The self-stress of the initial circular loop of radius 18 nm acting to shrink it is ∼150 MPa (calculated using the simple expression (3.27)). Hence there is at least[40] $820 + 150 = 970$ MPa total σ_{13} shear stress acting on the dislocation segments which unpin via the Orowan mechanism in this simulation. When calculated using the effective obstacle separation L_{eff} of 24 nm, the Orowan stress $\mu b/L_{\text{eff}}$ is 970 MPa, in agreement with the Orowan stress ≤ 970 MPa indicated by this simulation.

Finally, at large enough negative values of the applied σ_{13} shear load, the initial loop expands rather than shrinks (this is not shown on the plot). In other words, a non-zero applied σ_{13} shear load provides an additional force (which can be negative), which drives the initial loop to shrink, and hence the dislocations to glide against the inclusions. However, in what follows this driving force is provided solely by the dislocation self-force as the applied σ_{13} shear load is set to zero. The data shown in figure 7.3 suggest this is reasonable, and it is justified further in § 7.3.1.

7.2.3 Demonstrative behaviour: applied σ_{12} shear load

The first of the three example simulations highlighted to demonstrate the overall simulation behaviour is shown in figure 7.4. In this simulation, a constant σ_{12} shear load of 410 MPa is applied to the simulation box, which is the same loading condition as was used in the dislocation-inclusion test simulation in § 6.2.4. Like in that test simulation, the applied σ_{12} shear load leads to the climb of the near-screw segments after pinning occurs. This is shown after 1.32 s of simulated time in figure 7.4(a), and again looking down the [100] direction in figure (b). The near-screw segments close to inclusion C are climbing in the $[00\bar{1}]$ direction due to the σ_{12} shear load, and the near-screw segments close to inclusion A are climbing in the [001] direction (again, this difference is due to the opposite signs of the near-screws).

Figures 7.4(c) and (d) show the subsequent dislocation configuration after 1.76 s of

[40] The self-stress will in fact be higher than ∼150 MPa when the dislocations become glide pinned, i.e. once the initially circular loop has partially shrunk, and deformed by bowing around the obstacles.

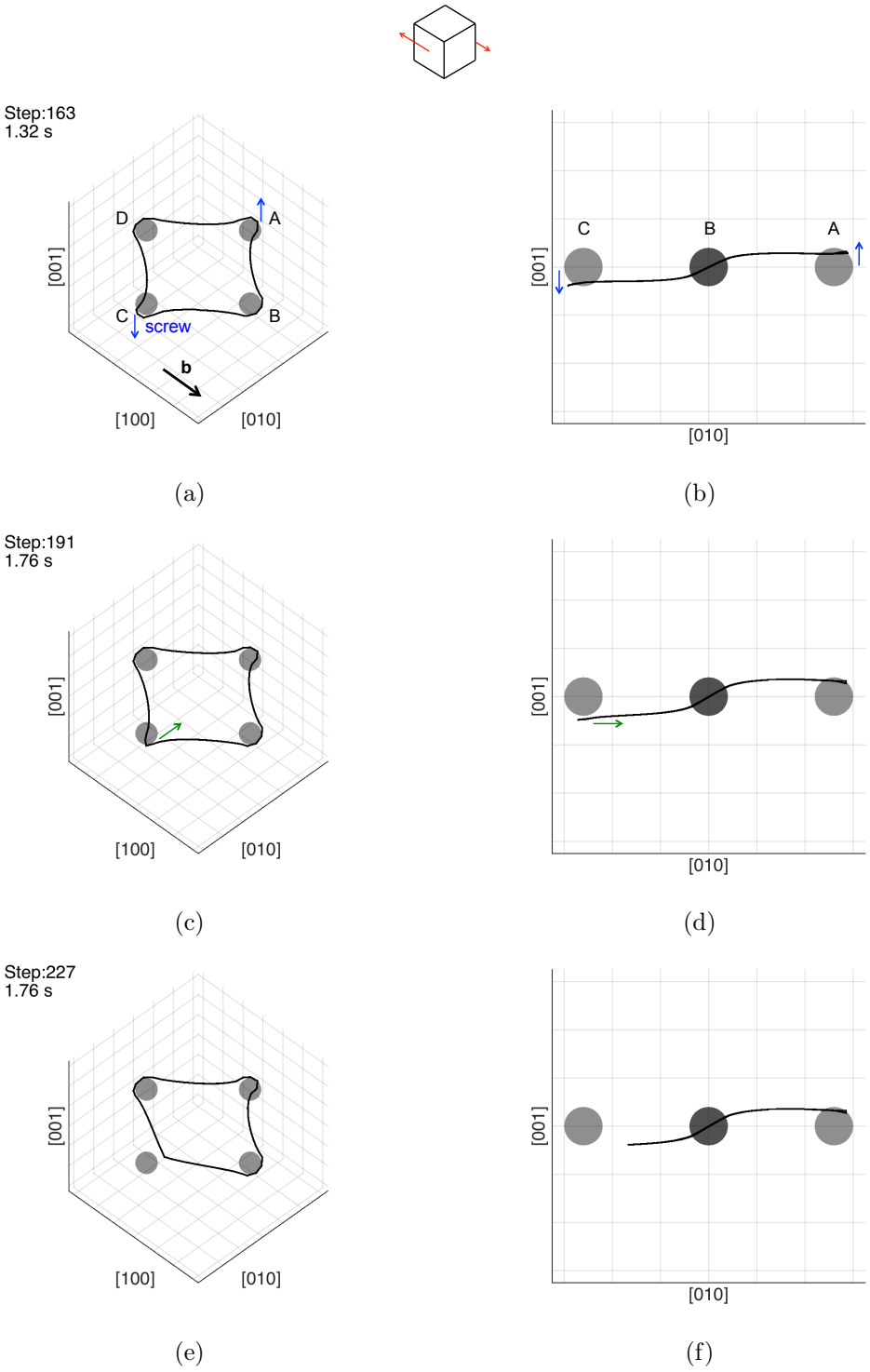


Figure 7.4: An applied σ_{12} shear load of 410 MPa at 700 °C. One of the near-screw dislocations is able to climb under inclusion C and unpin from it after 1.76 s.

simulated time. The glide-pinned dislocation segments have climbed down and around the impenetrable inclusion C, and have successfully unpinned from it. Subsequently, these segments continue to glide away from the inclusion on a ∼ps timescale, as shown in figures (e) and (f), in which 36 simulation steps have passed, but the simulation clock still reads 1.76 s. The behaviour of the two near-screw disclocations is asymmetric — one is able to unpin and the other is not — because of the asymmetric discretisation of the dislocation loop at the start of the simulation. This leads to one near-screw dislocation unpinning slightly before the other. The subsequent glide motion of the unpinned dislocation results in a change in the dislocation configuration which effectively halts the unpinning process of the second pinned dislocation. This can be seen in figures (e) and (f), where the unpinned dislocation has moved closer to the pinned dislocation via glide, and hence the force on the pinned dislocation in the $[00\bar{1}]$ direction is strong enough to halt the climb over inclusion A.

As discussed in § 6.2.4, the out of plane motion of the near-screw segments, whose screw parts are able to undergo cross slip, is nevertheless limited by rate of climb. Indeed, even the nodes at either end of a pure screw segment will experience an out of plane drag which is dominated by the significantly larger climb drag factor, since each of these nodes is also connected to a mixed segment (which has a non-zero edge component that experiences the climb drag).

In this simulation the near-edge dislocations are unable to climb over the top left and bottom right inclusions. This is because the sign of their (albeit small) screw part changes from one side of the inclusion to the other, and so when the dislocations interact with the shear load the screw parts with opposite signs result in climb in opposite directions, rotating the dislocation and preventing it from unpinning.

As the unpinning of the near-screw dislocations is a thermal climb process, the timescale for unpinning is that of thermal climb. At 700 °C, as in this simulation, that is of the order of seconds (compared to ∼ps for the initial glide relaxation and pinning).

The non-zero plastic strain components are plotted as a function of simulated time in figure 7.5. The time axis is in units of seconds, and so the vertical trend in the

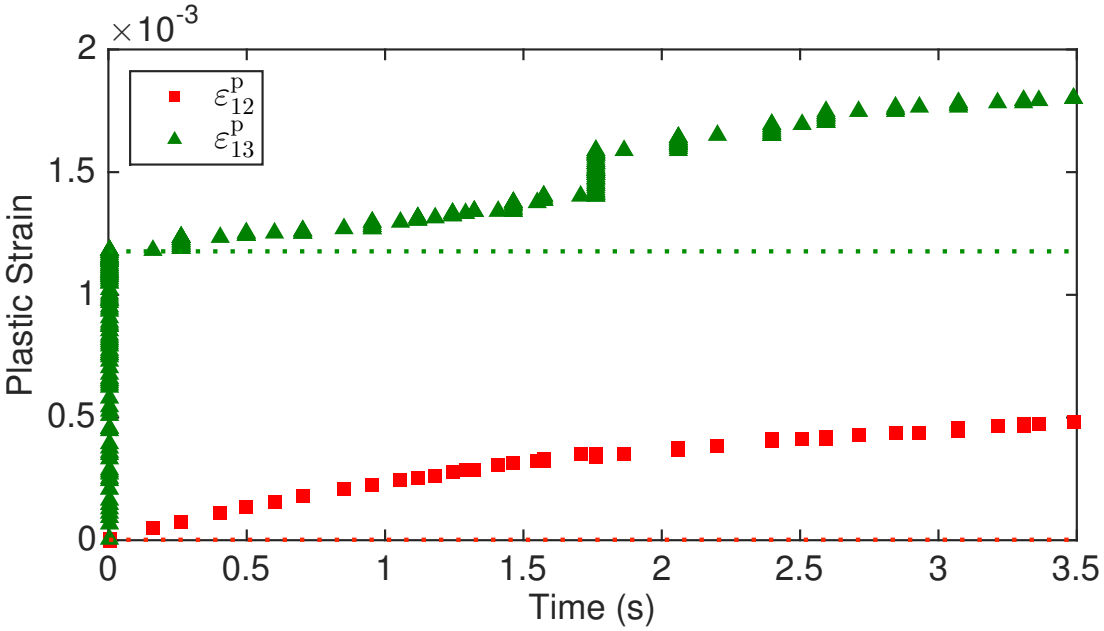


Figure 7.5: Non-zero plastic strain components as a function of simulated time due to an applied σ_{12} shear load of 410 MPa at 700 °C. The initial increase in $\varepsilon^{\mathrm{p}}_{13}$ strain is due to the initial shrinkage and pinning of the dislocations via glide. Subsequently the near-screw dislocations undergo climb, and one is able to climb under its pinning inclusion. The burst of $\varepsilon^{\mathrm{p}}_{13}$ "slip" at 1.76 s corresponds to the dislocation-inclusion unpinning event. The dotted horizontal lines indicate the "no climb" case, illustrating how capturing both glide and climb by using the dual time step method enables dislocation-inclusion unpinning to be simulated.

data points for the $\varepsilon^{\mathrm{p}}_{13}$ strain seen at $t = 0$ corresponds to the initial shrinkage and pinning of the dislocation loop which takes 18.9 ps (unresolveable on this plot). Once the climb starts, it proceeds at a steady, albeit much slower, rate, as indicated by the steadily increasing $\varepsilon^{\mathrm{p}}_{12}$ strain. During this time, the near-screw dislocations move out of plane, and in doing so, the impenetrable zone "seen" by the pinned dislocation segments slowly decreases. This leads to the slow increase seen in the $\varepsilon^{\mathrm{p}}_{13}$ strain as the near-screw dislocations climb out of their glide plane. At 1.76 s there is a burst of $\varepsilon^{\mathrm{p}}_{13}$ "slip", corresponding to the dislocation-inclusion unpinning event.

The dotted horizontal lines in figure 7.5 indicate what would be simulated in the "no climb" case, that is, without using the dual time step method to capture appreciable amounts of climb. This illustrates how simulating both glide and climb using the dual time step method enables new dislocation configurations, and hence dislocation-inclusion unpinning, to be modelled.

7.2.4 Demonstrative behaviour: applied σ_{11} compressive load

The second example simulation involves applying a σ_{11} compressive load of 820 MPa — the same loading condition as was used in the dislocation-inclusion test simulation in § 6.2.5 — and this is shown in figure 7.6. The applied σ_{11} compressive load leads to the thermal climb of the near-edge segments (rather than the near-screw ones) over/under inclusions B and D after pinning occurs. The near-screw dislocations are unable to climb over the inclusions A and C, again in a similar way to the near-edge dislocations in the previous simulation.

The panels on the right in figure 7.6 are this time viewed down the $[0\bar{1}0]$ direction in order to display the near-edge unpinning clearly. The first unpinning event, which occurs after 1.31 s, is shown in figures (c) and (d). The near-edges climb up and over inclusion B. The second unpinning event, which is distinct from the first — it is 14 simulation steps later, but the clock still reads 1.31 s — is shown in figures (e) and (f). The near-edges climb down and under inclusion D.

Figure 7.7 shows the plastic strain components as a function of simulated time. The three stages of the simulation can be seen very clearly. The initial $\varepsilon^{\mathrm{p}}_{13}$ strain is due to the initial glide of the dislocations until they become pinned. The bulk of the plot shows the steady thermal climb of the near-edge dislocations over/under the inclusions, as indicated by the steady increase in the $\varepsilon^{\mathrm{p}}_{11}$ strain, accompanied by a relatively small increase in the $\varepsilon^{\mathrm{p}}_{13}$ strain (as the size of the impenetrable zone "seen" by the pinned dislocations decreases, allowing the dislocations to bow out slightly more). Both unpinning events happen at the same simulated time (at least at this time resolution) of 1.31 s, shown clearly by the single $\varepsilon^{\mathrm{p}}_{13}$ "slip" event on the right of the plot. In comparing this simulation to the last one, it is worth noting that the unpinning time is roughly the same — ∼1 second — for both screw and edge unpinning via thermal climb at this temperature of 700 °C.

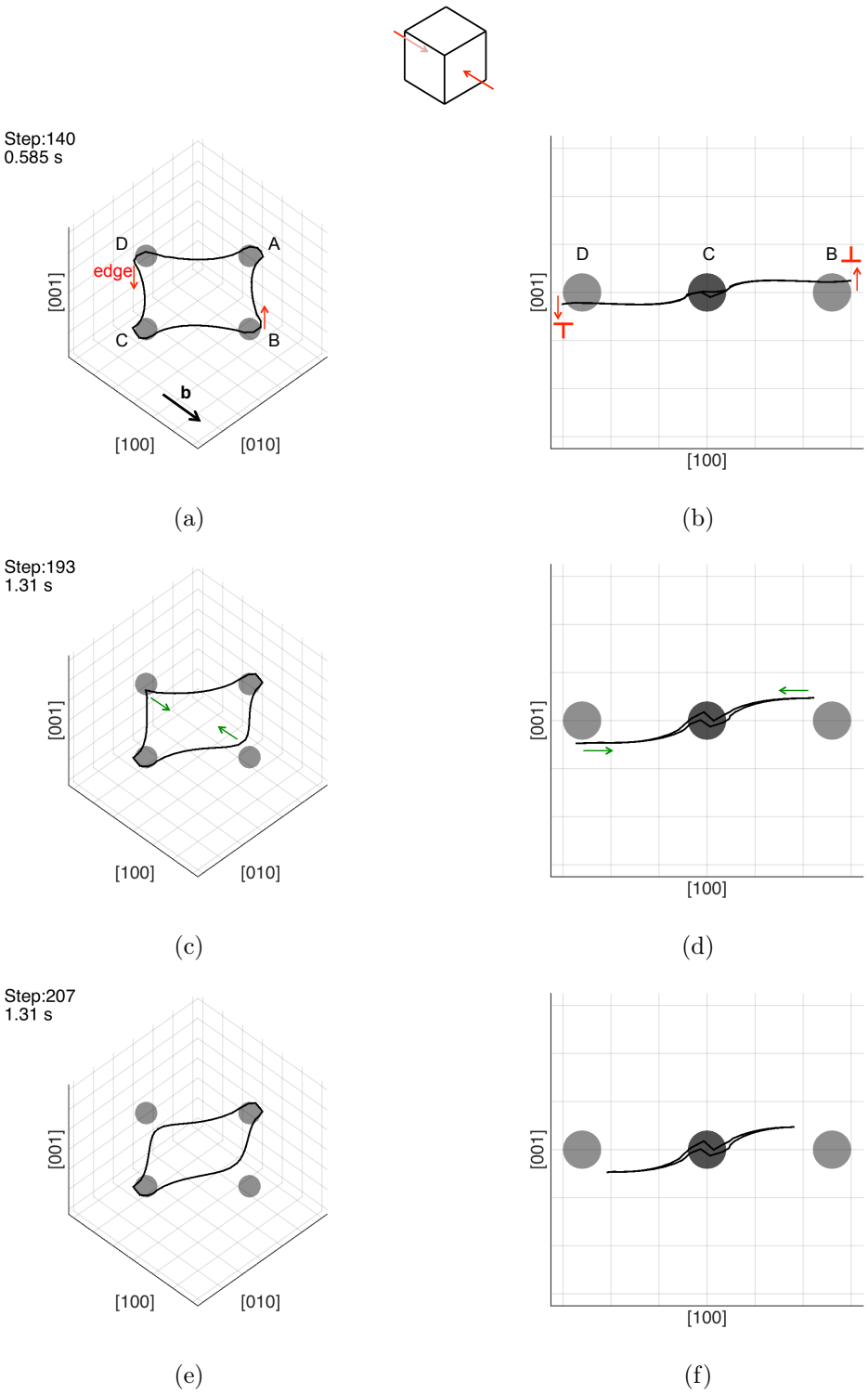


Figure 7.6: An applied σ_{11} compressive load of 820 MPa at 700 °C. The near-edge dislocations are able to climb over/under inclusions B and D, and unpin from them after 1.31 s.

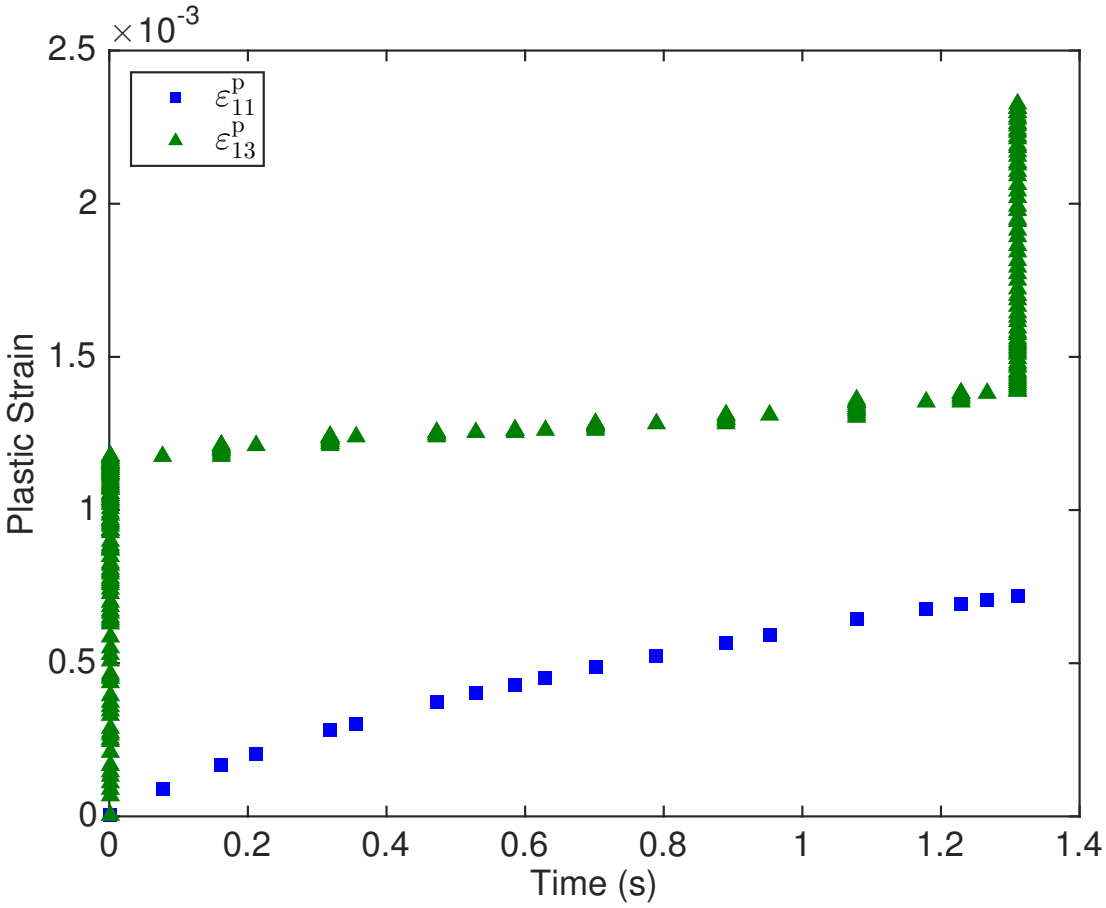


Figure 7.7: Plastic strain components as a function of simulated time due to an applied σ_{11} compressive load of 820 MPa at 700 °C. The three stages of the simulation are clearly visible. Both dislocation-inclusion unpinning events occur at 1.31 s, indicated by the burst of $\varepsilon^{\mathrm{p}}_{13}$ "slip" on the right of the plot.

7.2.5 Demonstrative behaviour: defect supersaturations present

Lastly, figure 7.8 shows a simulation in which there is no applied load, but there are equal vacancy and interstitial supersaturations of 10^{-9} defects present in the simulation box — the same defect supersaturations that were present in the dislocation-inclusion test simulation in §6.2.6. In this simulation, the near-edge dislocations unpin as in the previous σ_{11} compressive load simulation, but they climb over/under inclusions in the opposite direction to the σ_{11} compressive load case. This is due to the fact that the absorption of supersaturated interstitials at the dislocations dominates the osmotic climb, so there is an effective net increase of matter in the box, resulting in an overall tensile strain rather than a compressive one. Indeed, this can be seen clearly in the plastic strain component plot in figure 7.9. The $\varepsilon^{\mathrm{p}}_{11}$ strain induced by the dislocation

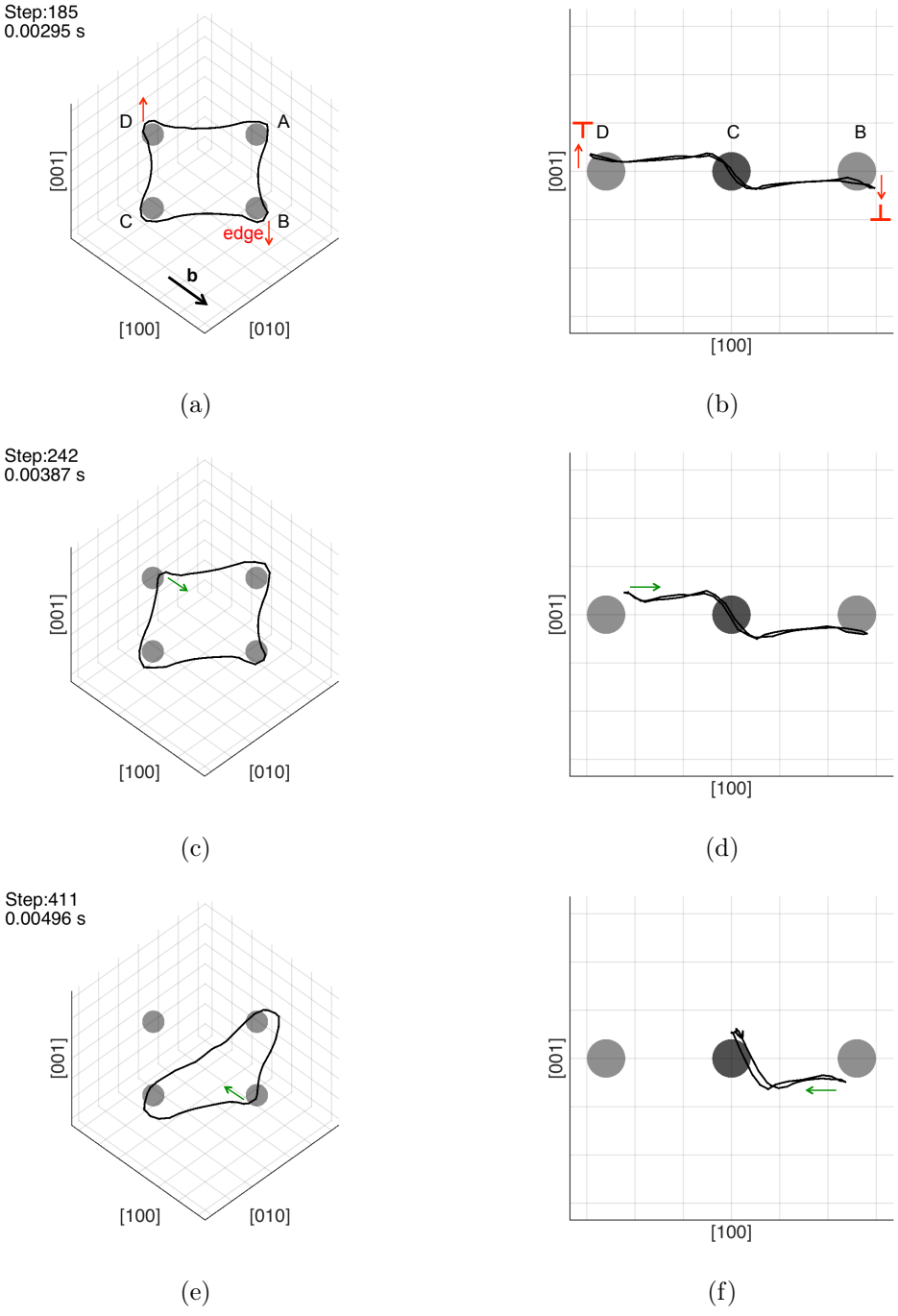


Figure 7.8: Equal vacancy and interstitial supersaturations of 10^{-9} defects present (but no applied load) at 700 °C. The near-edge dislocations are able to climb over/under inclusions D and B, and unpin from them after 3.87 ms and 4.96 ms respectively. This is similar behaviour to the previous σ_{11} compressive load simulation, except that the dislocations climb in the opposite directions, and the unpinning via climb is ∼ms rather than ∼s.

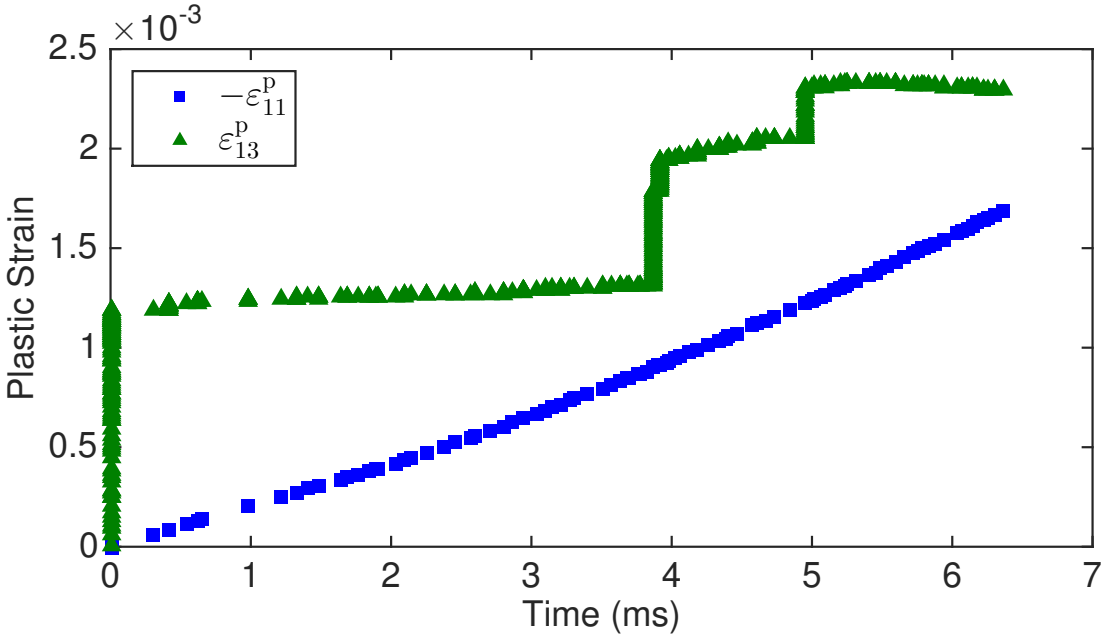


Figure 7.9: Plastic strain components as a function of simulated time due to equal vacancy and interstitial supersaturations of 10^{-9} defects (but no applied load) at 700 °C. Two distinct unpinning events are visible at 3.87 ms and 4.96 ms. Note that the $\varepsilon^{\mathrm{p}}_{11}$ strain is negative compressive strain, i.e. it corresponds to tensile strain.

climb is negative compressive strain, i.e. it corresponds to tensile strain.

A striking feature of this simulation is that the timescale for climb, and hence the dislocation-inclusion unpinning times, is of the order of milliseconds rather than seconds as previously. There are two distinct unpinning events, at 3.87 ms and 4.96 ms, as shown in the snapshots in figures 7.8(c)–(f), and clearly visible in the plot in figure 7.9.

In what follows, when two distinct unpinning events are seen in a single simulation, both unpinning times are used in the analysis.

7.3 Dislocation-inclusion unpinning time analysis

7.3.1 Dependence on applied σ_{13} shear load

The first set of simulated unpinning times are plotted in figure 7.10. It shows the effect of varying an applied σ_{13} shear load, for the fixed applied σ_{12} shear load of 410 MPa case (shown in figure 7.4). The temperature is 700 °C. The spread in the data suggests that there is a negligible trend in the unpinning times when varying the applied σ_{13} shear load, especially when considering the two data points for which $\ell_{\max}$ was set to $7a$ instead of $8a$, which seem to indicate that the spread in the data is the result of subtle variations in the loop discretisation, as was the case in the glide pinning time simulations shown previously in figure 7.3. Hence it seems reasonable not to apply any σ_{13} shear load in subsequent simulations in which an applied σ_{12} shear load is present.

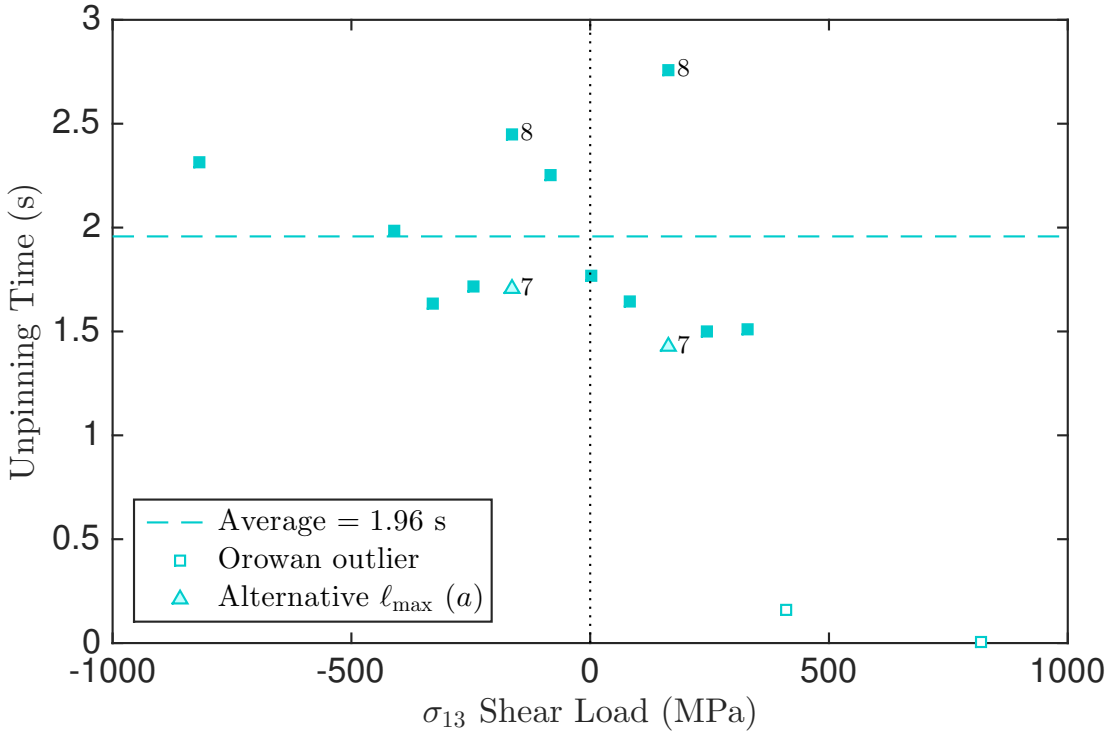


Figure 7.10: The effect of varying the applied σ_{13} shear load on the dislocation-inclusion unpinning time, for a fixed applied σ_{12} shear load of 410 MPa. The temperature is 700 °C. Given the spread in the data, varying σ_{13} appears to have a negligible effect on the unpinning time, provided the σ_{13} load combined with the dislocation self-force is well below the Orowan stress.

It is however worth discussing the two data points which are clear outliers. The unpin-

ning time when $\sigma_{13} = 820$ MPa is 18.2 ps (indistinguishable from 0 s on this linear scale of ∼s). In this simulation the near-screw dislocations unpinned from their inclusions via the Orowan mechanism, and no climb motion occured whatsoever. As argued in § 7.2.2, this is expected given that the σ_{13} load of 820 MPa combined with the dislocation self-force of (at least) ∼150 MPa is greater than or equal to the Orowan stress, which was calculated to be 970 MPa.

Interestingly, the unpinning time of 0.16 s when $\sigma_{13} = 410$ MPa, though not ∼ps, is still about an order of magnitude lower than the other data points. In this particular simulation, the pinned near-screw dislocations underwent relatively little climb, but subsequently they were nevertheless able to overcome their pinning inclusions via the Orowan mechanism. This behaviour also seems reasonable, as even though the total σ_{13} shear stress of at least $410 + 150 = 560$ MPa was initially below the Orowan stress, the dislocation self-force increased as the dislocations climbed and bowed around the inclusions further, and in this case the Orowan mechanism was able to proceed after the self-force had increased sufficently.

As these two simulations mentioned involve the (non-climb) Orowan unpinning mechanism, they are plotted as outliers in figure 7.10, and excluded from the average shown on the plot. Because the simulations involving an applied σ_{13} shear load of 328 MPa or less do not involve the Orowan mechanism, it remains reasonable not to apply any σ_{13} shear load in subsequent simulations in which an applied σ_{12} shear load is present.

Similar data, again showing the effect of varying an applied σ_{13} shear load, this time for the fixed applied σ_{11} compressive load of 820 MPa case (shown in figure 7.6), are shown in figure 7.11. Again the temperature is 700 °C. This time there appears to be some trend of increasing unpinning time with increasing applied σ_{13} shear load, but it seems to flatten off for the negative values of the applied shear load, hence the choice of an exponential fit. As the applied σ_{13} shear load increases from zero the unpinning time starts to increase appreciably, but then the Orowan mechanism is seen once more. At 410 MPa a small amount of climb occurs, followed by Orowan unpinning, resulting in an unpinning time of 1.31 s. When the applied σ_{13} shear load is 820 MPa no climb occurs at all, and the dislocations are able to unpin in 18.1 ps. Once more this behaviour

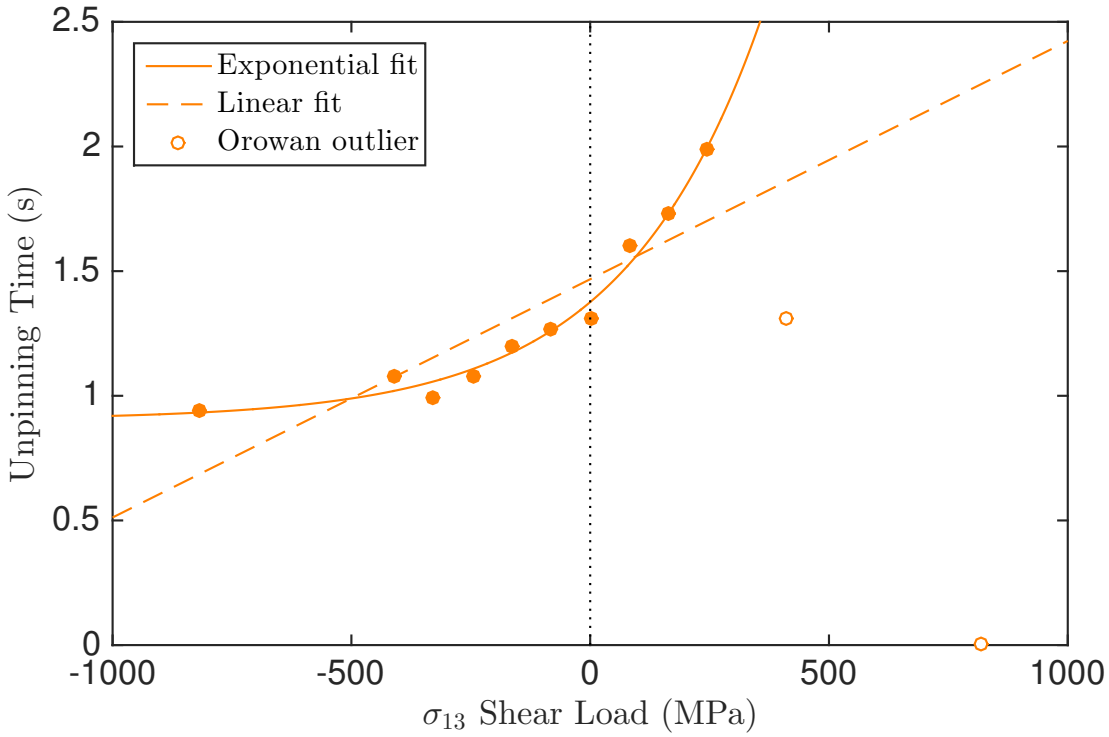


Figure 7.11: The effect of varying the applied σ_{13} shear load on the dislocation-inclusion unpinning time, for a fixed applied σ_{11} compressive load of 820 MPa. The temperature is 700 °C. There appears to be some trend of increasing unpinning time with increasing applied σ_{13} shear load, but it seems to flatten off for the negative values of σ_{13}, and is only present for the positive values provided the σ_{13} load combined with the dislocation self-force is well below the Orowan stress.

broadly agrees with the calculated Orowan stress of 970 MPa, and choosing the applied σ_{13} shear load to be zero in subsequent simulations involving an applied σ_{11} compressive load again seems reasonable.

7.3.2 Dependence on temperature

Figure 7.12 shows the temperature dependence of the simulated unpinning times from 300–700 °C. Both an applied σ_{12} shear load of 410 MPa and an applied σ_{11} compressive load of 820 MPa are shown at five different temperatures. The plot clearly demonstrates the very strong temperature dependence of unpinning times, both for near-screw and near-edge dislocations. Unpinning takes seconds at 700 °C, whereas it takes hours at 500 °C and decades at 300 °C. This is to be expected as the dislocation-inclusion unpinning in these cases is a thermal climb process, mediated by the equilibrium vacancy

population[41].

A small number of simulated unpinning times for different values of the applied loads at 300 °C and 500 °C are also shown. This is to indicate the relatively small effect the value of the load has on the unpinning time when compared to the effect of changing the temperature. Many of the plots in this chapter are for the fixed temperature of 700 °C, in order to show the effect changing one variable has on another. It is important to remember when considering these plots, that were the temperature to be changed to 500 °C or 300 °C, the trends would remain the same as those at the fixed temperature of 700 °C , but the overall *scale* of the trends would be altered by orders of magnitude. For each subsequent plot at at fixed temperature of 700 °C, the order of magnitude of the scale at 500 °C and 300 °C is stated explicitly.

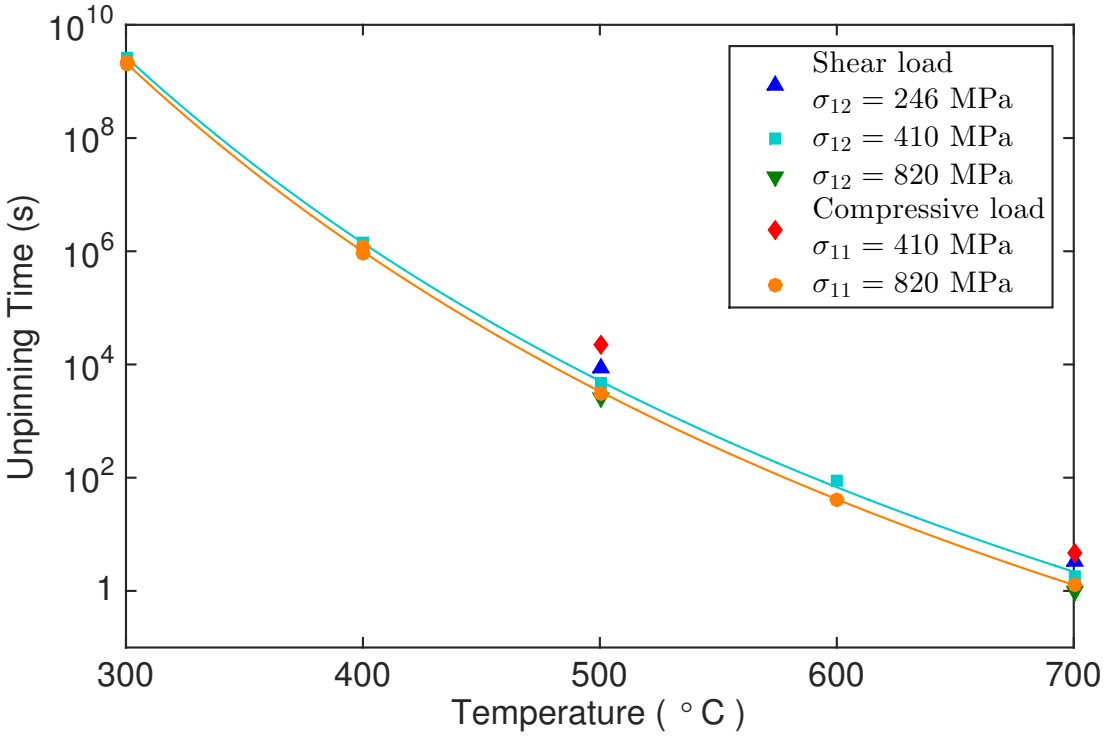


Figure 7.12: Temperature has a very strong effect on the unpinning time when applying either a σ_{12} shear or a σ_{11} compressive load. Dislocation-inclusion unpinning, for both near-screw and near-edge dislocations, takes seconds at 700 °C, hours at 500 °C, and decades at 300 °C. This is to be expected for a thermal climb process. The value of the load has a relatively small effect on the unpinning time when compared to the temperature effect.

[41] At low temperatures, point defect transmission round the dislocation loop via pipe diffusion might dominate the climb. However, this is only relevant for the artificial simulation of a closed loop, not for real threading dislocations.

7.3.3 Dependence on applied load

Figure 7.13 shows the effect that varying the value of an applied σ_{12} shear or σ_{11} compressive load has on the unpinning time at 700 °C. An inverse dependence of the unpinning time on the load fits the data fairly well. The σ_{12} shear load is asymptotic to a value of –78 MPa, but fixing this asymptote to be 0 MPa is also reasonably consistent with the data points. In constrast, the σ_{11} compressive load is clearly asymptotic to a non-zero value, which comes to 310 MPa.

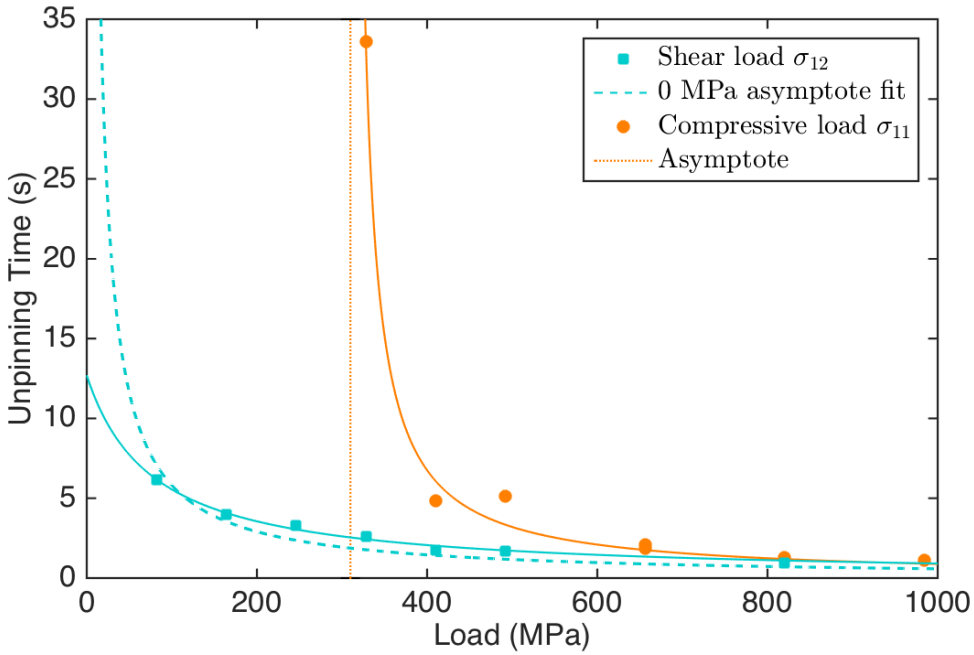


Figure 7.13: The unpinning time varies inversely with the value of an applied σ_{12} shear or σ_{11} compressive load, although the two cases have different asymptotic values. The temperature is 700 °C. The unpinning time scale would be of the order of hours if the temperature were 500 °C, and decades if it were 300 °C.

The inverse dependence can be explained by the fact that the rate of climb is proportional to the load in the linear climb mobility law used (see § 2.3.6). As the dislocations have a fixed distance through which to climb before unpinning (roughly the radius of the inclusion plus a dislocation core radius), increasing the climb rate by increasing the load should inversely decrease the time it takes for the dislocation to traverse this distance. The non-zero threshold load for unpinning in the σ_{11} compressive load case implies that during the climb of the near-edge dislocations, the restoring stress acting

to force the near-edges back down/up to their initial habit plane must peak at roughly 310 MPa. This restoring stress can only be due to the dislocation configuration itself, which is feasible given the fact that the edge parts in one half of the initial loop climb up whereas the edge parts in the other half climb down, resulting in an anti-symmetric configuration (see the panels on the right in figure 7.6). Because of this, the self-force, which acts to shrink the loop via glide, also provides a restoring force back down/up to the original habit plane.

As for the σ_{12} shear load case, the 0 MPa (or indeed –78 MPa) threshold for unpinning implies that there is no such restoring force on the near-screw dislocations as they climb up/down. This seems to contradict the fact that in this case a similar anti-symmetric configuration occurs (see the panels on the right in figure 7.4), and so the near-screws of opposite sign which have climbed up/down should produce some restoring force. However, it is possible this restoring force simply peaks at a relatively small value, and so is not captured by the fits to the present data. If the small restoring force were $\sim$78 MPa or less, it is particularly easy to see how such a threshold value would be obscured.

Importantly, the presence of a such a restoring force is specific to these simulations which involve an initial dislocation loop. In a realistic situation, in which a threading dislocation moves through a distribution of impenetrable obstacles, there will be no such restoring force on the dislocation as it climbs around the obstacles, and so there will be no threshold load for unpinning to occur. However, the loop setup nevertheless enables straightforward, self-consistent comparisons to be made between the various competing factors under consideration.

The unpinning times in the plot are of the order of seconds as the temperature is 700 °C. Identical trends are expected at lower temperatures, but of the order of hours at 500 °C, and decades at 300 °C.

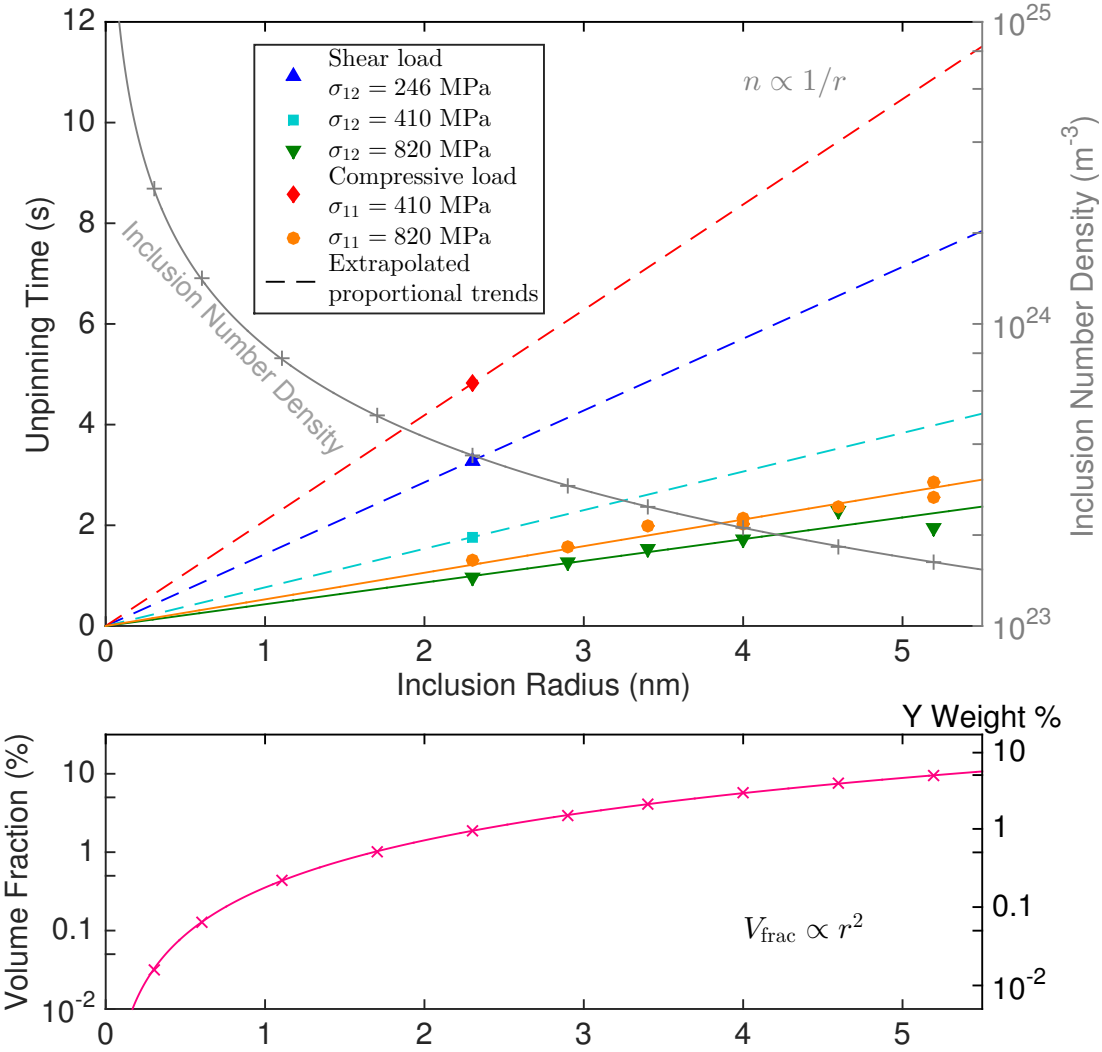


Figure 7.14: The unpinning time varies proportionally with inclusion radius when applying a σ_{12} shear or σ_{11} compressive load. As the inclusion radius increases, the spread in the unpinning times for different values of the load also increases proportionally. The unpinning times are of the order of seconds at 700 °C, but this would be hours at 500 °C, and decades at 300 °C. As these simulations were carried out at fixed effective obstacle separation, the inclusion number density and inclusion volume fraction/yttrium weight percentage vary with the radius, which is also shown.

7.3.4 Dependence on obstacle size

In the following simulations, the inclusion radius was varied. The resulting unpinning times are shown in figure 7.14. The effective obstacle separation, i.e. side length of the square of four inclusions, was kept at 24 nm. Hence both the inclusion number density

and inclusion volume fraction[42] necessarily varied as a function of the inclusion radius. The variation in these two quantities is also shown on the plot.

The unpinning times for the σ_{12} shear and σ_{11} compressive loads, both of 820 MPa, vary proportionally with the inclusion radius. This is because increasing the inclusion radius increases the distance the dislocations must climb before unpinning, and so for a given climb rate the time taken to unpin will increase proportionally. The data points for three different load values (two σ_{12} shear and one σ_{11} compression) for the default inclusion radius of 2.3 nm are also shown, and a proportional relationship is extrapolated from them. This is in order to demonstrate the fact that increasing the inclusion radius also proportionally increases the range of unpinning times at different load values. However, for the range of inclusion radii of 0–5.5 nm shown, the unpinning times are all within one order of magnitude of each other. Again, all these unpinning times are of the order of seconds at this temperature of 700 °C, but they would be of the order of hours at 500 °C, and decades at 300 °C, whilst still obeying the proportional trend with inclusion radius, and varying by no more than one order of magnitude within the explored inclusion radius and load space.

The inclusion number density n and volume fraction V_{frac} depend solely on the inclusion radius r (and the effective obstacle separation L_{eff}, which in this case was fixed). Using the expression for $L_{\text{eff}}(r, n)$ given later in (7.7), and straightforward geometry, expressions for $n(r)\big|_{L_{\text{eff}}}$ and $V_{\text{frac}}(r)\big|_{L_{\text{eff}}}$ can be found. They are

$$n(r)\bigg|_{L_{\text{eff}}} = \frac{1}{2L_{\text{eff}}^2} \cdot \frac{1}{r}, \tag{7.3}$$

and

$$V_{\text{frac}}(r)\bigg|_{L_{\text{eff}}} = \frac{4}{3}\pi r^3 \cdot n(r)\bigg|_{L_{\text{eff}}} = \frac{2}{3}\frac{\pi}{L_{\text{eff}}^2} \cdot r^2. \tag{7.4}$$

These functions are also plotted in figure 7.14. The number density at the radii of the data points is of the order of a few 10^{23} m^{-3}, which agrees well with the experimental values. However, the volume fraction and corresponding yttrium weight percentage are of the order of a few percentage points, which is higher than the values from experiment

[42] Assuming inclusions composed entirely of Y_2O_3, the Y wt% is calculated from the inclusion volume fraction using (7.1).

of 0.1–0.5 Y wt%.

In order to ensure both the number density and volume fraction are consistent with experimental values, simulations would need to be carried out using different values of the effective obstacle separation (by changing the side length of the square of four inclusions). When comparing the unpinning times resultant from such simulations, one of (r, n, V_{frac}) could be varied, another would be held constant, and the third would vary parametrically with the first one. Although simulations using different values of the effective obstacle separation were not carried out, such a parametric study of the present data at fixed L_{eff} is performed in § 7.5.4 by using the simple model for estimating the strain rate described in § 7.4, which incorporates additional dependence on L_{eff} and thus allows it to vary.

7.3.5 Dependence on defect supersaturation

The simulated unpinning times due to a range of (equal) supersaturations of vacancies and intersititals as a function of temperature are shown in figure 7.15, together with the data for a σ_{12} shear load of 410 MPa and a σ_{11} compressive load of 820 MPa from figure 7.12 for comparison. Simulations at five different temperatures from 300 to 700 °C were performed at six supersaturation values varying in powers of ten from 10^{-11} to 10^{-6} fractional concentration of defects. A further six simulations were performed for much smaller supersaturations varying from 10^{-17} to 10^{-12} defects at 400 °C. The data points from all but one of these additional simulations are each used to plot an extrapolated trend (corresponding to the fit of the data for the 10^{-11} defects case). In the simulation of 10^{-17} defects no unpinning occured, and so there is no data point on the plot for this simulation.

The most striking feature of the plot is that all the simulated unpinning times due to a defect supersaturation are many orders of magnitude smaller than those due to the applied loads from § 7.3.2, with the exception of the value for 10^{-11} defects at 700 °C, which is still a few times less than the corresponding applied load values. However, as indicated by the parts of the extrapolated trends which lie above the applied load

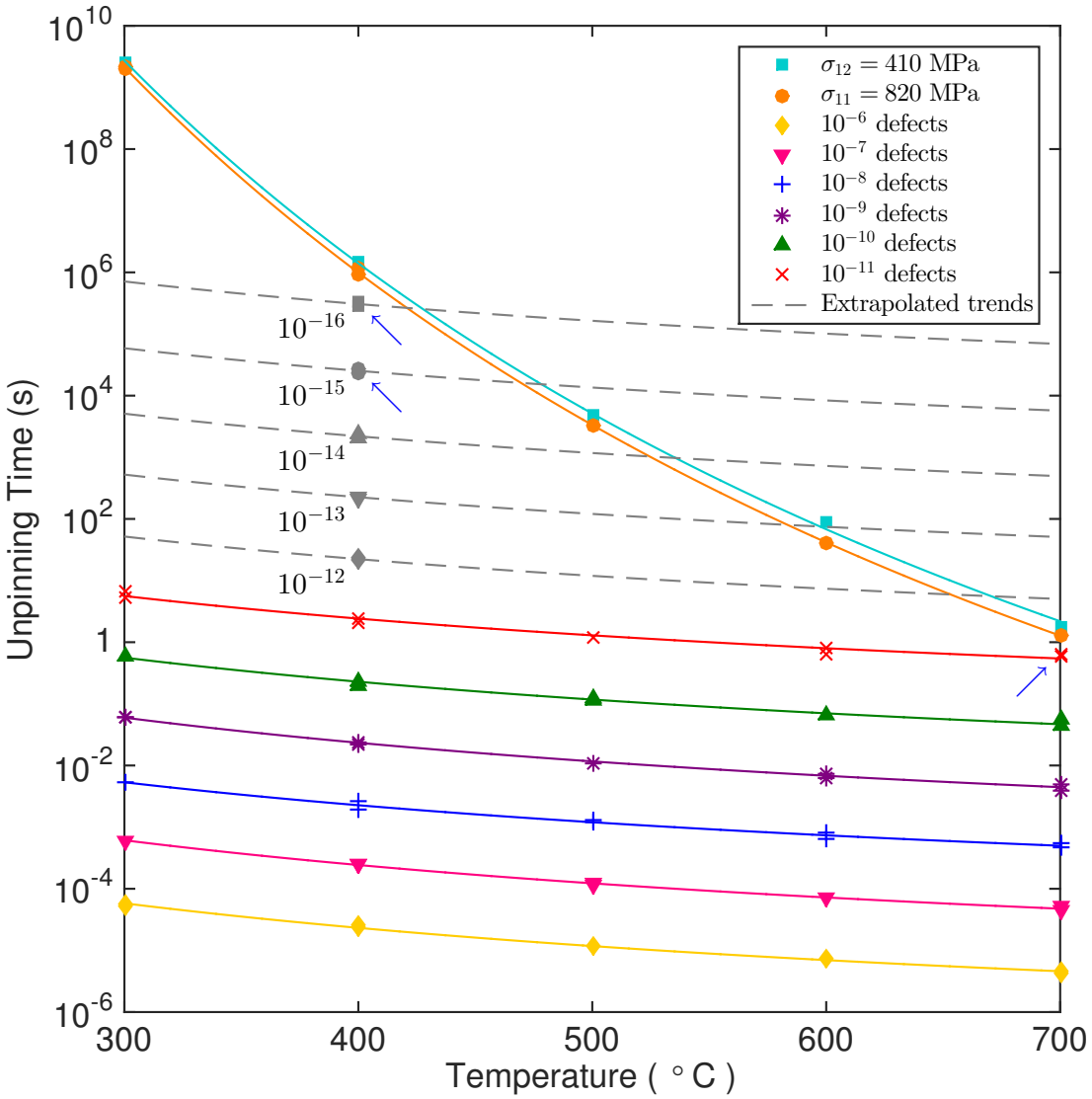


Figure 7.15: All the defect supersaturations simulated yield unpinning times which are orders of magnitude smaller than the applied load cases. The temperature dependence of the unpinning time at a given supersaturation is much weaker than the applied load cases: the unpinning time only decreases by about one order of magnitude as the temperature is decreased from 700 to 300 °C.

curves, the unpinning times have the potential to be larger than in the applied load cases, provided the temperature is high enough and the supersaturation is small enough.

Another important feature is the much weaker temperature dependence of the supersaturation curves. Whereas the applied load unpinning times vary from seconds at 700 °C up to decades at 300 °C, the supersaturation unpinning times only change by about one order of magnitude. For example, a supersaturation of 10^{-11} defects yields

an unpinning time of a few tenths of a second at 700 °C, but it only increases to about ten seconds at 300 °C.

As already mentioned, at 400 °C no unpinning occurred in the 10^{-17} defects case, but it did in the 10^{-16} defects case. This is simply because of the choice of the simulation setup: an initial dislocation loop encircling the inclusions. The osmotic climb velocity due to a supersaturation between 10^{-17} and 10^{-16} must correspond to the thermal climb velocity due to the restoring force of roughly 310 MPa on the near-edge dislocations, as justified previously in § 7.3.3. In the case of a threading dislocation climbing around impenetrable obstacles, there is no such restoring force, and unpinning is expected to continue to occur for supersaturations of 10^{-17} and below at 400 °C. Hence the supersaturation curves are expected to continue successively up the plot for even lower supersaturations, resulting in even larger unpinning times, many of which will lie above the applied load curves.

The three blue arrows in figure 7.15 indicate the cases in which the value of the defect supersaturation is *below* the thermal vacancy population at the given temperature. At 400 °C the equilibrium vacancy concentration is $10^{-14.98}$, and at 700 °C it is $10^{-10.40}$. Hence in the simulations indicated *there is no* vacancy supersaturation, only an interstitial one. However, this does not affect the unpinning times as the interstitial supersaturations dominate, as justified in chapter 3. The equilibrium interstitial concentration at 400 °C is $10^{-29.95}$, and at 700 °C it is $10^{-20.72}$, both far below the supersaturations shown on the plot. This implies that unpinning of a threading dislocation should be able to occur everywhere except the very top of the plot, where the successive supersaturation curves would reach $<10^{-20.72}$.

Clearly knowledge of the value of the steady-state defect supersaturation available to drive osmotic dislocation climb is essential when trying to predict the dislocation-inclusion unpinning time, and whether it is comparatively larger or smaller than the corresponding times for unpinning via thermal climb (in the presence of an applied load).

The data points shown in figure 7.15 are plotted again in figure 7.16 as a function of

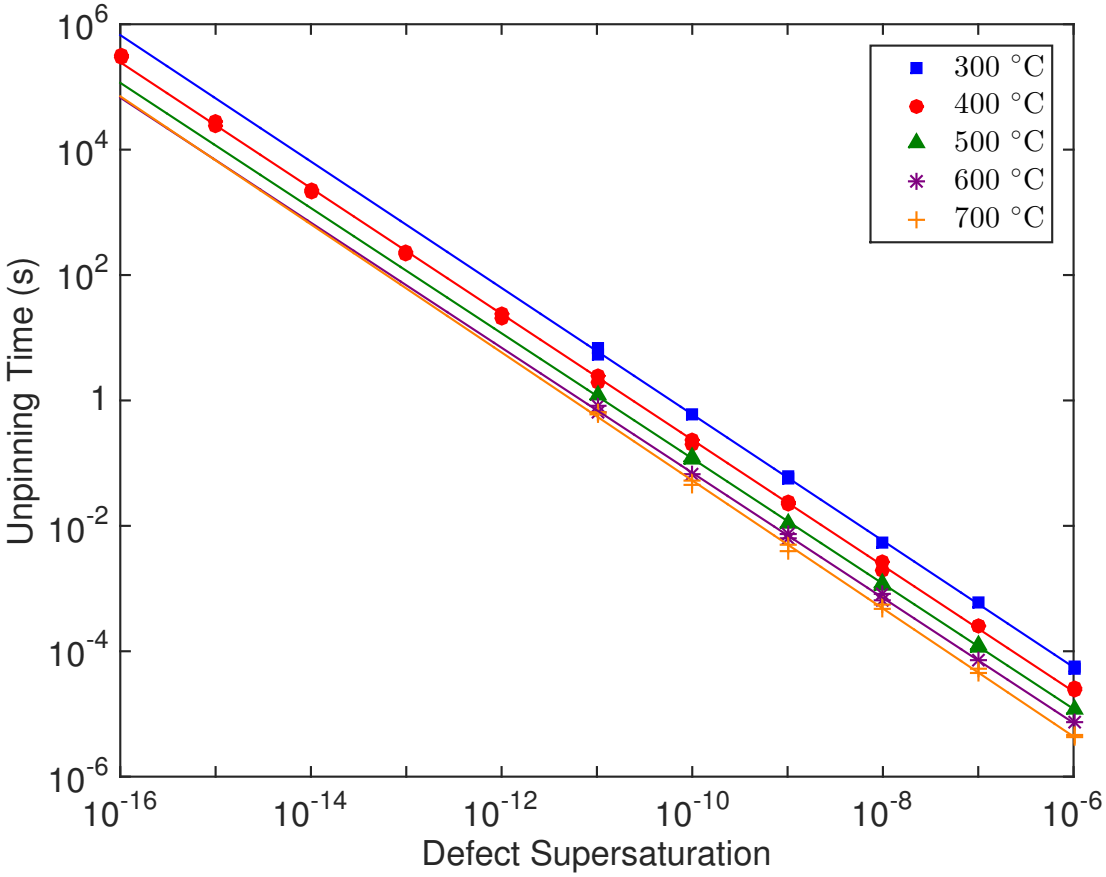


Figure 7.16: Increasing the defect supersaturation by a single order of magnitude at a given temperature decreases the unpinning time by one order of magnitude. The spread in the lines of different temperature from 300 to 700 °C is also only about one order of magnitude. Hence the unpinning time is much more sensitive to the defect supersaturation at a given temperature than it is to the temperature for a given supersaturation.

the defect supersaturation. At a given temperature, increasing the supersaturation by a single order of magnitude leads to a decrease in the unpinning time of one order of magnitude. This is to be expected, as the osmotic climb velocity is proportional to the osmotic force, which in turn is proportional to the value of the supersaturation. Increasing the supersaturation increases the osmotic climb rate, proportionally decreasing the time taken to climb around the obstacles.

The spread in the lines of different temperature from 300 to 700 °C is also only about one order of magnitude. This plot serves to highlight how much more sensitive the unpinning time is to a change in the defect supersaturation at a given temperature than it is to a change in the temperature at a given supersaturation. Again, it is clear that in order to

accurately predict the order of magnitude of the unpinning time, knowledge of the order of magnitude of defect supersaturation is required, whereas the exact temperature has a relatively small effect on the predicted value. This is in contrast to the applied load cases considered previously, where the predicted unpinning time is most sensitive to a change in the temperature.

7.4 Creep strain rate estimation from the unpinning time

The dislocation-inclusion unpinning time will affect the creep behaviour of the particle-reinforced material at the macroscale. In order to estimate the creep strain rate, the simple model illustrated in figure 7.17 is used, which utilises the simulated single obstacle unpinning times already discussed.

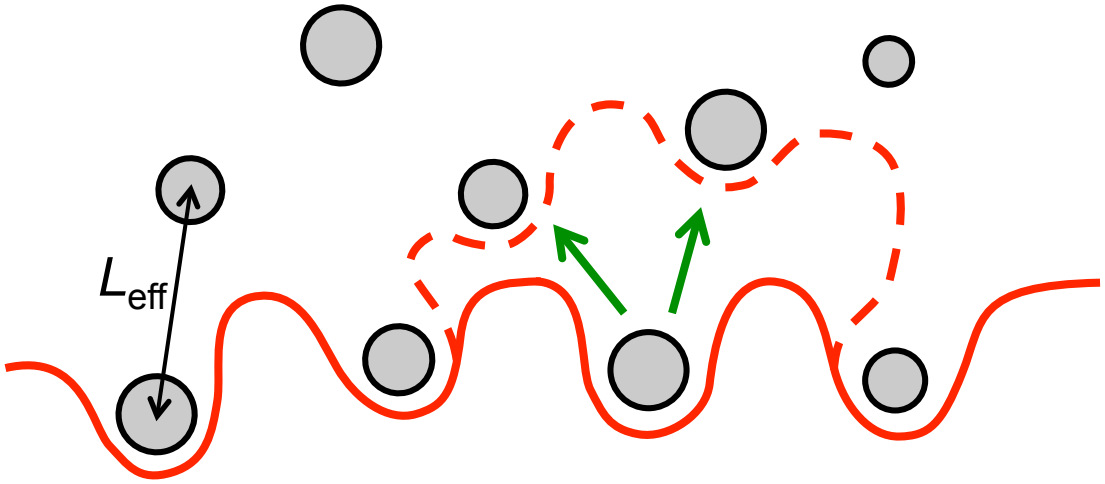


Figure 7.17: If on average pinned dislocations take a known time to climb over a single obstacle, and then they glide quasi-instantaneously to the next pinned configuration, the average dislocation velocity is approximately the average effective obstacle separation L_{eff} divided by the known unpinning time. In this schematic representation, the glide plane of the dislocation is the plane of the page: the initial configuration (the solid red line) lies in one habit plane, whereas after the unpinning event part of the dislocation has climbed over an obstacle and now lies in a different habit plane (the dashed line).

In a particle-reinforced material, the threading mobile dislocations glide until they become pinned on the impenetrable particles on a relatively fast timescale. The pinned parts of the dislocation then climb around the obstacles on a much longer timescale (at least in the unpinning simulations conducted in this work), until they are able to unpin and glide away to the next pinned configuration. This subsequent glide happens quasi-instantaneously on the climb timescale. If the average time it takes part of the dislocation to overcome a single obstacle via climb is known, then the average dislocation velocity is approximately the average effective obstacle separation divided by the known unpinning time. The macroscopic creep strain rate can then be estimated using

the Orowan equation (5.3):

$$\dot{\varepsilon} = \rho b \bar{v} = \rho b \frac{L_{\text{eff}}}{t_{\text{unpin}}}, \tag{7.5}$$

where ρ is the average dislocation density, $\bar{v}$ is the average dislocation velocity, L_{eff} is the average effective obstacle separation, and t_{unpin} is the average dislocation-inclusion unpinning time.

For a random distribution of spherical obstacles of number density n in 3D space, the corresponding average obstacle separation in 3D L is $\sim n^{-\frac{1}{3}}$. This assumes each obstacle's "volume of influence" is a cube of volume n^{-1}. L is independent of the radii of the spherical inclusions. However, L is *not* the *effective* average obstacle separation "seen" by gliding dislocations, L_{eff}. What is meant by this quantity is the average separation of inclusions which intersect a 2D plane in 3D space, corresponding to the set of possible glide planes of the threading dislocations. Like L, L_{eff} must depend on the inclusion number density, but unlike L it must also depend on the average radius r of the inclusions. As r tends to zero, L_{eff} must tend to infinity, as it is impossible for any point-like inclusions to intersect a 2D plane in 3D space. For finite values of r, L_{eff} will be less than L for a given number density, provided r is a sensible value (it cannot be larger than the resultant $L/2$, as this would be unphysical: the 3D obstacle separation cannot be less than the obstacle radii). It is important to note that even if the inclusions all have identical radii, the circles of intersection with a 2D plane will necessarily have radii which vary, and are $\leq r$. This is why the circular projections of the obstacles in 2D in figure 7.17 are not of uniform size, despite the assumption that the obstacles all have the same (3D) radius. On average, the circles of intersection each have an area of $2/3 \cdot \pi r^2$, which can be shown by straightforward integration.

An approximate expression for L_{eff} as a function of both n and r can be found as follows. Consider the three nearby inclusions illustrated in black in figure 7.18. The locus of their centres defines a 2D plane, the orientation of which is completely arbitrary in 3D space. Now, consider the fourth nearby inclusion (in blue) which intersects this pre-defined plane. The centre of the fourth inclusion is assumed to lie on the pre-defined plane as well, and the four inclusions are assumed to be arranged in a square configuration on the pre-defined plane. On average, the area of this square approximates

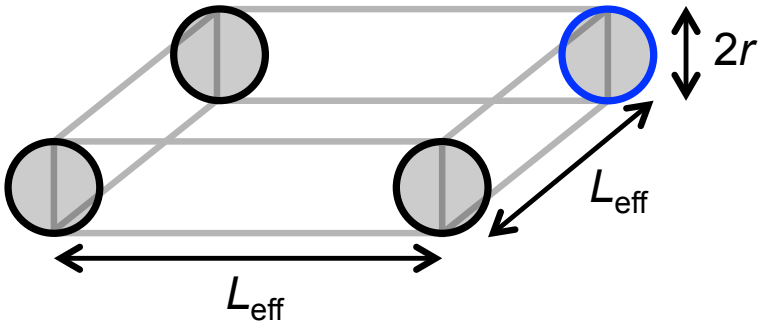


Figure 7.18: Configuration of four coplanar inclusions for estimating the effective average obstacle separation L_{eff}. As the volume indicated contains precisely one inclusion, it must be approximately equal to the reciprocal of the 3D inclusion number density n.

to the area of a more general quadrilateral of any four nearby coplanar inclusions. The orientation of the plane defined by all four inclusions is not arbitrary, but corresponds to pre-defining a specific plane in 3D space. Hence the side length of the square of inclusions is approximately equal to L_{eff}, the effective average obstacle separation on a pre-defined 2D plane. The volume defined by the four inclusions as illustrated in the schematic contains precisely one inclusion, i.e. it is analogous to a primitive unit cell, but of inclusions rather than atoms. This volume is simply equal to $2r \cdot L_{\text{eff}}^2$. Furthermore, as this volume contains one inclusion, it must also be approximately equal to the reciprocal of the 3D inclusion number density n. Equating these two expressions for the volume yields

$$2r \cdot L_{\text{eff}}^2 = \frac{1}{n}, \tag{7.6}$$

and hence $L_{\text{eff}}(n, r)$ is given by

$$L_{\text{eff}}(n, r) = \left(\frac{1}{2r \cdot n}\right)^{\frac{1}{2}}. \tag{7.7}$$

Finally, the expression for the estimated strain rate becomes

$$\dot{\varepsilon} = \rho b \frac{L_{\text{eff}}}{t_{\text{unpin}}} = \rho b \frac{1}{t_{\text{unpin}}} \left(\frac{1}{2r \cdot n}\right)^{\frac{1}{2}}. \tag{7.8}$$

In the unpinning time simulations performed, L_{eff} was fixed by the configuration of the inclusions, and the inclusion radius r was also fixed in all but the simulations in

which it was the independent variable of interest (§ 7.3.4). Clearly, fixing both L_{eff} and r necessarily fixes n, and fixing L_{eff} but changing r requires n to vary accordingly. In these simulations, (7.8) shows that the estimated strain rate is simply inversely proportional to the simulated unpinning time, and varies proportionally with choice of dislocation density ρ.

§ 7.5.4 studies the way in which the estimated creep strain rate changes when varying either the inclusion radius, number density or volume fraction V_{frac}, whilst allowing L_{eff} to vary accordingly, using (7.8). For each of the studies one variable must be held constant whilst another is varied, and the third varies parametrically with the independent variable. This is done using the simulated unpinning time data available, for which L_{eff} was fixed. It is assumed, not unreasonably, that using these simulated unpinning times together with (7.8) accurately capture the creep strain rate variation with one of (r, n, V_{frac}) whilst another is fixed.

Throughout § 7.5, the estimated creep strain rate is plotted using the simulated unpinning time data, and the (average) dislocation density ρ of 2.2×10^{15} m^{-2}. This value is the dislocation density captured by the initial dislocation loop in the simulations, and is consistent with dislocation densities of $\sim 10^{15}$ m^{-2} observed in 80% cold-rolled ODS EUROFER (Renzetti et al., 2012). However, (7.8) can be used to estimate the creep strain rate were ρ to be different, for example $\sim 10^{14}$ m^{-2}, as observed in a hot-worked RAFM ODS alloy (Zhang et al., 2015), or $\sim 10^{13}$ m^{-2}, which is not unreasonable for non-worked, as hot isostatically pressed (HIPed) RAFM alloys, which have been observed to have "relatively low" dislocation densities (He et al., 2012; Oksiuta et al., 2014).

7.5 Creep strain rate analysis

7.5.1 Dependence on temperature

Figure 7.19 shows the temperature dependence of the estimated thermal creep strain rate from 300–700 °C, for the dislocation density of 2.2×10^{-15} m^{-2}. Both an applied σ_{12} shear load of 410 MPa and an applied σ_{11} compressive load of 820 MPa are shown at five different temperatures, together with two different σ_{12} and one different σ_{11} values at 500 and 700 °C, in order to indicate the relatively small effect the value of the load has on the estimated creep strain rate when compared to the effect of changing the temperature.

The plot clearly demonstrates the very strong temperature dependence of the thermal

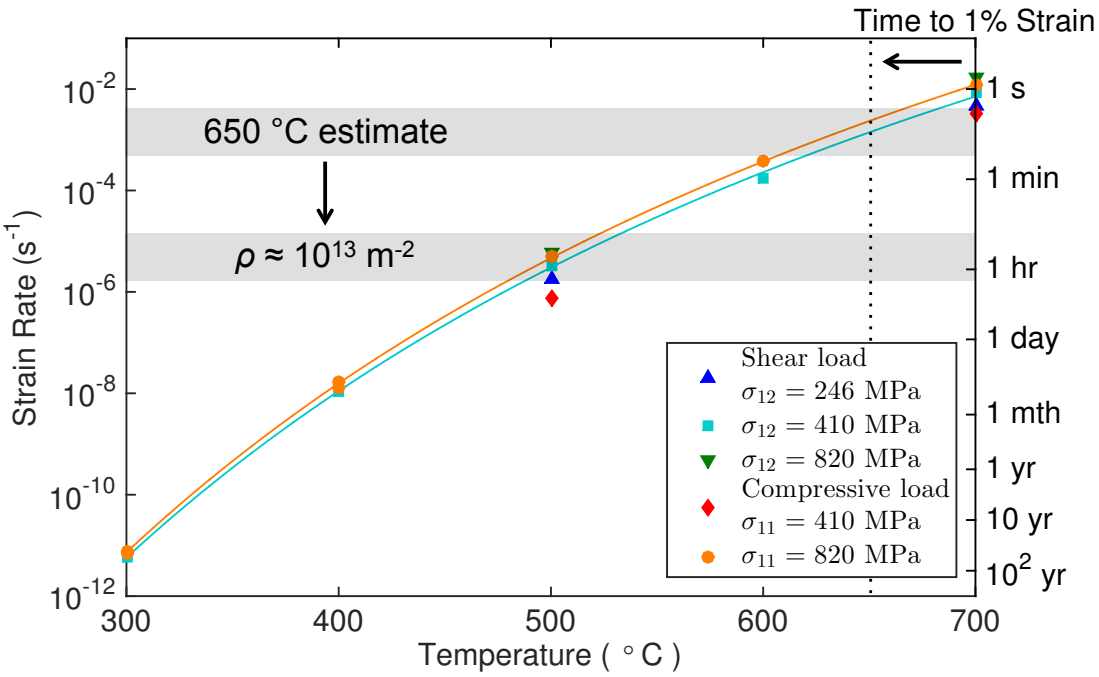


Figure 7.19: Temperature has a very strong effect on the creep strain rate when applying either a σ_{12} shear or a σ_{11} compressive load, as expected for thermal creep. The value of the load has a relatively small effect on the creep strain rate when compared to the temperature effect. The time to 1% strain is of the order of seconds at 700 °C, hours at 500 °C, and decades at 300 °C, for a dislocation density ρ of 2.2×10^{-15} m^{-2}. If $\rho \approx 10^{-13}$ m^{-2} instead, the data is shifted down the plot by just over two orders of magnitude. The method of estimating the order of magnitude of the strain rate for this lower value of ρ at 650 °C is indicated on the plot.

creep rate, as is expected for a thermal vacancy mediated climb process. The time to 1% strain is seconds at 700 °C, whereas it is hours at 500 °C and decades at 300 °C. However, this is proportional to the dislocation density ρ in (7.8). For example, were ρ to be $\sim 10^{14}$ m^{-2} instead, then the time to 1% strain would be minutes at 700 °C, days at 500 °C and >100 years at 300 °C.

A prediction of the order of magnitude of the creep strain rate at a given temperature can be made using figure 7.19. The value of this prediction will depend on the specifics of the applied load, together with those of the obstacle size, number density and volume fraction, but as is discussed throughout this section, these have a relatively small effect on the thermal creep strain rate estimation compared to a change in the temperature. As can be seen from the figure, a shift in the temperature of just 50 °C leads to change in the predicted creep strain rate (for a given load and set of dispersion properties) of at least one order of magnitude.

Yu et al. (2005) have observed a steady state creep strain rate of 1.45×10^{-6} s^{-1} in ODS EUROFER 97 at 650 °C subjected to an applied tensile stress of 200 MPa. The creep strain rate predicted by figure 7.19 at a temperature of 650 °C is $\sim 10^{-3}$ s^{-1} (as indicated on the plot) for the dislocation density of 2.2×10^{-15} m^{-2}, which is ~3 orders of magnitude higher than the experimental result. However, the sample Yu et al. tested was non-worked, as HIPed material (rather than a cold-worked material), so assuming a lower dislocation density of $\sim 10^{13}$ m^{-2} is appropriate. Using this value instead, the predicted creep strain rate becomes $\sim 5 \times 10^{-6}$ s^{-1} (again as indicated on the plot), which agrees with the order of magnitude of their experimental result.

This provides some evidence that the observed creep response of (as HIPed) ODS alloys is dominated by the bulk diffusion of thermal vacancies to dislocations pinned by the oxide particles, allowing them to climb over these obstacles, unpin from them, and glide away to the next pinned configuration. Both the diameter of 4.6 nm and number density of 3.7×10^{23} m^{-3} of the impenetrable obstacles in the simulations conducted here are representative of real oxide dispersions (Gorley, 2014). The average particle size and number density in the ODS EUROFER 97 tested by Yu et al. is unknown, as Schäublin et al. (2006) did not measure it. Schäublin et al. do present a high resolution

micrograph of a single oxide particle with a radius of ∼9 nm, but it is unlikely that this relatively large particle is representative of the average particle size, as the micrograph is shown in order to demonstrate the lack of coherence seen between the oxide and the matrix, which necessarily requires as large an oxide particle as can be found.

However, the volume fraction of 1.9% Y_2O_3 particles simulated, and hence the yttrium content of 0.94 wt%, is somewhat high — for example, the ODS EUROFER used by Yu et al. contained 0.3 wt% of Y_2O_3 particles, corresponding to 0.24 wt% of yttrium. However, decreasing the obstacle number density or radii will necessarily lead to a decrease in the Y wt% captured by this model. The effect this has on the dispersion properties, and the predicted creep strain rate, will be discussed in § 7.5.4. Firstly, however, the load dependence of the predicted creep strain rate is examined in the next section.

7.5.2 Dependence on applied load

Figure 7.20 shows the effect varying the value of an applied σ_{12} shear or σ_{11} compressive load has on the predicted creep strain rate at 700 °C, for the higher dislocation density of 2.2×10^{-15} m^{-2}. The data clearly exhibit a linear dependence on the applied load. The zero strain rate intercept of the σ_{12} shear load fit is −26.5 MPa, but enforcing a 0 MPa intercept results in a linear fit which is just as consistent with the data points. In contrast, the σ_{11} compressive load clearly has a non-zero intercept, which comes to 292 MPa.

As explained in § 7.3.3, the inverse dependence of the dislocation-inclusion unpinning time — and hence this linear dependence of the predicted strain rate — on the applied load is expected from the linear form of the climb mobility law. A striking feature of figure 7.20 is the very similar gradients for the two different types of loading, both of $\sim 2 \times 10^{-5}$ s^{-1}/MPa. Futhermore, the non-zero intercept in the σ_{11} compressive load was suggested to be an artefact of these specifc simulations involving an initial dislocation loop. In § 7.3.3 it was argued that in a realistic situation there will be no threshold load for unpinning to occur.

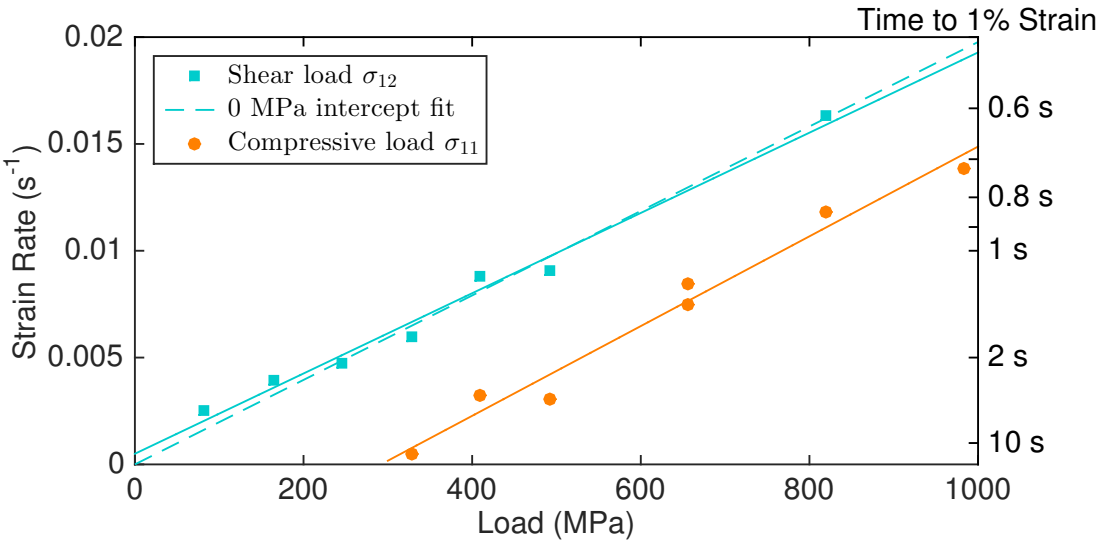


Figure 7.20: The predicted creep strain rate varies linearly with the value of an applied σ_{12} shear or σ_{11} compressive load, although the two cases have different zero strain rate intercepts. If the dislocation density were $\sim 10^{13}$ m^{-2} (instead of 2.2×10^{-15} m^{-2}), the strain rate scale would be $\sim 10^{-5}$ s^{-1}. Alternatively, the time to 1% strain would be of the order of hours if the temperature were 500 °C (instead of 700 °C), and decades if it were 300 °C.

Considering both these factors, the creep strain rate in a real ODS material is predicted by these simulations to vary linearly with an applied load at a given temperature and dislocation density, roughly following the fit of the σ_{12} data. As usual, for these simulations the temperature was 700 °C, and the dislocation density for the strain rate calculation was 2.2×10^{-15} m^{-2}. Under these conditions, estimating the strain rate due to an applied load of 200 MPa (for the experimental comparison) simply means dividing the σ_{12} strain rate at 410 MPa by just over two, which results in an estimate of $\sim 5 \times 10^{-3}$ s^{-1}. Following through the reasoning in § 7.5.1 as indicated in figure 7.19 — in which the strain rate estimate is reduced by a factor of $\sim 2.2 \times 10^{-3}$ — leads to a decrease in the estimated strain rate for the ODS EUROFER comparison by a factor of just over two, resulting in $\sim 2 \times 10^{-6}$ s^{-1}. Not only is this once more the same order of magnitude as the experimental value of Yu et al. of 1.45×10^{-6} s^{-1}, but it is closer still. This is more encouraging evidence that some real physics has been captured by the present models in these simulations. However, the issue of the difference between the volume fraction/yttrium content of the obstacles captured by the simulations and that of the experimental alloy still needs to be addressed.

7.5.3 Dependence on obstacle size

The predicted creep strain rate data for different values of the inclusion radius, whilst keeping the effective obstacle separation constant at 24 nm, are shown in figure 7.21. The subsequent variation in the inclusion number density and volume fraction is also shown on the plot.

The predicted creep strain rates for the σ_{12} shear and σ_{11} compressive loads, both of 820 MPa, vary inversely with the inclusion radius, as larger obstacles require more climb to occur between unpinning events, reducing the overall strain rate. The data points for the three different load values for the default inclusion radius of 2.3 nm are shown, and an inverse relationship is extrapolated from them. This demonstrates the fact that increasing the inclusion radius also inversely decreases the range of unpinning times at different load values. For the range of inclusion radii of 0–5.5 nm shown, the predicted creep strain rates are all within one order of magnitude of each other.

Using the trends plotted in figure 7.21, the change in the predicted creep strain rate, and the particle radius and number density, for the yttrium content of 0.3 wt% (rather than 0.94 wt%) can be estimated for this case of a fixed effective obstacle separation of 24 nm. A yttrium content of 0.3 wt% is commonly used in experimental ODS alloys, as is the case of the ODS EUROFER 97 studied by Yu et al.. This yttrium content corresponds to a decrease in the particle radius from 2.3 to ∼1.3 nm (as indicated on the bottom plot in the figure), and an increase in the particle number density from 3.7 to $\sim 6 \times 10^{23}$ m^{-3} (as indicated on the middle plot). Hence the predicted creep strain rates for the 2.3 nm particle case increase, but by a factor of less than two. This increases the estimated creep strain rate for a 200 MPa load at 650 °C in ODS EUROFER 97 of $\sim 2 \times 10^{-6}$ s^{-1} in § 7.5.2 to $\sim 4 \times 10^{-6}$ s^{-1}, which is still reasonably consistent with the experimental value of Yu et al. of 1.45×10^{-6} s^{-1}. The smaller particle size and higher number density also remain consistent with real oxide dispersions.

However, the dependence of the estimated creep strain rate on the particle radius and number density (in addition to the simulated unpinning time data) captured by (7.8) allows the constraint of a fixed effective obstacle separation to be circumvented, and the

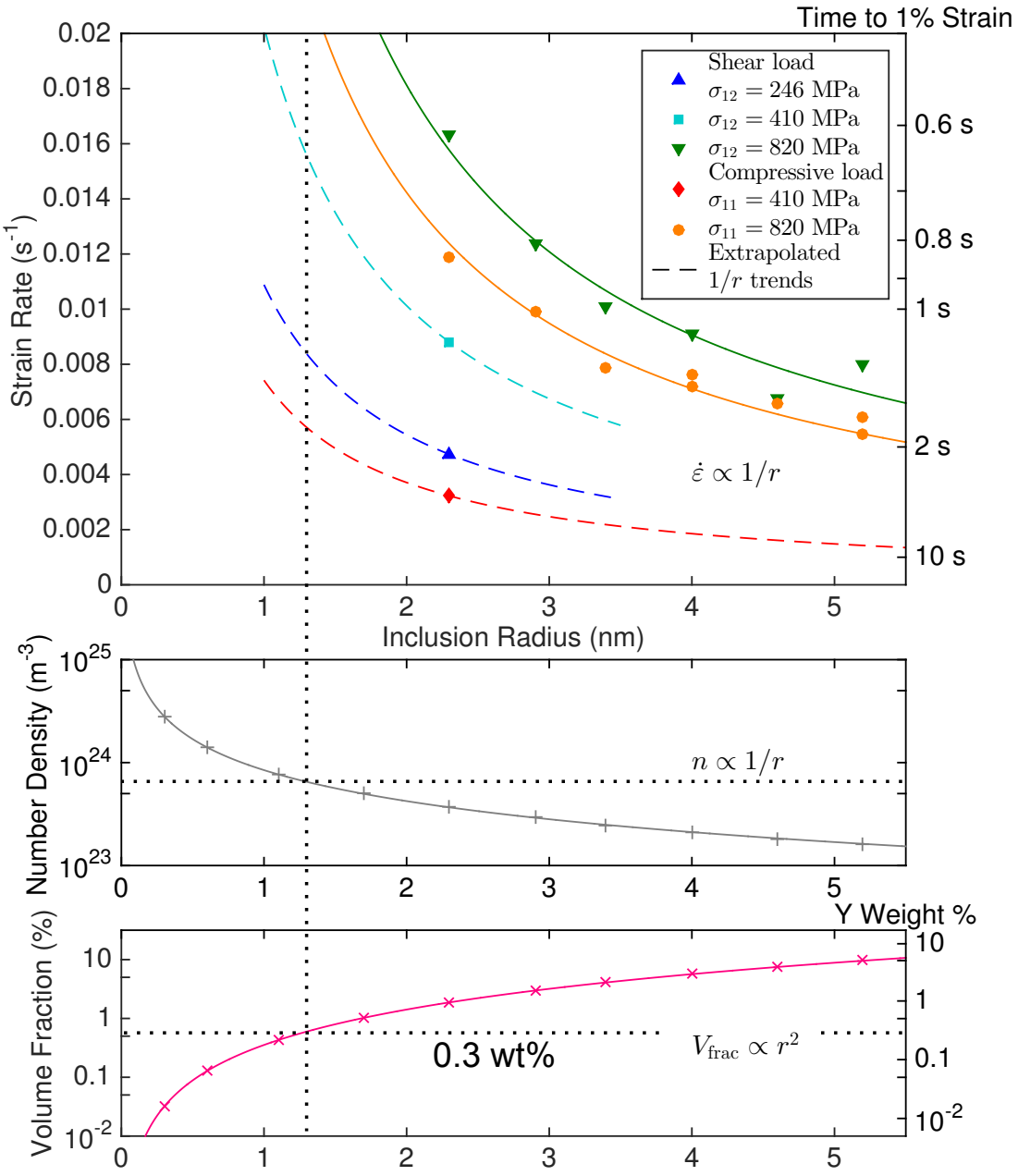


Figure 7.21: The predicted creep strain rate varies inversely with inclusion radius when applying a σ_{12} shear or σ_{11} compressive load. As these simulations were carried out at fixed effective obstacle separation, the inclusion number density and volume fraction/yttrium content vary with the radius, which is also shown. If the dislocation density were $\sim 10^{13}$ m^{-2} (instead of 2.2×10^{-15} m^{-2}), the strain rate scale would be $\sim 10^{-5}$ s^{-1}. Alternatively, the time to 1% strain would be of the order of hours if the temperature were 500 °C (instead of 700 °C), and decades if it were 300 °C. The case of a yttrium content of 0.3 wt% is indicated by the dotted lines.

effects of varying particle radius, number density and volume fraction parametrically can be investigated

7.5.4 Parametric dependences: obstacle size, number density and volume fraction

Dependence on obstacle size for fixed number density

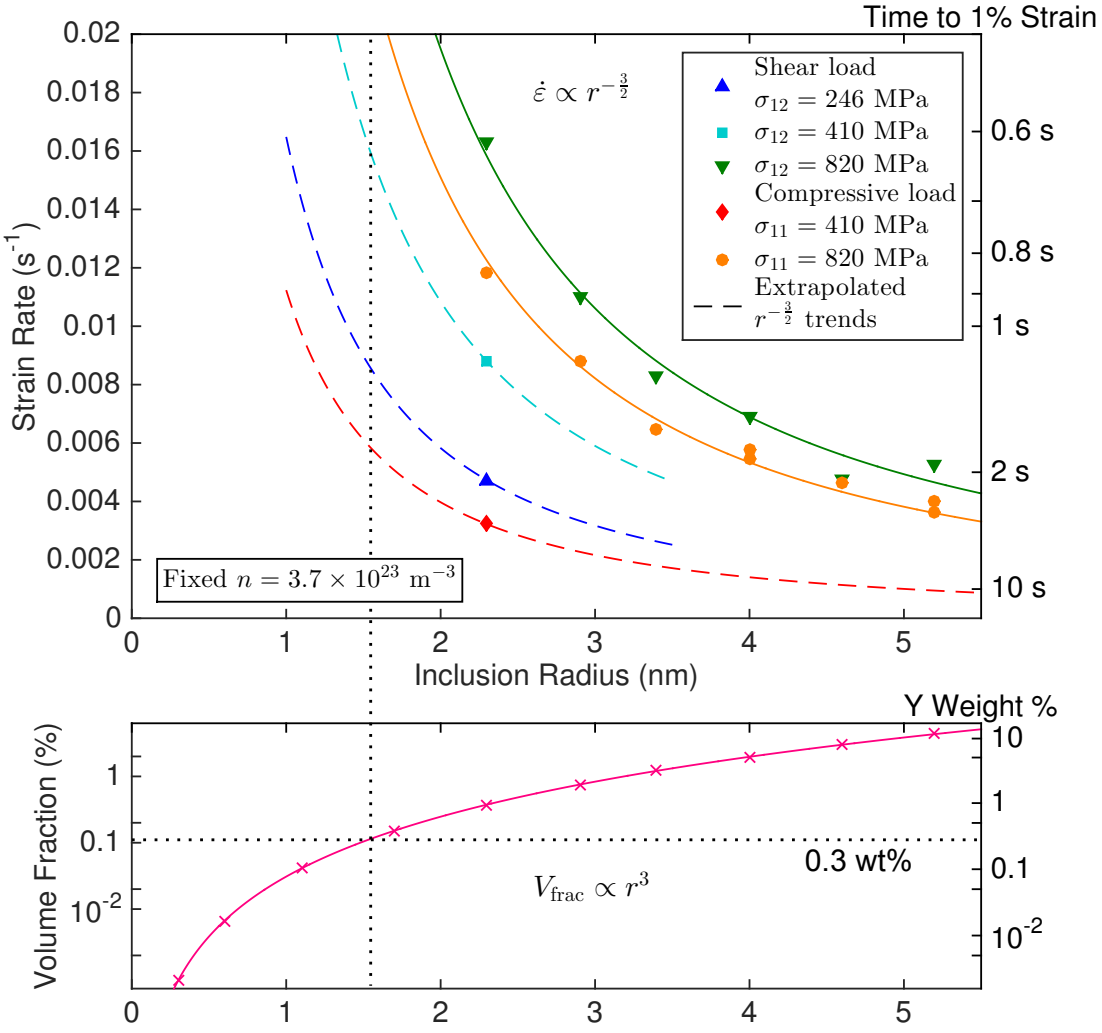


Figure 7.22: For the case of varying the obstacle radius whilst the number density is held constant, the predicted creep strain rate exhibits a stronger dependence on r of the form $\dot{\varepsilon}(r)\big|_n \propto r^{-\frac{3}{2}}$. In this case, the volume fraction $V_{\text{frac}}(r)\big|_n \propto r^3$. The case of a yttrium content of 0.3 wt% is indicated by the dotted lines.

If, as in figure 7.21, the obstacle radius r is varied, but now the number density n is held constant — in this case at 3.7×10^{23} m^{-3} — the predicted creep strain rates exhibit a

stronger dependence on r of the form $\dot{\varepsilon}(r)\big|_n \propto r^{-\frac{3}{2}}$, which is shown in figure 7.22. In this case of a fixed n, the particle volume fraction as a function of r, $V_{\text{frac}}(r)\big|_n$, is given by

$$V_{\text{frac}}(r)\Big|_n = \frac{4}{3}\pi n \cdot r^3, \tag{7.9}$$

which is also plotted.

The differences between this figure and the previous one are relatively unremarkable however. For the 0.3 Y wt% experimental comparison, the representative obstacle radius is increased slightly to ∼1.6 nm, but the strain rate estimate remains $\sim 4\times10^{-6}$ s^{-1}, as was the case in § 7.5.3. This is because as the radius has increased from ∼1.3 to ∼1.6 nm, it is slightly closer to 2.3 nm. When estimating the factor of increase in the strain rates from the 2.3 nm case for the ∼1.6 nm case, this counters the effect of the stronger r dependence exhibited by the strain rate, resulting in a similar increase by a factor of less than two as in § 7.5.3.

Dependence on obstacle number density for fixed size

If instead the obstacle number density n is varied, and the obstacle radius r is held constant — in this case at 2.3 nm — the predicted creep strain rates exhibit a power law dependence on n of the form $\dot{\varepsilon}(n)\big|_r \propto n^{-\frac{1}{2}}$, which is shown on a log-log scale in figure 7.23. Because r is fixed, there is only one data point available for each of the loading conditions simulated. However, the form of (7.8) gives the n dependence of the estimated strain rate explictly, and allows demonstrative plots to be extrapolated from these single data points.

In this case of a fixed r, the particle volume fraction as a function of n, $V_{\text{frac}}(n)\big|_r$, is given by

$$V_{\text{frac}}(n)\Big|_r = \frac{4}{3}\pi r^3 \cdot n, \tag{7.10}$$

i.e. it varies proportionally with n. This is also plotted in figure 7.23 (on a log-log scale).

For the 0.3 Y wt% experimental comparison, the representative obstacle number density must be decreased from 3.7×10^{23} m^{-3} to $\sim 1\times10^{23}$ m^{-3}. At this lower number density,

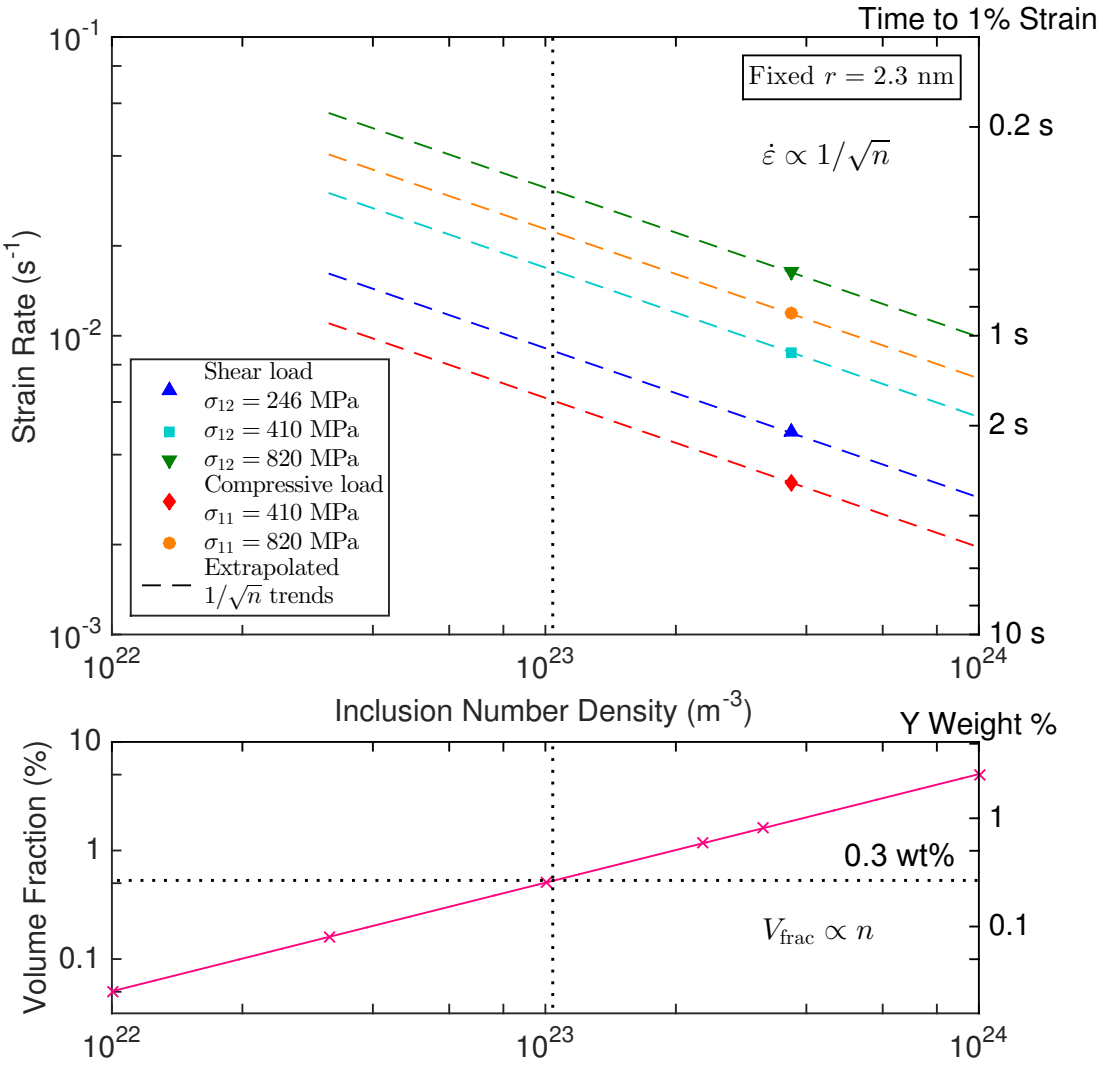


Figure 7.23: For the case of varying the obstacle number density whilst the obstacle radius is held constant, the predicted creep strain rate exhibits a power law dependence on n of the form $\dot{\varepsilon}(n)\big|_r \propto n^{-\frac{1}{2}}$, which is plotted here on a log-log scale. In this case, the volume fraction is directly proportional to n (also shown on a log-log scale). The case of a yttrium content of 0.3 wt% is indicated by the dotted lines.

the strain rates are predicted to increase by a factor of about two from their values when $n = 3.7 \times 10^{23}$ m^{-3}. In this case, the strain rate estimate for a 200 MPa load at 650 °C in ODS EUROFER 97 becomes[43] $\sim 5 \times 10^{-6}$ s^{-1}, which is once more consistent with the experimental value of Yu et al. of 1.45×10^{-6} s^{-1}. The lower number density of $\sim 1 \times 10^{23}$ m^{-3} in this particular estimate is also not unreasonable.

[43] The estimated strain rate of $\sim 2 \times 10^{-6}$ s^{-1} from § 7.5.2 is simply multiplied by the factor of about two.

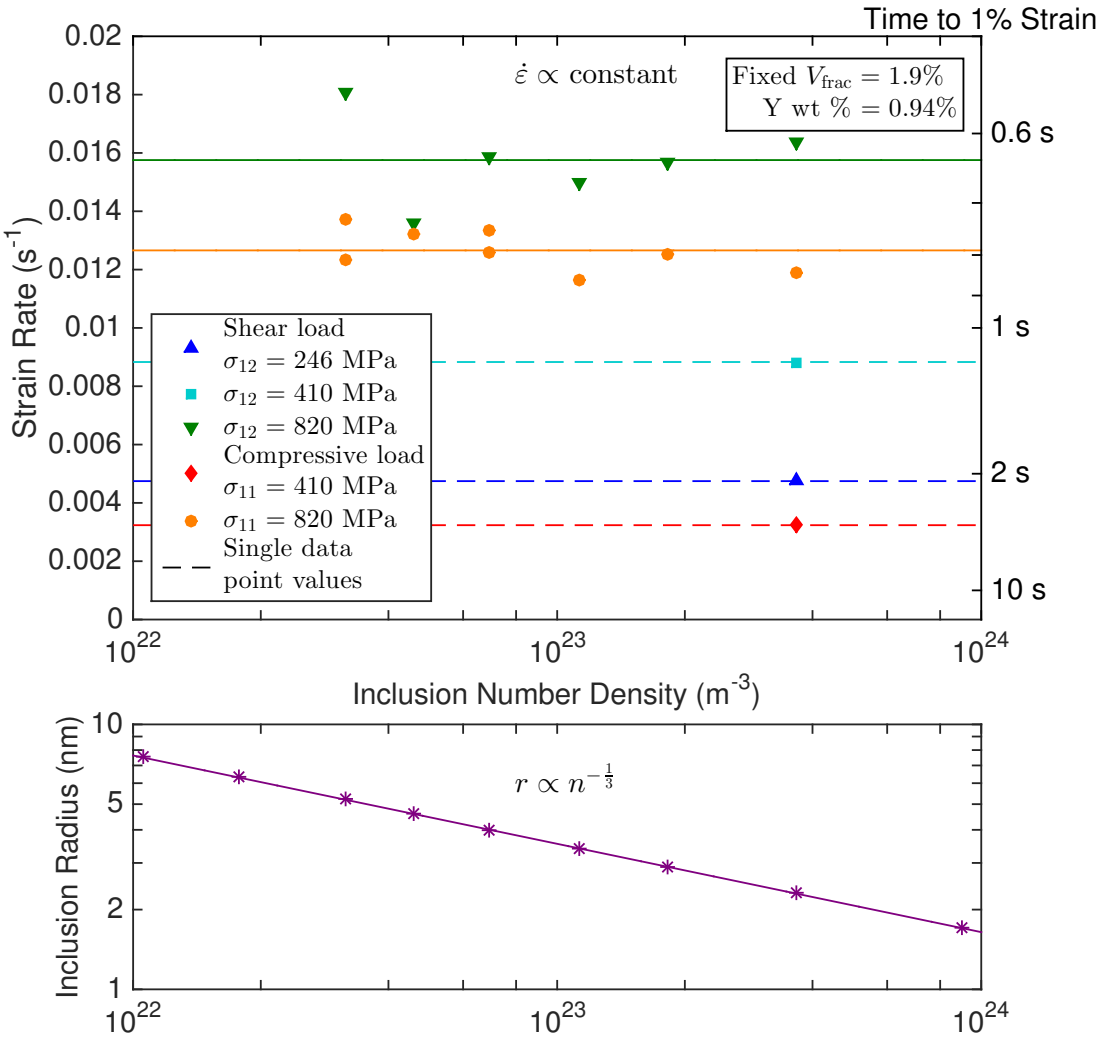


Figure 7.24: For the case of varying the obstacle number density whilst the volume fraction is held constant, the predicted creep strain rate exhibits no dependence on the number density. This is a remarkable result. In this case, the inclusion radius $r(n)\big|_{V_{\text{frac}}} \propto n^{-\frac{1}{3}}$.

Dependence on obstacle number density for fixed volume fraction

If, as in the previous plot, the obstacle number density n is varied, but now the obstacle volume fraction/yttrium content is held constant — in this case at 1.9%/0.94 Y wt% — the predicted creep strain rates exhibit no dependence on the number density whatsoever, as shown in figure 7.24. In this case of a fixed V_{frac}, the obstacle radius as a function of n, $r(n)\big|_{V_{\text{frac}}}$, is given by

$$r(n)\Big|_{V_{\text{frac}}} = \left(\frac{3V_{\text{frac}}}{4\pi}\right)^{\frac{1}{3}} \cdot n^{-\frac{1}{3}}, \tag{7.11}$$

which is also plotted (on a log-log scale).

This is quite remarkable: the simulations using the present models predict that for a fixed volume fraction of impenetrable obstacles, the specifics of their average size and number density should not affect the steady state creep rate for a given temperature and load.

Furthermore, this implies that when using the previous two plots to estimate the strain rates correpsonding to the 0.3 Y wt% case, the resulting differences in r and n should not affect the strain rate estimation. This was indeed found to be the case, with the estimation experimental strain rate comparison coming to $\sim 4\times10^{-6}$ s^{-1} using the r dependence at fixed n (figure 7.22), and $\sim 5\times10^{-6}$ s^{-1} using the n dependence at fixed r (figure 7.23).

It is however worth considering the limiting cases of n and r for fixed V_{frac}, and whether the approximately uniform creep strain rates captured here will persist in these limits.

As n becomes very large, the obstacle radii become very small, until the obstacles consist of only a few atoms each. In this limit the strain rate should still remain uniform, as gliding dislocations will still become pinned on these few-atom obstacles, and still unpin from them via climb, in the same was as with larger obstacles. Values of n (and r) larger (and smaller) than this are unphysical, i.e. for a fixed obstacle volume fraction, the limit of n is not inifinite, but correpsonds to this case of small obstacles of only a few atoms each.

As n becomes very small, the obstacle radii become very large, the limit of which is only one, very large obstacle. Approaching this limit, the strain rate will become lower than previously, because some of the gliding dislocations will not become pinned on any obstacles (those whose glide planes do not intersect any of the few obstacles remaining) before exiting at the surface of the material or reaching a different obstacle where it becomes fully pinned, such as a grain boundary. In this case, the density of dislocations becoming pinned and subsequently unpinning via climb is effectively reduced, hence reducing the creep strain rate via the Orowan equation (7.5). Estimating the values of n and r for which the creep strain rate will start to exhibit a decrease is challenging, as

it depends on a number of factors, including individual grain size, obstacle geometry, and the nature of the obstacle distribution — be it random, or a regular array of some kind (such as in nickel base superalloys).

However, both these limits are extremes, and the values n and r explored in figure 7.24 broadly capture the range of obstacle number densities and radii seen in experimental ODS alloys.

Dependence on obstacle volume fraction for fixed number density

Finally, if the obstacle volume fraction V_{frac} is varied, and the number density n is held constant — again at 3.7×10^{23} m^{-3} — the predicted creep strain rates exhibit a power law dependence on V_{frac} of the form $\dot{\varepsilon}(V_{\text{frac}})\big|_n \propto V_{\text{frac}}^{-\frac{1}{2}}$, which is shown in figure 7.25. In this case of a fixed n, the obstacle radius as a function of V_{frac}, $r(V_{\text{frac}})\big|_n$, is given by

$$r(V_{\text{frac}})\Big|_n = \left(\frac{4}{3}\pi n\right)^{-\frac{1}{3}} \cdot V_{\text{frac}}^{\frac{1}{3}} \tag{7.12}$$

which is also plotted. This is simply the same relationship as shown in the lower plot in figure 7.22, which is a plot of $V_{\text{frac}}(r)\big|_n$, but with the axes exchanged.

For the 0.3 Y wt% experimental comparison, the increase in the strain rate compared to the 0.94 Y wt% data points can be seen to be just over a factor of two. Hence the strain rate estimate for comparison with the experimental value of Yu et al. of $1.45{\times}10^{-6}$ s^{-1} for a load of 200 MPa at 650 °C is this time[44] $\sim 6{\times}10^{-6}$ s^{-1}, once more in agreement with the order of magnitude, and approximately equal to the previous estimates of $\sim$4 and $\sim 5{\times}10^{-6}$ s^{-1}, as expected (since the plot in figure 7.24 implied that the data exhibits no change in the predicted strain rate as r and n are varied whilst V_{frac} remains fixed). The estimated obstacle radius for 0.3 Y wt% in this fixed n case comes to $\sim$1.3 nm, which is the same as the previous estimate of $\sim$1.3 nm from figure 7.21, and similar to the previous estimate of $\sim$1.6 nm from figure 7.22. All of these estimated obstacle radii are consistent with experiment (Gorley, 2014).

[44] The estimated strain rate of $\sim 2{\times}10^{-6}$ s^{-1} from § 7.5.2 is simply multiplied by the factor of just over two.

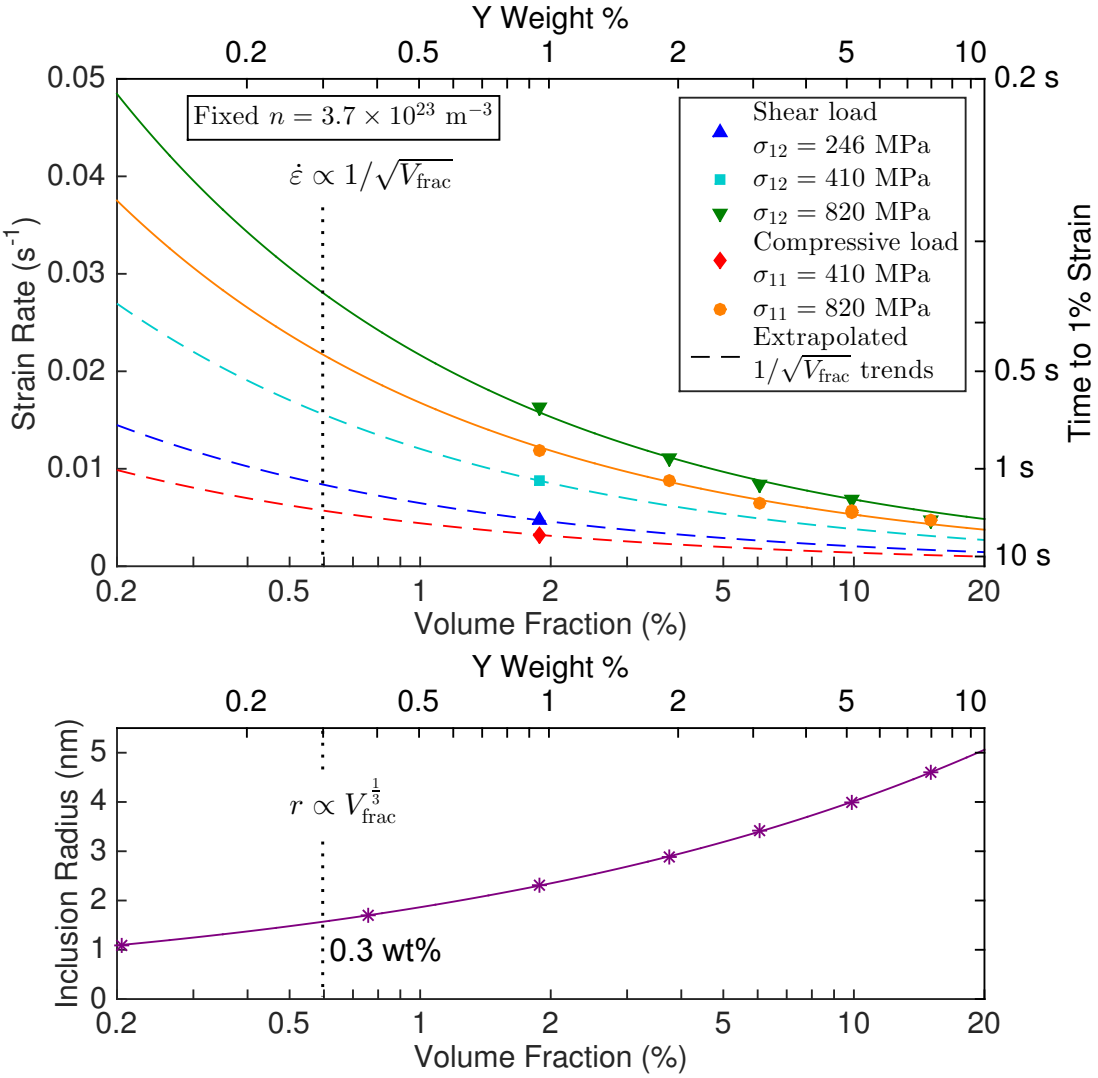


Figure 7.25: For the case of varying the obstacle volume fraction/yttrium content whilst the number density is held constant, the predicted creep strain rate exhibits a power law dependence on V_{frac} of the form $\dot{\varepsilon}(V_{\text{frac}})\big|_n \propto V_{\text{frac}}^{-\frac{1}{2}}$. In this case, the obstacle radius $r(V_{\text{frac}})\big|_n \propto V_{\text{frac}}^{\frac{1}{3}}$. The case of a yttrium content of 0.3 wt% is indicated by the dotted lines.

Parametric dependences summary

The different forms of the predicted strain rate dependence on the different dispersion properties as these are varied parametrically with each other are summarised in table 7.1, together with the parametric dependences themselves.

Independent quantity	Fixed quantity	Strain rate dependence	Dependent quantity	Figure
Obstacle radius r	L_{eff}	$\propto r^{-1}$	$n \propto r^{-1}$ $V_{\text{frac}} \propto r^2$	7.21
	n	$\propto r^{-\frac{3}{2}}$	$V_{\text{frac}} \propto r^3$	7.22
	V_{frac}	constant	$n \propto r^{-3}$	—
Number density n	r	$\propto n^{-\frac{1}{2}}$	$V_{\text{frac}} \propto n$	7.23
	V_{frac}	constant	$r \propto n^{-\frac{1}{3}}$	7.24
Volume fraction V_{frac}	n	$\propto V_{\text{frac}}^{-\frac{1}{2}}$	$r \propto V_{\text{frac}}^{\frac{1}{3}}$	7.25
	r	$\propto V_{\text{frac}}^{-\frac{1}{2}}$	$n \propto V_{\text{frac}}$	—

Table 7.1: The predicted strain rate dependences on the different dispersion properties, together with their parametric dependences.

The two cases which were not plotted: varying r for fixed V_{frac}, and varying V_{frac} for fixed r; are both included in the table. This is done by using the expression given in (7.8) for $L_{\text{eff}}(r, n)$ in the same way as in all the strain rate calculations, together with the result that $\dot{\varepsilon} \propto r^{-1}$ in the fixed L_{eff} case. In the fixed r cases (only one of which was plotted), each loading condition only has one data point, so the trends necessarily have to be extrapolated, again using the form of (7.8).

The most striking result of these investigations is the prediction that the creep strain rate of an alloy which is reinforced with impenetrable particles depends on the temperature, applied load, and particle volume fraction, but the values of the particle size and number density should not affect the creep response. This is perhaps surprising, but it is not unreasonable. Increasing the particle size at fixed volume fraction leads to an increase in the amount of climb which needs to occur for unpinning to take place, leading to an increase in the unpinning time, and a decrease in the creep strain rate. However,

the number density necessarily decreases in this scenario, which increases the (effective) obstacle separation, and hence increases the plastic strain accumulated per unpinning event. This work suggests these two effects balance each other out equally, at least for the assumption of impenetrable obstacles which are non-misfitting.

In terms of designing ODS alloys to have increased creep resistance by varying their dispersion properties, this work suggests increasing the particle volume fraction, i.e. the alloy's oxide content, will decrease the resultant creep rate, and that the specifics of the oxide size and number density do not have an effect. However, as the creep rate $\dot{\varepsilon} \propto V_{\text{frac}}^{-\frac{1}{2}}$, increasing the yttrium content from 0.3 to 0.5 wt% — the highest yttrium content seen in conventional ODS alloys — results in a decrease in the creep rate of only ∼25% (estimated from figure 7.25). For a decrease of 50% in the creep rate, a yttrium content of 1–2% would be required, assuming purely Y_2O_3 particles.

Furthermore, another significant outcome of these dependences is the relatively small effect the dispersion properties have on the thermal creep strain rates predicted from the simulated unpinning time data, at least for the range of dispersion properties considered. After these investigations, the estimated strain rate at 650 °C, for an applied stress of 200 MPa, a dislocation density of $\sim 10^{13}$ m^{-2}, and now with a yttrium content of 0.3 wt% still comes to $\sim 5 \times 10^{-6}$ s^{-1}. This is consistent with the experimental value of Yu et al. of 1.45×10^{-6} s^{-1}, especially as this is just an estimate of the order of magnitude of the strain rate.

7.5.5 Dependence on defect supersaturation

The estimated creep strain rates due to a range of equal irradiation-induced supersaturations of vacancies and interstitials as a function of temperature are shown in figure 7.26, together with the data for a σ_{12} shear load of 410 MPa and a σ_{11} compressive load of 820 MPa from figure 7.19 for comparison.

The creep strain rate curves for the applied load cases in figure 7.26 correspond to thermal creep, whereas those plotted for the defect supersaturations capture irradiation creep behaviour, at least the contribution to irradiation creep due to the absorption of the damage point defects at the obstacle-pinned dislocations in a particle-reinforced material. Thus the supersaturations considered here represent the steady-state point defect populations which interact with the dislocations during irradiation. The dislocations are assumed to be perfect sinks for these point defects.

The most striking feature of figure 7.26 is that the creep strain rates due to defect supersaturations can be many orders of magnitude larger than the thermal creep rates, depending on the value of the supersaturations. Another important feature is the much weaker temperature dependence of the supersaturation curves. Whereas the time to 1% thermal creep strain varies from seconds at 700 °C up to decades at 300 °C, the (higher) supersaturation strain rates only decrease by about one order of magnitude over this range.

The dislocation density is the higher value of 2.2×10^{15} m^{-2}. Were it to be $\sim 10^{13}$ m^{-2} instead, all the curves shown would be shifted down by just over two orders of magnitude.

As explained previously for figure 7.15, the defect supersaturation curves are expected to continue successively down the plot for even lower supersaturations, resulting in even lower strain rates, many of which will lie below the thermal creep curves. The three blue arrows on the plot again indicate the cases in which the value of the defect supersaturation is below the thermal vacancy population at the given temperature.

The irradiation creep data points at the different temperatures are plotted again in

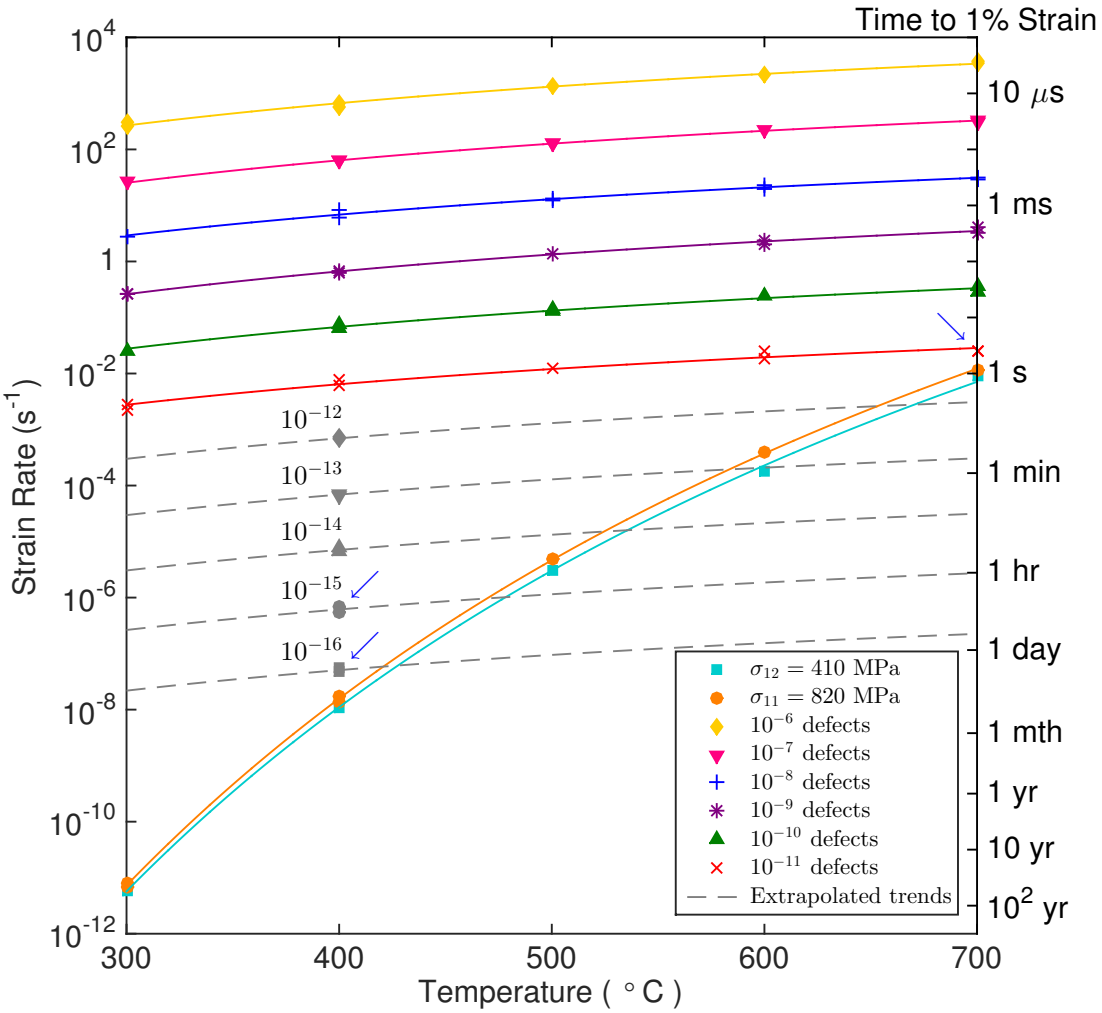


Figure 7.26: Defect supersaturations (shown in units of fractional atomic concentration) can result in irradiation creep strain rates which are orders of magnitude larger than the thermal creep in the applied load cases. The temperature dependence of the irradiation creep at a given supersaturation is much weaker than for thermal creep: the strain rate only increases by about one order of magnitude as the temperature is increased from 300 to 700 °C. This is to be expected for irradiation creep.

figure 7.27 as a function of the defect supersaturation. This serves to highlight how much more sensitive the creep strain rate is to a change in the defect supersaturation at a given temperature than vice versa, as described in detail for figure 7.16.

The curves shown in figure 7.26 suggest that irradiation creep will dominate over thermal creep in ODS alloys provided the steady-state defect supersaturations are high enough: $\geq 10^{-11}$ (fractional atomic concentration of) defects over the temperature range of 300–700 °C. However, for defect supersaturations $<10^{-11}$ defects, there will be a threshold

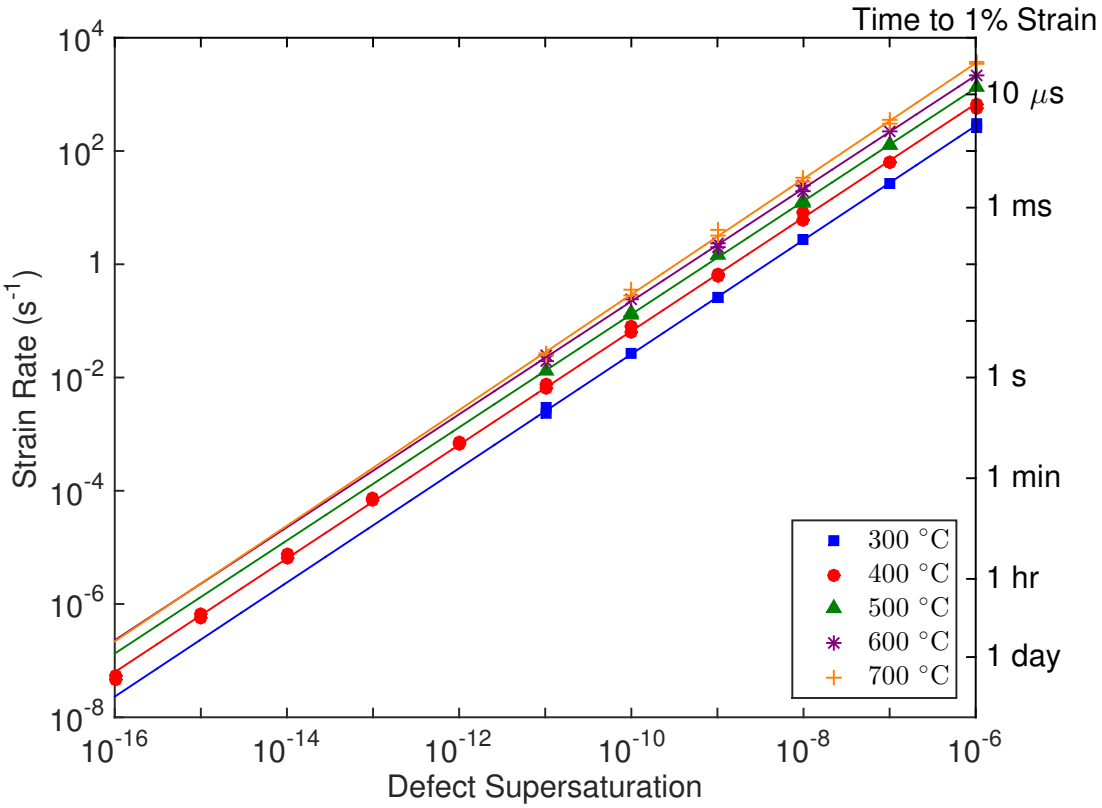


Figure 7.27: Increasing the defect supersaturation (in units of fractional atomic concentration) by a single order of magnitude at a given temperature increases the irradiation creep rate by one order of magnitude. The spread in the lines of different temperature from 300 to 700 °C is also only about one order of magnitude. Hence the irradiation creep rate is much more sensitive to the defect supersaturation at a given temperature than vice versa.

temperature above which thermal creep dominates. The value of this threshold temperature depends on the value of the defect supersaturations. For example, for 10^{-16} defects, the threshold temperature is ∼430 °C, and for 10^{-14} defects, it is ∼550 °C.

As discussed in chapter 3, finding a theoretical value for the steady-state defects supersaturations is very challenging. However, a lower bound of $\sim 10^{-16}$ defects was suggested from the in situ experimental observations of damage loops in non-ODS bcc iron under self-ion irradiation made by Xu (2013). In an ODS ferrous alloy, this corresponds to a lower bound for the irradiation-to-thermal creep threshold temperature of ∼430 °C (using the plot in figure 7.26). However, in real ODS alloys, the oxide particles are widely considered to act as sinks for the irradiation-induced point defects, so the supersaturations interacting with the dislocations could feasibly be smaller than this lower bound estimated from non-ODS data. This would lead to an irradiation-to-thermal

creep threshold temperature of lower than ∼430 °C.

Chen and Hoffelner (2009) observed irradiation creep dominating over thermal creep over the temperature range of 300–500 °C during in situ helium implantation of an ODS alloy, implying a higher lower bound of $\sim 10^{-14}$ defects interacting with the dislocations in similar ODS steels (again estimated using figure 7.26). Incidentally, they did not observe a significant change in the irradiation creep response between dispersions with different particle sizes and number densities[45], which is expected from the simulation results discussed in § 7.5.4.

Finally, figure 7.26 suggests that irradiation creep will dominate over thermal creep in ODS alloys at the fusion reactor operating temperature of ∼650 °C, provided the point defect supersaturations available to drive dislocation climb are $>10^{-12}$ defects, which was argued to be feasible in § 3.3.8. The resulting irradiation creep rate depends strongly on the value of the defect supersaturations, as illustrated in figure 7.27.

[45] Chen and Hoffelner compared a 0.4 Y_2O_3 wt% ODS alloy containing 2–3 nm sized dispersoids with a number density of 1.2×10^{24} m^{-3} with a 0.5 Y_2O_3 wt% one containing 28 nm sized dispersoids with a number density of 5.1×10^{20} m^{-3}.

7.6 Summary

In § 7.2 the simulation setup was described: four coplanar, impenetrable, spherical inclusions encircled by a coplanar shear dislocation loop, whose self-force acts to shrink it, driving the dislocations against the obstacles. Applied shear loads of different amounts acting to shrink (or expand) the shear loop were found to have little effect on the glide pinning time, provided the applied load combined with the loop's self-force is below the Orowan stress. Capturing both glide and climb — mediated by the bulk diffusion of both vacancies and interstitials as described in chapter 3 — using the dual time step method enables dislocation-inclusion unpinning via climb to be simulated. The three types of unpinning simulation performed were discussed in detail, namely an applied shear load, an applied compressive load, and no applied load but defect supersaturations present.

§ 7.3 analysed the effects of varying the temperature, applied load, obstacle size, and defect supersaturation on the simulated dislocation-inclusion unpinning times. They exhibited a very strong temperature dependence, as expected for a themal vacancy mediated process. In the applied load cases, this temperature dependence was seen to dominate over the effects of changing the applied load and obstacle size. Unpinning times due to the presence of defect supersaturations were seen to be far less temperature-dependent, and to vary inversely with the value of the defect supersaturations, as expected for an osmotic climb process.

A simple model for estimating the creep strain rate from the simulated dislocation-inclusion unpinning time data was described in § 7.4, which incorporates additional dependence on the dispersion properties and the dislocation density.

In § 7.5, creep strain rate estimates were carried out using the unpinning time data. There were a number of interesting results:

1. The thermal creep strain rates were seen to be strongly temperature-dependent, as expected.

2. The effect of varying the applied load was seen to have relatively small effect on

the creep rates, as the creep rates increased proportionally with the applied stress.

3. The dispersion properties were also seen to have relatively small effect on the creep rates. Remarkably, the creep rates exhibit no dependence on the particle size and number density for a given volume fraction of obstacles.

4. The creep rates vary inversely with the root of the particle volume fraction. Hence increasing the yttrium content from 0.3 to 0.5 wt% results in a decrease in the creep rate of only ∼25%.

5. An estimated thermal creep strain rate of $\sim 5 \times 10^{-6}$ s^{-1} for an appropriate set of conditions was compared to an experimentally measured value of 1.45×10^{-6} s^{-1} in ODS EUROFER 97, showing encouraging consistency between the models used in these simulations and reality.

6. The irradiation creep strain rates were seen to vary much less strongly with temperature, also as expected. The irradiation creep rates increase proportionally with the value of the point defect supersaturations available to drive dislocation climb.

7. Irradiation creep was seen to dominate over thermal creep in ODS alloys at the fusion reactor operating temperature of ∼650 °C, provided the irradiation-induced point defect supersaturations available to drive dislocation climb are $>10^{-12}$ defects.

8. The results of Chen and Hoffelner (2009), together with the estimated creep rates, indicate a lower bound of $\sim 10^{-14}$ defects during helium implantation of an ODS alloy.

9. The irradiation creep rate in ODS alloys under fusion reactor operating conditions is predicted to have the potential to be orders of magnitude larger than the thermal creep rate at this temperature, as it is proportional to the value of the steady-state point defect supersaturations available to drive dislocation climb, and these supersaturations are very challenging to estimate theoretically.

Chapter 8

Conclusions and further work

The unprecedented amounts of neutron irradiation experienced by the first wall and blanket in a tokamak, together with the high operating temperatures required, present a significant materials challenge. ODS steels are promising candidate structural materials for use in fusion (and Gen IV fission) reactors, but the physics behind their improved mechanical properties and irradiation resistance is poorly understood. This work investigates some of the nanoscale processes which occur in RAFM steels, and their particle-reinforced ODS counterparts, under both non-irradiation and irradiation conditions.

8.1 Theoretical modelling of dislocation climb

An expression for the climb velocity of an edge dislocation was derived using an existing point defect bulk diffusion model of climb (§ 3.2). The developed model captures climb mediated by both vacancies and interstitials, and incorporates the effect of supersaturations of these defects on the climb rate. Calculations were then carried out for bcc iron using this model (§ 3.3).

It was found that in the absence of any defect supersaturation, the model predicts that the climb of dislocations due to the climb component of the P–K force acting on them will be mediated by the bulk diffusion of the thermal vacancy defects, which is consistent with current thought. However, the model shows that the osmotic climb of dislocations

caused by the presence of equal steady-state supersaturations of vacancies and interstitials will instead be dominated by the interstitials, and hence will proceed in the direction of climb favoured by the absorption of interstitial defects at the dislocations. This is because the osmotic climb rate is proportional to the *relative* supersaturation of defects: the ratio of the supersaturation to the background thermal concentration. This ratio is significantly larger for interstitials than for vacancies of roughly equal supersaturations due to the larger interstitial formation energy. Steady-state defect supersaturations are expected under fusion neutron irradiation conditions, so this is an important result, but finding the magnitude of the effective supersaturations which interact with the dislocations theoretically or experimentally is very challenging, and they are not necessarily equal.

However, interstitial loops have been observed to dominate the damage loop population during in situ irradiation of bcc iron. It was argued that the preferential osmotic absorption of supersaturated interstitials over vacancies at damage loops provides a explanation for this observation, as predicted by the model when equal supersaturations are assumed (§ 3.3.5). The model also predicts that at high enough temperatures, and for low enough steady-state supersaturations (which corresponds to low enough irradiation dose rates), interstitial loops should not been seen either.

If this model is correct, then an experimental measurement of the temperature at which interstitial loops are no longer seen provides a measurement of the steady-state interstitial (and hence vacancy) supersaturation which is available to drive dislocation climb (§ 3.3.6). Comparison of the model with the available experimental data (§ 3.3.8) provides a lower bound of $\sim 10^{-16}$ fractional atomic concentration of defects for the steady-state defect supersaturations in the in situ self-ion irradiated bcc iron observed.

This model has some limitations: the formation and growth of damage proto-loops is not captured (although the preferential osmotic absorption of interstitials could also be applied to this problem), nor is the presence of other point defect sinks such as grain boundaries, free surfaces, and indeed dispersoids. The steady-state defect supersaturations available to drive dislocation climb, which are incorporated into the model as free parameters, circumvent the need to capture these other sinks, but as discussed in

§ 3.3.5 these are very difficult predict or measure accurately.

8.2 3D DDD simulations of dislocation climb over obstacles

The vacancy and interstitial bulk diffusion model of dislocation climb was implemented into a 3D DDD code (§ 4.3), together with a dual glide and climb time step method (§ 4.5), and spherical inclusions which are impenetrable to dislocations (§ 6.2), in order to simulate creep in a dispersion-strengthened alloy. Simulations of dislocation-inclusion unpinning via climb were conducted (§ 7.2). These involved an applied shear load, an applied compressive load, or no applied load but defect supersaturations present; all for a range of conditions.

The simulated dislocation-inclusion unpinning times in the absence of any defect supersaturation exhibited a very strong temperature dependence (§ 7.3.2), as expected for a thermal vacancy mediated process. The temperature dependence was seen to dominate over the effects of changing the applied load (§ 7.3.3) and obstacle size (§ 7.3.4). Unpinning times due to the presence of defect supersaturations were seen to be far less temperature dependent (§ 7.3.5), and to vary inversely with the value of the defect supersaturations, as expected for this osmotic climb process.

A simple model for estimating the creep strain rate from the simulated dislocation-inclusion unpinning time data was described (§ 7.4), which incorporates additional dependence on the dispersion properties and the dislocation density. Creep strain rate estimates were carried out using the simulated unpinning time data (§ 7.5).

The thermal creep strain rates were seen to be strongly temperature dependent (§ 7.5.1), as expected. Varying the applied load was seen to have a relatively small effect (§ 7.5.2), as the creep rates increased proportionally with the applied stress. The dispersion properties were also seen to have a relatively small effect (§ 7.5.3, 7.5.4). Remarkably, the creep rates exhibit no dependence on the particle size and number density for a given volume fraction of obstacles. The creep rates vary inversely with the root of the

particle volume fraction, and hence increasing the yttrium content from 0.3 to 0.5 wt% results in a decrease in the creep rate of only ∼25%. An estimated thermal creep strain rate of $\sim 5 \times 10^{-6}$ s^{-1} for an applied load of 200 MPa at 650 °C was compared to an experimentally measured value of 1.45×10^{-6} s^{-1} in ODS EUROFER 97[46] (§ 7.5.1, 7.5.2, 7.5.4), showing encouraging consistency between the models used in these simulations and reality.

The predicted irradiation creep strain rates were seen to vary much less strongly with temperature (§ 7.5.5), also as expected. They increase proportionally with the value of the point defect supersaturations available to drive dislocation climb. Irradiation creep was seen to dominate over thermal creep in ODS alloys at the fusion reactor operating temperature of ∼650 °C, provided the irradiation induced point defect supersaturations available to drive dislocation climb are $>10^{-12}$ defects. These estimated creep rates, when compared to experimental data, indicate a lower bound of $\sim 10^{-14}$ defects during helium implantation of an ODS alloy. The irradiation creep rate in ODS alloys under fusion reactor operating conditions is predicted to have the potential to be orders of magnitude larger than the thermal creep rate at this temperature, as it is proportional to the value of the steady-state point defect supersaturations available to drive dislocation climb. However, again these supersaturations are very challenging to estimate theoretically.

The simulations conducted throughout chapter 7 involved a shear dislocation loop shrinking due to its own self-force, in order to drive dislocations against the impenetrable obstacles. The high loop self-forces present in the simulations introduce additional effects which would not influence real threading dislocations. Although care was taken to identify these effects and eliminate them from the predictions made using the simulation results, more physical dislocation configurations could be employed in the overall simulation scheme.

[46] Purely Y_2O_3 particles were assumed, and a yttrium content of 0.3 wt% — as was the case in the experimental ODS alloy — was used for this estimate.

8.3 Further work

There are a number of ways in which this work could be extended, improved upon, and applied to dispersion (or precipitation) strengthened alloys, as well as materials under irradiation conditions.

1. The theoretical climb calculations could be performed for other bcc materials for use in nuclear applications, such as tungsten. Similar predictions to those made in this work could be made regarding the damage loop populations seen in such materials during and after irradiation at different temperatures.

2. Were irradiation experiments in bcc iron to be performed at progressively higher temperatures than 460 °C in order to observe the transition temperature at which interstitial loops are no longer seen, it would indicate the order of magnitude of the steady-state defect supersaturations. The model in this work could then be verified by comparing the steady-state supersaturation calculated from the experimentally measured transition temperature with a theoretical value for what the supersaturation should be at the transition temperature. Finding such a theoretical value is very challenging, but KMC methods show some promise.

3. The model could be extended to include non-steady-state defect supersaturations, which continously change to reflect the amount of dislocation climb which has taken place. This would enable the simulation of populations of damage loops during post-irradiation annealing for comparison with in situ experimental observations.

4. Simulations could be performed in which a threading dislocation is driven against the impenetrable obstacles instead of a shear dislocation loop. This would eliminate the unrealistic effects of the loop self-forces on the dislocation-inclusion unpinning time behaviour.

5. Misfitting inclusions, either impenetrable or penetrable, could be implemented, and their effects investigated. Non-spherical inclusion geometry would also be straightforward to implement. For example, large, cubic obstacles could be used

to perform simulations of both thermal and irradiation creep in nickel base superalloys.

6. Simulations involving a larger simulation box with more obstacles and dislocation line length present could be performed. Using a time-dependent applied load, stress-strain curves could then be produced for comparison with experiment, and to assess if climb plays any role in the temperature dependent yield strength of ODS alloys.

7. `DDLab`, the 3D DDD code used, could be developed to incorporate anisotropic elasticity, which is important for bcc iron at temperatures approaching $\sim$900 °C.

8. MD simulations of damage cascades could be performed in which there is a threading dislocation pinned against an impenetrable obstacle present in the simulation box. The irradiation-induced climb and subsequent unpinning of the dislocation could then be compared with the results of this work, or the results of the simulations described in point 4.

Lastly, this work suggests in situ creep testing of ODS alloys under fusion reactor relevant irradiation conditions is needed more than ever in order to assess the irradiation creep resistance of these alloys. An increase of orders of magnitude in the irradiation creep rate compared to thermal creep appears to be possible. If this turns out to be the case, it will severely limit the feasibility of using ODS alloys for fusion (and Gen IV fission) applications.

References

Akasaka, N., Yamashita, S., Yoshitake, T., Ukai, S., and Kimura, A. (2004). Microstructural changes of neutron irradiated ODS ferritic and martensitic steels. *Journal of Nuclear Materials*, 329-333:1053–1056.

Alinger, M. J. (2004). *On the formation and stability of nanometer scale precipitates in ferritic alloys during processing and high temperature service*. PhD thesis, University of California, Santa Barbara.

Amelinckx, S., Bontinck, W., Dekeyser, W., and Seitz, F. (1957). On the formation and properties of helical dislocations. *Philosophical Magazine*, 2(15):355–378.

Arakawa, K., Satoh, Y., Arai, S., and Kiritani, M. (2000). Fluctuation of point defect reactions observed during the growth of dislocation loops under electron irradiation. *Philosophical Magazine A*, 80(9):2041–2055.

Arsenlis, A., Cai, W., Tang, M., Rhee, M., Oppelstrup, T., Hommes, G., Pierce, T. G., and Bulatov, V. V. (2007). Enabling strain hardening simulations with dislocation dynamics. *Modelling and Simulation in Materials Science and Engineering*, 15(6):553–595.

Arzt, E. (1988). High temperature properties of dispersion strengthened materials produced by mechanical alloying: Current theoretical understanding and some practical implications. *New Materials by Mechanical Alloying Techniques*, pages 185–200.

Aubry, S., Fitzgerald, S. P., Dudarev, S. L., and Cai, W. (2011). Equilibrium shape of dislocation shear loops in anisotropic α-Fe. *Modelling and Simulation in Materials Science and Engineering*, 19(6):065006.

Ayas, C., van Dommelen, J. A. W., and Deshpande, V. S. (2014). Climb-enabled discrete dislocation plasticity. *Journal of the Mechanics and Physics of Solids*, 62:113–136.

Bacon, D. J., Barnett, D. M., and Scattergood, R. O. (1979). Anisotropic continuum theory of lattice defects. *Progress in Materials Science*, 23:51–262.

Bacon, D. J., Kocks, U. F., and Scattergood, R. O. (1973). The effect of dislocation self-interaction on the Orowan stress. *Philosophical Magazine*, 28(6):1241–1263.

Bakó, B., Clouet, E., Dupuy, L. M., and Blétry, M. (2011). Dislocation dynamics simulations with climb: kinetics of dislocation loop coarsening controlled by bulk diffusion. *Philosophical Magazine*, 91(23):3173–3191.

Bakó, B., Weygand, D., Samaras, M., Chen, J., Pouchon, M. A., Gumbusch, P., and Hoffelner, W. (2007). Discrete dislocation dynamics simulations of dislocation interactions with Y2O3 particles in PM2000 single crystals. *Philosophical Magazine*, 87(24):3645.

Balint, D. S., Deshpande, V. S., Needleman, A., and van der Giessen, E. (2006). Size effects in uniaxial deformation of single and polycrystals: a discrete dislocation plasticity analysis. *Modelling and Simulation in Materials Science and Engineering*, 14(3):409.

Barnett, D. M. (1972). The precise evaluation of derivatives of the anisotropic elastic Green's functions. *Physica Status Solidi B*, 49:741–748.

Bartsch, M., Wasilkowska, A., Czyrska-Filemonowicz, A., and Messerschmidt, U. (1999). Dislocation dynamics in the oxide dispersion strengthened alloy INCOLOY MA956. *Materials Science and Engineering: A*, 272(1):152–162.

Björkas, C. and Nordlund, K. (2007). Comparative study of cascade damage in Fe simulated with recent potentials. *Nuclear Instruments and Methods in Physics Research Section B: Beam Interactions with Materials and Atoms*, 259(2):853–860.

Bloom, E. E. (1998). The challenge of developing structural materials for fusion power systems. *Journal of Nuclear Materials*, 258-263(1998):7–17.

Bloom, E. E., Busby, J. T., Duty, C. E., Maziasz, P. J., McGreevy, T. E., Nelson, B. E., Pint, B. A., Tortorelli, P. F., and Zinkle, S. J. (2007). Critical questions in materials science and engineering for successful development of fusion power. *Journal of Nuclear Materials*, 367-370:1–10.

Bolt, H., Barabash, V., Krauss, W., Linke, J., Neu, R., Suzuki, S., Yoshida, N., and ASDEX Upgrade Team (2004). Materials for the plasma-facing components of fusion reactors. *Journal of Nuclear Materials*, 329-333:66–73.

Bulatov, V. V. and Cai, W. (2006). *Computer Simulations of Dislocations*. Oxford University Press.

Bullough, R. and Newman, R. C. (1970). The kinetics of migration of point defects to dislocations. *Reports on Progress in Physics*, 33(1):101–148.

Burgers, J. M. (1939). Some considerations on the fields of stress connected with dislocations in a regular crystal lattice. *Proceedings of the Koninklijke Nederlandse Academie van Wetenschappen*, 42:293.

Cai, W., Arsenlis, A., Weinberger, C. R., and Bulatov, V. V. (2006). A non-singular continuum theory of dislocations. *Journal of the Mechanics and Physics of Solids*, 54(3):561–587.

Cai, W. and Bulatov, V. V. (2004). Mobility laws in dislocation dynamics simulations. *Materials Science and Engineering: A*, 387-389(December 2003):277–281.

Caillard, D. and Martin, J. L. (2003). *Thermally Activated Mechanisms in Crystal Plasticity*. Pergamon Press, Amsterdam.

CCFE (2012). JET web page, http://www.ccfe.ac.uk/JET.aspx [Accessed 10 September 2015].

Certain, A., Kuchibhatla, S., Shutthanandan, V., Hoelzer, D. T., and Allen, T. R. (2013). Radiation stability of nanoclusters in nano-structured oxide dispersion strengthened (ODS) steels. *Journal of Nuclear Materials*, 434(1-3):311–321.

Chen, J. and Hoffelner, W. (2009). Irradiation creep of oxide dispersion strengthened (ODS) steels for advanced nuclear applications. *Journal of Nuclear Materials*, 392(2):360–363.

Christian, J. W. (1983). Some surprising features of the plastic deformation of body-centered cubic metals and alloys. *Metallurgical Transactions A*, 14(7):1237–1256.

Cottrell, A. H. (1953). *Dislocations and Plastic Flow in Crystals*. Oxford University Press.

Cottrell, A. H. and Bilby, B. A. (1949). Dislocation theory of yielding and strain ageing of iron. *Proceedings of the Physical Society A*, 62(1):49–62.

Cunningham, N. (2008). *Determining processing variable effects on nano-particle distributions in nanostructured ferritic alloys*. Masters thesis, University of California, Santa Barbara.

de Schepper, L., Segers, D., Dorikens-Vanpraet, L., Dorikens, M., Knuyt, G., Stals, L. M., and Moser, P. (1983). Positron annihilation on pure and carbon-doped α-iron in thermal equilibrium. *Physical Review B*, 27(9):5257–5269.

de Wit, R. (1959). Self-energy of a helical dislocation. *Physical Review*, 116(3):592.

Decker, R. F., Rush, A., Dano, A., and Freeman, J. W. (1956). *Abnormal grain growth in nickel-base heat-resistant alloys*. Technical note 4082, National Advisory Committee for Aeronautics.

Derlet, P. M., Nguyen-Manh, D., and Dudarev, S. L. (2007). Multiscale modeling of crowdion and vacancy defects in body-centered-cubic transition metals. *Physical Review B*, 76(5):054107.

Devincre, B., Kubin, L. P., Lemarchand, C., and Madec, R. (2001). Mesoscopic simulations of plastic deformation. *Materials Science and Engineering: A*, 309-310:211–219.

Dieter, G. E. (1986). *Mechanical Metallurgy*. McGraw-Hill Inc.

Dudarev, S. L. (2003). Coherent motion of interstitial defects in a crystalline material. *Philosophical Magazine*, 83(31-34):3577–3597.

Dudarev, S. L. (2013). Density functional theory models for radiation damage. *Annual Review of Materials Research*, 43:35–61.

El-Genk, M. S. and Tournier, J.-M. (2005). A review of refractory metal alloys and mechanically alloyed-oxide dispersion strengthened steels for space nuclear power systems. *Journal of Nuclear Materials*, 340(1):93–112.

Eshelby, J. D. (1954). Distortion of a Crystal by Point Imperfections. *Journal of Applied Physics*, 25(2):255–261.

Eshelby, J. D. (1957). The determination of the elastic field of an ellipsoidal inclusion, and related problems. *Proceedings of the Royal Society A*, 241(1226):376–396.

Eshelby, J. D. (1959). The Elastic Field Outside an Ellipsoidal Inclusion. *Proceedings of the Royal Society A*, 252(1271):561–569.

Eshelby, J. D. (1966). A simple derivation of the elastic field of an edge dislocation. *British Journal of Applied Physics*, 17:1131.

Eshelby, J. D., Frank, F. C., and Nabarro, F. R. N. (1951). The equilibrium of linear arrays of dislocations. *Philosophical Magazine*, 42(327):351–364.

Eshelby, J. D., Read, W. T., and Shockley, W. (1953). Anisotropic elasticity with applications to dislocation theory. *Acta Metallurgica*, 1:251–259.

Eyre, B. L. and Bullough, R. (1965). On the formation of interstitial loops in b.c.c. metals. *Philosophical Magazine*, 12(115):31–39.

Finnis, M. W. and Sinclair, J. E. (1984). A simple empirical N-body potential for transition metals. *Philosophical Magazine A*, 50(1):45–55.

Fitzgerald, S. P. (2010). Frank-Read sources and the yield of anisotropic cubic crystals. *Philosophical Magazine Letters*, 90(3):209–218.

Fitzgerald, S. P. and Aubry, S. (2010). Self-force on dislocation segments in anisotropic crystals. *Journal of Physics: Condensed Matter*, 22(29):295403.

Fitzgerald, S. P., Aubry, S., Dudarev, S. L., and Cai, W. (2012). Dislocation dynamics simulation of Frank-Read sources in anisotropic α-Fe. *Modelling and Simulation in Materials Science and Engineering*, 20(4):045022.

Fitzgerald, S. P. and Dudarev, S. L. (2008). Dislocation pile-ups in Fe at high temperature. *Proceedings of the Royal Society A: Mathematical, Physical and Engineering Sciences*, 464(2098):2549–2559.

Fitzgerald, S. P. and Dudarev, S. L. (2009). Interaction between dislocations in bcc iron at high temperature. *Journal of Nuclear Materials*, 386-388:67–70.

Fitzgerald, S. P. and Yao, Z. (2009). Shape of prismatic dislocation loops in anisotropic α-Fe. *Philosophical Magazine Letters*, 89(9):581–588.

Fivel, M. (2008). Discrete dislocation dynamics: an important recent break-through in the modelling of dislocation collective behaviour. *Comptes Rendus Physique*, 9(3-4):427–436.

Frank, F. C. and Read, W. T. (1950). Multiplication Processes for Slow Moving Dislocations. *Physical Review*, 79:722–723.

Friedel, J. (1964). *Dislocations*. Pergamon Press.

Fu, C.-C., dalla Torre, J., Willaime, F., Bocquet, J.-L., and Barbu, A. (2005). Multiscale modelling of defect kinetics in irradiated iron. *Nature Materials*, 4(1):68–74.

Gao, Y. and Cocks, A. C. F. (2009). Thermodynamic variational approach for climb of an edge dislocation. *Acta Mechanica Solida Sinica*, 22(5):426–435.

Garner, F. A., Toloczko, M. B., and Sencer, B. H. (2000). Comparison of swelling and irradiation creep behavior of fcc-austenitic and bcc-ferritic/martensitic alloys at high neutron exposure. *Journal of Nuclear Materials*, 276(1-3):123–142.

Gavazza, S. D. and Barnett, D. M. (1976). The self-force on a planar dislocation loop in an anisotropic linear-elastic medium. *Journal of the Mechanics and Physics of Solids*, 24(4):171–185.

Gilbert, M. R. and Dudarev, S. L. (2010). Ab initio multi-string Frenkel-Kontorova model for a b = a/2[111] screw dislocation in bcc iron. *Philosophical Magazine*, 90(7-8):1035–1061.

Gilbert, M. R., Dudarev, S. L., Zheng, S., Packer, L. W., and Sublet, J.-C. (2012). An integrated model for materials in a fusion power plant: transmutation, gas production, and helium embrittlement under neutron irradiation. *Nuclear Fusion*, 52(8):083019.

Gilbert, M. R., Queyreau, S., and Marian, J. (2011). Stress and temperature dependence of screw dislocation mobility in α-Fe by molecular dynamics. *Physical Review B*, 84(17):174103.

Gorley, M. J. (2014). *Powder processing of oxide dispersion strengthened alloys for nuclear applications*. PhD thesis, University of Oxford.

Gross, R. A. (1984). *Fusion Energy*. Wiley.

Gururaj, K. and Robertson, C. (2011). Plastic deformation in ODS ferritic alloys: A 3D dislocation dynamics investigation. *Energy Procedia*, 7:279–285.

Hafez-Haghighat, S. M., Eggeler, G., and Raabe, D. (2013). Effect of climb on dislocation mechanisms and creep rates in γ'-strengthened Ni base superalloy single crystals: A discrete dislocation dynamics study. *Acta Materialia*, 61(10):3709–3723.

Hall, E. O. (1951). The deformation and ageing of mild steel: III Discussion of results. *Proceedings of the Physical Society B*, 64(9):747.

Hasegawa, H., Finnis, M. W., and Pettifor, D. G. (1985). A calculation of elastic constants of ferromagnetic iron at finite temperatures. *Journal of Physics F: Metal Physics*, 19:19–34.

Hasegawa, H. and Pettifor, D. G. (1983). Microscopic theory of the temperature-pressure phase diagram of iron. *Physical Review Letters*, 50(2):130–133.

Hayashi, T., Sarosi, P. M., Schneibel, J. H., and Mills, M. J. (2008). Creep response and deformation processes in nanocluster-strengthened ferritic steels. *Acta Materialia*, 56(7):1407–1416.

He, P., Klimenkov, M., Lindau, R., and Möslang, A. (2012). Characterization of precipitates in nano structured 14% Cr ODS alloys for fusion application. *Journal of Nuclear Materials*, 428(1-3):131–138.

Hirsch, M. W. (2014). Tokamak (scheme) web page, http://bit.ly/1L4ZTaD [Accessed 10 September 2015].

Hirth, J. P. and Lothe, J. (1982). *Theory of Dislocations*. John Wiley and Sons, Inc., second edition.

Hoelzer, D. T., Bentley, J., Sokolov, M. A., Miller, M. K., Odette, G. R., and Alinger, M. J. (2007). Influence of particle dispersions on the high-temperature strength of ferritic alloys. *Journal of Nuclear Materials*, 367-370:166–172.

Hsiung, L. L., Fluss, M. J., Tumey, S. J., Choi, B. W., Serruys, Y., Willaime, F., and Kimura, A. (2010). Formation mechanism and the role of nanoparticles in Fe-Cr ODS steels developed for radiation tolerance. *Physical Review B*, 82(18):184103.

Hull, D. and Bacon, D. J. (2011). *Introduction to Dislocations*. Butterworth Heinemann. Elsevier.

IEA (2011). Key World Energy Statistics. Technical report, International Energy Agency, http://bit.ly/1FIIOYc [Accessed 14 April 2014].

Ishino, S. (1996). Implications of fundamental radiation damage studies in the research and development of materials for a fusion reactor. *Journal of Nuclear Materials*, 239:24–33.

Itakura, M., Kaburaki, H., and Yamaguchi, M. (2012). First-principles study on the mobility of screw dislocations in bcc iron. *Acta Materialia*, 60(9):3698–3710.

ITER (2015). ITER: The world's largest tokamak web page, https://www.iter.org/mach [Accessed 10 September 2015].

Kabir, M., Lau, T. T., Rodney, D., Yip, S., and van Vliet, K. J. (2010). Predicting dislocation climb and creep from explicit atomistic details. *Physical Review Letters*, 105(9):095501.

Kasada, R., Toda, N., Yutani, K., Cho, H. S., Kishimoto, H., and Kimura, A. (2007). Pre- and post-deformation microstructures of oxide dispersion strengthened ferritic steels. *Journal of Nuclear Materials*, 367-370:222–228.

Keh, A. S. (1965). Work hardening and deformation sub-structure in iron single crystals deformed in tension at 298 K. *Philosophical magazine*, 12(115):37–41.

Keralavarma, S. M., Cagin, T., Arsenlis, A., and Amine Benzerga, A. (2012). Power-law creep from discrete dislocation dynamics. *Physical Review Letters*, 109(26):265504.

Khraishi, T. A., Yan, L., and Shen, Y.-L. (2004). Dynamic simulations of the interaction between dislocations and dilute particle concentrations in metal-matrix composites (MMCs). *International Journal of Plasticity*, 20(6):1039–1057.

Kinchin, G. H. and Pease, R. S. (1955). The displacement of atoms in solids by radiation. *Reports on Progress in Physics*, 18(1):1.

Klueh, R. L. (2005). Elevated temperature ferritic and martensitic steels and their application to future nuclear reactors. *International Materials Reviews*, 50(5):287–310.

Klueh, R. L., Maziasz, P. J., Kim, I. S., Heatherly, L., Hoelzer, D. T., Hashimoto, N., Kenik, E. A., and Miyahara, K. (2002). Tensile and creep properties of an oxide dispersion-strengthened ferritic steel. *Journal of Nuclear Materials*, 307-311:773–777.

Klueh, R. L., Shingledecker, J. P., Swindeman, R. W., and Hoelzer, D. T. (2005). Oxide dispersion-strengthened steels: A comparison of some commercial and experimental alloys. *Journal of Nuclear Materials*, 341(2-3):103–114.

Kroupa, F. (1960). Circular edge dislocation loop. *Czechoslovak Journal of Physics*, 10(4):284–293.

Kroupa, F. and Price, P. B. (1961). Conservative climb of a dislocation loop due to its interaction with an edge dislocation. *Philosophical Magazine*, 6(62):243–247.

Kurtz, R. J., Odette, G. R., Yamamoto, T., Gelles, D., Miao, P., and Oliver, B. M. (2007). The transport and fate of helium in martensitic steels at fusion relevant He/dpa ratios and dpa rates. *Journal of Nuclear Materials*, 367-370:417–422.

Larson, F. R. and Miller, J. (1952). A time-temperature relationship for rupture and creep stresses. *Transactions of the American Society of Mechanical Engineers*, 74:765–775.

LeSar, R. and Rickman, J. M. (2002). Multipole expansion of dislocation interactions: Application to discrete dislocations. *Physical Review B*, 65(14):144110.

Lewthwaite, G. W. (1966). The force on a dislocation. *Philosophical Magazine*, 13(122):437–439.

Louchet, F. and Kubin, L. P. (1975). Formation of helical dislocations in pure niobium single crystals under electron irradiation. *Radiation Effects*, 26(July):67.

Louchet, F., Kubin, L. P., and Vesely, D. (1979). In situ deformation of b.c.c. crystals at low temperatures in a high-voltage electron microscope: Dislocation mechanisms and strain-rate equation. *Philosophical Magazine A*, 39(4):433–454.

Love, G. R. (1964). Dislocation pipe diffusion. *Acta Metallurgica*, 12(6):731–737.

Low, J. R. and Turkalo, A. M. (1962). Slip band structure and dislocation multiplication in silicon-iron crystals. *Acta Metallurgica*, 10(3):215–227.

Margvelashvili, I. G. and Saralidze, Z. K. (1974). Influence of an elastic field of a dislocation on steady-state diffusion fluxes of point defects.

Marian, J., Martínez, E., Lee, H.-J., and Wirth, B. D. (2009). Micro/meso-scale computational study of dislocation-stacking-fault tetrahedron interactions in copper. *Journal of Materials Research*, 24(12):3628–3635.

Marian, J., Wirth, B. D., Schäublin, R., Odette, G. R., and Perlado, J. M. (2003). MD modeling of defects in Fe and their interactions. *Journal of Nuclear Materials*, 323(2-3):181–191.

Martin, J. W. (1968). *Precipitation Hardening*. Pergamon Press, New York.

Mason, D. R., Yi, X., Kirk, M. A., and Dudarev, S. L. (2014). Elastic trapping of dislocation loops in cascades in ion-irradiated tungsten foils. *Journal of Physics: Condensed Matter*, 26(37):375701.

Meinshausen, M., Meinshausen, N., Hare, W., Raper, S. C. B., Frieler, K., Knutti, R., Frame, D. J., and Allen, M. R. (2009). Greenhouse-gas emission targets for limiting global warming to 2 degrees C. *Nature*, 458(7242):1158–1162.

Mordehai, D., Clouet, E., Fivel, M., and Verdier, M. (2008). Introducing dislocation climb by bulk diffusion in discrete dislocation dynamics. *Philosophical Magazine*, 88(6):899–925.

Mordehai, D., Clouet, E., Fivel, M., and Verdier, M. (2009). Annealing of dislocation loops in dislocation dynamics simulations. *Institute of Physics Conference Series: Materials Science and Engineering*, 3:12001.

Mrovec, M., Nguyen-Manh, D., Pettifor, D. G., and Vitek, V. (2004). Bond-order potential for molybdenum: Application to dislocation behavior. *Physical Review B*, 69(9):094115.

Nabarro, F. R. N. (1947). Dislocations in a simple cubic lattice. *Proceedings of the Physical Society*, 59(2):256–272.

Nabarro, F. R. N. (1951). The synthesis of elastic dislocation fields. *Philosophical Magazine*, 42:213.

Nix, W. D., Gasca-Neri, R., and Hirth, J. P. (1971). A contribution to the theory of dislocation climb. *Philosophical Magazine*, 23(186):1339–1349.

Norgett, M. J., Robinson, M. T., and Torrens, I. M. (1975). A proposed method of calculating displacement dose rates. *Nuclear Engineering and Design*, 33(1):50–54.

Novokshanov, R. and Roberts, S. G. (2009). 3D dislocation dynamics modelling of interactions between prismatic loops and mobile dislocations in pure iron. *Journal of Nuclear Materials*, 386-388:64–66.

Odette, G. R. (1988). On mechanisms controlling swelling in ferritic and martensitic alloys. *Journal of Nuclear Materials*, 155-157:921–927.

Odette, G. R., Alinger, M. J., and Wirth, B. D. (2008). Recent developments in irradiation-resistant steels. *Annual Review of Materials Research*, 38(1):471–503.

Oksiuta, Z., Ozieblo, A., Perkowski, K., Osuchowski, M., and Lewandowska, M. (2014). Influence of HIP pressure on tensile properties of a 14Cr ODS ferritic steel. *Fusion Engineering and Design*, 89(2):137–141.

Orowan, E. (1947). Discussion. In *Symposium on Internal Stresses in Metals and Alloys*, page 451. Institute of Metals, London.

Peach, M. and Koehler, J. S. (1950). The forces exerted on dislocations and the stress fields produced by them. *Physical Review*, 80(3):436–439.

Peierls, R. (1940). The size of a dislocation. *Proceedings of the Physical Society*, 52(1):34.

Petch, N. J. (1953). The cleavage strength of polycrystals. *Journal of the Iron and Steel Institute*, 174:25.

Prekel, H. L., Lawley, A., and Conrad, H. (1968). Dislocation velocity measurements in high purity molybdenum. *Acta Metallurgica*, 16(3):337–345.

Raabe, D. (1998). On the consideration of climb in discrete dislocation dynamics. *Philosophical Magazine A*, 77(3):751–759.

Reed, R. C. (2008). *The Superalloys: Fundamentals and Applications*. Cambridge University Press, Cambridge.

Renzetti, R. A., Sandim, H. R. Z., Bolmaro, R. E., Suzuki, P. A., and Möslang, A. (2012). X-ray evaluation of dislocation density in ODS-Eurofer steel. *Materials Science and Engineering: A*, 534:142–146.

Rhee, M., Stolken, J. S., Bulatov, V. V., de la Rubia, T., Zbib, H. M., and Hirth, J. P. (2001). Dislocation stress fields for dynamic codes using anisotropic elasticity: methodology and analysis. *Materials Science and Engineering: A*, 309-310:288–293.

Rhee, M., Zbib, H. M., Hirth, J. P., Huang, H., and de la Rubia, T. (1998). Models for long-/short-range interactions and cross slip in 3D dislocation simulation of BCC single crystals. *Modelling and Simulation in Materials Science and Engineering*, 6(4):467–492.

Ribis, J. and Lozano-Perez, S. (2014). Nano-cluster stability following neutron irradiation in MA957 oxide dispersion strengthened material. *Journal of Nuclear Materials*, 444(1-3):314–322.

Sand, A. E., Nordlund, K., and Dudarev, S. L. (2014). Radiation damage production in massive cascades initiated by fusion neutrons in tungsten. *Journal of Nuclear Materials*, 455(1-3):207–211.

Scattergood, R. O. and Bacon, D. J. (1975). The Orowan mechanism in anisotropic crystals. *Philosophical Magazine*, 31(1):179–198.

Schäublin, R., Ramar, A., Baluc, N., de Castro, V., Monge, M., Leguey, T., Schmid, N., and Bonjour, C. (2006). Microstructural development under irradiation in European ODS ferritic/martensitic steels. *Journal of Nuclear Materials*, 351(1-3):247–260.

Schiller, P. (1993). Review of materials selection for fusion reactors. *Journal of Nuclear Materials*, 206:113–120.

Schmid, E. (1931). Beitraege zur Physik und Metallographie des Magnesiums. *Zeitschrift für Elektrochemie*, 37:447–459.

Seki, Y., Tabara, T., Aoki, I., Ueda, S., Nishio, S., and Kurihara, R. (1998). Impact of low activation materials on fusion reactor design. *Journal of Nuclear Materials*, 263:1791–1797.

Shao, L., Wei, C.-C., Gigax, J., Aitkaliyeva, A., Chen, D., Sencer, B. H., and Garner, F. A. (2014). Effect of defect imbalance on void swelling distributions produced in pure iron irradiated with 3.5MeV self-ions. *Journal of Nuclear Materials*, 453(1-3):176–181.

Silcox, J. and Whelan, M. J. (1960). Direct observations of the annealing of prismatic dislocation loops and of climb of dislocations in quenched aluminium. *Philosophical Magazine*, 5(49):1–23.

Soisson, F., Becquart, C. S., Castin, N., Domain, C., Malerba, L., and Vincent, E. (2010). Atomistic Kinetic Monte Carlo studies of microchemical evolutions driven by diffusion processes under irradiation. *Journal of Nuclear Materials*, 406(1):55–67.

Stoller, R. E., Toloczko, M. B., Was, G. S., Certain, A. G., Dwaraknath, S., and Garner, F. A. (2013). On the use of SRIM for computing radiation damage exposure. *Nuclear Instruments and Methods in Physics Research Section B: Beam Interactions with Materials and Atoms*, 310:75–80.

Stork, D., Agostini, P., and Boutard, J. L. (2014). Materials R&D for a timely DEMO: Key findings and recommendations of the EU Roadmap Materials Assessment Group. *Fusion Engineering and Design*.

Takaki, S., Fuss, J., Kuglers, H., Dedek, U., and Schultz, H. (1983). The resistivity recovery of high purity and carbon doped iron following low temperature electron irradiation. *Radiation Effects*, 79(1-4):87–122.

Tandon, G. P. and Weng, G. J. (1984). The effect of aspect ratio of inclusions on the elastic properties of unidirectionally aligned composites. *Polymer Composites*, 5(4):327–333.

Tarleton, E., Balint, D. S., Gong, J., and Wilkinson, A. J. (2015). A discrete dislocation plasticity study of the micro-cantilever size effect. *Acta Materialia*, 88:271–282.

Tarleton, E. and Roberts, S. G. (2009). Dislocation dynamic modelling of the brittle–ductile transition in tungsten. *Philosophical Magazine*, 89(31):2759–2769.

Taylor, G. I. (1934). The mechanism of plastic deformation of crystals. Part I. Theoretical. *Proceedings of the Royal Society of London A: Mathematical, Physical and Engineering Sciences*, 145(855):362–387.

Toloczko, M. B., Garner, F. A., and Maloy, S. A. (2012). Irradiation creep and density changes observed in MA957 pressurized tubes irradiated to doses of 40–110 dpa at 400–750 C in FFTF. *Journal of Nuclear Materials*, 428(1-3):170–175.

Turunen, M. J. (1976). A general equation of motion for dislocation climb. *Acta Metallurgica*, 24:463–467.

Ukai, S. and Fujiwara, M. (2002). Perspective of ODS alloys application in nuclear environments. *Journal of Nuclear Materials*, 307-311:749–757.

van der Giessen, E. and Needleman, A. (1995). Discrete dislocation plasticity: a simple planar model. *Modelling and Simulation in Materials Science and Engineering*, 689.

Vitek, V. (2004). Core structure of screw dislocations in body-centred cubic metals: relation to symmetry and interatomic bonding. *Philosophical Magazine*, 84(3-5):415–428.

Vitek, V., Mrovec, M., and Bassani, J. L. (2004). Influence of non-glide stresses on plastic flow: from atomistic to continuum modeling. *Materials Science and Engineering: A*, 365(1-2):31–37.

Vitek, V. and Paidar, V. (2008). Non-planar dislocation cores: A ubiquitous phenomenon affecting mechanical properties of crystalline materials. In *A Tribute to F. R. N. Nabarro*, volume 14 of *Dislocations in Solids*, pages 439–514. Elsevier.

Volterra, V. (1907). Sur l'équilibre des corps élastiques multiplement connexes. *Annales scientifiques de l'École Normale Supérieure*, 24:401–517.

Ward, D. J. and Dudarev, S. L. (2008). Economically competitive fusion. *Materials Today*, 11(12):46–53.

Was, G. S. (2007). *Fundamentals of Radiation Materials Science*. Springer-Verlag Berlin Heidelberg.

Wasilkowska, A., Bartsch, M., Messerschmidt, U., Herzog, R., and Czyrska-Filemonowicz, A. (2003). Creep mechanisms of ferritic oxide dispersion strengthened alloys. *Journal of Materials Processing Technology*, 133(1-2):218–224.

Weertman, J. (1965). The Peach–Koehler equation for the force on a dislocation modified for hydrostatic pressure. *Philosophical Magazine*, 11(114):1217–1223.

Wen, H., Ma, P.-W., and Woo, C. H. (2013). Spin-lattice dynamics study of vacancy formation and migration in ferromagnetic BCC iron. *Journal of Nuclear Materials*, 440(1-3):428–434.

Weng, G. J. (1992). Explicit evaluation of Willis' bounds with ellipsoidal inclusions. *International Journal of Engineering Science*, 30(1):83–92.

Weygand, D., Friedman, L. H., van der Giessen, E., and Needleman, A. (2001). Discrete dislocation modeling in three-dimensional confined volumes. *Materials Science and Engineering: A*, 309-310:420–424.

Whelan, M. J. (1966). On the annealing of dislocation loops by climb. *Philosophical Magazine*, 14(127):195–196.

Williams, C. A., Hyde, J. M., Smith, G. D. W., and Marquis, E. A. (2011). Effects of heavy-ion irradiation on solute segregation to dislocations in oxide-dispersion-strengthened Eurofer 97 steel. *Journal of Nuclear Materials*, 412(1):100–105.

Wolfer, W. G. (1982). A novel approach to compute the relaxation volume of self-interstitials in metals. *Journal of Physics F: Metal Physics*, 12(3):425.

Wolfer, W. G. (2007). The dislocation bias. *Journal of Computer-Aided Materials Design*, 14(3):403–417.

Xiang, Y., Cheng, L.-T., Srolovitz, D. J., and E, W. (2003). A level set method for dislocation dynamics. *Acta Materialia*, 51(18):5499–5518.

Xiang, Y. and Srolovitz, D. J. (2006). Dislocation climb effects on particle bypass mechanisms. *Philosophical Magazine*, 86(25-26):3937–3957.

Xu, S. (2013). *A study of irradiation damage in iron and Fe-Cr alloys*. PhD thesis, University of Oxford.

Yao, Z., Jenkins, M. L., Hernández-Mayoral, M., and Kirk, M. A. (2010). The temperature dependence of heavy-ion damage in iron: A microstructural transition at elevated temperatures. *Philosophical Magazine*, 90(35-36):4623–4634.

Yin, J., Barnett, D. M., Fitzgerald, S. P., and Cai, W. (2012). Computing dislocation stress fields in anisotropic elastic media using fast multipole expansions. *Modelling and Simulation in Materials Science and Engineering*, 20(4):045015.

Yu, G., Nita, N., and Baluc, N. (2005). Thermal creep behaviour of the EUROFER 97 RAFM steel and two European ODS EUROFER 97 steels. *Fusion Engineering and Design*, 75-79:1037–1041.

Zhang, G., Zhou, Z., Mo, K., Miao, Y., Liu, X., Almer, J., and Stubbins, J. F. (2015). The evolution of internal stress and dislocation during tensile deformation in a 9Cr ferritic/martensitic (F/M) ODS steel investigated by high-energy X-rays. *Journal of Nuclear Materials*, 467:50–57.

Zhong, S. Y., Ribis, J., Klosek, V., de Carlan, Y., Lochet, N., Ji, V., and Mathon, M. H. (2012). Study of the thermal stability of nanoparticle distributions in an oxide dispersion strengthened (ODS) ferritic alloys. *Journal of Nuclear Materials*, 428(1-3):154–159.

Ziegler, J. F., Biersack, J. P., and Littmark, U. (1985). *The Stopping and Range of Ions in Matter*. Pergamon Press.

Ziegler, J. F., Ziegler, M. D., and Biersack, J. P. (2010). SRIM — The stopping and range of ions in matter (2010). *Nuclear Instruments and Methods in Physics Research Section B: Beam Interactions with Materials and Atoms*, 268(11-12):1818–1823.

Zinkle, S. J. and Snead, L. L. (2014). Designing radiation resistance in materials for fusion energy. *Annual Review of Materials Research*, 44(1):241–267.

Zinkle, S. J. and Was, G. S. (2013). Materials challenges in nuclear energy. *Acta Materialia*, 61(3):735–758.

Appendix A

Climb via point defect bulk diffusion: calculations for tungsten

A.1 Comparison of thermal and osmotic climb velocities

Figure A.1 shows the same thermal and osmotic climb velocity comparison as shown in figure 3.5 (§ 3.3.5), but calculated for tungsten instead of bcc iron over the (higher) temperature range of 700–1200 °C. The values of the various properties of tungsten used for these calculations are compared with those of bcc iron in table A.1. Because the elastic constants of tungsten differ from those of bcc iron, the 1 GPa load used for

Quantity	Iron	Tungsten
a	0.287 nm	0.316 nm
Ω	0.0118 nm^3	0.0103 nm^3
μ	82 GPa	161 GPa
ν	0.305	0.28
E_f^v	2 eV	3.8 eV
E_m^v	0.6 eV	1.8 eV
E_f^i	4 eV	9 eV
E_m^i	0.3 eV	0.013 eV

Table A.1: Comparison of the various properties of bcc iron used in § 3.3 with those of tungsten used in this appendix. Any properties not listed here were not altered from the values used in § 3.3.

the thermal case in figure A.1 corresponds to the self-force of a loop of width ∼11 nm (estimated using the simple expression in (3.27)).

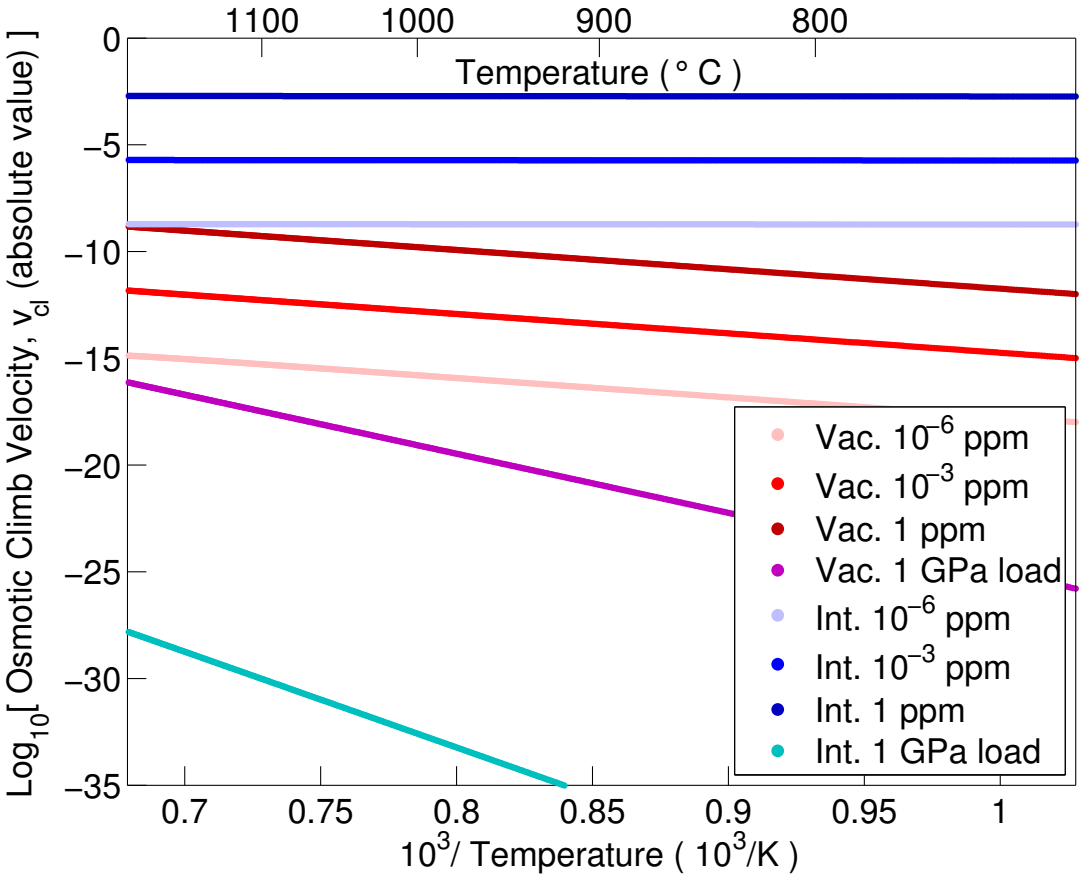


Figure A.1: Comparison between thermal and osmotic climb velocities (in units of ms^{-1}), for a 1 GPa compressive load in the thermal case. The osmotic climb due to supersaturated interstitials dominates the behaviour at all the temperatures shown.

The figure indicates that in tungsten the transition temperature at which interstitial loops of this size are seen to shrink and disappear rather than grow is >1200 °C for the three defect supersaturations shown.

A.2 Supersaturation estimation from the transition temperature

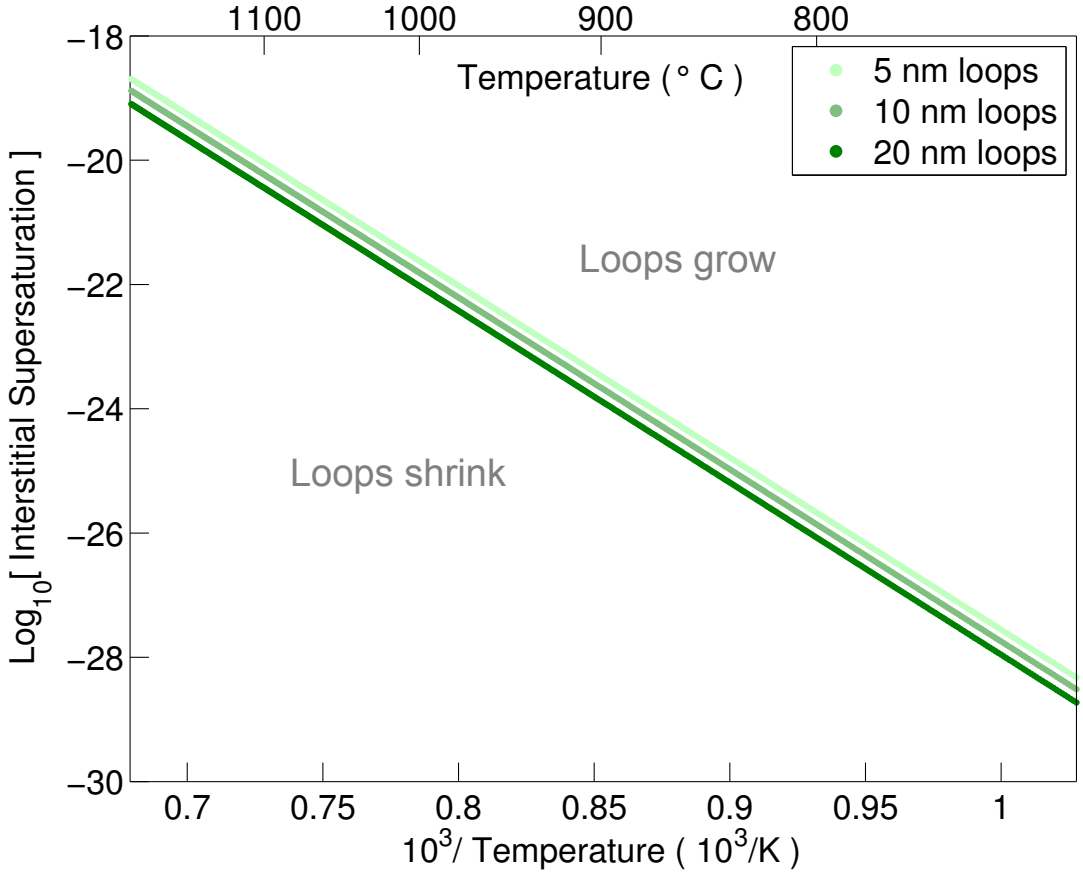


Figure A.2: Interstitial supersaturation dependence on loop behaviour transition temperature (3.31), using the full expression (3.34) to calculate the loop self-force.

Figure A.2 shows the same steady-state interstitial supersaturation estimation from the loop behaviour transition temperature (§ 3.3.6) as shown in figure 3.7 (§ 3.3.7), but again calculated for tungsten over the temperature range of 700–1200 °C.

The plot shows that if a transition temperature were observed in tungsten over this temperature range, it would indicate a steady-state interstitial supersaturation available to drive dislocation climb of no more than 10^{-18} fractional atomic concentration of defects (10^{-12} ppm).

Appendix B

New original **DDLab** code

The functionality of the 3D DDD code **DDLab** as released is discussed in § 2.4.1 and § 4.2. The new original code added to **DDLab** as described in the code development and testing chapters 4 and 6 is included in this appendix. This is by no means an exhaustive record of the additions and alterations made to the **DDLab** code over the course of this work, but it serves to demonstrate some of the new original implementation which is relevant to this thesis.

Throughout this appendix, blocks of additional lines of code are indicated by `% DHT` or similar.

B.1 Code added to existing scripts

B.1.1 An example **input_dd3d** script

```
%% Input for dual timestep DDLab

%% Define globals

global Bscrew Bedge Beclimb Bline

%% Define new globals (DHT)

global BeclimbVac BeclimbInt BlineRatio mobilityInt
global k eV
global MU_SI a_SI Bglide_SI
```

```
12 global atomVol
13 global vacFormEnergy vacMigrEnergy
14 global intFormEnergy intMigrEnergy
15 global diffCoeffPreExpo
16 global radiusCore radiusInfinity
17 global temperature
18 global c0Vac c0Int cInfinityVac cInfinityInt
19 global osmoticForceVac osmoticForceInt
20 global inclusions impenetrable
21 global plotColor doGlide climbstep
22
23 %% Generate dislocation network (DHT)
24
25 % Default plot color is black
26 plotColor = 'k';
27
28 % gen...Loop(1) - radius of loop
29 % gen...Loop(2) - offset from loop plane = 0
30 % Vacancy loop
31 %[rn,links] = generateVacancyLoop(18,0);
32
33 % Interstital loop
34 %[rn,links] = generateInterstitialLoop(18,0);
35
36 % Shear loop
37 [rn,links] = generateShearLoop(18,0);
38
39 %% Inclusion input parameters (DHT)
40
41 %  inclusions(i,1) - radius of inclusion i
42 %  inclusions(i,2:4) - 3 cpt vector position of inclusion i
43 %  inclusions(i,5) - volumetric misfit of inclusion i (not used if impenetrable)
44
45 % No inclusions
46 %inclusions = [];
47
48 % Single inclusion
49 inclusions = [8 0 0 0 -0.1];
50
51 % Multiple inclusions
52 %inclusions = [20  50  50 0 -0.1;
53 %              20  40 -50 0 -0.1;
54 %              20 -50  40 0 -0.1;
55 %              20 -40 -40 0 -0.1];
56
57 % Multiple inclusions
58 %inclusions = [8  52   0   0 -0.1;
59 %              8   0  52   0 -0.1;
60 %              8 -52   0   0 -0.1;
61 %              8   0 -52   0 -0.1];
62
63 % 0 for penetrable inclusions
64 % 1 for impenetrable inclusions
65 impenetrable = 1;
66
67 %% Initialise new globals (DHT)
68
69 % SI Constants
70 k = 1.3806488e-23;    % Boltzmann's constant k
71 eV = 1.602176565e-19; % 1 eV
72
```

```
% SI properties of bcc iron for use converting between SI and DDLab units
MU_SI = 82e9;      % Shear modulus, 82 GPa
a_SI = 2.8665e-10; % Lattice parameter, 2.886 Angstroms
Bglide_SI = 1e-4;  % Glide drag factor, 1e-4 Pa s (guestimate)
                   % so [T] = Bglide_SI/MU_SI = 1.22e-15 s i.e. 1.22 fs

% Other SI properties of bbc iron
atomVol = 11.8e-30;      % Atomic volume, 11.8 cubic Angstroms
vacFormEnergy = 2*eV;    % Vacancy formation energy, 2 eV
vacMigrEnergy = 0.6*eV;  % Vacancy migration energy, 0.6 eV
intFormEnergy = 4*eV;    % Interstitial formation energy, 4 eV
intMigrEnergy = 0.3*eV;  % Interstitial migration energy, 0.3 eV
diffCoeffPreExpo = 2e-4; % Diffusion coefficient pre-exponent

% Simulation parameters
radiusCore = 2; % Dislocation core radius in Burgers vectors
radiusInfinity = 4000; % Outer cut-off radius in Burgers vectors

%% Initialise parameters

MU = 1;
NU = 0.305;
maxconnections=8;
lmax = 8; % Default value = 1000
lmin = 4; % Default value = 200
areamin=lmin*lmin*sin(60/180*pi)*0.5;
areamax=20*areamin;
a=lmin/sqrt(3)*0.5;
Ec = MU/(4*pi)*log(a/0.1);

% Number of simulation steps
% Put 1 more than you actually want!
% N.B. If all dislocations disappear before simulation is over safe exit will ...
    occur
totalsteps=31;

dt0=1e15; % Maximum timestep = 1.22 s

mobility='mobbcc0';
% Different mobility file required for intersitial climb
mobilityInt='mobbcc0Int';

%Drag (Mobility) parameters
Bscrew=1;
Bedge=1;

%% Temperature dependent climb (DHT)

% Temperature in Kelvin
% 700 degress Celcius
temperature = 973;

% Calculate equilibrium defect concentrations
c0Vac=exp(-vacFormEnergy/(k*temperature));
c0Int=exp(-intFormEnergy/(k*temperature));

% Set defect supersaturations

    % Uncomment for no supersaturations and hence no osmotic forces
    %cInfinityVac=c0Vac;
    %cInfinityInt=c0Int;
```

```
133
134     % Uncomment for both supersaturations = e.g. 1 ppb
135     cInfinityVac=1E-9;
136     cInfinityInt=1E-9;
137
138 BeclimbVac=calcClimbDragVac;
139 BeclimbInt=calcClimbDragInt;
140 Beclimb=BeclimbVac; % Initialise for vacancies
141 osmoticForceVac=calcOsmoticForceVac;
142 osmoticForceInt=calcOsmoticForceInt;
143
144 % Set factor by which Bline is smaller than other drag factors
145 BlineRatio=1E-4; % Default
146
147 Bline=BlineRatio*min(Bscrew,Bedge);
148
149 %% Timestep switching (DHT)
150
151 doGlide = 1; % Start with glide
152
153 climbstep = 0; % Initialise
154
155 % Set minimum strain ratio threshold for glide-to-climb switch
156 minStrainRatio = 1E-3;
157
158 % Set number of climb steps performed before returning to glide
159 maxclimbsteps = 2;
160 minglidesteps = 2;
161
162 %% Movie frame recording (DHT)
163
164 doMovie=0; % On == 1, Off == anything else
165 frameCounter=0; % Initialise
166 frameFreq=1;
167
168 %% Initialise more parameters
169
170 integrator='int_eulerforward';
171 rann = 0.5*a;
172 rntol = 0.5*rann;
173 doremesh=1;
174 docollision=1;
175 doseparation=1;
176 plotfreq=1;
177
178 % Set cubic visualisation box half side-width
179 plim=20; % 60 for most loop and inclusion sims of r=50 loops
180          % 200 when necessary (certain glide + climb sims)
181          % 65 for real inclusion size and number density
182
183 %% Applied stress (DHT)
184
185 % In units of MU = 82 GPa
186
187 appliedstress = zeros(3,3);                    % Zero applied stress
188 %appliedstress = 1e-3.*[0 5 0; 5 0 0; 0 0 0];  % 12 Shear load
189 %appliedstress = 1e-3.*[0 0 5; 0 0 0; 5 0 0];  % 13 Shear load
190 %appliedstress = 1e-3.*[0 0 0; 0 0 5; 0 5 0];  % 23 Shear load
191 %appliedstress = 1e-3.*[10 0 0; 0 0 0; 0 0 0]; % Uniaxial 11 tension/compression
192 %appliedstress = 1e-3.*[0 0 0; 0 10 0; 0 0 0]; % Uniaxial 22 tension/compression
193 %appliedstress = 1e-3.*[0 0 0; 0 0 0; 0 0 10]; % Uniaxial 33 tension/compression
```

```
%appliedstress =1e-3.*[2 0 1; 0 2 -1; 1 -1 0]; % Default value

%% View angle (DHT)

%viewangle=[90 0];    % Down x axis for b=[100] prismatic loop
%viewangle=[0 0];     % Down y axis for rubber-banding b=[100] prismatic loop
%viewangle=[0 90];    % Down z axis
viewangle=[45 45];   % 45 degrees to both x and y axes,
                      % and elevated 45 degrees out of xy plane
                      % for rubber-banding b=[100] prismatic loop
%viewangle=[45 0];    % 45 degrees to both x and y axes
                      % for rubber-banding b=[100] prismatic loop
%viewangle=[45 -45 ]; % Default value

%% Initialise final parameters

printfreq=1;
printnode=3;
rmax=1; % Default value = 100
```

B.1.2 The dual time step **main_dd3d** script

```
%% Dual timestep DDLab

%% Description as released

%Dislocation Dynamics simulation in 3-dimension
%
%the best way to run it is by "rundd3d"
%
%Features:
%infinite boundary condition (no pbc)
%linear mobility law (mobfcc0,mobfcc1)
%no remesh, no collision detection, no reaction
%N^2 interaction (no neighbor list, no fast multipole)

%Data structure:
%NMAX:    maximum number of nodes (including disabled ones)
%LINKMAX: maximum number of links (including disabled ones)
%rn: (NMAX,4) array of nodal positions (last column is flag: -1 means disabled)
%vn: (NMAX,3) array of nodal velocities
%fn: (NMAX,3) array of nodal forces
%links: (LINKMAX,8) array of links (id1,id2,bx,by,bz,nx,ny,nz)

%% Compile any c source code

% compile the c source code for seg-seg force evaluation and makes a dynamic ...
    linked library
% DHT
% Only necessary to do this if the c file has been edited
%mex -O SegSegForces.c
%mex -O SegSegForcesMex.c % This one!
%

%% Preliminaries

```

```
%default value if run by itself (e.g. not through "rundd3d")
% cleanup the empty node and link entries at the end of the initial data ...
    structures
[rn,links]=cleanupnodes(rn,links);

%genererate the connectivity list from the list of links
[connectivity,linksinconnect]=genconnectivity(rn,links,maxconnections);
consistencycheck(rn,links,connectivity,linksinconnect);

%prepare for figures
figure(1);

data=zeros(totalsteps,1);
sumdata=zeros(totalsteps,1);
plasticStrain11=zeros(totalsteps,1);
plasticStrain12=zeros(totalsteps,1);
plasticStrain13=zeros(totalsteps,1);
plasticStrain21=zeros(totalsteps,1);
plasticStrain22=zeros(totalsteps,1);
plasticStrain23=zeros(totalsteps,1);
plasticStrain31=zeros(totalsteps,1);
plasticStrain32=zeros(totalsteps,1);
plasticStrain33=zeros(totalsteps,1);
if(~exist('dt','var'))
    dt=dt0;
end
dt=min(dt,dt0);
mdold=10;
counter=0;

% DHT
% Define plastic strain for glide-to-climb switch check
plasticStrainOld = zeros(3,3); % Initialise
plasticStrain = zeros(3,3,totalsteps);
%

% DHT
% Need curstep counter since for loop changed to while loop (for easy safe exits)
curstep = 1; % Initialise
glidestep = 0;

%% Main while loop

while curstep <= totalsteps

    % DHT
    % Store data for pretty plotting
    varnameRN = genvarname('RN', who);
    eval([varnameRN ' = rn;']);
    varnameLINKS = genvarname('LINKS', who);
    eval([varnameLINKS ' = links;']);
    varnameDATA = genvarname('DATA', who);
    eval([varnameDATA ' = sum(data)*Bglide_SI/MU_SI;']);
    %

    % DHT
    % Safe exit if all dislocations (well, nodes) have disappeared
    if isempty(rn)
        plotandlabelnodes(rn,links,plim,viewangle,curstep,data,doGlide);
        frameCounter = recordFrame(doMovie,curstep,1,frameCounter);
        break
```

```
94      end
95
96      %integrating equation of motion
97      [rnnew,vn,dt,fn,fseg]=feval(integrator,rn,dt,dt0,MU,NU,a,Ec,...
98          links,connectivity,appliedstress,rmax,rntol,mobility);
99      % plastic strain and plastic spin calculations
100     [ep_inc,wp_inc]=calcplasticstrainincrement(rnnew,rn,links,(2*plim)^3);
101
102     % DHT
103     % Increment plastic strain tensor
104     plasticStrainNew = plasticStrainOld + ep_inc;
105     plasticStrain11(curstep,1) = plasticStrainNew(1,1);
106     plasticStrain12(curstep,1) = plasticStrainNew(1,2);
107     plasticStrain13(curstep,1) = plasticStrainNew(1,3);
108     plasticStrain21(curstep,1) = plasticStrainNew(2,1);
109     plasticStrain22(curstep,1) = plasticStrainNew(2,2);
110     plasticStrain23(curstep,1) = plasticStrainNew(2,3);
111     plasticStrain31(curstep,1) = plasticStrainNew(3,1);
112     plasticStrain32(curstep,1) = plasticStrainNew(3,2);
113     plasticStrain33(curstep,1) = plasticStrainNew(3,3);
114     %
115
116     if(mod(curstep-1,printfreq)==0)
117         if doGlide == 1 % GLIDE STEP
118             disp(fprintf('step%3d dt=%e v%d=(%e,%e,%e)',...
119                 curstep,dt,printnode,vn(printnode,1),vn(printnode,2),...
120                 vn(printnode,3)));
121         else            % CLIMB STEP
122             disp(fprintf(2,'step%3d dt=%e v%d=(%e,%e,%e)',...
123                 curstep,dt,printnode,vn(printnode,1),vn(printnode,2),...
124                 vn(printnode,3)));
125         end
126     end
127     if(mod(curstep-1,plotfreq)==0)
128         plotandlabelnodes(rn,links,plim,viewangle,curstep,data,doGlide);
129     end
130
131     % DHT
132     % Movie frame recording
133     if(mod(curstep-1,frameFreq)==0)
134         frameCounter = recordFrame(doMovie,curstep,plotfreq,frameCounter);
135     end
136     %
137
138     rnnew=[rnnew(:,1:3) vn rnnew(:,4)];
139     linksnew=links;
140     connectivitynew=connectivity;
141     linksinconnectnew=linksinconnect;
142     fsegnew=fseg;
143
144     if(doseparation)
145         %spliting of nodes with 4 or more connections
146         [rnnew,linksnew,connectivitynew,linksinconnectnew,fsegnew]=...
147           separation(rnnew,linksnew,connectivitynew,linksinconnectnew,...
148                      fsegnew,mobility,MU,NU,a,Ec,2*rann,appliedstress);
149     end
150
151     if(docollision)
152         %collision detection and handling
153         [rnnew,linksnew,connectivitynew,linksinconnectnew,fsegnew]=...
154           collision(rnnew,linksnew,connectivitynew,linksinconnectnew,...
```

```
                    fsegnew,rann,MU,NU,a,Ec,mobility,appliedstress);
end

if(doremesh)
    %remesh
    [rnnew,linksnew,connectivitynew,linksinconnectnew,fsegnew]=...
        remesh(rnnew,linksnew,connectivitynew,linksinconnectnew,...
               fsegnew,lmin,lmax,areamin,areamax,MU,NU,a,Ec,...
               appliedstress,mobility);
end

rn=[rnnew(:,1:3) rnnew(:,7)];
vn=rnnew(:,4:6);
links=linksnew;
connectivity=connectivitynew;
linksinconnect=linksinconnectnew;
fseg=fsegnew;
%store run time information
%time step
data(curstep,1)=dt;
sumdata(curstep,1)=sum(data)*Bglide_SI/MU_SI;

%% Glide-to-climb switch check (DHT)

if curstep ~= 1 && doGlide == 1 % Avoid dividing by zero error when
                                % old plastic strain is zero
    % GLIDE STEP
    glidestep = glidestep + 1;
    % Time-step switch check
    % Default
    strainRatio = abs(1-...
        (sqrt(trace(plasticStrainNew'*plasticStrainNew))/...
         sqrt(trace(plasticStrainOld'*plasticStrainOld))));
    % Use deviatoric strains instead
    %plasticStrainNewDev = plasticStrainNew -...
    %    ((1/3)*trace(plasticStrainNew)).*eye(3,3);
    %plasticStrainOldDev = plasticStrainOld -...
    %    ((1/3)*trace(plasticStrainOld)).*eye(3,3);
    %strainRatio = abs(1-...
    %    (sqrt(trace(plasticStrainNewDev'*plasticStrainNewDev))/...
    %     sqrt(trace(plasticStrainOldDev'*plasticStrainOldDev))));
    if strainRatio < minStrainRatio && glidestep > minglidesteps - 1
        doGlide = 0; % Switch to climb
        climbstep = 0;
        Bscrew=Beclimb;
        Bedge=Beclimb;
        Bline=BlineRatio*Beclimb;
    end
elseif curstep ~= 1
    % CLIMB STEP
    climbstep = climbstep + 1;
    if climbstep == maxclimbsteps
        doGlide = 1; % Switch back to glide
        glidestep = 0;
        Bscrew=1;
        Bedge=1;
        Bline=BlineRatio*min(Bscrew,Bedge);
    end
end

%%
```

```
216
217     % DHT
218     plasticStrainOld = plasticStrainNew;
219     curstep = curstep + 1;
220     %
221
222     save restart
223
224 end
225 %
226
227 save restart
```

B.2 Code added to existing functions

B.2.1 `segforcevec` (excerpt)

Only the first 147 lines are shown.

```
1  function [fseg]=segforcevec(MU,NU,a,Ec,rn,links,sigext,linkid)
2  %compute nodal driving force of dislocation network by stress formula
3  %(vectorized version)
4  %rn: nodal position
5  %links: dislocation segments (connectivity, Burgers vector)
6  %sigext: external stress (applied)
7
8  %segment contribution to node force
9
10 %NMAX: max number of nodes[NMAX,m]=size(rn);
11 [NMAX,m]=size(rn);
12 if(m~=4)
13     disp('rn should have 4 columns!');
14     return;
15 end
16 [LINKMAX,m]=size(links);
17
18 %construct segment list
19 segments=constructsegmentlist(rn,links);
20 if linkid==0
21     %PK force due to applied stress
22     %t0=clock;
23     fpk=pkforcevec(sigext,segments);
24     %t=etime(clock,t0); disp(sprintf('pkforcevec time = %6.2f seconds\n',t));
25
26     % DHT
27     % Osmotic force due to vacancy supersaturation
28     fos=osmoticforcevec(segments);
29     %
30
31     %self force due to self stress
32     %t0=clock;
33     [fs0,fs1]=selfforcevec(MU,NU,a,Ec,segments);
34     %t=etime(clock,t0); disp(sprintf('selfforcevec time = %6.2f seconds\n',t));
```

```
35
36      %remote force due to remote stress
37      %t0=clock;
38      %[fr0,fr1]=remoteforcevec(MU,NU,a,segments,0);
39      [fr0,fr1]=remoteforcevec_mex(MU,NU,a,segments,0);
40      %t=etime(clock,t0); disp(sprintf('remoteforcevec time = %6.2f seconds\n',t));
41
42      %add force contributions together
43      % DHT
44      %fseg=[fpk, fpk]*0.5+[fs0, fs1]+[fr0, fr1];
45      fseg=[fpk, fpk]*0.5+[fos, fos]*0.5+[fs0, fs1]+[fr0, fr1];
46      %
47  else
48      %PK force due to applied stress
49      %t0=clock;
50      fpk=pkforcevec(sigext,segments(linkid,:));
51      %t=etime(clock,t0); disp(sprintf('pkforcevec time = %6.2f seconds\n',t));
52
53      % DHT
54      % Osmotic force due to vacancy supersaturation
55      fos=osmoticforcevec(segments(linkid,:));
56      %
57
58      %self force due to self stress
59      %t0=clock;
60      [fs0,fs1]=selfforcevec(MU,NU,a,Ec,segments(linkid,:));
61      %t=etime(clock,t0); disp(sprintf('selfforcevec time = %6.2f seconds\n',t));
62
63      %remote force due to remote stress
64      %t0=clock;
65      %[fr0,fr1]=remoteforcevec(MU,NU,a,segments,linkid);
66      [fr0,fr1]=remoteforcevec_mex(MU,NU,a,segments,linkid);
67      %t=etime(clock,t0); disp(sprintf('remoteforcevec time = %6.2f seconds\n',t));
68
69      %add force contributions together
70      % DHT
71      %fseg=[fpk, fpk]*0.5+[fs0, fs1]+[fr0, fr1];
72      fseg=[fpk, fpk]*0.5+[fos, fos]*0.5+[fs0, fs1]+[fr0, fr1];
73      %
74  end
75
76  %%%%%%%%%%%%%%%%%%%%%%%%%%%%%%%%%%%%%%%%%%%%%%%%%%%%%%%%%%%%%%%%%%%%%%%%%%%%%%%
77
78  function segments=constructsegmentlist(rn,links)
79
80  [LINKMAX,m]=size(links);
81
82  segments=zeros(LINKMAX,14);
83  nseg=0;
84  for i=1:LINKMAX,
85      n0=links(i,1);
86      n1=links(i,2);
87      if((n0~=0)&(n1~=0))
88          nseg=nseg+1;
89          segments(nseg,:)=...
90              [links(i,1:5),rn(n0,1:3),rn(n1,1:3),links(i,6:8)];
91      end
92  end
93  segments=segments(1:nseg,:);
94
95  %%%%%%%%%%%%%%%%%%%%%%%%%%%%%%%%%%%%%%%%%%%%%%%%%%%%%%%%%%%%%%%%%%%%%%%%%%%%%%%
```

```
96
97  function f=pkforcevec(sigext,segments)
98  %nodal force on dislocation segments due to applied stress sigext
99  %(vectorized version)
100 %format of segments array:
101 % (n0,n1,bx,by,bz,x0,y0,z0,x1,y1,z1,nx,ny,nz)
102 [nseg,m]=size(segments);
103 f=zeros(nseg,3);
104
105 b=segments(:,3:5);
106 sigb=sigext*b';
107 r0=segments(:,6:8);
108 r1=segments(:,9:11);
109 r01=r1-r0;
110
111 for i=1:nseg,
112     f(i,:)=cross(sigb(:,i)',r01(i,:));
113 end
114
115 %%%%%%%%%%%%%%%%%%%%%%%%%%%%%%%%%%%%%%%%%%%%%%%%%%%%%%%%%%%%%%%%%%%%%%%%%%%%
116 function f=osmoticforcevec(segments)
117 % DHT
118 %nodal force on dislocation segments due to osmotic force
119 %(vectorized version)
120
121 % DHT
122 global osmoticForceVac
123
124 %format of segments array:
125 % (n0,n1,bx,by,bz,x0,y0,z0,x1,y1,z1,nx,ny,nz)
126 [nseg,~]=size(segments);
127 f=zeros(nseg,3);
128
129 b=segments(:,3:5);
130 r0=segments(:,6:8);
131 r1=segments(:,9:11);
132 r01=r1-r0;
133
134 L=sqrt(sum(r01.*r01,2)); % Lengths of dislocation segments
135 LInv=1./L;
136 t=r01.*[LInv LInv LInv]; % Tangent line direction of dislocation
137
138 f=osmoticForceVac.*cross(b,t);
139
140 %normals=segments(:,12:14);
141 %for i=1:nseg
142 %    f(i,:)=(fTemp(i,:)*normals(i,:)').*normals(i,:);
143 %end
144
145 %%%%%%%%%%%%%%%%%%%%%%%%%%%%%%%%%%%%%%%%%%%%%%%%%%%%%%%%%%%%%%%%%%%%%%%%%%%%
146
147 % Code continues...
```

B.2.2 `segforcevecInt` (excerpt)

Only the `osmoticforcevec` subroutine is shown. The rest of the code is identical to that in `segforcevec`.

```
116 function f=osmoticforcevec(segments)
117 % DHT
118 %nodal force on dislocation segments due to osmotic force
119 %(vectorized version)
120
121 % DHT
122 global osmoticForceInt
123
124 %format of segments array:
125 % (n0,n1,bx,by,bz,x0,y0,z0,x1,y1,z1,nx,ny,nz)
126 [nseg,~]=size(segments);
127 f=zeros(nseg,3);
128
129 b=segments(:,3:5);
130 r0=segments(:,6:8);
131 r1=segments(:,9:11);
132 r01=r1-r0;
133
134 L=sqrt(sum(r01.*r01,2)); % Lengths of dislocation segments
135 LInv=1./L;
136 t=r01.*[LInv LInv LInv]; % Tangent line direction of dislocation
137
138 f=osmoticForceInt.*cross(b,t);
139
140 %normals=segments(:,12:14);
141 %for i=1:nseg
142 %    f(i,:)=(fTemp(i,:)*normals(i,:)').*normals(i,:);
143 %end
```

B.2.3 `mobbcc0`

```
1  function [vn,fn] = mobbcc0(fseg,rn,links,connectivity,nodelist,conlist)
2  %mobility law function (model: BCC0)
3  global Bscrew Bedge Beclimb Bline
4
5  % DHT
6  global doGlide inclusions impenetrable radiusCore
7  %
8
9  %numerical tolerance
10 eps=1e-12;
11
12 % length of the nodelist for which the velocity will be calculated
13 L1=size(nodelist,1);
14 % if no nodelist is given then the nodelist becomes the whole node population
15 % this portion of the code sets up that nodelist along with the connlist
16 % that contains all of the nodal connections
```

```
if L1==0
  L1=size(rn,1);
  nodelist=linspace(1,L1,L1)';
  [L2,L3]=size(connectivity);
  conlist=zeros(L2,(L3-1)/2+1);
  conlist(:,1)=connectivity(:,1);
  for i=1:L2
    connumb=conlist(i,1);
    conlist(i,2:connumb+1)=linspace(1,connumb,connumb);
  end
end
% now cycle through all of the nodes for which the velocity must be calculated

for n=1:L1
  n0=nodelist(n);       %n0 is the nodeid of the nth node in nodelist
  numNbrs=conlist(n,1); %numNbrs is the number of connections for node n0 in ...
      conlist
  fn(n,:)=zeros(1,3);   % initialize the total force and the total drag matrix
  Btotal=zeros(3,3);
  for i=1:numNbrs
    ii=conlist(n,i+1);                % connectionid for this connection
    linkid=connectivity(n0,2*ii);
    posinlink=connectivity(n0,2*ii+1);
    n1=links(linkid,3-posinlink);
    rt=rn(n1,1:3)-rn(n0,1:3);         % calculate the length of the link and ...
        its tangent line direction
    L=norm(rt);
    if L>0.0
      fsegn0=fseg(linkid,3*(posinlink-1)+[1:3]);
      fn(n,:)=fn(n,:)+fsegn0; % nodeid for the node that n0 is connected to
      burgv=links(connectivity(n0,2*ii),3:5); % burgers vector of the link
      linedir=rt./L;

      % DHT
      % The following 3 + 1 lines are commented out to allow non
      % [111]-type dislocations to glide with the glide drag
      % (rather than glide and climb isotropically with the climb
      % drag - a fudge used to reproduce sessile [111] junction
      % formation).
      %if abs(burgv(1)*burgv(2)*burgv(3))<eps
      %    Btotal=Btotal+(2.0*L).*((Beclimb).*eye(3)+...
      %           (Bline-Beclimb).*(linedir'*linedir));
      %else

        cth2=(linedir*burgv')^2/(burgv*burgv'); % calculate how close to ...
            screw the link is
        Btotal=Btotal+(2.0*L).*((Bscrew).*eye(3)+...
               (Bline-Bscrew).*(linedir'*linedir)); % build the drag matrix ...
                   assuming that the dislocation is screw type
        if ( 1 - cth2 ) >eps

          % DHT
          ndir=cross(burgv,linedir)./sqrt((burgv*burgv')*(1-cth2)); % correct ...
              the drag matrix for dislocations that are not screw type
          %ndir=links(connectivity(n0,2*ii),6:8);
          %

          mdir=cross(ndir,linedir);

          % DHT
          % Calculate climb only cpt of the force on this segment
```

```
73            fsegn0cl=(fsegn0*ndir').*ndir;
74            % If glide step
75            if doGlide==1
76              % Subtract climb only cpt from nodal force
77              fn(n,:)=fn(n,:)-fsegn0cl; % nodeid for the node that n0 is ...
                    connected to
78            else % If climb step
79              % Subtract glide only cpt from nodal force
80              fn(n,:)=fn(n,:)-fsegn0+fsegn0cl; % nodeid for the node that n0 is ...
                    connected to
81            end
82            %
83
84            Bglide=1/sqrt(1/Bedge^2 + (1/Bscrew^2 - 1/Bedge^2)*cth2);
85
86            % DHT
87            % The following line is adjusted to include the
88            % dislocation specific factor of Beclimb (it is simply (bsin(theta))^2)
89            % which is missing up to this point
90            %Bclimb=sqrt( Beclimb^2 + ( Bscrew^2 - Beclimb^2 ) * cth2);
91            Bclimb=sqrt((Beclimb*sum(burgv*burgv')*(1-cth2))^2 +...
92                        (Bscrew^2 -...
93                          (Beclimb*sum(burgv*burgv')*(1-cth2))^2 )*cth2);
94            %
95
96            Btotal=Btotal+(2.0*L).*((Bglide-Bscrew).*(mdir'*mdir) +...
97                                    (Bclimb-Bscrew).*(ndir'*ndir));
98          end
99        %end
100       %
101     end
102   end
103
104   if rcond(Btotal)<eps
105
106     [evec,eval]=eig(Btotal); % find eigenvalues and eigen vectors of drag matrix
107     evalmax=eval(1,1);
108     eval=eval./evalmax;
109     fvec=fn(n,:)'./evalmax;
110     for i=2:3 % invert drag matrix and keep zero eigen values as zero
111       if eval(i,i)>eps
112         eval(i,i)=1/eval(i,i);
113       else
114         eval(i,i)=0.0d0;
115       end
116     end
117     vn(n,:)=(evec*eval*evec'*fvec)'; % calculate the velocity
118   else
119     vn(n,:)=(Btotal\fn(n,:)')'; % Btotal was wellconditioned so just take the ...
          inverse
120   end
121
122 %  if numNbrs==2
123 %    ii=conlist(n,2);
124 %    n1=links(connectivity(n0,2*ii),3-connectivity(n0,2*ii+1));
125 %    ii=conlist(n,3);
126 %    n2=links(connectivity(n0,2*ii),3-connectivity(n0,2*ii+1));
127 %    rt=rn(n1,1:3)-rn(n2,1:3);
128 %    L=norm(rt);
129 %    linedir=rt./L;
130 %    vn(n,:)=((eye(3)-linedir'*linedir)*vn(n,:)')';
```

```
%  end

end

% DHT
if ~isempty(inclusions) && impenetrable==1
  % Loop through nodal positions
  [nincl,~] = size(inclusions);
  for node = 1:L1
    n0=nodelist(node);
    numNbrs = conlist(node,1);
    nodePosition = rn(n0,1:3);
    % Loop through inclusions
    for incl = 1:nincl
      % If this node is inside this inclusion
      inclRadius = inclusions(incl,1);
      inclPosition  = inclusions(incl,2:4);
      vectorFromNodeToInclCentre = inclPosition - nodePosition;
      distanceFromNodeToInclCentre = norm(vectorFromNodeToInclCentre);
      if distanceFromNodeToInclCentre < (radiusCore + inclRadius)
        for i = 1:numNbrs
          ii = conlist(node,i+1);
          linkid = connectivity(n0,2*ii);
          posinlink = connectivity(n0,2*ii+1);
          n1 = links(linkid,3-posinlink);
          rt = rn(n1,1:3) - rn(n0,1:3);
          L = norm(rt);
          burgv = links(connectivity(n0,2*ii),3:5);
          linedir = rt./L;
          cth2 = (linedir*burgv')^2/(burgv*burgv');
          if ( 1 - cth2 ) > eps
            ndir = cross(burgv,linedir)./sqrt((burgv*burgv')*(1-cth2));
            % Only allow the node to move in climb direction
            vn(node,:) = (vn(node,:)*ndir').*ndir;
          end
        end
        % If node is climbing further into inclusion
        dt = 1/norm(vn(node,:));
        newNodePosition = rn(n0,1:3) + vn(node,:).*dt;
        newVectorFromNodeToInclCentre = inclPosition - newNodePosition;
        newDistanceFromNodeToInclCentre =...
          norm(newVectorFromNodeToInclCentre);
        if newDistanceFromNodeToInclCentre < inclRadius
          % Fully pin it (zero velocity)
          vn(node,:) = [0 0 0];
        end
        %
      end
    end
  end
end
%
```

B.2.4 `mobbcc0Int`

```
function [vn,fn] = mobbcc0Int(fseg,rn,links,connectivity,nodelist,conlist)
%mobility law function (model: BCC0)
global Bscrew Bedge Beclimb Bline

% DHT
global inclusions impenetrable radiusCore
%

% DHT
% Switch to interstitial climb drag
global BeclimbVac BeclimbInt BlineRatio doGlide
Beclimb=BeclimbInt;
if doGlide==0
  Bscrew=Beclimb;
  Bedge=Beclimb;
  Bline=BlineRatio*Beclimb;
end
%

%numerical tolerance
eps=1e-12;

% length of the nodelist for which the velocity will be calculated
L1=size(nodelist,1);
% if no nodelist is given then the nodelist becomes the whole node population
% this portion of the code sets up that nodelist along with the connlist
% that contains all of the nodal connections
if L1==0
  L1=size(rn,1);
  nodelist=linspace(1,L1,L1)';
  [L2,L3]=size(connectivity);
  conlist=zeros(L2,(L3-1)/2+1);
  conlist(:,1)=connectivity(:,1);
  for i=1:L2
    connumb=conlist(i,1);
    conlist(i,2:connumb+1)=linspace(1,connumb,connumb);
  end
end
% now cycle through all of the nodes for which the velocity must be calculated

for n=1:L1
  n0=nodelist(n);       %n0 is the nodeid of the nth node in nodelist
  numNbrs=conlist(n,1); %numNbrs is the number of connections for node n0 in ...
      conlist
  fn(n,:)=zeros(1,3);   % initialize the total force and the total drag matrix
  Btotal=zeros(3,3);
  for i=1:numNbrs
    ii=conlist(n,i+1);                % connectionid for this connection
    linkid=connectivity(n0,2*ii);
    posinlink=connectivity(n0,2*ii+1);
    n1=links(linkid,3-posinlink);
    rt=rn(n1,1:3)-rn(n0,1:3);         % calculate the length of the link and ...
        its tangent line direction
    L=norm(rt);
    if L>0.0
      fsegn0=fseg(linkid,3*(posinlink-1)+[1:3]);
```

```
55        % DHT
56        % Line 53 has been moved to line 79
57        %fn(n,:)=fn(n,:)+fsegn0;
58        %
59        burgv=links(connectivity(n0,2*ii),3:5); % burgers vector of the link
60        linedir=rt./L;
61
62        % DHT
63        % The following 3 + 1 lines are commented out to allow non
64        % [111]-type dislocations to glide with the glide drag
65        % (rather than glide and climb isotropically with the climb
66        % drag - a fudge used to reproduce sessile [111] junction
67        % formation).
68        %if abs(burgv(1)*burgv(2)*burgv(3))<eps
69        %    Btotal=Btotal+(2.0*L).*((Beclimb).*eye(3)+...
70        %           (Bline-Beclimb).*(linedir'*linedir));
71        %else
72
73          cth2=(linedir*burgv')^2/(burgv*burgv'); % calculate how close to ...
              screw the link is
74          Btotal=Btotal+(2.0*L).*((Bscrew).*eye(3)+...
75              (Bline-Bscrew).*(linedir'*linedir)); % build the drag matrix ...
                  assuming that the dislocation is screw type
76          if ( 1 - cth2 ) >eps
77
78            % DHT
79            ndir=cross(burgv,linedir)./sqrt((burgv*burgv')*(1-cth2)); % correct ...
                  the drag matrix for dislocations that are not screw type
80            %ndir=links(connectivity(n0,2*ii),6:8);
81            %
82
83            mdir=cross(ndir,linedir);
84
85            % DHT
86            % Calculate climb only cpt of the force on this segment
87            fsegn0=(fsegn0*ndir').*ndir;
88            % Line (79) has been moved from line 53
89            % NB this means any "pure screw" segments do not contribute any ...
                  force to the node
90            fn(n,:)=fn(n,:)+fsegn0; % nodeid for the node that n0 is connected to
91            %
92
93            Bglide=1/sqrt(1/Bedge^2 + (1/Bscrew^2 - 1/Bedge^2)*cth2);
94            % DHT
95            % The following line is adjusted to include the
96            % dislocation specific factor of Beclimb (it is simply (bsin(theta))^2)
97            % which is missing up to this point
98            %Bclimb=sqrt( Beclimb^2 + ( Bscrew^2 - Beclimb^2 ) * cth2);
99            Bclimb=sqrt((Beclimb*sum(burgv*burgv')*(1-cth2))^2 +...
100                       (Bscrew^2 -...
101                         (Beclimb*sum(burgv*burgv')*(1-cth2))^2)*cth2);
102           %
103           Btotal=Btotal+(2.0*L).*((Bglide-Bscrew).*(mdir'*mdir) +...
104                                   (Bclimb-Bscrew).*(ndir'*ndir));
105         end
106       %end
107       %
108     end
109   end
110
111   if rcond(Btotal)<eps
```

```
112
113     [evec,eval]=eig(Btotal); % find eigenvalues and eigen vectors of drag matrix
114     evalmax=eval(1,1);
115
116     % DHT
117     % Avoid NaN or Inf when evalmax==0
118     if evalmax==0
119       evalmax=eps;
120     end
121     %
122
123     eval=eval./evalmax;
124     fvec=fn(n,:)'./evalmax;
125     for i=2:3 % invert drag matrix and keep zero eigen values as zero
126       if eval(i,i)>eps
127         eval(i,i)=1/eval(i,i);
128       else
129         eval(i,i)=0.0d0;
130       end
131     end
132     vn(n,:)=(evec*eval*evec'*fvec)'; % calculate the velocity
133   else
134     vn(n,:)=(Btotal\fn(n,:)')'; % Btotal was wellconditioned so just take the ...
          inverse
135   end
136
137 %  if numNbrs==2
138 %    ii=conlist(n,2);
139 %    n1=links(connectivity(n0,2*ii),3-connectivity(n0,2*ii+1));
140 %    ii=conlist(n,3);
141 %    n2=links(connectivity(n0,2*ii),3-connectivity(n0,2*ii+1));
142 %    rt=rn(n1,1:3)-rn(n2,1:3);
143 %    L=norm(rt);
144 %    linedir=rt./L;
145 %    vn(n,:)=((eye(3)-linedir'*linedir)*vn(n,:)')';
146 %  end
147
148 end
149
150 % DHT
151 if ~isempty(inclusions) && impenetrable==1
152   % Loop through nodal positions
153   [nincl,~] = size(inclusions);
154   for node = 1:L1
155     n0=nodelist(node);
156     nodePosition = rn(n0,1:3);
157     % Loop through inclusions
158     for incl = 1:nincl
159       % If this node is inside this inclusion
160       inclRadius = inclusions(incl,1);
161       inclPosition  = inclusions(incl,2:4);
162       vectorFromNodeToInclCentre = inclPosition - nodePosition;
163       distanceFromNodeToInclCentre = norm(vectorFromNodeToInclCentre);
164       if distanceFromNodeToInclCentre < (radiusCore + inclRadius)
165         % If node is climbing further into inclusion
166         dt = 1/norm(vn(node,:));
167         newNodePosition = rn(n0,1:3) + vn(node,:).*dt;
168         newVectorFromNodeToInclCentre = inclPosition - newNodePosition;
169         newDistanceFromNodeToInclCentre = norm(newVectorFromNodeToInclCentre);
170         if newDistanceFromNodeToInclCentre < inclRadius
171           % Fully pin it (zero velocity)
```

```
172           vn(node,:) = [0 0 0];
173         end
174         %
175       end
176     end
177   end
178 end
179 %
180
181 % DHT
182 % Switch back to vacancy climb drag
183 Beclimb=BeclimbVac;
184 if doGlide==0
185   Bscrew=Beclimb;
186   Bedge=Beclimb;
187   Bline=BlineRatio*Beclimb;
188 end
189 %
```

B.2.5 drndt

```
1  function [vnvec,fn,fseg] = drndt(t,rnvec,flag,MU,NU,a,Ec,...
2      links,connectivity,appliedstress,mobility)
3
4  % DHT
5  global Bscrew Bedge Bline BlineRatio Beclimb doGlide climbstep mobilityInt
6  %
7
8  %unscramble rn
9  rn=[reshape(rnvec,length(rnvec)/3,3),flag];
10
11 %rn(:,1:3)
12
13 %nodal driving force
14 % Calculate forces on segments including osmotic force due to vacancy ...
       supersaturation
15 fseg=segforcevec(MU,NU,a,Ec,rn,links,appliedstress,0);
16
17 %mobility function
18 % Calculate nodal velocities using vacancy climb drag
19 [vn,fn]=feval(mobility,fseg,rn,links,connectivity,[],[]);
20
21 % DHT
22 % If climb step
23 if doGlide == 0
24     % Calculate forces on segments including osmotic force due to ...
           interstitial supersaturation
25     fsegInt = segforcevecInt(MU,NU,a,Ec,rn,links,appliedstress,0);
26     % Calculate nodal velocities using interstital climb drag
27     % Different mobility file required to avoid double counting of non-climb ...
           forces
28     [vnInt,fnInt] = feval(mobilityInt,fsegInt,rn,links,connectivity,[],[]);
29     % Sum results
30     vn = vn + vnInt;
31     fn = fn + fnInt;
32 end
```

```
%

%fixed nodes (flag==7) are not allowed to move
vn=vn.*((rn(:,4)~=7)*[1 1 1]);

%make up the last
vnvec=reshape(vn,length(vn(:,1))*3,1);

%vn
%disp(sprintf('t=%20.10e ...
    vn(1,:)=(%20.10e,%20.10e,%20.10e)',t,vn(1,1),vn(1,2),vn(1,3)));
%pause(0.2)
%if(t>0)
%   pause
%end
```

B.3 New functions

B.3.1 `calcClimbDragVac`

```
function [climbDragVac] = calcClimbDragVac
% DHT
% Climb drag

global k
global MU_SI a_SI Bglide_SI
global atomVol vacFormEnergy vacMigrEnergy diffCoeffPreExpo
global radiusCore radiusInfinity
global temperature

% DDLab base units are:
% [D] = Bglide (glide drag factor = [PT] = [FT/L^2])
% [L] = a (lattice parameter)
% [P] = MU (shear modulus = [F/L^2])

% Switch to DDLab units
k_DD = k/(MU_SI*a_SI^3);
atomVol_DD = atomVol/a_SI^3;
diffCoeffPreExpo_DD = diffCoeffPreExpo*Bglide_SI/(MU_SI*a_SI^2);

% Calculate self-diffusion coefficient in DDLab units
selfDiffCoeff_DD = diffCoeffPreExpo_DD*...
                   exp(-(vacFormEnergy+vacMigrEnergy)/(k*temperature));

% Calculate Beclimb in DDLab units
climbDragVac = k_DD*temperature*log(radiusInfinity/radiusCore)/...
            (2*pi*selfDiffCoeff_DD*atomVol_DD);

end
```

B.3.2 calcOsmoticForceVac

```
function [osmoticForceVac] = calcOsmoticForceVac
% DHT
% Osmotic force

global k MU_SI a_SI atomVol temperature c0Vac cInfinityVac

if cInfinityVac < c0Vac
    osmoticForceVac = 0;
else

    % DDLab base units are:
    % [D] = Bglide (glide drag factor = [PT] = [FT/L^2])
    % [L] = a (lattice parameter)
    % [P] = MU (shear modulus = [F/L^2])

    % Switch to DDLab units
    k_DD = k/(MU_SI*a_SI^3);
    atomVol_DD = atomVol/a_SI^3;

    % Calculate osmoticForce in DDLab units
    osmoticForceVac = -((k_DD*temperature)/atomVol_DD)*...
                        (1-(cInfinityVac/c0Vac));

end

end
```

B.3.3 calcClimbDragInt

```
function [climbDragInt] = calcClimbDragInt
% DHT
% Climb drag

global k
global MU_SI a_SI Bglide_SI
global atomVol intFormEnergy intMigrEnergy diffCoeffPreExpo
global radiusCore radiusInfinity
global temperature

% DDLab base units are:
% [D] = Bglide (glide drag factor = [PT] = [FT/L^2])
% [L] = a (lattice parameter)
% [P] = MU (shear modulus = [F/L^2])

% Switch to DDLab units
k_DD = k/(MU_SI*a_SI^3);
atomVol_DD = atomVol/a_SI^3;
diffCoeffPreExpo_DD = diffCoeffPreExpo*Bglide_SI/(MU_SI*a_SI^2);

% Calculate self-diffusion coefficient in DDLab units
selfDiffCoeff_DD = diffCoeffPreExpo_DD*...
```

```
                    exp(-(intFormEnergy+intMigrEnergy)/(k*temperature));

% Calculate Beclimb in DDLab units
climbDragInt = k_DD*temperature*log(radiusInfinity/radiusCore)/...
            (2*pi*selfDiffCoeff_DD*atomVol_DD);

end
```

B.3.4 `calcOsmoticForceInt`

```
function [osmoticForceInt] = calcOsmoticForceInt
% DHT
% Osmotic force

global k MU_SI a_SI atomVol temperature c0Int cInfinityInt

if cInfinityInt < c0Int
    osmoticForceInt = 0;
else

    % DDLab base units are:
    % [D] = Bglide (glide drag factor = [PT] = [FT/L^2])
    % [L] = a (lattice parameter)
    % [P] = MU (shear modulus = [F/L^2])

    % Switch to DDLab units
    k_DD = k/(MU_SI*a_SI^3);
    atomVol_DD = atomVol/a_SI^3;

    % Calculate osmoticForce in DDLab units
    osmoticForceInt = ((k_DD*temperature)/atomVol_DD)*...
        (1-(cInfinityInt/c0Int));

end

end
```